Alma Mater Studiorum - Università di Bologna

DOTTORATO DI RICERCA IN

FISICA

Ciclo 36

Settore Concorsuale: 02/B1 - FISICA SPERIMENTALE DELLA MATERIA

Settore Scientifico Disciplinare: FIS/03 - FISICA DELLA MATERIA

STUDY OF CHARGE, SPIN, AND STRUCTURAL ORDERINGS IN QUANTUM MATERIALS USING NUCLEI AND MUONS AS LOCAL PROBES

Presentata da: Jonathan Frassineti

Coordinatore Dottorato

Alessandro Gabrielli

Supervisore

Samuele Sanna

Co-supervisore

Vesna Mitrović

Esame finale anno 2024

Alla mia famiglia, che mi ha cresciuto.

A Lucia, che mi ha reso un uomo migliore.

Senza di loro, non sarei qui oggi.

Abstract

Quantum Materials are many body systems displaying emergent phenomena caused by quantum collective behaviour, such as superconductivity, charge density wave, fractional hall effect, and exotic magnetism. Among quantum materials, two families have recently attracted attention: kagome metals and Kitaev materials.

The kagome metals have a unique crystal structure made up of triangular lattice layers that are used to form the kagome layer. Due to superconductivity, magnetism, and charge ordering states such as the Charge Density Wave (CDW), unexpected physical phenomena such as the massive Anomalous Hall Effect (AHE) and possible Majorana fermions develop in these materials.

Kitaev materials are a type of quantum material with a unique spin model named after Alexei Kitaev. They include fractional fluctuations of Majorana fermions and non-topological abelian anyons, both of which might be used in quantum computing. Furthermore, they provide a realistic framework for the development of quantum spin liquid (QSL), in which quantum fluctuations produce long-range entanglements between electronic states despite the lack of *classical* magnetic ordering.

In my research, I performed several nuclear magnetic resonance (NMR), nuclear quadrupole resonance (NQR), and muon spin spectroscopy (μSR) experiments to explain and unravel novel phases of matter within this unusual family of materials. NMR has been found to be an excellent tool for studying these materials' local electronic structures and magnetic properties. I could use NMR to determine, for the first time, the structure of a novel kagome superconductor, RbV_3Sb_5, below the CDW transition, and to highlight the role of chemical doping in the CDW phase of AV_3Sb_5 superconductors.

μSR has been used to investigate the effect of doping on kagome material samples in order to study the presence and behaviour of an anomalous phase

developing at low temperatures and possibly related to time-reversal symmetry breaking.

Anomalous oscillations of the muon asymmetry observed in the normal state of A15 compounds gave us the possibility to accurately study the quantum entanglement between muon and nuclear spin greater than 1/2, providing a proof of concept for how μSR can be used to probe charge-related phenomena.

Finally, the use of μSR in addition to neutron scattering experiments, DFT, and CEF calculations revealed the magnetic excitation spectra of the Kitaev antiferromagnet Na_2PrO_3, revealing unusual information about the nature of its magnetic ground-state.

Contents

Collaborations

This Ph.D. work has been conducted in different locations with prestigious research groups.

I would like to thank Prof. Samuele Sanna who supervised me and helped me start the Ph.D. project in the best way possible. In addition to this, his experience in NMR and μSR guided me across the three years in organizing, discussing, and presenting my works properly.

From the Department of Physics at Brown University, Providence, RI, USA, I would like to thank Prof. Vesna F. Mitrović and Kemp W. Plumb, whose guidance has been incredibly helpful during my research period abroad as a Visiting Research Fellow; furthermore, the NMR lab of Prof. Mitrović's group was an important part of my personal understanding and development of the NMR skills I have now.

Going to the Department of Mathematical, Physical, and Informatics Sciences at the University of Parma, Italy, I would like to thank Prof. Giuseppe Allodi, Dr. Pietro Bonfá, Dr. Ifeanyi John Onourah, and Prof. Roberto de Renzi. With Prof. Allodi I learned what NMR is and how to perform NMR experiments, and I recognize that his experience, knowledge, and patience have no equals across the world. Dr. Bonfá has been one of the best collaborators I ever had since I started my Master's Thesis in 2020; his expertise in ab-initio calculations and Computational Physics helped me a lot to develop high-quality projects in my Ph.D. The help of Dr. Ifeanyi John Onourah has been incredibly precious in developing new computer simulations for both muon and neutron experimental techniques. Finally, the expertise and knowledge of Prof. Roberto de Renzi do not require an introduction, and I thank him a lot for his help.

Finally, I would like to thank the group of Prof. Stephen D. Wilson at the University of California, Santa Barbara, and the group of Prof. Stephen Blundell at Oxford University. With them, I participated in astonishing projects involving NMR and μSR, which have been published in prestigious journals.

List of acronyms

AcqD – Acquisition Delay

AFM – Antiferromagnet

AHE – Anomalous Hall Effect

CDW – Charge-Density Wave

CEF – Crystal Electric Field

DFT – Density Functional Theory

DOS – Density of States

EFG – Electric Field Gradient

FID – Free Induction Decay

FM – Ferromagnet

FWHM – Full-Width-Half-Maximum

HWHM – Half-Width-Half-Maximum

INS – Inelastic Neutron Scattering

IR – Inversion Recovery

KSL – Kitaev Spin Liquid

LF – Longitudinal-Field

μSR – Muon Spin Spectroscopy

NMR – Nuclear Magnetic Resonance

NQR – Nuclear Quadrupole Resonance

PAS – Principal Axis System

PW90 – Pulse Width of 90°

QSL – Quantum Spin Liquid

RD – Repetition Delay

rf – Radiofrequency

RinH – Receiver Inhibition

RixD – Repetition Delay

RSB – Rotational Symmetry Breaking

RT – Room Temperature

RxAT – Receiver Attenuation

SNR – Signal-to-Noise Ratio

SR – Saturation Recovery

SSE – Spin-Stimulated Echo

TF – Transverse-Field

TRSB – Time-Reversal Symmetry Breaking

TxAT – Transmission Attenuation

ZF – Zero-Field

Introduction

Quantum materials, one of the most exciting groups of materials currently, have distinctive and unique features that originate from the quantum mechanical behavior of their component particles. These materials are defined by their strong electron-electron interactions, complicated electronic band structures, and distinct phases of matter. There is significant potential for current technology and basic physics research to understand and use the features of quantum materials. Recently layered quantum materials containing hexagonal arrays have attracted a lot of attention thanks to their peculiar Fermi topology and/or the presence of anisotropic interactions and frustration. Kagome and Kitaev materials have been increasingly studied and characterized in the very last few years, making them one of the most appealing classes of quantum materials. The investigation of these two material families is the main object of this thesis work.

The term *kagome* comes from a traditional Japanese wooden basket and specifies an exotic two-dimensional geometrical array composed of overlapping triangles and large hexagonal voids. It gives a unique platform to comprehend the interweaving between diverse electronic orderings such as superconductivity, long-range magnetism, and CDW, owing to its innate geometrical frustration.

The so-called Kitaev materials, named after Alexei Kitaev, who first developed a theory to explain the ground-state of these materials, are composed of honeycomb edge-sharing lattices that provide strong geometrical frustration and a possible realization of Kitaev Spin Liquid (KSV), characterized by anisotropic interactions. These materials provide a fruitful platform for creating new magnetic orderings and understanding the significance of diverse exchange interactions in shaping the ground-state Hamiltonian.

Among all the potential experimental methods in Condensed Matter Physics, Nuclear Magnetic Resonance (NMR), Nuclear Quadrupole Resonance (NQR), and Muon Spin Spectroscopy (μSR) have the great advantage of studying the material properties by using nuclei and muons as local probes to obtain insights into the electrical structure, magnetic properties, and superconducting behavior of kagome metals and Kitaev materials.

NMR is a method for examining the surroundings and behavior of nuclei, utilizing their inherent magnetic moments, sensitive to local dipolar and hyperfine interactions. NQR, similarly, exploits the interaction of the nuclear electric quadrupole with the electric field gradient around the nucleus and is sensitive to charge-related phenomena.

On the other hand, μSR is an experimental approach that employs muons as local magnetic probes, which are unstable subatomic particles emitting positrons. When muons have been implanted in a material, they function as small magnetic dipoles that are particularly sensitive to local magnetic fields. Crucial information on the material's magnetic and superconducting characteristics can be obtained by probing local magnetic field behavior trough the spatial and temporal decay emission.

Chapter 1 presents a broad introduction to quantum materials, their physical characteristics, and their applications, with a special emphasis on kagome and Kitaev materials.

In Chapter 2, we present the theoretical specifics and the experimental settings of the NMR and NQR techniques.

In Chapter 3, we present the theoretical specifics and the experimental settings of the μSR technique, following the scheme of Chapter 2.

Chapter 4 is devoted to the findings acquired by employing NMR spectroscopy in my Ph.D. research, with a special emphasis on kagome superconductors.

In Chapter 5, we are going to illustrate μSR results applied to quantum materials, notably kagome superconductors.

Chapter 6 concerns the use of μSR to exploit intriguing quantum phenomena like the quantum entanglement between muons and high nuclear spins as a probe of the charge environment.

Chapter 7 will discuss the use of μSR in conjunction with neutron scattering experimental data to comprehend the magnetic ground-state of Kitaev antiferromagnet Na_2PrO_3.

Finally, the chapter Conclusions reports a summary of the main outcomes of this work.

Chapter 1

General background: quantum materials

This Ph.D. thesis is primarily concerned with the physical characterization of novel quantum materials, and we will provide a general overview of them in this first part. In addition, the fundamental physical properties and technological applications of quantum materials will be discussed.

1.1 Definition of quantum materials

The word *quantum materials*, as the name implies, refers to a large group of materials in which quantum mechanics plays a significant and representative role in our macroscopic world. This is not the same as a material whose physical properties are governed by quantum mechanics, as all materials are; a very simple example is represented by semiconductors, which are at the heart of our technological advancement in electronics and informatics, and whose behaviour cannot be described in terms of classical physics.

The idea of free or nearly free electrons, which is based on electrons that are not in contact with one another under a constant lattice potential, has proven beneficial in understanding the fundamental electronics of solid-state systems, including metal and semiconducting behavior. Interactions between particles, such as electron-electron and electron-phonon interactions, have a significant impact on the physical properties of materials in strongly correlated systems, where the Coulomb interaction cannot be ignored and is comparable to or stronger than the kinetic energy of electrons [1]. Superconductivity (SC), complex magnetism, charge density waves (CDW), spin density waves (SDW), nematic/smectic orders, pair density waves (PDW), Mott insulating behavior, and other novel quantum phases with broken symmetry can be produced by electron correlation, which can also cause instabilities at the Fermi surface and drive electronic fluctuations.

All these exotic quantum phenomena have been hugely demonstrated in novel materials such as heavy fermion materials, high-temperature superconductors, complex oxide perovskites, transition metal dichalcogenides, and twisted graphene [2–5]. They do not have to be separate; they can coexist in the same substance and even compete each other. In cuprate superconductors, for example, superconductivity is competing with CDW and SDW phases, and a potential "mother phase" has been identified as PDW.

As a result, the correct definition of "quantum materials" is a family of materials whose primary physical properties are controlled by the strong electrical interaction that gives rise to distinct phases of matter. Superconductivity is a simple example, where the strong electron-phonon-electron interaction produces a macroscopic representation of the ground-state electronic wavefunction. Various types of quantum materials have emerged in recent years, generating considerable interest in the field of condensed matter physics, with the goal of discovering new phases of matter and harnessing them for practical uses. Some examples are Kagome lattices, topological insulators, Weyl semimetals, and quantum spin liquids [6–19]. In this work, we are going to talk about the first and the latter class of materials. Figure 1.1 shows a graphical representation of some of the classes of quantum materials under study in recent years, along with present and future technological applications. In general, quantum materials, according to [21], are those with novel topological or entanglement properties, i.e., materials with an entanglement that exceeds what Fermi statistics require and topological responses, such as

Figure 1.1: Different classes of Quantum materials, with present and future applications of them (taken from [20]).

the quantized vortices found in superconductors [22]. An invariance indicator describes how this phase is connected to magnetic flux, which leads to the creation of these vortices in the superconducting condensate. This integer winding number is a fundamental example of a topological invariant, which is a trait that endures in a system despite smooth changes. Around a vortex, the phase may only wind by an integer multiple of 2.

Cooper pairs are another example of spin or electron entanglement in complex magnets. Conventional graphics are incapable of accurately depicting any of these extraordinary physical phenomena. We can distinguish between innovative and more typical types of quantum order provided by topology and entanglement using phase transitions. This is why the material study has only touched the surface of these tremendously complex quantum states of matter. Figure 1.2 shows some of the above-mentioned quantum phenomena occurring in quantum materials. After all this introduction, let us dive into the classes of materials I personally studied in this Ph.D. thesis, namely Kagome and Kitaev materials.

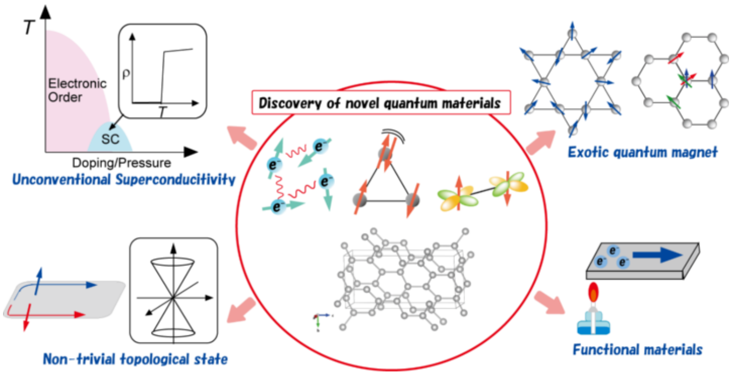

Figure 1.2: Different classes of Quantum materials, along with some peculiar physical phenomena which occur inside them (taken from [23]).

1.2 Kagome materials

Despite the 'fancy' appellation, the term *kagome* has been used in condensed matter physics for a long time to characterize novel materials and their characteristic lattice structure. This word is derived from a Japanese phrase that refers to a traditional Japanese woven bamboo basket design. The primary similarity between the subject of investigation and the materials under consideration is their geometric organisation. There is a certain arrangement of equilateral triangles and regular hexagons in both circumstances, where each hexagon is surrounded by a ring of equilateral triangles, and each equilateral triangle is surrounded by a continuous chain of neighbouring hexagons. This unusual geometric configuration is known as "regular hexagonal and triangular tiling" and is derived from the combination of regular hexagonal and triangular tessellation patterns. Two hexagons and two triangles alternate around each vertex, and their edges create an infinite number of lines. Figure 1.3 shows a graphical representation of what a kagome lattice structure is. This lattice is one of the most fascinating places to study new quantum phenomena in condensed matter. Because of its triangular lattice, it readily hosts geometrical frustration, which leads to magnetic frustration in some kagome magnets, such as the mineral Herbrtsmithite with the chemical formula $ZnCu_3(OH)_6Cl_2$ [24, 25]. This material is also expected to produce valance bond solid states [26] and strongly correlated quantum spin liquid

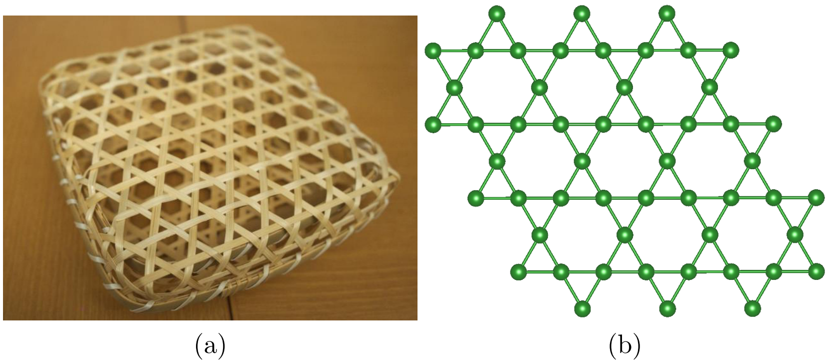
(a) (b)

Figure 1.3: (a) Japanese 'kagome' basket and (b) Kagome lattice structure.

states [27]. Topological Dirac/Weyl/nodal line points, van Hove singularities (vHSs), and flat bands are also observed in this peculiar electronic band structure. The vHSs and flat bands have high state densities and enhanced effective masses, resulting in significant correlations around these bands. Because every kagome material has an electrical band structure, we will use the term kagome metal as a synonym for kagome material. The intrinsic geometric frustration induced by the kagome lattice's triangle structure provides a fertile platform for studying the interplay of magnetic, charge, and ordering frustrated events. A pictorial example of a frustrated magnetic kagome lattice, whose spin cannot order in a classical anti/ferromagnetic way, is shown in Figure 1.4. The electron interaction in the kagome lattice can be described with a Hubbard model, and the typical Hamiltonian takes the form [29, 30]:

$$\begin{aligned}\mathcal{H} &= \mathcal{H}_0 + \mathcal{H}_{int}\\ \mathcal{H}_0 &= \sum_{\{i,j\}\sigma} \left(t_{ij}\hat{c}^{+}_{i\sigma}\hat{c}_{j\sigma} + h.c.\right) + \mu\sum_{i,\sigma} n_{i,\sigma}\\ \mathcal{H}_{int} &= U_0\sum_{i} n_{i\uparrow}n_{i\downarrow} + \frac{U_1}{2}\sum_{<i,j>,\sigma,\sigma'} n_{i,\sigma}n_{j,\sigma'}\end{aligned} \tag{1.1}$$

$\mathcal{H}_0$ describes the tight-binding Hamiltonian, which comprises the chemical potential μ and the hopping integral t_{ij}. The latter defines the kinetic energy of electrons hopping from one site to a neighbouring one. Furthermore, we define the annihilation operator of electrons on the i site with spin σ as $\hat{c}_{i\sigma}$,

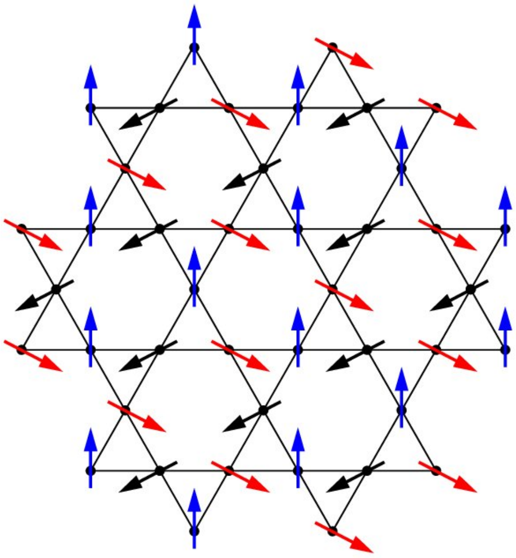

Figure 1.4: Section of the kagome lattice with spins in the fully ordered $\sqrt{3} \times \sqrt{3}$ structure (taken from [28]).

with property $n_{i,\sigma} = \hat{c}^{+}_{i\sigma}\hat{c}_{i\sigma}$. Going on, $\mathcal{H}_{int}$ represents the Hamiltonian of the system consisting of the local Hubbard interaction with scale U_0 and the Coulomb interaction of scale U_1 between the nearest neighboring atoms.

We may explain the general features of "kagome bands," the three bands that are commonly associated with kagome lattice, and the effect of other variables on those bands and their accompanying physical properties using this formulation [1]. The corresponding electronic and band structures are highlighted in Figure 1.5. The fundamental band structure of the ideal kagome lattice (t_{ij} is the same for nearest neighbour sites in upward and downward triangles, e.g. $t_1 = t_2$ in Figure 1.5b) is the same without considering electron interactions and symmetry breakdown. If we consider a tight bonding model, Figure 1.5(c) represents the classical features of a doubly degenerated flat band connected with other bands, a Dirac point around the K point, and van-Hove singularities around the M point (Figure 1.5c) [29, 30, 32]. The density of states (DOS) and electron effective mass at the Fermi level are considerably increased at the flat band and vHSs, where the high electron correlation must be taken into account (Figure 1.5c). Furthermore,

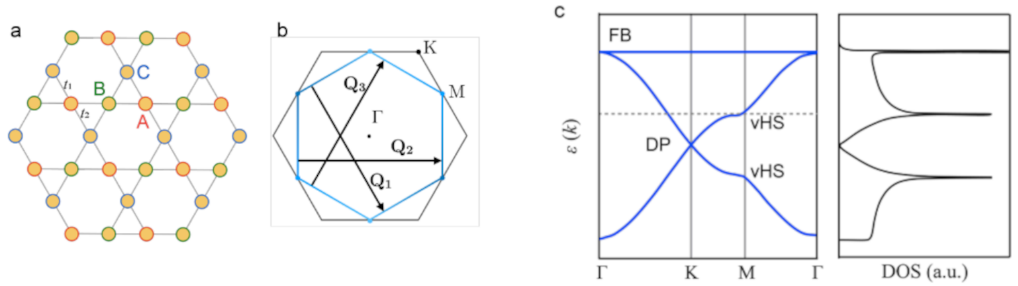

Figure 1.5: Kagome lattice structure and electronic band property. a) The fundamental structure of an ideal kagome lattice. b) Schematic of the Fermi surfaces in the Hexagonal Brillouin zone, with three ordering wave factors Q_i, $i = 1, 2, 3$. This sub-image is from the reference [31]. c) Labelled schematic of the ideal kagome lattice band structure and accompanying DOS, van Hove singularity (vHS), Dirac point (DP), and flat band (FB). This graphic is based on the reference [1].

the hexagonal Fermi surface in momentum space is useful in the context of Fermi surface nesting because it allows for the formation of links between parallel Fermi surface sheets via three unique nesting vectors (as shown in Figure 1.5(b)). It is worth mentioning that near the van Hove singularities (vHSs), Fermi surface nesting becomes very evident, resulting in a significant increase in electronic susceptibility and, eventually, Fermi surface instability. At the vHSs point, the Fermi surface nesting is significant, resulting in diverging electronic susceptibility and Fermi surface instability. When symmetry is broken, as in some of the previously discussed phase transitions, these kagome bands may be modified and can generate new nontrivial topological states such as CDW, nematic, and superconducting ones.

Over the previous four decades, a wide variety of kagome metals have been developed and studied. Some examples include classical ferromagnets like $Co_3Sn_2S_2$ [33, 34] and non-collinear ferromagnet Fe_3Sn_2 [35, 36], with the presence of Weyl fermions and magnetic skyrmions; occurrence of Dirac points and flat bands in the antiferromagnet FeSn [37] and in the paramagnet CoSn [38, 39], and chiral spin structures in the non-collinear antiferromagnet Mn_3X (X=Sn, Ge) [40, 41]. After this general introduction to Kagome materials, in the following, we will focus on the specific AV_3Sb_5 (A = K, Rb, Cs) family that has been studied in this work.

1.2.1 AV_3Sb_5 kagome metals (A = Rb, Cs, K)

Recently, there has been a substantial increase in study interest in topological kagome metals, notably those labelled as AV_3Sb_5(with A indicating potassium (K), cesium (Cs), and rubidium (Rb)). This increased interest is primarily due to the remarkable discoveries made within these materials, where a variety of physical phenomena, such as superconductivity, charge density wave (CDW), nematic order, and a significant anomalous Hall effect, have been observed to coexist within a single material, with their emergence and evolution dependent on temperature variations [42–44] . These complicated, symmetry-breaking, ordered states are discovered to compete or interweave with one another, much like high-temperature superconductors. These metals are made up of an alkali metal (Rb, Cs, K), a vanadium kagome layer, and antimony interstitial layers separated into two inequivalent sites (Sb1 and Sb2). The schematic representation of the unit cell for the RbV_3Sb_5 sample (equal to the CsV_3Sb_5 and KV_3Sb_5 ones) is shown in Figure 1.6. The alkali metal is found at the corners of the unit cell, distant from the central plane, as seen in Figure 1.6. Because most of the interactions that give rise to

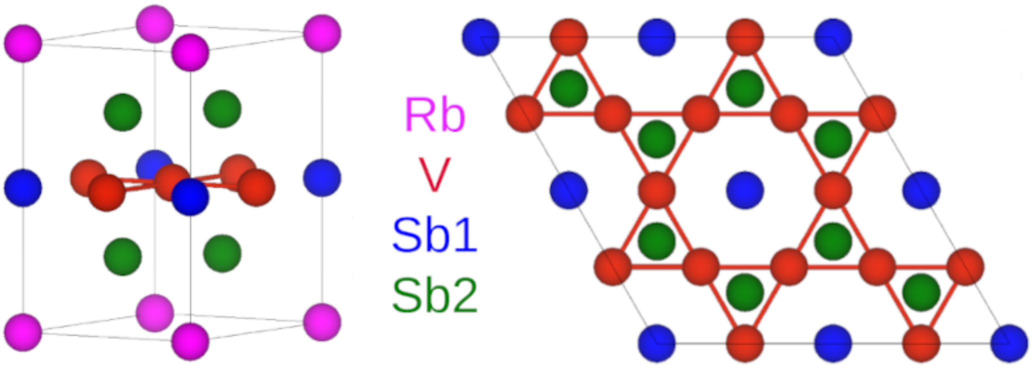

Figure 1.6: On the left, the unit cell of the "pristine" (i.e., normal) crystalline structure of RbV_3Sb_5. On the right, the 2-dimensional kagome layer formed by vanadium atoms.

their particular physics occur in the kagome layer, these materials are usually referred to as "2-D kagome metals." As an example, as recently established in prior research [6], the in-plane (in the kagome layer) resistivity is ~ 600 times less than the out-of-plane (along the c axis) resistivity. The lattice parameters for this unit cell are $a = b = 5.42$ Å, $c = 9.09$ Å, and the space group is hexagonal P6/mmmm. We now reach the "core" of the crystalline structure, the kagome layer. It is composed of vanadium atoms (shown in red in Figure 1.6), with a V-V distance of $d_{V-V} \sim 2.74$ Å. Intercalated inside it are antimony Sb1 sites (in blue) located at the middle plane's edges, whose distance to the nearest V atoms is equivalent to the V-V distance ($d_{V-Sb1} \sim 2.74$ Å). Finally, the antimony Sb2 sites are located above and below the kagome plane, resulting in graphene-like layers with a length of $d_{Sb2-Sb2} \sim 3.16$ Å. The AV_3Sb_5 prototype has just three structural degrees of freedom (a and c lattice parameters, z-coordinate on Sb2) due to the high symmetry of the P6/mmm space group and the tiny unit cell.

As already stated, the lattice frustration inherently present within AV_3Sb_5 kagome metals promotes distinct physical phenomena that can coexist. At $T_c \sim 0.8 - 2.5$ K (0.8 K for RbV_3Sb_5 and KV_3Sb_5, 2.5 K for CsV_3Sb_5), these systems experience a superconducting transition, [7], the cause of which is unknown. Furthermore, for higher temperatures in the range $T_x = 68 - 103$ K (68 K for KV_3Sb_5, 94 K for CsV_3Sb_5, and 103 K for RbV_3Sb_5), certain anomalies in magnetization and specific heat have been discovered, indicating the possibility of another transition. Because the majority of the previously cited kagome materials exhibit some kind of long-range magnetic ordering, preliminary studies have focused on the search for the magnetism of electronic origin within this novel class of materials, but the results from muon exclude the presence of local magnetic moments inside AV_3Sb_5 samples [42]. With this insight, subsequent studies using X-rays, STM, and Angle-resolved photoemission spectroscopy (ARPES) discovered evidence confirming a specific type of charge ordering happening at T_x, namely a Charge-density Wave (CDW) transition.

The CDW transition is a collectively ordered phase of the charge degrees of freedom that spontaneously destroys the underlying lattice's translation symmetry. It might be due to significantly different microscopic physics. One of the most prevalent situations is the Peierls scenario, in which the instability is caused by Fermi surface nesting. For the sake of simplicity, consider a 1-dimensional atomic lattice with atoms separated by a constant z distance. According to Ref. [45], if an energy gap is opened at $k = \pm k_F$, where k_F is the Fermi wavevector, the energies of the occupied states below E_F (the Fermi energy) are dropped, lowering the overall electronic energy. By rebuilding the Fermi surface and opening a gap, this system expends energy in the form of strain but saves more energy than if it had not. Peierls pointed out that a modulation of the positions of the lattice atoms of the form:

$$\delta u_n = \delta u \; cos\,[Qz + \phi] \tag{1.2}$$

with wavevector $Q = 2k_F$ (and wavelength $\lambda_c = \pi/k_F$) would produce gaps at $\pm k_F$. At lower temperatures, the expenditure of elastic energy associated with changing atomic positions is offset by a rise in conduction electron energy. As a result, the charge density wave (CDW) configuration emerges as the preferred ground-state form [46]. Thermal excitation of electrons across a gap reduces electrical energy increase at high temperatures, stabilizing the metal state [47]. According to [48], the second-order transition between metal and CDW states is known as the Peierls transition. A complicated order parameter $\Psi = \Delta e^{i\phi}$ characterizes the CDW state. The magnitude Δ governs the extent of the electronic energy gap as well as the amplitude δu of atomic displacements. The phase ϕ determines the CDW's location in relation to the underlying lattice.

Electrons included within a charge density wave (CDW) have the ability to form standing waves while also conducting electrical current. Electron transport in such a CDW arrangement can appear as a strongly coupled flow along a linear chain structure, similar to the behaviour found in superconductors. It is crucial to highlight that, unlike superconductors, electrical CDW currents display erratic behaviour, which is mostly due to their electrostatic properties. This effect is caused by electrons' intrinsic wavelike nature, which is a manifestation of the fundamental quantum mechanical concept of wave-particle duality. As a result, the electronic charge density within metallic crystals is spatially modulated, characterised by periodic oscillations or "bumps" in charge distribution. The creation of these standing waves results from the superposition of opposing momentum electron states represented by wavefunctions, determining the behaviour of all electronic wave functions. In terms of electrical charge, the periodic deformation of the atomic lattice, which is essentially a superlattice, is linked with the CDW. A graphical representation of a CDW transition is shown in Figure 1.7. The

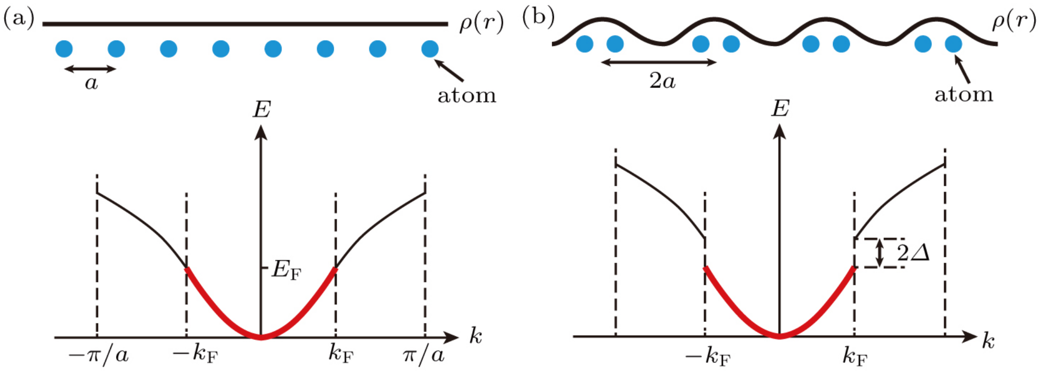

Figure 1.7: A graphic illustration of a one-dimensional periodic metallic lattice experiencing a charge density wave (CDW) transition and a Peierls-distorted insulating lattice, is shown here. (a) Without electron-phonon interaction, the periodicity a of lattice has a uniform charge density distribution, and all electron states inside this lattice extend up to the Fermi level. (b) When the electron-phonon interaction is considered, the insertion of Peierls distortion generates a consistently modulated charge density inside the lattice, establishing an energy gap at the Fermi level. Reproduced with permission from [49].

kagome metals AV_3Sb_5 go through this one-of-a-kind transition, which coexists with the superconducting one. In this context, some questions arise, such as what the superlattice formed by the CDW modulation is below T_x (which will be called T_{cdw} going forward), how to detect the formation of this superlattice, how the superconducting state and the CDW state interact below T_c, and if there are any other intriguing instabilities in the temperature range $T_c \leq T \leq T_{cdw}$. Most of these concerns will be answered and investigated in the next chapters when I provide my experimental results for AV_3Sb_5 samples. Table 1.1 shows the kagome metals characterized personally by means of NMR and μSR, their composition and form, either single crystal (SC) or polycrystalline (powder). Overall, AV_3Sb_5 kagome metals provide an intriguing and intriguing platform for revealing the link between various types of topological phase transitions, the origin of which is still being studied by a large number of research organizations all over the world.

Table 1.1: List of kagome metals of the AV_3Sb_5 family characterised by means of NMR and μSR, along with their composition, form, and technique used.

Composition	**Doping**	**Label**	**Form**	**Tecnhique**	**Chapter**
RbV_3Sb_5	Undoped	RVS	Crystal	NMR/NQR	Chapter 4
KV_3Sb_5	Undoped	KVS	Crystal	NQR	Chapter 4
CsV_3Sb_5	Undoped	CVS	Crystal	NQR	Chapter 4
$CsV_3Sb_{5-x}Sn_x$	x = 0.05	CVS-Sn05	Powder	NQR	Chapter 4
	x = 0.08	CVS-Sn08	Powder	μSR	Chapter 5
	x = 0.35	CVS-Sn35	Powder	μSR	Chapter 5
$CsV_3Sb_{5-x}Te_x$	x = 0.04	CVS-Te04	Powder	NQR	Chapter 4
	x = 0.06	CVS-Te06	Powder	NQR	Chapter 4
	x = 0.08	CVS-Te08	Powder	μSR	Chapter 5

1.3 Kitaev materials

This section will be devoted to the explanation of Kitaev materials. Among all the references that will be cited, the major contributions to this text will be taken from the review [50]. Kitaev materials have recently received a lot of interest due to their exciting potential for unique unconventional magnetism, particularly the realization of quantum spin liquids in lattice geometries other than one [51–53]. Due to the intricate interactions between the electronic, spin, and orbital degrees of freedom, transition-metal oxides with partly filled 4*d* and 5*d* electron shells have received a lot of research interest. According to Ref. [54], this complexity arises from an equilibrium combining electronic correlations, spin-orbit entanglement, and crystal-field phenomena that are mostly accidental.

The fundamental building block of Kitaev materials is bond-directional interactions, which are comparable to Ising-like interactions and in which the orientation of the exchange easy axis relies on the spatial alignment of an exchange bond. When compared to other exchange methods, these interactions have the highest coupling intensity. The microscopic reasons for these bond-directional interactions in transition-metal compounds with a d^5 electron configuration were made clear by Khaliullin and Jackeli [51, 55].

According to Khaliullin and Jackeli work, the geometric configuration of neighbouring IrO_6 octahedra is a crucial factor influencing the microscopic exchange interactions of magnetic moments focused on the iridium ions positioned at the cores of these octahedral formations. They find two critical options, which are illustrated (with an extension) in Figure 1.8. It is intriguing to note that two nearby IrO_6 octahedra in the perovskite iridates class—which includes compounds like Sr_2IrO_4—share a common corner. This geometric arrangement results in a single Ir-O-Ir exchange channel, often known as the 180° link, connecting the two iridium ions. Despite the strong existence of spin-orbit coupling along this bond type, the dominating interaction mechanism is described by a symmetric Heisenberg exchange between the spin-orbit entangled moments with angular momentum j = 1/2.

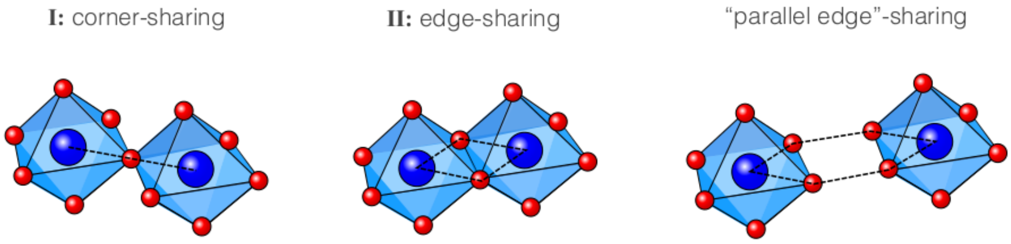

Figure 1.8: Several geometric orientations of nearby IrO_6 octahedra result in diverse kinds of (dominant) exchange interactions between the magnetic moments located at the core of these octahedra. A dominant symmetric Heisenberg exchange is obtained for corner-sharing geometry (I), whereas a dominating bond-directional, Kitaev-type exchange is found for edge-sharing geometry (II). Taken from [50].

In the context of materials having a distinctive structural arrangement, a scenario arises when two IrO_6 octahedra close to one another share an edge. This design shows two distinct Ir-O-Ir exchange channels with a 90° bonding shape. The existence of these two exchange channels acquires critical significance since they lead to various outcomes: either a destructive interference of the symmetric Heisenberg exchange when the interaction is restricted to the j = 1/2 bands or a considerable attenuation of certain residual Heisenberg exchange contributions when a complete multi-orbital model that incorporates the (virtual) j = 3/2 bands is utilised. The type of shared edge at their junction determines the specific pairing of d-orbitals linked to the two neighbouring octahedra that lead to this bond-directionality in the exchange coupling. Moving on, the general form of the Hamiltonian governing the interactions between j = 1/2 spin-orbit entangled moments of Kitaev materials is as follows:

$$\mathcal{H} = - \sum_{\gamma-bonds} J\mathbf{S}_i\mathbf{S}_j + K S_i^{\gamma} S_j^{\gamma} + \Gamma\left(S_i^{\alpha} S_j^{\beta} + S_i^{\beta} S_j^{\alpha}\right) \tag{1.3}$$

where the sum is applied to nearest-neighbor spins coupled by a bond $\langle i, j \rangle$ along the $\gamma = (x, y, z)$ direction. J represents the isotropic Heisenberg coupling, and bond-directional couplings include:

- a Kitaev term of strength K that couples the spin component γ along a γ-bond;
- a symmetric off-diagonal exchange Γ that couples the two orthogonal spin components $a, b \perp \gamma$ for a bond along the $\gamma = (x, y, z)$ direction.

Different exchange couplings have different relative strengths and indications, depending on the material. But all Kitaev materials share the dominance of the Kitaev coupling (K) over the Heisenberg coupling (J), denoted as $K > J$. This ratio between the Kitaev and Heisenberg exchange interactions is extremely stable in the context of honeycomb iridates. The microscopic model given in Equation (1.3), also known as the $JK\Gamma$ model, is often simplified in the Heisenberg-Kitaev model ($\Gamma = 0$) [56]. Bond-directional interactions create significant exchange frustration since these interactions cannot be reduced concurrently, as shown in Figure 1.9. Because of exchange frustration, which is related to geometric frustration in that lattice geometry imposes constraints that cannot be satisfied simultaneously, residual ground-state entropy is created and magnetic ordering is suppressed. It is intriguing that a significant fraction of the j = 1/2 Mott insulators cannot undergo a finite-temperature phase transition according to the conventional Kitaev honeycomb model [58, 59]. The Coulomb phase instead undergoes a thermal crossover at absolute zero [60]. The pure Kitaev model, defined by J and Γ being equal to zero, is crucial in studying condensed matter physics. It is renowned for supporting both gapped and gapless quantum spin-liquid ground states. Furthermore, it is one of the few microscopic models that can be accurately solved analytically [61]. This particular concept gave rise to the broader category of materials known as Kitaev materials. This model has been studied extensively since the realisation of Kitaev Spin Liquids (KSLs) which are obtained as the exact solution of the Kitaev spin model and are

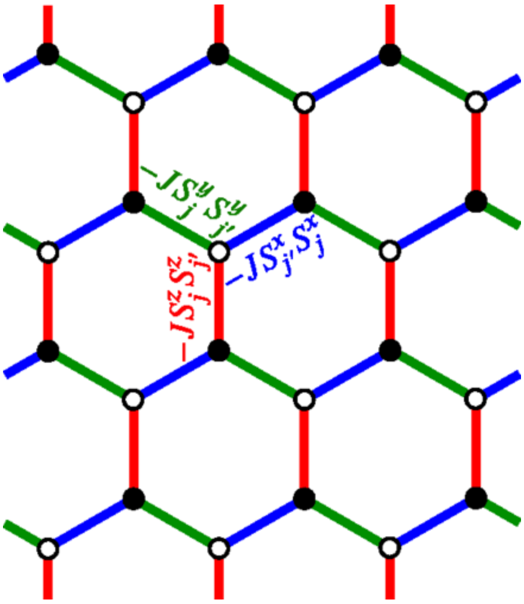

Figure 1.9: The Kitaev model of the honeycomb structure is depicted schematically. The bond-dependent Ising-type interaction -$JS^\gamma_j S^\gamma_{j'}$ (γ = x,y,z) is specified on the bonds denoted by blue, green, and red for = x, y, and z, respectively. Taken from [57].

characterised by quantum frustrations that arise from the bond-dependent anisotropic Kitaev interactions driven by $J_{\text{eff}} = 1/2$ Kramers doublets spin-orbit entangled local magnetic moments.

1.3.1 Kitaev antiferromagnet Na_2PrO_3

In this subsection, I will briefly talk about one specific material in the huge class of Kitaev materials: the antiferromagnet Na_2PrO_3. More will be discussed in the relative section of Chapter 6, where I will describe my experimental work on Na_2PrO_3 using μSR and neutron scattering techniques. As its name suggests, this material undergoes an antiferromagnetic transition at $T_N \simeq 4.9$ K, and its honeycomb lattice structure provides isotropic Heisenberg J interactions as well as anisotropic bond-dependent Kitaev interactions K among Pr^{4+} ions. Furthermore, this material has attracted a lot of attention since, by moving on beyond the Jackeli-Khaliullin mechanism, it has recently been established that features of dominant Kitaev interactions are realizable in compounds with the f1 electronic configuration, such as Ce^{3+} and Pr^{4+} [53, 62].

Some of the most important questions regarding this material included the possible realization of a Kitaev Spin Liquid (KSL), the determination of the antiferromagnetic structure below T_N, and the precise description of the ground-state exchange interactions in the magnetic order, which will be answered in the dedicated part of Chapter 7.

Chapter 2

NMR technique and experimental methods

This chapter will describe the theory underlying the experimental technique of Nuclear Magnetic Resonance (NMR), along with its experimental realization. The latter includes the experimental setup, the cryogenic apparatus, and the software acquisition of the NMR signal.

2.1 Theory of NMR

Protons and neutrons make up each atom, with electrons circling around them. The nucleus (protons and neutrons) and electrons each have an inherent magnetic moment known as spin. This item is entirely quantum and has no classical analog. The technique we'll be discussing is called Nuclear Magnetic Resonance (NMR) spectroscopy, and at its heart is the concept of nuclear spin, which is commonly abbreviated as I (the electronic spin is abbreviated as S).

Without an external magnetic field, the nuclear spins will be directed at random orientations inside the bulk matter The magnet's static magnetic field B_0 applied along a specified direction (usually the z axis in the laboratory reference system) forces the nuclear spin to align with it. In the case of a group of hydrogen atoms with a single proton with nuclear spin $I = 1/2$, there are only two possible orientations of I: $I = +1/2$ and $I = -1/2$. Because the +1/2 spin state has a lower energy, more than half of the hydrogen atoms in the analyzed ensemble will be in this state, whereas slightly less than half will be in the -1/2 state. The energy gap between the two spin states grows as B_0 increases.

The application of a second, oscillating magnetic field B_1(t), significantly less in modulus than the static one, in the perpendicular plane to B_0 causes the nuclear spins to tilt and follow the second field. This occurs only when the frequency of the oscillating field B_1(t) is $\sim$ to one of the intrinsic nuclear energy levels, thus the term Nuclear Magnetic Resonance. After a short time, B_1(t) is turned off, and the nuclear spin realigns to the static field B_0, i.e., they "relax" back to the equilibrium state. In a word, this is the idea behind NMR technology.

We have just given a basic overview of the NMR technique here, and we will go into further detail about the physics behind it, the experimental results that may be obtained, and the applications of the technology. These subsections will be mostly derived from books [63–66], and [67], a Ph.D. thesis. The first two books are considered reference texts for Nuclear Magnetism and its application to NMR spectroscopy; the third book focuses on the practical aspects of NMR spectroscopy (electronics, spectrometers, signal generation, and so on); and the final book is a theoretical essay on Nuclear Quadrupole Resonance (NQR), NMR's "cousin" in zero-field. Finally, the above-mentioned Ph.D. thesis is largely based on the aforementioned scholarly references. For the classical and quantum description of nuclear spin dynamics, please refer to Appendix A.

2.1.1 Electrostatic interaction between Nucleus and Electrons

In the case of only magnetic interaction among the nuclei and the static magnetic field B_0, without the accountancy of other interactions (which will be discussed later), the Zeeman effect removes the degeneracy of the energy levels, thus giving rise to $2I + 1$ energy levels (where I is the nuclear spin) equally spaced by an energy difference of:

$$\Delta E = -\gamma \hbar B_0 \tag{2.1}$$

where γ is the gyromagnetic ratio of the nuclei under study. We must be concerned with the hyperfine structure in order to explore all of the other conceivable interactions between nuclei and electrons. The hyperfine structure of electronic spectra in condensed materials can reveal higher orders of the electrostatic interaction between nuclear and electron charges. This interaction can be linked to the effects of the nucleus's small size. The energy of Coulomb interaction between the electron cloud and the nucleus, denoted by the classical charge densities $\rho_e \ (r_e)$ and $\rho_n \ (r_n)$, respectively, is introduced as:

$$W_E = \int \int dr_e dr_n \frac{\rho_e(r_e)\rho_n(r_n)}{|r_n - r_e|} \tag{2.2}$$

We will use the following expansion:

$$\frac{1}{|r_n - r_e|} = 4\pi \sum_{l=0}^{\infty} \sum_{m=-l}^{l} \frac{1}{2l+1} \frac{r_<^l}{r_>^{l+1}} Y_l^{m*}(\theta_n, \phi_n) Y_l^m(\theta_e, \phi_e) \tag{2.3}$$

where r_e and r_n are in spherical coordinates. $Y_l^m(\theta, \phi)$ are the spherical harmonics, and $r_{</>}$ denotes the smaller or bigger difference between r_e and r_n. We shall always assume that $r_e > r_n$ in the following, ignoring the implausible penetration of electrons into the nucleus. Using the expansion Equation (2.2), we can separate the integrand of Equation (2.2) into two pieces that rely on the variables r_e and r_n. As a result, the energy W_E is rewritten as follows:

$$W_E = \sum_{l,m} A_l^m B_l^{m*} \tag{2.4}$$

where:

$$\begin{aligned} A_l^m =&(\frac{4\pi}{2l+1})^{\frac{1}{2}} \int dr_n \rho_n(r_n) r_n^l Y_l^m(\theta_n, \phi_n) \\ B_l^m =&(\frac{4\pi}{2l+1})^{\frac{1}{2}} \int dr_e \rho_n(r_e) r_e^{-(l+1)} Y_l^m(\theta_e, \phi_e) \end{aligned} \tag{2.5}$$

Further calculations are reported in Appendix A. Finally, we obtain the nuclear Hamiltonian responsible for the quadrupole coupling in the laboratory frame:

$$\begin{aligned} \mathcal{H}_Q = \langle\psi_e| \mathcal{H}_2 |\psi_e\rangle = \sum_m \mathcal{Q}_2^m V^{-m} \\ = \frac{eQ}{I(2I-1)} \big[\frac{1}{2}(3I_z^2 - I(I+1))V^0 \\ +\frac{\sqrt{6}}{4}\big((I_Z I_+ + I_+ I_z)V^{-1} + (I_z I_- + I_- I_z)V^{+1} + I_+^2 V^{-2} + I_-^2 V^{+2}\big)\big] \end{aligned} \tag{2.6}$$

$V_{ij} = \langle \mathcal{V}_{ij} \rangle$ denotes a symmetric tensor. As a result, we may select the coordinate system that coincides with the axes XYZ, known as the Principal Axis System (PAS). The axes are arranged so that the eigenvalues are sorted as $|V_Z Z| \geq |V_X X| \geq |V_Y Y|$. The amounts are introduced as follows:

$$eq = V_{zz} \qquad \eta = (V_{XX} - V_{YY})/V_{ZZ} \tag{2.7}$$

where η refers to the asymmetry parameter of the EFG tensor and offers an approximation of the deviation from the EFG's axial symmetry. Equation (2.7)'s three components follow the following relationship (Laplace equation): $\nabla^2 V = V_X X + V_Y Y + V_Z Z = 0$, implying that $0 \leq \eta \leq 1$. The quadrupolar Hamiltonian can be represented more compactly in the PAS as:

$$\mathcal{H}_Q = \frac{e^2 qQ}{4I(2I-1)}(3I_Z^2 - I(I+1) + \frac{1}{2}\eta(I_+^2 + I_-^2)) \tag{2.8}$$

2.1.2 Quadrupolar Effects on Nuclear Energy Spectrum

The complete Hamiltonian of a nucleus under the influence of a magnetic field and the electrostatic interaction with the surrounding electrons is as follows, according to the quadrupole interaction:

$$\mathcal{H} = -\gamma\hbar B_0 \cdot I + \frac{e^2qQ}{4I(2I-1)}(3I_Z^2 - I(I+1) + \frac{1}{2}\eta(I_+^2 + I_-^2)) \tag{2.9}$$

where I_z, I_+, and I_- indicate the spherical components of I in the coordinate system of the principal axes of the electric field gradient. Experimentally, we can have two instances. The quadrupole energy eigenvalues are computed first in the low magnetic field limit, and then the influence of the magnetic field is added as a perturbation. The quadrupole term is handled as a perturbation of the Zeeman-splitted energy levels at the high field limit.

High magnetic fields

As a first observation, we assume that the sample under consideration is monocrystalline in order to establish a different coordinate system S_Q in which each nucleus contains the electric field gradient tensor V_{ij} in the diagonal form. It is more convenient to align the z-axis with B_0 and examine the system from the laboratory reference frame S_{lab} when examining the system in the high-field limit. Thus, the cartesian frame will coincide with the XYZ frame, but the EFG tensor's principal axis system (PAS) will coincide with the XYZ frame. We also assume that the EFG has axial symmetry ($\eta = 0$). In this case, we can always align the axes x and X in S_{lab} and S_Q so that the planes xz and XZ coincide. The new Hamiltonian with this formulation is:

$$\mathcal{H} = \mathcal{H}_Z + \mathcal{H}_Q \tag{2.10}$$

with the two components (Zeeman and Quadrupolar) defined as:

$$\begin{aligned}
&\mathcal{H}_Z = -\gamma\hbar B_0 I_z \\
&\mathcal{H}_Q = \frac{e^2qQ}{4I(2I-1)}\begin{cases} \frac{1}{2}(3cos^2\theta - 1)(3I_z^2 - I(I+1) & \Delta m = 0 \\ +\frac{3}{2}sin\theta cos\theta\left[I_z(I_+ + I_-) + (I_+ + I_-)I_z\right] & \Delta m = \pm 1 \\ +\frac{3}{4}sin^2\theta(I_+^2 + I_-^2) & \Delta m = \pm 2 \end{cases}
\end{aligned} \tag{2.11}$$

where $I\pm$ has been redefined as $I_x \pm iI_y$. The energy levels are found by computing the perturbative contributions of increasing order, as in:

$$E_m = E_m^{(0)} + E_m^{(1)} + E_m^{(2)} + ... \tag{2.12}$$

We also introduce the following parameters:

$$\nu_Q = \frac{3e^2qQ}{2hI(2I-1)} \quad a = I(I+1) \quad \mu = cos\theta \quad \nu_L = \frac{\gamma B_0}{2\pi} \tag{2.13}$$

Then, second-order perturbation theory gives the following results:

$$\begin{aligned}
E_m^{(0)} &= -\gamma\hbar B_0 m = -h\nu_L m \\
E_m^{(1)} &= \frac{1}{4}h\nu_Q(3\mu^2 - 1)(m^2 - \frac{1}{3}a) \\
E_m^{(2)} &= -h\left(\frac{\nu_Q^2}{12\nu_L}\right)m\begin{cases} \frac{3}{2}\mu^2(1-\mu^2)(8m^2 - 4a + 1) \\ +\frac{3}{8}(1-\mu^2)^2(-2m^2 + 2a - 1) \end{cases}
\end{aligned} \tag{2.14}$$

The Zeeman-splitted energy levels $E(0)_m$ are evenly spaced in the absence of the quadrupole interaction, and assuming that only transitions with $\Delta m = \pm 1$ are permitted, there will be a unique resonance frequency:

$$\nu_L = \frac{E_{m-1}^{(0)} - E_m^{(0)}}{h} \quad \text{for all } m \tag{2.15}$$

as already mentioned in Equation (2.1). When the quadrupole energy is taken into account, the perturbative corrections to the energy levels depend on m, and the resulting resonance frequencies will be multiple:

$$\nu_m = \frac{E_{m-1} - E_m}{h} = \nu_L + \nu_m^{(1)} + \nu_m^{(2)} + ... \quad \text{where} \quad \nu_m^{(n)} = \frac{E_{m-1}^{(n)} - E_m^{(n)}}{h} \tag{2.16}$$

For instance, the 1^{st}-order correction to the resonance frequency is:

$$\nu_m^{(1)} = \frac{E_{m-1}^{(1)} - E_m^{(1)}}{h} = \nu_Q \left(\frac{1}{2} - m\right) \frac{3\mu^2 - 1}{2} \tag{2.17}$$

The apparent implication of this statement is that the first-order correction to the transition $\frac{1}{2} \Leftrightarrow -\frac{1}{2}$ vanishes for half-integer spins. If we ignore higher-order contributions, the corresponding line will remain fixed in place; however, transitions between states $m \neq \frac{1}{2}$ and $m \neq -\frac{1}{2}$ will drift apart and produce the so-called *satellite lines*, which are arranged in an equal number above and below the $\frac{1}{2} \Leftrightarrow -\frac{1}{2}$ one. If an electromagnetic pulse is administered at precise resonance ($\omega = \omega_0$), the Taylor series for the exponential operator is as follows:

$$exp\left\{-ia(\mathbf{n} \cdot \mathbf{I})t\right\} = \sum_{j=0}^{\infty} \frac{(-i\omega_1 t)^j}{j!} I_x^j \tag{2.18}$$

Since $I_x = (I_+ + I_-)/2$, the contributions to the probability of transition between adjacent states will come only from the terms of odd order, and primarily from the 1^{st} order term. Hence, we find:

$$\begin{aligned} P_{m-1,m}(t) &\propto \left|\langle m-1|\, exp\left\{-ia(\mathbf{n} \cdot \mathbf{I})t\right\} |m\rangle\right|^2 \\ &= \left|\langle m-1| \sum_{j=0}^{\infty} \frac{(-i\omega_1 t)^j}{j!} I_x^j \,|m\rangle\right|^2 \\ &= \left|\sum_{j=0}^{\infty} \frac{(-i\omega_1 t)^j}{2j!} \langle m-1|\, (I_+ + I_-)^j \,|m\rangle\right|^2 \\ &\propto \left|\langle m-1|\, I_x \,|m\rangle\right|^2 \end{aligned} \tag{2.19}$$

The final step is necessary since the term $j = 1$ has the largest weight due to the factor $1/2j$. This finding may also be used when quadrupole effects are included, in the approximation where perturbative corrections to the states $|m\rangle$ are ignored. As a result, it gives a straightforward formula for predicting the relative strengths of the lines divided by quadrupole interaction in the NMR spectrum. We may estimate the parameter ν_Q of a nucleus with half-integer spin from Equation (2.17) by measuring the frequency difference between the central line and the following ones at different angles θ. The contrast of such experimental measures and the fitted theoretical plot for a Na^{23} nucleus with spin $I = 3/2$ is illustrated in Figure. Figure 2.1(a). We

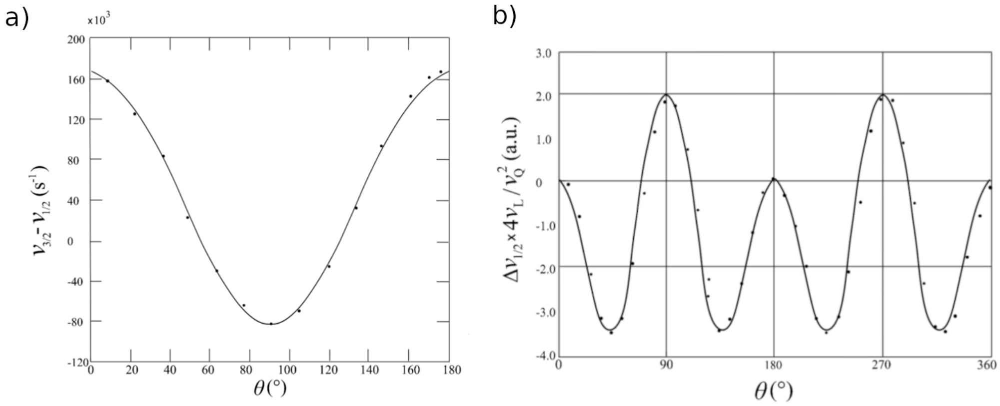

Figure 2.1: a) The frequency difference in NO_3Na between the central line and the symmetrically positioned satellites as a function of the angle θ between B_0 and the crystal axis. The dots indicate experimental data, and the straight curve is a fit plot that is consistent with the theoretical expectation Equation (2.18) (derived from [63]). b) The angle θ between the magnetic field B_0 and the crystal axis affects the centre resonance frequency $\nu_{1/2}$ of Al^{27} in Al2O_3. The y-axis represents the frequency deviation with respect to $\nu_{1/2}$ $(\theta = 0)$, rescaled by the factor $4\nu_L/\nu_Q^2$. The dots represent the experimental data, whereas the straight line represents the predicted plot $2(1-\mu^2)(1-9\mu^2)$ [63].

discover $\nu_Q = 167$ kHz by fitting data using the function $\propto (3\mu^2 - 1)/2$. The applied field B_0 in this experiment was such that $nu_L = 7.17$ MHz, implying an extremely tiny ratio ν_Q/ν_L. This indicates that the energy scale of quadrupole effects is substantially lower than that of Zeeman effects, and higher-order perturbative adjustments to energy levels can be safely ignored.

The 2^{nd} order correction is especially essential when the 1^{st} one disappears, as in the $1/2 \Leftrightarrow -1/2$ transition. In this scenario, we may deduce the following from Equation (2.14):

$$\nu^{2}_{1/2} = -\frac{\nu_Q^2}{16\nu_L}(a - \frac{3}{4})(1 - \mu^2)(9\mu^2 - 1) \qquad (2.20)$$

The relevance of this phrase is clearly established by the ratio ν_Q/ν_L. A system where the contribution of Equation (2.20) is plainly visible is the nucleus of Al^{27} ($I = 5/2$) in the Al_2O_3 compound. Indeed, as seen in Figure 2.1(b), the central line fluctuates significantly as a function of the angle θ. The experimental points closely match the theoretical plot of $\nu^{2}_{1/2}$ order correction. As ν_Q is comparable to $nu_L = 2.6$ MHz, the resultant measure of ν_Q verifies that the 2^{nd} order term is not insignificant this time. When the gradient of the electric field is not axially symmetric, the first-order adjustment to the energy levels is:

$$E^{(1)}_m = \frac{1}{4}h\nu_Q \left[3cos^2\theta - 1 + \eta sin^2\theta cos2\phi\right](m^2 - \frac{1}{3}a) \qquad (2.21)$$

where θ and ϕ are the polar and azimuthal angles of the magnetic field B_0 in the EFG's major axis system. According to this formula, monitoring the NMR spectra for different sample orientations offers enough information to establish the direction of the primary axes of the electric field gradient as well as the values of η and ν_Q.

Zero field spectrum

The pure Quadrupolar Hamiltonian of the nucleus, as seen from the coordinate system of the principal axes of the electric field gradient, is:

$$\mathcal{H}_Q = \frac{e^2qQ}{4I(2I-1)}[3I_Z^2 - I(I+1) + \frac{1}{2}\eta(I_+^2 + I_-^2)] \qquad (2.22)$$

An electromagnetic pulse with the right frequency that connects with the magnetic moment, similar to the pure Zeeman condition, can trigger transitions between the quadrupole energy levels.

If we assume that the electric field gradient is axially symmetric ($\eta = 0$), the solution to the Equation (2.22) eigenvalue issue is straightforward.

$$E_m = \frac{e^2qQ}{4I(2I-1)}[3m^2 - I(I+1)] \tag{2.23}$$

From this result, one immediately realizes that the energy level corresponding to $I_z = \pm m$ is two-fold degenerate. The transition from $|1/2| \leftrightarrow |3/2|$, will equate to one line for $I = 3/2$. The associated frequency projections are:

$$\nu_{3/2} = \frac{1}{2}\frac{e^2qQ}{h} \tag{2.24}$$

The transition from $|0| \leftrightarrow |1|$ and $|1| \leftrightarrow |2|$ will equate to two lines for $I = 2$. The associated frequency projections are, in this case:

$$\nu_1 = \frac{1}{8}\frac{e^2qQ}{h} \quad \nu_2 = 3\nu_1 \tag{2.25}$$

In general, the frequency transitions from $|m-1| \leftrightarrow |m|$ and $|m'-1| \leftrightarrow |m'|$ obey the following rule:

$$\frac{\nu_m}{\nu_{m'}} = \frac{2|m|-1}{2|m'|-1} \tag{2.26}$$

The distinction between integer and half-integer spins can be found in Appendix A.

2.1.3 Dipolar coupling and Knight Shift

Aside from the dominant Zeeman interaction and the Quadrupolar interaction (which, as previously stated, can be a perturbation or the main interaction in the system), there are other sources of interactions between nuclei-nuclei and nuclei-electrons that can cause the NMR lines to broaden or sift at different frequencies. The primary contributor in the first situation is dipolar coupling among nuclei, which generates a widening of the spectral line, whereas the major contributors in the second case are the Knight shift and chemical shielding. Because we are working with solid-state systems, specifically metals, the first of the two is the more important. This is due to the fact that metal electrons are highly mobile and de-localized, resulting in a significant interaction with the nuclei ensemble under examination. Chemical shift is substantially more pronounced in molecules and chemical compounds, where core electrons are important.

Dipolar coupling

Apart from many inherent and extrinsic sources of widening (such as the inhomogeneity of the applied magnetic field), the dipolar coupling is the primary cause of NMR line broadening. The following section is based primarily on Ref.[68]. The coupling of two magnetic dipoles causes the dipole interaction. Traditionally, the energy of two interacting dipoles μ_1 and μ_2 separated by a distance r is given by:

$$E_D = \frac{\mu_0}{4\pi}\left[\frac{\boldsymbol{\mu_1}\cdot\boldsymbol{\mu_2}}{r^3} - \frac{3\left(\boldsymbol{\mu_1}\cdot\mathbf{r}\right)\left(\boldsymbol{\mu_2}\cdot\mathbf{r}\right)}{r^5}\right] \tag{2.27}$$

By substituting $\mu_1 = \gamma_1\hbar I_1$ and $\mu_2 = \gamma_2\hbar I_2$, the Hamiltonian reads:

$$\mathcal{H}_D = \frac{\mu_0}{4\pi}\frac{\gamma_1\gamma_2\hbar^2}{r^3}\left[\mathbf{I_1}\cdot\mathbf{I_2} - \frac{3\left(\mathbf{I_1}\cdot\mathbf{r}\right)\left(\mathbf{I_2}\cdot\mathbf{r}\right)}{r^2}\right] \tag{2.28}$$

After turning into spherical coordinates and doing some calculations, the dipolar Hamiltonian reads:

$$\mathcal{H}_D = \frac{\mu_0}{4\pi}\frac{\gamma_1\gamma_2\hbar^2}{r^3}\left[A + B + C + D + E + F\right] \tag{2.29}$$

where the terms A-F are given by:

$$\begin{aligned}
A &= I_{1z}I_{2z}(3cos^2\theta - 1)\\
B &= -\frac{1}{4}\left[I_{1+}I_{2-} + I_{1-}I_{2+}\right](3cos^2\theta - 1)\\
C &= -\frac{3}{2}\left[I_{1+}I_{2z} + I_{1z}I_{2+}\right](sin\theta cos\theta)exp(-i\phi)\\
D &= -\frac{3}{2}\left[I_{1-}I_{2z} + I_{1z}I_{2-}\right](sin\theta cos\theta)exp(+i\phi)\\
E &= -\frac{3}{4}\left[I_{1+}I_{2+}\right]sin^2\theta exp(-2i\phi)\\
F &= -\frac{3}{4}\left[I_{1-}I_{2-}\right]sin^2\theta exp(+2i\phi)
\end{aligned} \tag{2.30}$$

Only terms A and B commute with I_z, resulting in a Hamiltonian time-independent Hamiltonian. As the magnetic field travels down the z-axis in Equation (2.30), θ is the angle created by the internuclear vector and the magnetic field B_0. We have a *homonuclear* or *heteronuclear* dipolar coupling depending on whether the two interacting nuclei are the same element or not (for further information, please read [68]). The direction of the inter-nuclear vector and the inverse cube of the distance impact both heteronuclear and homonuclear dipolar coupling, and they typically result in larger lines in single crystals and powders.

Knight shift

When electron states are not coupled by molecule states or bonds, the applied field can cause spin degeneracy in electronic states, such as electron states near the Fermi level in a metallic band. The contact hyperfine term may then be induced by the electronic atomic moment, resulting in the formation of a B_{eff} component. The frequency shift, often known as the Knight shift, is proportional to the metallic band's Pauli spin susceptibility χ [69–71]. We can start from the interaction between nuclei and electron spins:

$$\mathcal{H}_{ne} = -\gamma\hbar\sum_{i,k} I_i A_{i,k} s_k \tag{2.31}$$

using the hyperfine coupling term $A_{i,k}$. The hyperfine field at the i-th nucleus may thus be calculated as $h_i = \sum_k A_{i,k} s_k$. If the average polarisation of the electron spins is not zero $\langle s \rangle$, the local field felt by the nucleus will be $h_i = \sum_k A_{i,k} \langle s_k \rangle$. With the presence of an external magnetic field, the nuclei will feel the following shift in the local magnetic field:

$$H = H_0 + \sum_k A_{i,k} \langle s_k \rangle \tag{2.32}$$

and the resonance frequency will be shifted to $\omega = \omega_0(1 + \Delta K)$, where:

$$\Delta K = \frac{\sum_k A_{i,k} \langle s_k \rangle}{H_0} = \sum_k A_k \chi(q = 0,\ \omega = 0) \tag{2.33}$$

The shift in the NMR resonance spectrum may thus be used to calculate the static uniform susceptibility associated with electron spins that interact with nuclear spins. In the case of simple metals, the obtained value of χ may be used to calculate the density of states at the Fermi level as follows:

$$\chi = (g\mu_B)^2 \rho(E_F)/2 \tag{2.34}$$

In the end, we can summarise all the possible interactions that arise in an NMR experiment. Figure 2.2 shows all the major interactions involved in the NMR and NQR measurements, including the Zeeman, quadrupolar, dipolar, and Knight shift ones.

2.1.4 Free Induction Decay (FID) and NMR/NQR spectrum

According to [64], the spectrum of the transitions caused by linearly polarised pulses in an NMR system is related to the Fourier transform of the free precession signal recorded after a $\pi/2$ pulse is delivered. This signal is theoretically expressed as the time dependence of the x component of the pulse-induced magnetization. For example, the signal of a pulse running

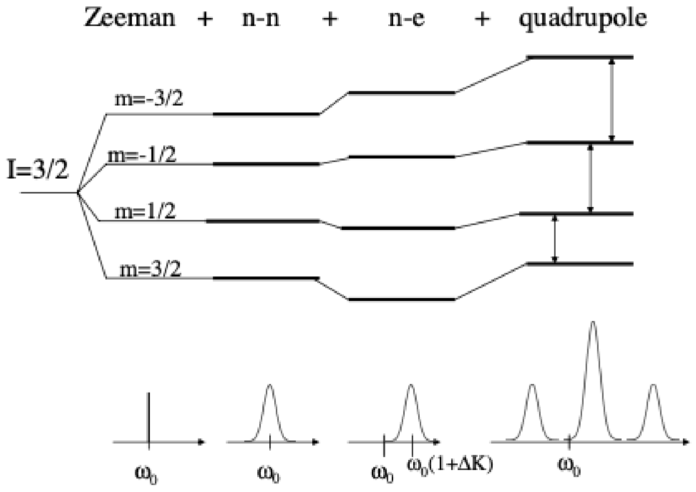

Figure 2.2: The diagram shows the hyperfine levels of a nucleus of $I = 3/2$, and illustrates the effect of the various interactions discussed up to now.

across the time period [0,t_P] would be:

$$G'(t) = M_x(t) = Tr\{\rho(t)M_x\}, \quad t > \tau \tag{2.35}$$

Combining signals received along the x and y axes, which represent the real and imaginary components, yields a complex signal. Thus, a more accurate formulation of Equation (2.35) would be:

$$\begin{gathered} G'(t) = M_+(t) = Tr\{\rho(t)M_+\}, \quad t > \tau \\ M_+ = M_x + iM_y \end{gathered} \tag{2.36}$$

In most experiments, the same coil that produces the pulse is also used to detect one of the magnetization components. Assume the coil completely covers the sample, and the magnetic field produced by magnetization is $B(t) = \mu_0 M(t)$. The magnetic flux across the circuit will be $\Phi(t) = B_x(t)NA$, where N is the total number of windings in the coil, A is its cross-sectional area, and x is its rotational direction. The voltage induced in the coil by the time-varying flux is defined by the Faraday-Neumann-Lenz law, which states:

$$V(t) = \frac{d\Phi(t)}{dt} \propto \frac{dM_x(t)}{dt} \tag{2.37}$$

The free precession signal fully represents the genuine signal found during NMR study. In developing our theoretical framework for NMR/NQR, we entirely overlooked the critical concept of spin relaxation. Thermalization and regional changes in the magnetic field gradually extinguish the transverse components of magnetization. As a result, the signal $G'(t)$ exhibits oscillations with zero amplitude; as a result, it is known as *Free Induction Decay*, or FID for short. In Figure 2.3(a), a graphic illustration is shown. The component of the magnetic field that is formed on the plane xy when a pulse precedes around the magnetic field $B_0 = B_0 k$ with frequency $\omega_0 = \omega_0 k = -\gamma B_0$ in a pure NMR experiment is $\omega_0 = \omega_0 k = B_0 k$. Without the effects of relaxation, the free precession signal would be:

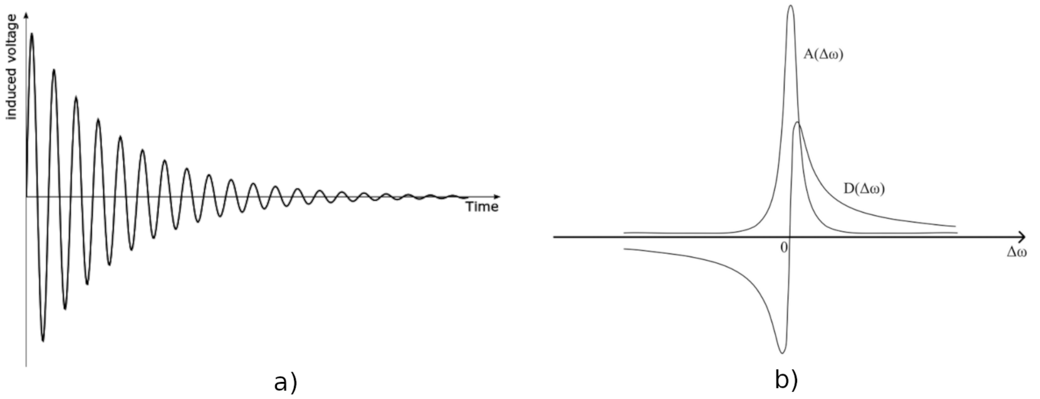

Figure 2.3: a) Free Induction Decay signal, whose voltage varies in time and decays after a certain period. b) Absorptive $A(\Delta\omega)$ and dissipative $D(\Delta\omega)$ Lorentzian functions of NMR spectra, i.e., the Fourier Transform of FID signal in a).

$$G'(t) = c[cos(\omega_0 t) + isin(\omega_0)t], \quad t > \tau \tag{2.38}$$

where c is an arbitrary (real) factor. The relaxation acts as an exponential decay with a time-constant T_2:

$$G'(t) = c[cos(\omega_0 t) + isin(\omega_0)t]e^{-t/T_2}, \quad t > 0 \tag{2.39}$$

and switching in the frequency domain, the Fourier transformation of the function reads:

$$\begin{aligned}\widehat{G}'(\omega) = \int_{-\infty}^{\infty} G'(t)e^{-\omega t}dt &= \frac{1/T2}{(1/T2)^2 + (\omega_0 - \omega)^2} + \frac{i(\omega_0 - \omega)}{(1/T2)^2 + (\omega_0 - \omega)^2} \\ &= A(\Delta\omega) - iD(\Delta\omega)\end{aligned} \tag{2.40}$$

where $\Delta\omega = \omega - \omega_0$. The absorptive and dispersive Lorentzian curves, $A(\Delta\omega)$ and $D(\Delta\omega)$, are respectively centered at frequency 0 and have a complete width at half height of $1/\pi T_2$ (Figure 2.3(b)), and have the form of:

$$A(\Delta\omega) = \frac{1/T2}{(1/T2)^2 + (\Delta\omega)^2} \quad D(\Delta\omega) = \frac{i(\omega_0 - \omega)}{(1/T2)^2 + (\Delta\omega)^2} \tag{2.41}$$

As a result, the longer the characteristic time T_2 (also known as the decoherence period), the more precise the localization of the peaks in the NMR spectrum. Furthermore, Equation (2.40) demonstrates that the Fourier analysis of the FID signal yields the frequencies of the system's transitions; in this example, this is just the position of the peak in the Fourier spectrum ω_0.

Bloch's equations show that when a signal $G'(t)$ of length t_P is delivered to a sample, it relaxes with two unique decay periods, T_1 and T_2. The in-phase and out-of-phase ($\pi/2$ phase) components of nuclear spin susceptibility may be derived from the in-plane components of magnetization, as illustrated below:

$$\chi'(\omega) = \frac{M_0}{H_0}\frac{\omega_0(\omega_0 - \omega)T_2^2}{1 + (\omega_0 - \omega)^2 T_2^2} \qquad \chi"(\omega) = \frac{M_0}{H_0}\frac{\omega_0 T_2}{1 + (\omega_0 - \omega)^2 T_2^2} \tag{2.42}$$

where χ' is the absorptive part A($\Delta\omega$) and χ" is the dissipative part D($\Delta\omega$)

as derived in Equation (2.41). When the sample is inserted into the NMR coil, there are shifts in the inductance and in the resistance of the circuit equal to:

$$L = L_0[1 + 4\pi\chi(\omega)] \qquad \Delta R = L_0\omega 4\pi\chi\text{"} \tag{2.43}$$

The average *rf* power absorbed by the nuclei per unit of time is:

$$P(\omega) = \frac{\chi_0}{2}\omega\omega_0 H_1^2 f(\omega)2\pi \quad\Longrightarrow\quad \chi\text{"}(\omega) = 2\pi f(\omega)\omega_0\chi_0 \tag{2.44}$$

where $f(\omega)d\omega$ denotes the percentage of nuclei that resonate in the frequency range ω, $\omega + d\omega$. When $\omega = \omega_0$, $\chi = \chi_0$. The signal is proportional to $P(\omega)$, which in turn is proportional to $\chi\text{"}(\omega)$. Finally, the NMR spectrum $f(\omega)$ is as follows:

$$f(\omega) \propto \chi\text{"}(\omega) = \frac{\omega}{k_B T}\int_0^\infty E^{i\omega t}\left\langle \overline{M_x(t)M_x(0)}\right\rangle dt \tag{2.45}$$

As a result, the NMR spectrum is a precise Fourier transformation of the transverse component function of nuclear magnetization at *omega* frequency.

2.1.5 Relaxations mechanisms

Spin-Spin Relaxation

In the following, we will refer to the reference [72]. Exogenous factors, such as variations in the homogeneity of the magnetic field across the sample volume caused by the magnet, can also have an impact on the decay of the Free Induction Decay (FID) signal in addition to internal factors. Considering this, the FID signal makes additional contributions as follows:

$$G(t) = G(0)e^{(-t/T_2')}e^{(-\gamma\Delta H t)} = G(0)e^{(-t/T_2^*)} \tag{2.46}$$

where the magnetic field distribution is denoted by ΔH. One of the primary duties is to record the NMR signal in an unknown material. Because the FID, and therefore the NMR signal, is heavily dependent on the decoherence time T_2, the pulse sequence and length must be adjusted to allow for the FID's potential fast decay. Experiments have shown that T_2 might be so short that it is impossible to record the FID signal. The *Spin-Echo* approach may be utilized to avoid signal deterioration before acquisition, and we will go through it in further depth. When using the pulse sequence, we assume that the magnetic field distribution is static.

The *Spin-Echo* technique, also known as the Hahn-echo method (since it was created in nuclear magnetic resonance by Erwin Hahn in 1950), uses two *rf* pulses rather than one (which is commonly used to detect the FID of nuclear magnetization). The FID that arises from an initial 90° excitation pulse decays with time due to spin relaxation and any inhomogeneous processes that cause spins in the sample to precess at various rates when using a one-pulse method alone. As a result, the initial relaxation results in irreversible magnetism loss. Inhomogeneous dephasing, on the other hand, may be eliminated by introducing a 180° inversion pulse that inverts the magnetization vectors after a predetermined delay τ_{echo}. A schematic representation is shown in Figure 2.4. The temporal evolution of in-plane nuclear spins is reversed as a result of the π *rf* pulse. As a result, the in-plane magnetization recovers at $2\tau_{echo}$, resulting in an echo signal, and the spins' dephasing is restored in the second half of the sequence. It is obvious that nuclear spin refocusing is achievable as long as the resonance frequency of each nucleus is the same throughout the first and second halves of the pulse sequence.

Spin-Lattice Relaxation

In the following we will refer to the reference [72]. Bloch equations demonstrate that the longitudinal component of nuclear magnetization relaxes back to its equilibrium value, which is controlled by the lattice temperature, with a characteristic relaxation time T_1. We have difficulty with the detection method for measuring this relaxation period. We can only detect a signal in the xy plane since the FID signal is the Fourier transform of the magnetization component perpendicular to the field. This is not the case for longitudinal magnetization recovery, which tends to align along the z axis. To address this issue, many experimental strategies have been investigated.

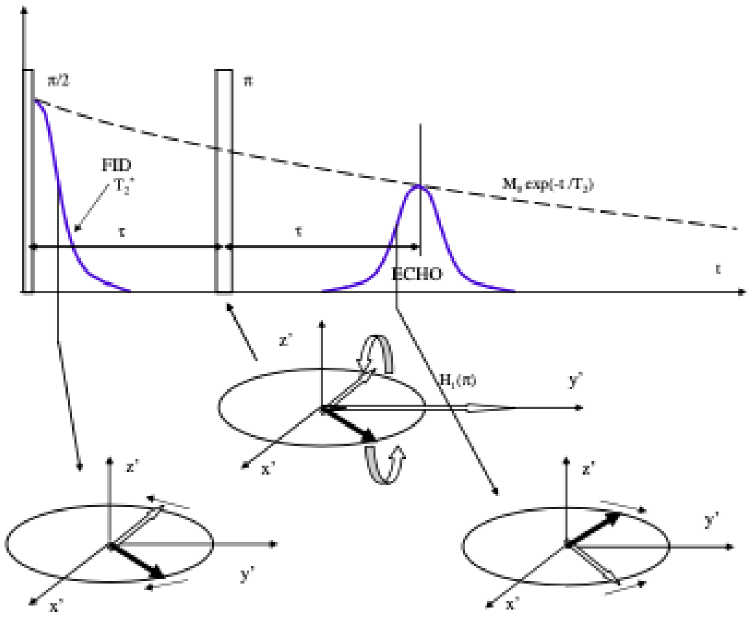

Figure 2.4: Schematic representation of the motion of spins in the case of a spin-echo technique. It also shows the pulse sequence and the decay of the echo.

Inversion Recovery (or $T_1 - IR$) is depicted in Figure 2.5 as a simple *rf* pulse sequence that may be used to measure T_1.

After switching the magnetization along z' with a π pulse, a τ delay is kept before a second $\pi/2$ pulse is applied. The second $\pi/2$ will reverse on the xy plane the proportion of magnetism that has relaxed back to equilibrium throughout time. T_1 may be computed by repeating the experiment with different τ values. Keeping in mind that $T_1 > T_2$ in solid-state materials, τ must vary up to a few seconds in some conditions. Nuclear magnetization will return to equilibrium depending on the likelihood of transitions between hyperfine levels connected to the time-dependent Hamiltonian or lattice excitations. The statistical populations at the hyperfine levels may also be used to understand the impact of the previous pulse sequence on longitudinal magnetization. If we investigate nuclei with $I = 1/2$ for convenience, the population difference between the two levels is really $M_z(t) \propto N_+ - N_-$.

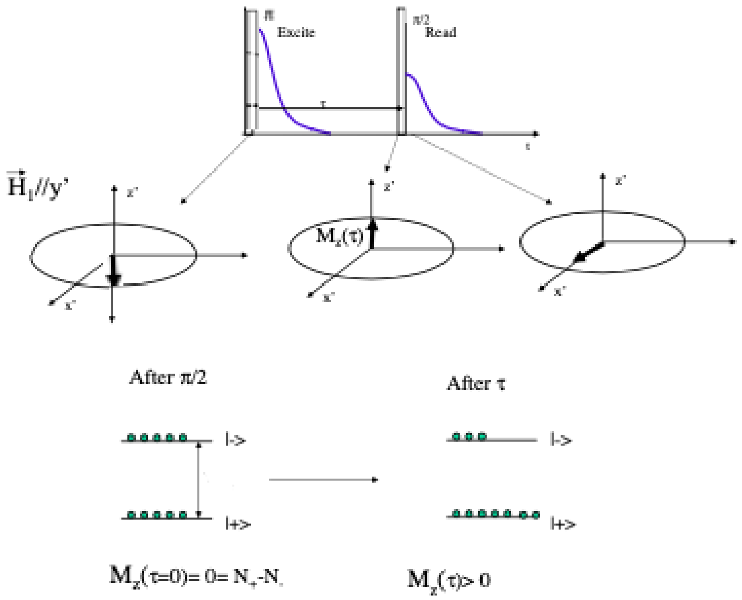

Figure 2.5: Schematic representation of spin-lattice relaxation and the pulse sequence used to measure it. In the bottom part, the effect of $\pi/2$ pulse on the population of states

The following differential equation must be solved in order to determine the temporal evolution of population density between the levels that receive radiation since, in general, with spin I, we have $2I+1$ states:

$$\frac{dN_m}{dt} = \sum_{n\neq m}(N_n\omega_{nm} - N_m\omega_{nm}) \tag{2.47}$$

In the case of $I = 1/2$:

$$M_z(\tau) = M_z(\tau \to \infty)(1 - e^{-\tau/T_1}) \quad \Longrightarrow \quad y(\tau) = \frac{M_z(\infty) - M_z(\tau)}{M_z(\infty)} = e^{-\tau/T_1} \tag{2.48}$$

Every transition that might occur for $I > 1/2$ and is driven by the time-dependent component of the Hamiltonian must be considered. When solving the system of differential equations, only transitions with $\Delta m = \pm 1$ must be considered if the fluctuations are associated with an effective fluctuating magnetic field (such as electron spin fluctuations). If the fluctuations are those of the electric field gradient, then in the case of quadrupolar interaction, one must account for $\Delta m = \pm 2$ transitions since $\mathcal{H}_Q$ is quadratic in the spin components.

2.2 NMR experimental setup

Regarding NMR spectroscopy, I will follow here the Ref. [66]. As already mentioned, NMR spectroscopy is a very powerful technique to explore local microscopic interactions of magnetic and electric nature. A very complex and big experimental apparatus is needed to account for this, since the total nuclear magnetization revealed when applying the *rf* field is tiny in modulus (order of μV). A giant superconducting/resistive magnet is needed to produce the static magnetic field B_0. Furthermore, depending on the temperatures at which we are meant to measure an NMR signal, a cryogenic setup is needed, thus enlarging and complicating the setup. Finally, the electronic circuit that transmits and receives the NMR signal from the sample has to be built properly, with many different pieces.

2.2.1 Static magnetic field

At the core of NMR spectroscopy is using a static magnetic field B_0 to align nuclear spins along it. In NMR spectroscopy, magnetic fields in the order of 7-10 T are used. Continuous magnetic fields in the 36-40 T range are feasible in some high-field facilities, as are pulsed magnetic fields up to 100 T. These magnetic fields can be generated using either superconducting coils cooled with liquid helium, permanent magnets, or electromagnets. An example of a superconducting NMR magnet is shown in Figure 2.6.

Superconducting magnets

There are two sorts of superconducting magnets in the academic context: persistent and non-persistent. Monofilament wire, recognised for its little resistance at joints, is the standard choice for manufacturing persistent magnets. This design enables continual current flow through the coil without

Figure 2.6: Example of an NMR superconducting magnet, from the University of Parma, Department of Physics, NMR laboratory of Prof. Giuseppe Allodi. Here, the magnetic field generated is 7.95 T.

requiring a constant driving force from the power source. In contrast, non-persistent magnets frequently utilise multifilament wire, which is capable of withstanding greater magnetic fields and generating stronger magnetic forces. However, multifilament wire exhibits increased electrical resistance due to its difficulty in creating solid connections. For NMR magnets employing multifilament wire, maintaining a dependable power supply is critical for high-resolution investigations, especially when operating at magnetic fields over 7 T. Typically, the power supply gradually energizes the coil while maintaining a temperature of liquid helium (2-He). An incorporated superconducting switch stops the electrical connection, allowing the power supply to be unplugged and removed, enabling persistent mode functionality. This design often allows for the deletion of certain electrical wires entering the primary coil and superconducting shim coils to limit heat transfer into the dewar and, subsequently, lower 2-He consumption. A pictorial scheme of an NMR superconducting magnet is shown in Figure 2.7. Modern persistent mode magnets feature exceptionally low 2-He boil-off rates, enabling continuous operation. With a 2-He reservoir surpassing 50 liters and a boil-off rate of only a fraction of a liter per day, these magnets can run for extended durations, possibly exceeding two months. The 2-He holding time, controlled by 2-He consumption rate and dewar capacity, is an important parameter in superconducting magnet operation. Minimizing the boil-off rate is advantageous, but its impact is restricted if the storage period is short. Larger dewars, housing the solenoid, are more efficient than smaller ones, demanding a capacity surpassing 50 liters for optimal efficiency. Standard NMR superconducting magnets often attain good field homogeneities, typically about 1 part in 10^6 across a broad sample volume, with the assistance of superconducting correction (shim) coils. These long-lasting rectifying coils require just slight changes. The introduction of ambient temperature adjustment coils can further enhance field homogeneity.

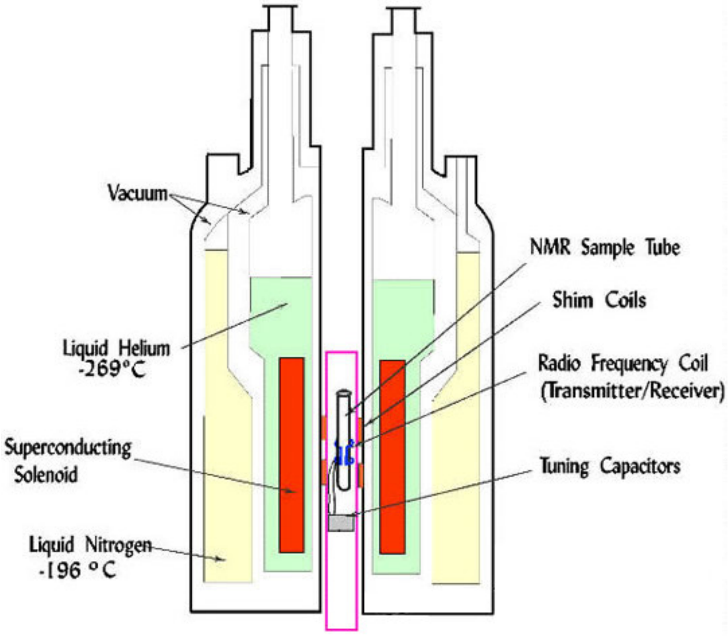

Figure 2.7: Scheme of a superconducting magnet used for NMR spectroscopy. Taken and adapted from [73].

Electromagnets

Electromagnets are made of an iron core that is magnetized by strong electrical currents. Controlling electric current is crucial for achieving stable magnetic fields in high-resolution electromagnets, particularly those with iron cores. The magnetic field strength depends on the iron core's permeability, which is temperature-sensitive. To ensure field stability, thermal management is essential, typically performed via temperature regulation and appropriate cooling. In high-resolution applications, more coils and feedback mechanisms based on nuclear magnetic resonance (NMR) signals are often used to lock and stabilize the magnetic field. While NMR locks flourish with moderate adjustments, they may lose synchronization with rapid field changes. Therefore, they are usually deployed alongside a "superstabilizer" or flux stabilizer, which responds to magnetic field changes by producing corrective currents in coils. This circuit operates like a low-pass filter, effectively dampening rapid field changes. Combining a flux stabilizer with an NMR lock ensures constant magnetic fields across short and extended periods.

Alternatively, field modulation can be applied using non-NMR probes like Hall-effect probes. This approach is less sensitive to temperature-induced permeability changes, offering the potential for high-resolution NMR magnets. Field-regulated magnets are simply tunable and give repeatability, allowing for huge field sweep ranges spanning up to 100 % of the magnetic field. It's worth remembering that electromagnets, save for superconducting variants, generate significant heat due to electric current flow across coils. Proper heat dissipation is vital in the laboratory setting and is frequently provided using water or air cooling systems, along with delivering the requisite electrical power.

2.2.2 Resonant circuit

The resonant circuit is essential to the Nuclear Magnetic Resonance (NMR) experimental setup. Creating a *rf* alternating pulse from a coil is a critical operation in the NMR technique that requires a detailed discussion. The resonant circuit, also known as an LC (inductor-capacitor) circuit, is easily built by selecting an inductor indicated as L and a capacitor designated as C. This circuit's resonance frequency (ω_0) can be estimated as follows:

$$\omega_0 \approx \frac{1}{\sqrt{LC}} \tag{2.49}$$

The impedance of the circuit is labelled Z, and its value in the resonance condition is $Z \simeq 50\ \Omega$. The specimen is placed into the coil L, which can be made of plain Copper (Cu) wire or other materials such as Silver (Ag) or flat wire constructed of Cu/Ag. This coil is a solenoid with specified characteristics such as length (l), resistance (R), and diameter (d). According to Equation (2.49), in the context of studying systems with high resonant frequencies, such as around 140 MHz in a magnetic field of 10 Tesla, the use of a circuit with a low inductance value (hence a reduced number of turns, N, in the coil) is required. The same logic applies to capacitance (C) choices. This connection may be stated clearly as follows:

$$\omega_0 \propto \frac{1}{\sqrt{N}} \tag{2.50}$$

A set resonant frequency for the LC circuit is insufficient to undertake studies requiring the study of multiple nuclei or to execute a *frequency scan* (where the resonant frequency is varied while keeping a fixed magnetic field to record the whole NMR/NQR spectra). As a result, a variable frequency that can be accurately altered based on the individual nucleus under research is required. NMR/NQR investigations use a variable capacitor and a fixed inductor L to accomplish this. It is worth mentioning that a different method for acquiring spectra can also be used, including fixing the *rf* field and adjusting the static magnetic field B_0. However, for the sake of this study, we will only consider the technique in which B_0 remains constant while the *rf* frequency varies.

Regarding the inductor L, informally known as "the coil," various parameters might influence the amount of *rf* power absorbed by the sample, hence influencing signal quality. Considering the coil as a solenoid first, its total volume is given by $V = \pi(d/2)^2 l$, where l and d signify length and diameter, respectively. The *filling factor* is the ratio of the volume occupied by the sample to the overall volume of the solenoid. A larger filling factor translates to more power absorption by the sample, resulting in a higher SNR with fewer experimental scans. Furthermore, to guarantee that the incident alternating *rf* field is equally distributed across the sample, thereby activating all nuclei with the same magnetic field intensity B_1, the sample length should not exceed half the length l of the solenoid, assuring uniform irradiation.

Tuning and matching capacitors

Regarding the capacitor component, the resonant circuit in NMR investigations requires both an adjustable frequency and maximum power transfer to the sample. A single capacitor in series with the coil L is insufficient to meet these two needs. As a result, a typical LC circuit used in NMR investigations includes the following components:

- an inductor L, commonly made of Cu/Ag wire, within which the sample is inserted;
- a *tuning* capacitor C_{tuning}, which is used to change the resonant frequency in order to "tune" the system to the desired frequency;
- a *matching* capacitor $C_{matching}$, which regulates the amount of power transferred to the sample to improve both the SNR and the *rf* field's irradiation frequency bandwidth.

The capacitor marked as $C_{matching}$ is used to manipulate the circuit's quality factor Q, a dimensionless measure characterising the efficiency of losses inside a resonant passive circuit. Q is defined as the ratio of average stored energy to average power loss. As a result, a lower loss equates to a greater Q. Resonators with high Q-factors have bigger amplitudes of resonance (at the resonant frequency); nevertheless, they have a limited frequency range around the resonant frequency within which the nuclei may successfully resonate. The process of "matching" the frequency in this context requires modifying the impedance ascribed to $C_{matching}$ to achieve a value of 50 Ω, a standard impedance characteristic of coaxial cables and associated equipment. As a result, the maximum amount of power is transferred to the sample when the LC circuit impedance coincides with the transmission/reception circuit (a topic to be discussed later). The typical scheme for this NMR circuit, along with a graphical representation of tuning and matching an NMR signal, is shown in Figure 2.8, with a real picture of the scheme in Figure 2.9.

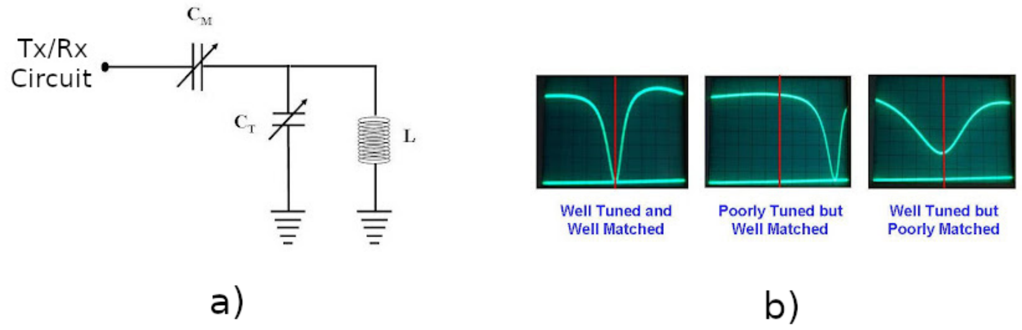

Figure 2.8: (a) The image of a general NMR circuit composed of the L coil and 2 capacitors, one for tuning (C_T) the frequency and the other for matching (C_M) the total impedance. (b) Oscilloscope visualization of an electronic signal when considering matching and tuning in a resonant circuit. Taken from [74].

I used this experimental setup at Brown University to conduct NMR experiments as a Visiting Research Fellow.

Transformer matching

Apart from this ”classical” NMR resonant circuit, another method exists to build an LC circuit that can be matched and tuned using only a single variable capacitor. This method has been taught to me by Professor Allodi at the University of Parma NMR laboratories. To account for the missing second capacitor (the ”matching” one, C_M) we can use the concept of *transformer* to match the impedance of a circuit by using two inductors, the sample one, L and the outer one, L'. Instead of using two capacitors (which are quite expensive and fragile, especially the glass ones), two inductors can be easily

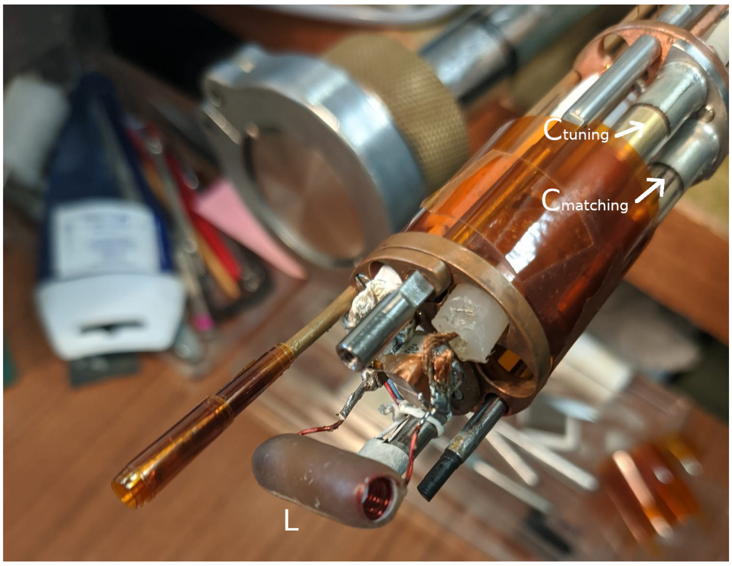

Figure 2.9: Image of a real LC circuit using the "classical" tuning-matching method. It can be clearly seen by the presence of the tuning and matching capacitors C_T and C_M, as well as the coil L embedded in epoxy for stability. Taken at the LNCMI - Laboratoire National des Champs Magnétiques Intenses, Grenoble, France.

made from plain Cu/Ag wire. The tuning capacitor C_T is always present since it is needed to tune the resonant frequency of the system, while the matching capacitor C_M is substituted by the impedance-matching that occurs between two inductors L and L'. Depending on the desired range of resonant frequencies needed, we can categorise a system into "low-frequencies" ($\omega < 90$ MHz) and "high-frequencies" ($\omega > 90$ MHz) modes. The two modes have different LC circuits with this new "transformer" procedure; in particular, the "low-frequencies" one will employ the use of an outer coil L' with a fewer number of turns N' respect to the sample one N; on the other side, in the "high-frequencies" scenario, it has been found to be more efficient to use an *auto-transformer* scheme, where the inductor L' is simply built by connecting part of the sample coil L to another source. The situation for the "transformer" and "auto-transformer" resonant circuits is shown in Figure 2.10, and a photograph of one of my real coils used with this method is shown in Figure 2.11.

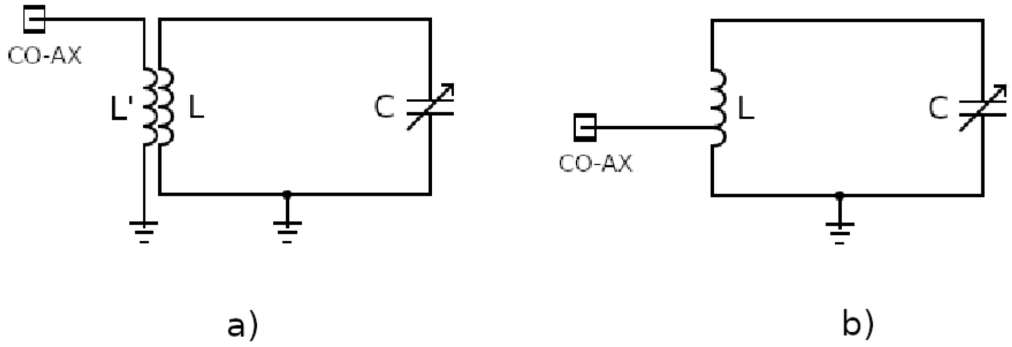

Figure 2.10: (a) "Transformer" LC circuit, good for resonant frequencies lower than 90 MHz. The outer coil L' is connected to the coaxial cable (and so to the NMR circuit), while the LC circuit made of the sample coil L and the tuning capacitor C (no subscripts needed since there is only one) is coupled to L', but physically disconnected from the NMR circuit. (b) "Auto-transformer" LC circuit, good for resonant frequencies higher than 90 MHz. The outer coil L' is simply built by connecting the coaxial to one of the turns of the sample coil L.

Using these methods based on the principle of "transformer", we can match the impedance of the circuit to the one of the NMR circuit by simply changing the number of turns N' (in case of $\omega < 90$ MHz) or by adjusting the position at which the coaxial cable is connected to the turns of L ($\omega > 90$ MHz). I used This experimental setup various times while conducting NMR/NQR experiments at the University of Parma.

2.2.3 Transmission and reception circuit

In the NMR circuit, the *rf* signal is transmitted and received through the same coil and cables. In order to properly excite the sample with the *rf* pulse and collect the NMR signal from it, we cannot keep both the transmission T_x and reception R_x open at the same time. For this reason, we use a particular scheme for the circuit. This scheme is shown in Figure 2.12. The transmission/receiver circuit comprises a pair of silicon diodes, one configured in reverse bias and the other in direct bias mode, with a threshold voltage denoted as $V_D \geq 0.6$ V. In the operational context, when the voltage exceeds

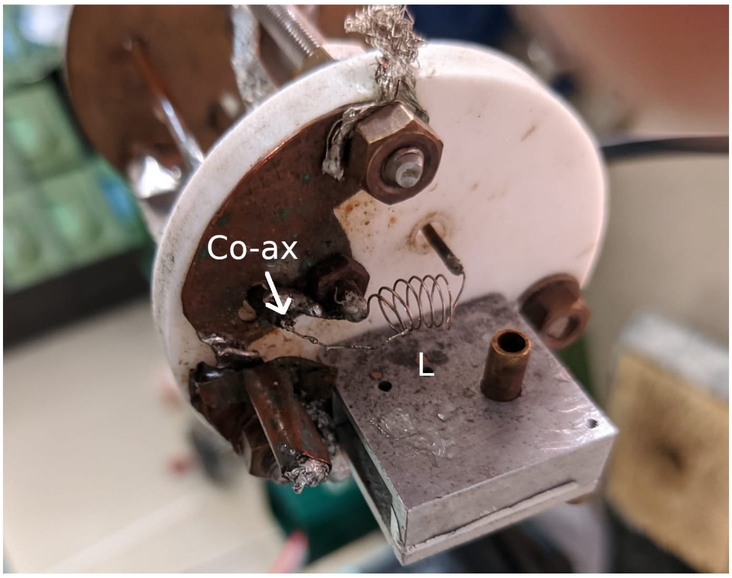

Figure 2.11: Image of a real LC circuit using the "auto-transformer" matching method. The resonant frequency was around 140 MHz. It can be recognized the point where the coaxial (on the left of the coil) is connected to one of the turns of the principal coil, as in Figure 2.10(b). The tuning capacitor C_T is not visible (it is behind the white plate). Taken at the University of Parma.

0.6 V, representing the **on** state, the diodes facilitate signal transmission through the circuit. Conversely, in the **off** state, characterized by voltage levels around 0 V, the diode functions as an open circuit. Another integral component of the transmission/receiver circuit is the $\lambda/4$ cable, which consists of coaxial cables with precise lengths designed to selectively permit a specific range of frequencies to propagate through them. The frequency for which a specific cable works as a $\lambda/4$ is described through Equation (2.51) [66]:

$$L_{\lambda/4}\,(\text{cm}) \simeq \frac{45}{\nu\;(\text{MHz})} \tag{2.51}$$

where $L_{\lambda/4}$ is the length of the $\lambda/4$ cable in cm and ν is the frequency of the signal to be passed in MHz. The cable under consideration exhibits a variety of signal transmission behaviours depending on the voltage level and frequency of the signal within its defined range. When exposed to high voltage levels, this cable acts as an open circuit as long as the signal frequency

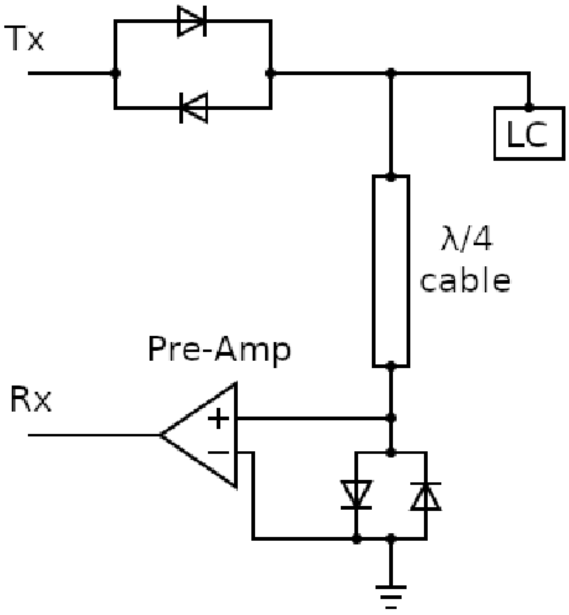

Figure 2.12: Schematic diagram of an NMR circuit, consisting of the transmission part and the reception part.

remains within the permitted range. When the voltage is low, about 0 V, the cable operates as a closed circuit. The appropriate $\lambda/4$ cables are selected depending on the anticipated operating frequency range. The $\lambda/4$ cable bridges the gap between the circuit and the preamplifier. The pre-amplifier, which is powered by a +15 V voltage source, is designed to amplify the sample signal. Notably, the incoming transmission signal from the sample is typically about 1 V, whereas the signal received is on the order of magnitude of microvolts (μV). As a result, the pre-amplifier is important in resurrecting the signal to around 1 volt before it is directed back to the spectrometer.

The operational principle of the system, which comprises of diodes and $\lambda/4$ cable, is as follows:

- when the signal comes from the spectrometer, it has a sufficiently high voltage level to pass the diode threshold, and it also bypasses the $\lambda/4$ cable at its first segment. This occurs because the cable operates as an open circuit when the voltage at one output is elevated for the specific frequency of the $\lambda/4$ cable. As a result, the signal is delivered directly to the LC circuit;

- when the signal departs the sample, it typically registers at the micro-volt (μV) level. The diodes in the T_x line do not improve the signal in this case due to their perfect diode qualities, which allow current to remain small as voltage approaches zero. As a result, the signal is not sent to the T_x line, and the $\lambda/4$ cable operates as an open circuit, reacting in the opposite way as in the prior example. The pre-amplifier then amplifies the signal before being examined by the spectrometer.

The transmission and reception phases are shown in Figure 2.13.

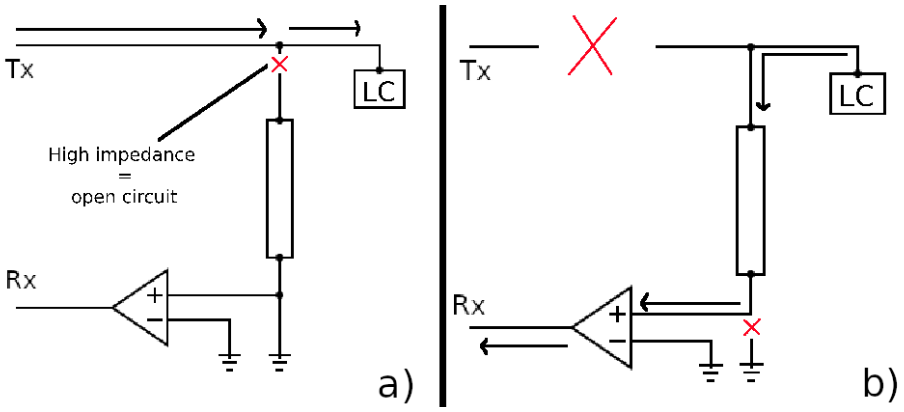

Figure 2.13: The diagram shows the working principles during the transmission phase (a) and the reception phase (b).

2.2.4 Spectrometer, generation and acquisition of the signal

The spectrometer is an electrical device that can create radio-frequency pulses with predetermined time durations and adjustable power amplitudes. This allows the user to precisely regulate the amplitude of the output signal by adjusting power attenuation, pulse duration, *rf* pulse frequency, phase alignment within the xyz reference frame, and several other parameters.

These factors include, among other things, the capacity to control transmission interruptions, signal acquisition time, and the creation of various pulse sequences, which frequently include several pulses. Furthermore, the spectrometer plays an important function in measuring electromagnetic radiation wavelengths that have interacted with the sample under inquiry. Its operational procedure includes the creation of *rf* waves, the stimulation of the sample, and the receipt of the signal after its contact with the sample. In Figure 2.14 it is shown the the Apollo RF spectrometer present in the Bologna NMR Lab, along with the software interface of the HyReSpect spectrometer [75] used at the University of Parma To effectively activate the nuclei inside the sample, the spectrometer signal must be increased. As a result, the use of an amplifier prior to transmitting the pulse to the LC circuit is now required. An amplifier is a type of electronic device that amplifies an electrical signal. It operates by receiving a weak input signal and converting it into a more robust output signal, sometimes with greater power or voltage levels. Amplifiers are distinguished by their gain, which measures the degree of signal amplification provided. Gain is defined as the ratio of the output

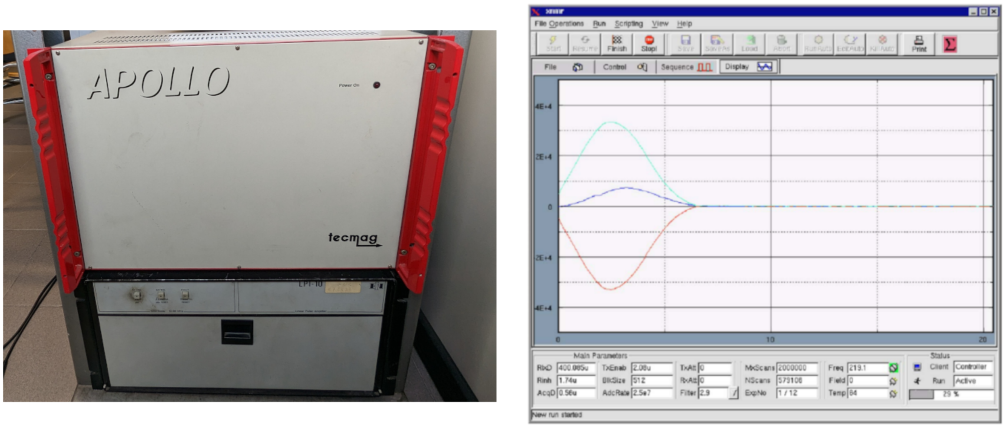

RxD 400.085u
Rinh 1.74u
AcqD 0.56u
TxEnab 2.08u
BlkSize 512
AdcRate 2.5e7
TxAtt 0
RxAtt 0
Filter 2.9
MxScans 2000000
NScans 579106
ExpNo 1 / 12
Freq 219.1
Field 0
Temp 84
Client Controller
Run Active
29 %
New run started

Figure 2.14: (left) The image of the Apollo Spectrometer along with the wide range amplifier below the spectrometer used in Bologna. (right) Screenshot of the gtknmr program during a running spin-echo experiment taken from [75]. The main window shows the plot of the two quadrature components of the signal (red, blue), plus its complex modulus (green)

signal's amplitude to the input signal's amplitude. Amplifiers are built to operate within specific frequency bands and have different features depending on their intended usage and needs. Power amplifiers, voltage amplifiers, and operational amplifiers are three types of amplifiers, each suited to a certain use. In our experiment, we employed a wide-range power amplifier. The negative feedback circuit topology of this power amplifier reduces signal noise and distortion across a wide frequency range.

It is critical to ensure the exact calibration of pulses in NMR investigations. For instance, gaining ideal results in a pulse-acquire experiment requires the use of a 90° pulse to achieve maximum signal strength, but magnetization inversion requires the use of a 180° pulse. As a result, pulse calibration emerges as a vital preparatory step before the start of each NMR investigation. The t_P pulse used to rotate the spins by $\pi/2$ radians from the z axis to the xy plane has to be calibrated. To do so, we can either choose a proper power attenuation of the spectrometer and make the t_P pulse vary, or fix the pulse duration t_P and let the attenuation of the power vary. This is due to the fact that, by recalling Equation (7.11):

$$\theta = -\gamma B_1 t_P \propto -\gamma \frac{t_p}{TxAtt} \tag{2.52}$$

where $TxAtt$ is the attenuation of the transmitted power, which is inversely proportional (higher attenuation → lower spectrometer power) to the strength of the applied *rf* field B_1. The attenuation factor also controls the NMR signal's amplification before irradiating the sample, which has an impact on the power $P(\omega)$ of the NMR signal. Because the transmission gain can differ between spectrometers and over time due to changes in hardware or other factors, attenuation calibration is crucial. The exact attenuation factor of the spectrometer must be ascertained and adjusted in order to achieve accurate and repeatable NMR observations. Attenuation calibration gives the optimal compromise between power and frequency window. The attenuation $TxAtt$ gives the right power ($P(\omega)$) and pulse length t_P gives the window of available frequency for the particular experiment. The pulse length is inversely proportional to the spectral width $\delta\omega$, the lower the pulse width, the greater the frequency range covered. Similarly, for power and attenuation, the lower the attenuation, the higher the power. We need the optimal attenuation to get a good signal, but also keep in mind that the sample does not get overheated due to very high power or a very short repetition delay.

$$TxAtt \propto \frac{1}{P(\omega)} \qquad t_P \propto \frac{1}{\Delta\omega} \tag{2.53}$$

For example, we first fix the pulse length t_P at some reasonable value and do the attenuation sweep to find the point where the signal is highest (which corresponds to the attenuation for the chosen pulse length, which gives a $\pi/2$ rotation). We repeat the process for different pulse lengths to get the best pulse length and attenuation for the experiment. This example, in the real case of Cu_2O sample, is shown in Figure 2.15.

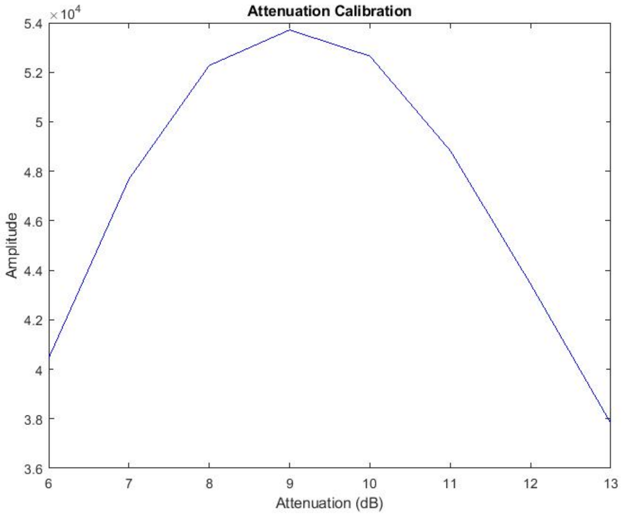

Figure 2.15: The plot shows the amplitude of the signal with respect to the attenuation of the outgoing power from the spectrometer. This is an example of attenuation calibration done on Cu_2O sample with pulse length of 5.5 μs and attenuation in dB to find the highest signal point.

2.2.5 Spectra acquisition and relaxation measurements

Spectra acquisition

The usual data collection procedure for capturing a single spin-echo signal, maintaining a constant transmitted *rf* strength while changing the frequency, is as follows. This method, also known as the "sweep-frequency" method, is extensively used to obtain the whole spectrum of a nucleus. This procedure uses the *Spin-Echo* technique, with the delay τ kept fixed at a specific value, since we do not want to measure the relaxation time T_2. Following an initial search for the optimal $\pi/2$ pulse, described in the previous Section 3.1.3, a series of spin-echo amplitude measurements, denoted as N, are performed. The spectrometer is switched off for R_{ixD} seconds before each spin-echo measurement. The transmission line is then energized, resulting in a pulse with a length of t_{P1} ($\pi/2$ pulse). Following an additional delay period denoted as D, a second pulse with a duration of $t_{P2} = 2t_{P1}$ is generated (required for spin-echo measurements so that the second pulse is precise π). After a R_{inH} waiting period, the receiver line is activated, and the analog-to-digital converter (ADC) is active after another A_{cqD} interval. After completing the initial acquisition, the spectrometer enters an idle state for R_{ixD} seconds before repeating the cycle [76]. Waiting times, such as R_{ixD}, are essential to prevent erroneous signals generated by transient events. These waiting periods must generally fulfill the relationship $R_{ixD} \geq 5T_1$ to ensure the recovery of the whole signal along the z-axis.

The results of all N spin-echo measurements are cumulatively integrated in real-time, as illustrated in Figure 2.16, to provide the final spin-echo amplitude. The *rf* frequency is then automatically modified, and the procedure described above is repeated until all of the desired frequencies have been tested. The spin-echo Fourier Transform peak value corresponds to the genuine NMR signal used for spectrum collection. The frequency-shifted and phase-corrected envelope Fourier transforms derived from several spin echoes captured at various reference frequencies can be used to recreate the whole spectrum, as did in Ref.[77]. This approach is a variant of the frequency step

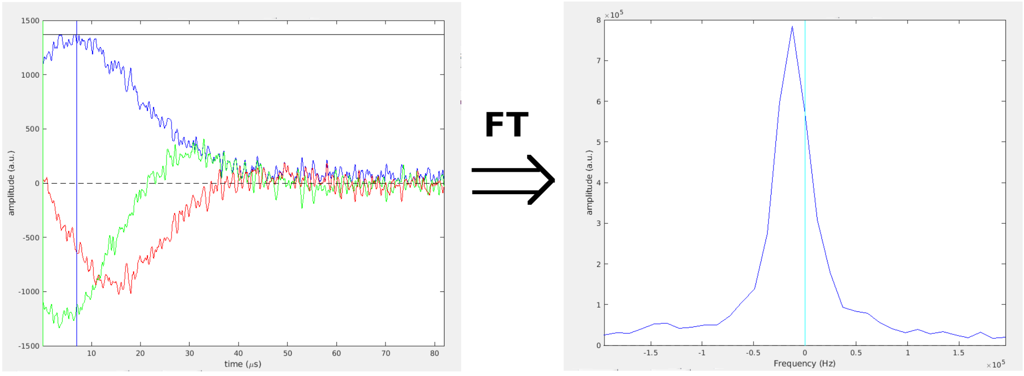

Figure 2.16: Average spin-echo signal measured by the spectrometer. The maximum amplitude is normalized by the number N of acquisitions, and then we obtain the Fourier Transform of the spin echo signal. The amplitude at 0 MHz is the NMR signal.

and sum method described in Ref.[78].

T_1 relaxation measurement

There are different methods to determine the relaxation rate T_1 during an NMR experiment. We report here on the three main sequences.

- Inversion Recovery (IR) - This sequence is made of two pulses, the first one able to tilt the spins by 180° and the second one by 90°. The recovery of the magnetization has the following behavior:

$$M_{\mathrm{IR}}(t) = M(0)[1 - 2e^{(-\tau/T1)}] \tag{2.54}$$

- Saturation Recovery (SR) - Saturation Recovery is another technique used in nuclear magnetic resonance (NMR) spectroscopy to measure the T_1 relaxation time of nuclear spins. Here, a series of radio-frequency pulses is applied to the sample at a fixed repetition rate, with each pulse saturating the magnetization of the sample. After a variable time delay τ, a 90-degree pulse is applied to the sample, which rotates the magnetization into the transverse plane. The signal is then detected by means of another 90° pulse, and the T_1 relaxation time is determined from the time constant of the exponential recovery of the signal towards its equilibrium value. By varying the delay time between the saturation pulses and the first "normal" pulse, the T_1 relaxation time of the sample can be measured. It is given by the equation 2.54:

$$M_{\mathrm{SR}}(t) = M(0)[1 - e^{(-\tau/T1)}] \tag{2.55}$$

- Spin-Stimulaed Echo (SSE) - In an SSE experiment, a 90-degree pulse is first applied to the sample, which tips the nuclear spins from their equilibrium position. The spins then begin to relax back to equilibrium, with the rate of relaxation governed by the T_1 relaxation time. After a time delay of τ_1, a 180-degree pulse is applied to the sample, which inverts the nuclear spins. The spins then continue to relax back to equilibrium, but now in an inverted state. At a time delay of τ_2, a second 90-degree pulse is applied, which creates a spin stimulated echo. The intensity of the SSE is proportional to the magnitude of the nuclear magnetization at time τ_1, which is influenced by the T_1 relaxation time. By varying the time delay τ_2 in the SSE experiment and measuring the intensity of the SSE as a function of τ_2, it is possible to determine the T_1 relaxation time of the nuclear spins. It is given by the equation 2.56 .

$$M_{\mathrm{SSE}}(t) = M(0)e^{(-\tau_2/T_1)} \tag{2.56}$$

The time-dependence of the magnetization recovery for the three T_1 techniques is shown in Figure 2.17. In each T_1 relaxation experiment, it is necessary to wait a proper time before the repetition of the run. In this case, as already written, we must wait a repetition time of $R_{ixD} \geq 5T_1$, in order to be sure that all the nuclear magnetization aligns back to B_0 before retiring the pulse sequence.

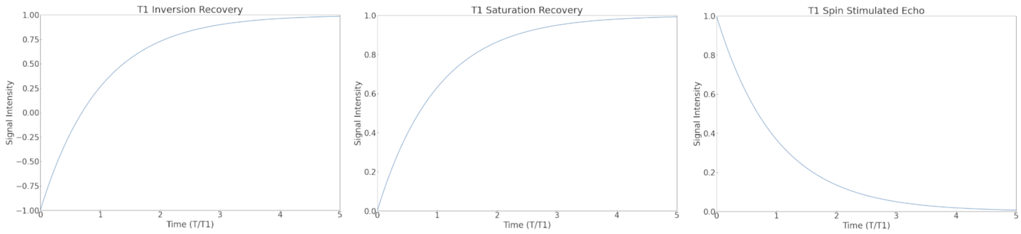

Figure 2.17: The time-dependence of the magnetization recovery for the T_1 pulse sequences described above.

T_2 relaxation measurement

In the measurement of the spin-spin relaxation time, the time dependence of the magnetization along the xy plane is shown in Figure 2.18 and is described by the following relation:

$$M(t) = M(0)e^{-\tau/T2} \tag{2.57}$$

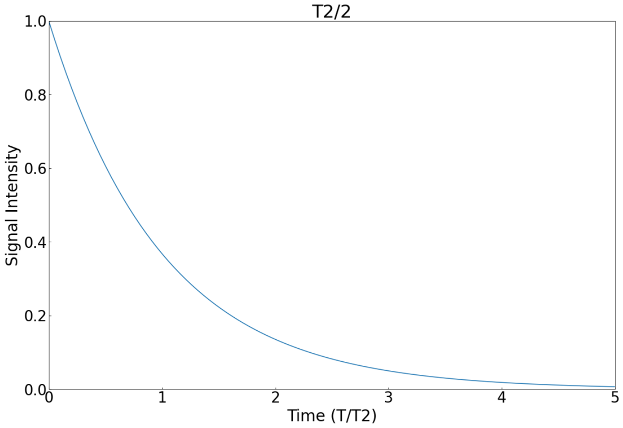

Figure 2.18: The time-dependence of the magnetization on the xy plane for the T_2 pulse sequence.

2.2.6 Cryogenic setup

To conduct experiments at temperatures lower than room temperature, it is necessary to cool the sample with liquid nitrogen (whose boiling point is 77 K) or, to go even lower in temperature, with liquid helium, which allows for temperatures of the order of 5–6 K (its boiling point is 4 K). Other techniques are capable of reaching temperatures of the order of 10–20 mK using a *diluition fridge*, but their explanations go beyond our scope since I didn't use these methods in my Ph.D. project. Going back, we can use a so-called *cryostat* to cool down our sample by means of liquid nitrogen or helium. Figure 2.19 shows a classical cryostat used in low-T NMR (along with the probe inserted) and the cryogenic setup used to flow liquid coolant in the circuit. Depending on the cryogenic liquid used, we can talk about

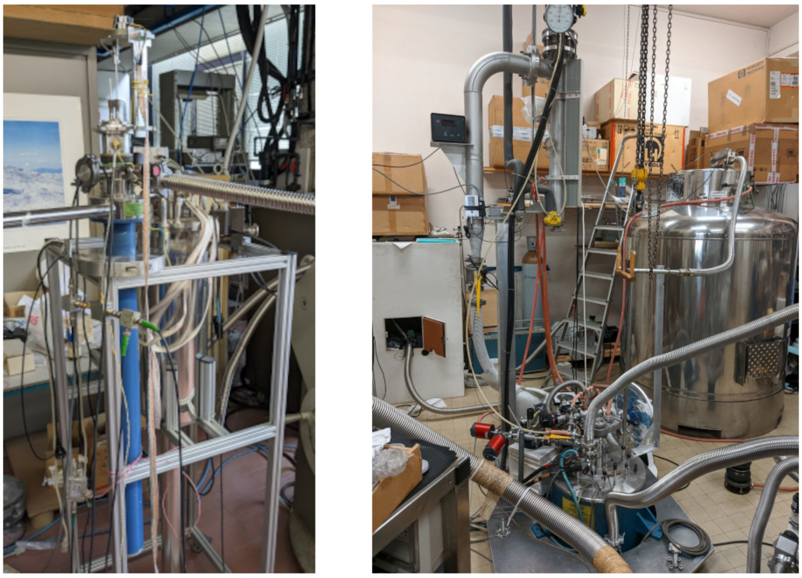

Figure 2.19: (left) NMR probe inserted into a classical cryostat for liquid nitrogen/helium measurements. On the left, is visible the tube where the transfer line is inserted, which pumps nitrogen/helium from the dewar. On the right, the tube that connects the pumping apparatus, capable of vacuuming the sample space, is visible. Taken at the University of Parma. (right) An NMR magnet situated under the floor, with a helium liquidifier behind it (big cilindric dewar on the right). Taken at LNCMI-Grenoble, France.

liquid nitrogen and liquid helium.

- When liquid nitrogen (LN2) is maintained in an uninsulated vessel for a period of time before boiling occurs, ice forms around the vessel as water vapour condenses. A vacuum zone is included in nitrogen cryostats to minimise boil-off rates and separate the external surfaces from the freezing liquid. The boiling point of LN2 (77 K) is insufficient to freeze the gases in the vacuum zone, necessitating the employment of a charcoal absorption pump to raise the vacuum in this area [79].
- Due to high heat losses from radiation and conduction, liquid helium (LHe) creates greater storage challenges. In the case of tiny cryostats, it is more efficient to store LHe in an external transport dewar and distribute helium through a "low loss" transfer line. In addition to the vacuum gap that separates the sample from room temperature, LHe cryostats contain an intermediary radiation shield designed to intercept radiative heat transfer from the ambient room temperature (300 K) [79].

The schematic representation of the liquid helium cryostat setup is shown in Figure 2.20. A temperature control system that includes a proportional-integral-derivative (PID) controller is typically offered with cryostats. In

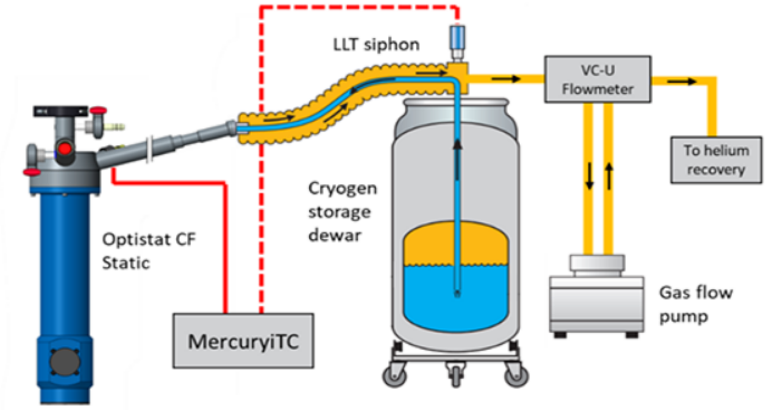

Figure 2.20: Helium cryostat experimental set-up. Taken from Ref. [79].

conjunction with the cryostat's heat exchanger, this controller adjusts the voltage across the heater in response to the flow of the cryogenic material or coolant [79].

We can summarize the entire NMR setup with a schematic figure, Figure 2.21, that comprises all the parts discussed above.

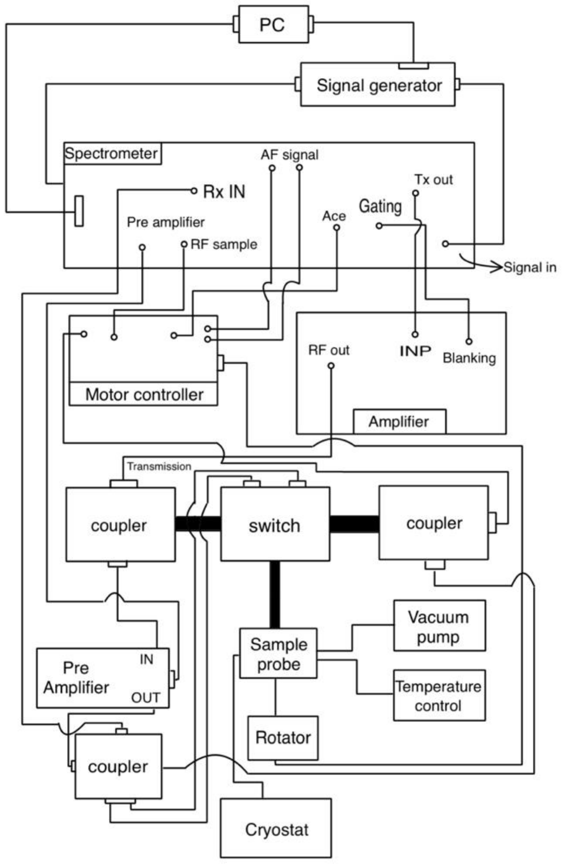

Figure 2.21: Schematic diagram of the experimental setup for a typical NMR experiment. Here, the motor controller automatically tunes the resonant frequency by adjusting the tuning capacitor C_T using a Linux script, while the switch on the bottom of the figure acts as a real switch in order to disconnect the NMR acquisition circuit while the motor is tuning the frequency, and vice-versa to block the motor from change frequency while obtaining the NMR signal.

Chapter 3

μSR technique and experimental methods

In this chapter, I will talk about the theoretical aspects and experimental realization of the μSR technique. More specifically, I will describe the theoretical basis of the muon relaxation and the experimental apparatus for the technique, including the realization of muon beams and the spectrometers used to analyze muons' decays.

3.1 Theory of μSR

This section's presentation and pictures are primarily drawn on sources [80, 81]. Muon is a powerful magnetic resonance technique that allows researchers to investigate the nature of magnetic fields in magnetic materials. The abbreviation μSR refers to muon spin rotation, relaxation, or resonance, depending on whether the muon spin motion is primarily a rotation (more precisely, a precession around a static magnetic field), a relaxation towards an equilibrium direction, or a more complex dynamics dictated by the addition of short radio frequency pulses. The positive muon μ^+ is a lepton elementary particle with the same spin as the electron, $S_{\mu^+} = 1/2$; it is an unstable particle with a mean lifetime of $\tau_{\mu^+} = 2.2\mu s$. It is mostly produced as a result of pion decay by cosmic rays. It has a mass of $m_{\mu^+} = 105.7\ MeV/c^2$, which is ~ 200 times the mass of an electron and $\sim 1/9$ the mass of a proton.

3.1.1 Muon properties and decay

Strong muon beams are generally formed in two steps at moderate-energy particle accelerators. First, a proton beam is fired at a thin target of graphite or beryllium, creating the following interactions between the beam's protons and the target's protons and neutrons:

$$\begin{aligned} p + p &\rightarrow \pi^+ + p + n \\ p + n &\rightarrow \pi^+ + n + n \end{aligned} \tag{3.1}$$

where p denotes the proton, n the neutron, and π the pion. The pion is an unstable particle that decays into a positive muon and a muon neutrino with a lifespan of $\tau_\pi = 26$ ns:

$$\pi^+ \rightarrow \mu^+ + \nu_\mu \tag{3.2}$$

The decay described above is important to the formation of polarised muon rays. The conservation of linear momentum requires the muon and neutrino to radiate in opposite directions when they are at rest in the pion reference system. The neutrino has negative helicity because of the parity violation, with the spin anti-parallel to the momentum. As a consequence, the muon's spin is anti-parallel to its linear momentum since the pion has no spin. Figure 3.1 shows the phenomenon of parity violation. The muons halt in the specimen of interest and decay with a probability proportional to e^{-t/τ_μ} after a time t. The muon decays via a weak nuclear reaction according to the formula below:

$$\mu^+ \rightarrow e^+ + \nu_e + \bar{\nu}_\mu \tag{3.3}$$

where ν_e denotes the neutrino and antineutrino associated with the positron and muon, respectively. Among these three particles, only the positron has been recognized. Its energy range is 0 to $E_{max} = 52.3$ MeV. The rule $2(3 - 2\epsilon)\epsilon^2$ describes the positron energy distribution, where ϵ is the positron's kinetic energy normalized to E_{max}. The direction of positron emission and

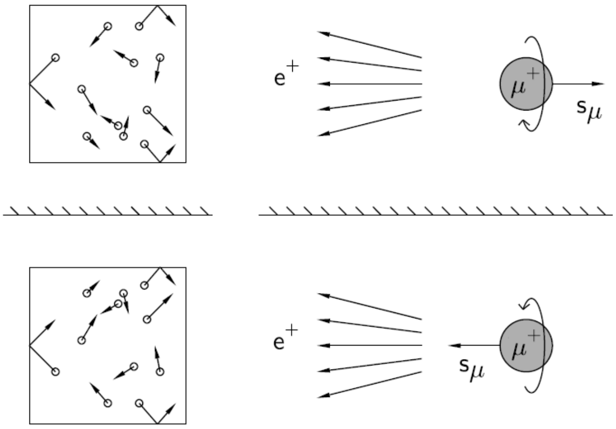

Figure 3.1: On the left, molecules clash with the walls of a box. Because these collisions do not violate parity, both the left-hand process and its mirror counterpart on the right-hand side may be observed in nature. The same cannot be stated for the muon decay process on the right. In the mirror, the direction of the muon spin is inverted, such that positrons are typically emitted in the opposite direction as the muon spin. Taken from [80].

the spin of the muon at decay time have a link that may be used to turn the muon spin into a local probe of matter. This correlation enables the observation of the direction of the muon spin during decay by observing the direction in which the positron is released, as illustrated in Figure 3.2. The likelihood of a positron being emitted at an angle θ, referred to as the direction of the muon spin, is defined as $W(\theta)$. Using the theory of weak interaction:

$$W(\theta) \propto [1 + a_{as}(\epsilon) cos\theta] \tag{3.4}$$

where $a_{as}(\epsilon)$ is the asymmetry parameter, depending on the normalized energy ϵ of the positron. The positron will be emitted the most along the muon spin axis (where $a_{as}(\epsilon) > 0$), as shown by the equation above. Positrons with the maximum possible kinetic energy have $a_{as} \to 1$ and are hence the most coveted, notwithstanding their scarcity. Lower-energy positrons have lower a_{as} values, and for a small number of low-energy positrons, a_{as} is even negative. Integrating over the energy, i.e., counting all the positrons, produces the asymmetry's mean value, $\bar{a}_{as} = 1/3$.

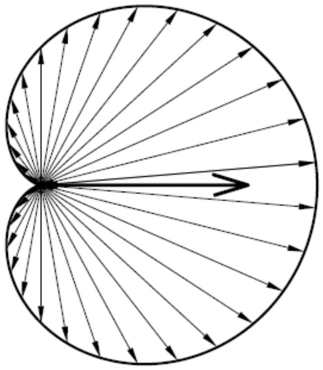

Figure 3.2: The angular distribution of positrons released in relation to the initial muon-spin direction. The graph depicts the predicted distribution of the most energetically released positrons. Taken from [80].

3.1.2 Precession and relaxation of the muon spin

In a magnetic field B, the muon-spin precesses with an angular frequency ω_μ given by $\omega_\mu = \gamma_\mu B$, where $\gamma_\mu = \frac{g}{2}\frac{e}{m_\mu}$ is the muon's gyromagnetic ratio. This is referred to as Larmor precession, and it has already been seen in NMR for a nucleus with spin I and a gyromagnetic factor γ. Precession frequencies are greater for lighter particles, such as electrons, and lower for heavier particles, such as protons. This explains why ESR (electron spin resonance), which investigates the behavior of electronic spins inside a magnetic field, is normally conducted at microwave frequencies (order of GHz), but NMR (nuclear magnetic resonance) is performed at radio frequencies (order of MHz).

Muon spin spectroscopy (μSR) covers a range of frequencies between the ones of NMR and of ESR; however, unlike other resonance methods, no electromagnetic field is required because the precessing muon may be tracked directly. A muon is implanted in a material with its polarisation oriented anti-parallel to its motion. If the material has its own magnetic field, no magnetic field is required for the muons to precess. In general, magnetic fields are delivered to the sample either perpendicular to the initial muon-spin direction (transverse field μSR or TF-μSR) or parallel to it (longitudinal field μSR or LF-μSR), as seen in Figure 3.3. The muon precesses in the applied magnetic field in the perpendicular (or transverse) case, and any dephasing in the measured oscillations indicates either an inhomogeneous internal field distribution or spin-spin relaxation. The parallel (or longitudinal) instance results in spin relaxation rather than spin precession. Inhomogeneous field distributions or spin-lattice relaxation processes might cause this. The zero field μSR (ZF-μSR) is a subset of the longitudinal field in which no magnetic field is supplied and spin relaxation occurs owing to the magnetic field existing inside the probing material.

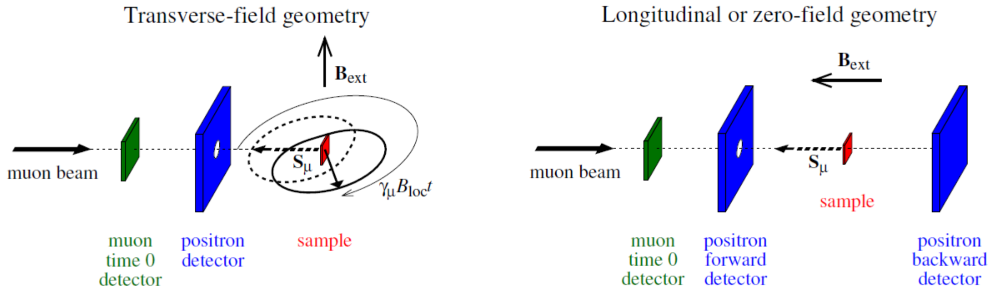

Figure 3.3: The two most prevalent forms of experimental geometry. The example arrows illustrate the muon spin direction: the dashed one at $t = 0$ and the solid one at t. When a muon is implanted into a sample, the likelihood of positron emission along the muon beam direction is shown by the dotted line in the transverse-field geometry panel. The solid line represents the same probability at time t later. Taken from [81].

The temporal evolution of the number of positrons detected in the forward and backward detectors (with regard to the muon-spin direction) is characterised by the functions $N_F(t)$ and $N_B(t)$, which are depicted in Figure 3.4. Due to the fact that muon decay is a radioactive process, these two components add up to an exponential decay. Thus, the temporal evolution of muon polarisation may be calculated by evaluating the normalized difference between these two functions using the asymmetry function $A(t)$, which is provided by:

$$A(t) = \frac{N_B(t) - \alpha N_F(t)}{N_B(t) + \alpha N_F(t)} \tag{3.5}$$

where the coefficient α should be 1, but changes due to instrumental factors (inhomogeneities in detectors' response, little misalignment of the sample with respect to the beam, etc...). This asymmetry function has a maximum value, A_{max}, for a specific experimental configuration, which depends on the initial beam polarisation (usually very close to 1), the intrinsic asymmetry of the weak decay, and the detector efficiency for positrons of various energies, and it is usually around $A_{max} \sim 0.25$.

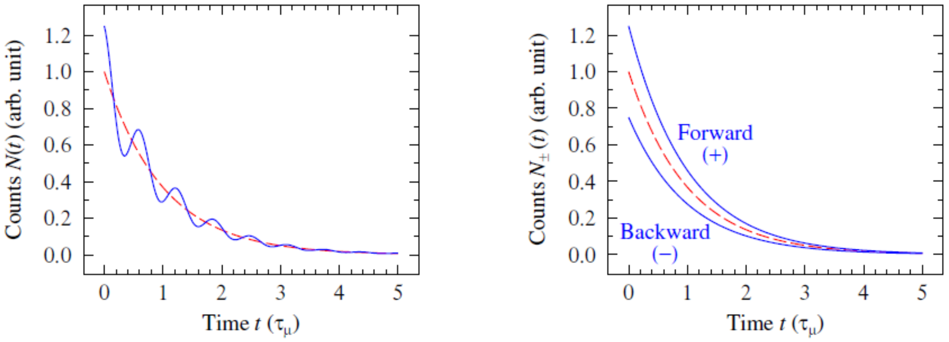

Figure 3.4: The simulation of a raw μSR spectrum in transverse geometry is shown on the left-hand side panel. The whole line represents the positron count $N(t)$. The simulation of raw μSR spectra in the case of longitudinal geometry is shown on the right-hand side panel. The two complete lines represent the counts in the forward and backward detectors. Both graphs have an initial asymmetry of $a_0 = 0.25$, and the dashed lines indicate the average (isotropic) exponential decay that accounts for the finite muon lifespan. Taken from [81].

3.1.3 Muon polarization in a magnetic field

Because of the muon's enormous magnetic moment, it is particularly sensitive to extremely weak magnetic fields, with sensitivity as low as 10^{-5} Tesla. As a result, it is particularly effective for studying materials with small magnetic moments. The study of ferromagnetic and antiferromagnetic materials, in which muons are employed to monitor temperature-dependent changes in the internal magnetic field, is one of the most fundamental applications of this technique.

Randomly oriented static magnetic fields

Because muons have a uniform stopping distribution over a sample, the related volume percentages of muons are perfectly proportional to the signal intensities in experimental spectra. As a result, this method works well when dealing with multiphase samples or samples with poor sorting. Unlike diffraction procedures, this method can usually determine magnetic order in materials where traditional magnetic neutron diffraction is difficult (though single crystal samples can be useful in some cases). The applied field (if used), the dipolar and demagnetization fields (which may be derived from magnetization), and the hyperfine field created by the applied field are all variables that influence the internal field at the muon site. Although it can be challenging in some cases, accurate comprehension of the muon site is necessary for quantitative interpretation of muSR research. Under ideal conditions, only a few possible interstitial locations are available for muon occupancy, with just one consistent with observed data.

Consider spin precession features to gain a better grasp of the muon's ability to investigate the unpredictability and dynamics of magnetism. When the local magnetic field at the muon site generates an angle θ with the muon's initial spin direction at the moment of implantation, the muon spin precesses around the magnetic field. The normalized decay positron asymmetry, or polarization, will be given by:

$$P(t) = cos^2\theta + sin^2\theta cos(\gamma_\mu Bt) \tag{3.6}$$

If the direction of the local magnetic field is entirely random, then averaging over all directions would yield:

$$P(t) = \frac{1}{3} + \frac{2}{3} cos(\gamma_\mu Bt) \tag{3.7}$$

If the intensity of the local magnetic field is selected from a Gaussian distribution with width Δ/γ_μ and centering on zero, then averaging across this distribution yields:

$$P(t) = \frac{1}{3} + \frac{2}{3} e^{-\Delta^2 t^2/2}(1 - \Delta^2 t^2) \tag{3.8}$$

Kubo and Toyabe were the first to get this outcome [82]. As depicted in Figure 3.5, the Kubo and Toyabe relaxation function would be predicted to decline from unity to a minimum and then return to an average value, in this instance, one-third.

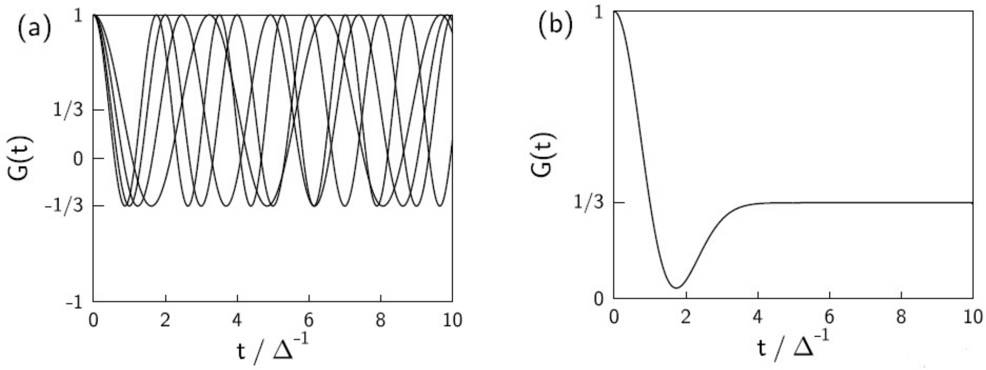

Figure 3.5: Left: the temporal evolution of muon spin polarisation for equation 3 with varying magnitudes of the local field B. Right: the Kubo-Toyabe relaxation function (Equation (3.8)) with its distinctive dip and recovery to a value of 1/3 is obtained by averaging components from the left picture. Taken from Ref. [81].

Fluctuating magnetic fields

At low temperatures, muons enter a stable state and exhibit precession in response to the effect of surrounding nuclear dipoles with random orientations relative to each other. Because of the directional variability, a field distribution is created, which often conforms to Gaussian distributions centred around zero. Any change in the geometry of the internal field distribution would have an effect on the recorded muon-spin time evolution. Individual muons in the sample will precess at slightly different frequencies, resulting in an increasing phase mismatch if the material has a reasonably uniform static internal field with just minor variations from site to site. This phenomenon manifests itself as a damping of data oscillations. When the field changes a lot, the damping effect may be so powerful that no oscillations are seen. However, it is crucial to distinguish between damping produced by fluctuations in the internal field and damping caused by basic material qualities.

One effective method for distinguishing between these conditions is to provide a magnetic field in the longitudinal direction, aligned with the initial muon-spin orientation. Because muons precess in both the internal and applied fields, the Kubo-Toyabe relaxation function is modified, as seen in Figure 3.5. This modification results in a longer "1/3-tail." Notably, when a sufficiently enough longitudinal magnetic field B_L is applied, the muon-spin remains almost constant and does not relax towards unity. The effects of muon hopping on relaxation are shown in Figure 3.6. The hopping rate, denoted as ν, determines the influence of muon hopping on relaxation dynamics. When $\nu = 0$, the relaxation profile corresponds to the zero-field

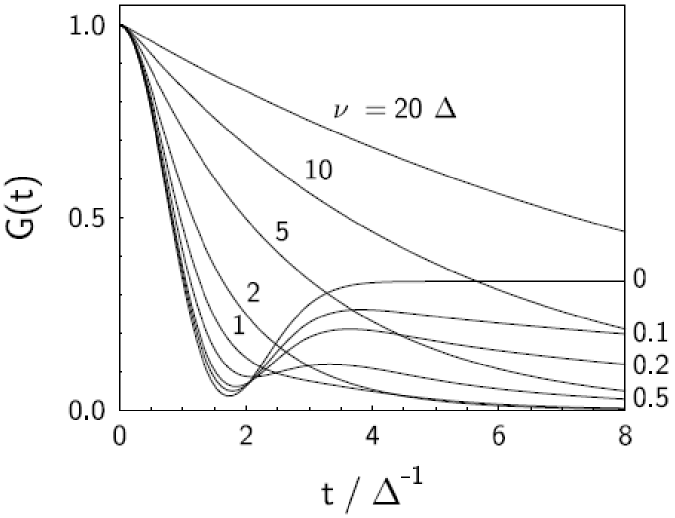

Figure 3.6: The relaxation function of a muon hopping at ν rate. After each hop, the internal field value is drawn from a Gaussian distribution with a width of Δ/μ. The curve shows the zero-field Kubo-Toyabe relaxation function for $\nu = 0$. Taken from Ref. [81].

Kubo-Toyabe curve. In circumstances of rapid hopping, the relaxation process is essentially governed by the muon's hopping dynamics, resulting in an exponential relaxation pattern. As the hopping dynamics rise, the relaxation rate falls. Slow hopping, on the other hand, has almost no effect on relaxing at extremely short intervals. During lengthy time periods, it is particularly visible in the relaxation function's *1/3-tail*. The relaxation function's greater sensitivity to progressive dynamics, as demonstrated by its long-time behaviour, enables monitoring of dynamics throughout a broad temporal spectrum.

3.2 μSR experimental setup

In the following section, we will describe the experimental setup of a typical μSR experiment. We will mainly follow the references [81, 83].

3.2.1 Different muons in time: pulsed vs continous

As taken from [81] and [83], the synthesis of pions, which is required for the production of muons in μSR studies, depends on a proton beam supplied by an accelerator. The temporal distribution of protons inside this beam significantly impacts the temporal distribution of muons in the subsequent muon beam. Two types of proton beams define this differentiation: *continuous* and *pulsed*.

In the case of a *continuous* beam, a muon detector is strategically placed near the muon beam, close to the sample of interest. A timing mechanism is activated when a muon passes through the detector. This temporal sequence begins with the implantation of the muon into the sample and ends with the detection of the positron released during the muon's decay, forming what is known as an "event." For the necessary logic to work properly, just one muon must be present in the sample at any one time. To avoid interference, data collection is briefly interrupted if a second muon is implanted before the positron detection from the disintegration of the first muon. To avoid such undesirable conditions, the intensity of the muon beam is carefully maintained by modifying the muon beam optics components. Using standard instrumentation, a muon precession frequency of roughly 600 MHz, corresponding to a local field of 4.4 T, may be detected using such a beam arrangement. However, it is crucial to note that this configuration has less imbalance at the higher frequencies. Furthermore, coincidence electronics and a veto counter make it easier to distinguish events coming from muons stopped within the sample from those in the surrounding environment. As a result, the obtained data is free of extraneous signals and precisely reflects the fundamental physics of the system under inquiry. Nonetheless, it is worth noting that continuous beams have a disadvantage in the shape of a rather high electrical background, which remains despite the use of coincidence electronics. This makes extracting polarisation functions from raw data more difficult and decreases the observability of slowly attenuated relaxation signals. This approach is used at the PSI facilities in Villigen, Switzerland, where spectrometers GPS, GPD, and FLAME are used.

On the other hand, a *pulsed* muon beam implants a bundle of muons into the sample at a predetermined reference time, with the positrons released during muon decays triggering a series of detectors. To handle the strength of the muon pulse, this system requires a significantly higher number of detectors than continuous sources. The time necessary to capture a spectrum is nearly comparable to the time required to record a continuous muon beam. The pulse width and the temporal spacing between individual pulses are two critical elements of the beam's temporal structure. The latter has a long lifespan in comparison to the muon lifetime. For example, the pulse form of the muon beam feeding the spectrometers at the ISIS facility is essentially Gaussian, with a full-width at half-maximum of around 80 ns and a pulse spacing spanning 20 ms. This one-of-a-kind temporal arrangement, distinguished by a scarcity of background particles occurring between the pulses, allows for detecting extremely weakly attenuated signals and unusually low precession frequencies as low as 0.04 mT. Unfortunately, the large beam size compared to the one for continuous sources brings as a consequence a bigger background, due to the bigger number of muons that stop in the sample holder, thus making it more difficult to determine the form of the polarisation function. Furthermore, it is vital to recognize that the relatively wide pulse width limits temporal resolution. A muon beam with a full-width at half-maximum of 80 ns is inadequate for examining systems with exponential relaxation rates larger than around 10 μs^{-1} or external magnetic fields greater than 50 mT.

3.2.2 Different muons in energy: decay, surface, cloud

From [81, 83], three distinct categories of muon beams, each characterized by different kinetic energy regimes, are at the disposal of researchers. We will talk about the high momentum muon beam, also called *decay* muons, followed by a discussion of the *surface* muon beam, culminating in delineating the recently developed low-energy muon beam (or *cloud* muons). The three categories are shown in Figure 3.7. The earliest beamlines constructed accommodated high-velocity muon beams. Muons are produced in these combinations by the decay of pions in motion. A fundamental component of these beamlines is the employment of a superconducting solenoid spanning many meters in length and creating a magnetic field of a few teslas, referred to as a decay channel. This device intercepts pions with predetermined momentum and directs them to the decay channel, where they decay. The emerging muons are collected by this solenoid, which follows helical paths as

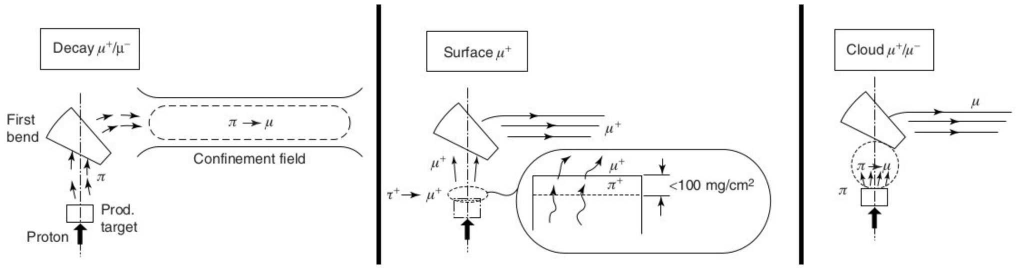

Figure 3.7: There are three types of muon sources created by energetic protons from accelerators (surface μ^+, cloud $\mu^\pm$, and decay $\mu^\pm$). Taken from Ref. [83].

they cross the channel, finally leading them to the sample. It should be noted that muons produced by pion backward decay have spins parallel to their velocity, as opposed to forward decay muons, particularly surface muons. As a result, in such high momentum setups, the polarisation of the muon beam is only 70-80 %, rather than almost 100 %. These beamlines are especially well-suited for generating muons with momentums ranging from 50 to 100 MeV/c, necessitating large sample masses. More material, however, can be put in front of the sample to lower muon momentum and, hence, sample mass. These beamlines are currently only utilized when particular experimental conditions, such as pressure cells or specialist sample containers, need muons to travel through obstacles on their way to the sample.

The volume of sample required for μSR investigations became obvious in the early 1980s as a limiting issue in the broad acceptance of these techniques within the condensed matter research community. Fortunately, the concept of a "surface muon beam" was first proposed in 1976. The concept behind this method is to set up the beamline to choose muons from pions at rest within the pion production target. Muons having a velocity of 29.79 MeV/c and a kinetic energy of 4.1 MeV decay from resting pions. A little amount of matter essentially stops these muons, with only those created at or near the target's surface able to escape and contribute to the beam. This incident validates the phrase "surface muons." In order to eliminate contaminating particles, notably positrons, which are abundantly produced at the pion production target, a "separator" is required while setting up a surface muon beamline. The separator exerts a magnetic and an electric field on the beam. These fields run parallel to one another and in the same direction as muon momentum. They are calibrated such that the Lorentz and Coulomb forces acting on the muons balance each other out, allowing the muon beam to pass through the separator unharmed. Particles having the same charge as muons but different velocities (e.g., positrons) deviate and are prevented from further propagation along the beamline due to an imbalance in the Lorentz and Coulomb forces. Unlike the magnetic field, the electric field does not interact with muon spin and does not generate Larmor precession. As a result, the muon spin polarisation rotates somewhat, but not insignificantly, away from the momentum direction, often in the 5 to 10-degree range.

Nonetheless, surface muon momentum is still rather high for studying thin films, nanomaterials, or multilayers. These muons can only traverse a few hundred micrometers because effective stopping needs 100 to 200 mg of material per square centimeter of cross-section. As a result, ”slow muons,” or particles with kinetic energies in the kiloelectronvolt range or below, are in high demand. The challenge is to maintain a high degree of polarisation while decelerating efficiently. As a moderator, a van der Waals gas (often Ne, N2, or Ar) is condensed onto a cold substrate. Surface muons with kinetic energy of 4.1 MeV hit the substrate, which is thin enough to prevent just half of the muons from passing through. They next travel through a gas layer, which is typically 200-300 nm thick and where electron interactions slow them down. This slowing process works well for kiloelectronvolt and higher muons but not so well for slower muons. As a result, the moderator generates muons of epithermal energy (less than 50 eV). Muon polarisation is greatly influenced since this process occurs quickly (a few picoseconds). The efficiency, which is roughly 10^{-4}, generates almost 8000 muons per second at the sample, allowing regular testing to be performed. The Paul Scherrer Institute (PSI) has a low-energy muon research (LEM) spectrometer. The ability to reaccelerate sluggish muons enables fine-tuning their stopping range within the material, which may range from nanometers at 10 eV to roughly 100 nm at 20 keV.

3.2.3 Large-scale facility and spectrometer

A schematic representation of a muon facility is shown in Figure 3.8, for the case of ISIS Neutron and Muon Source, STFC Rutherford Appleton Laboratory, Oxfordshire, UK. From [84], the European Muon Facility (EMU) at ISIS gathers a percentage of the first two pulses of surface muons released by the muon target when the ISIS synchrotron shoots protons toward the neutron target. Before reaching the spectrometer, these muons are concentrated and steered to control their impact location on the sample within the

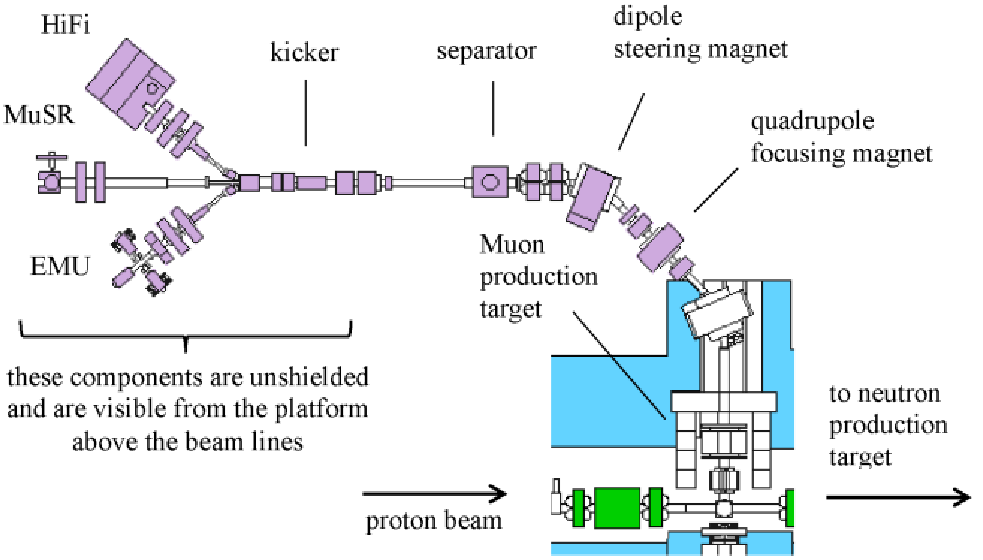

Figure 3.8: General layout of the European Muon Facility at ISIS. Taken from Ref. [84].

cryostat. As seen in the graphic above, this is done by combining dipole and quadrupole magnets. An electrostatic kicker is utilized right before the junction where the EMU and HiFi beamlines depart from the MuSR beamline to separate the two muon pulses emerging from the muon target. This kicker equipment employs a substantial DC voltage to divide the initial pulse of muons, guiding them into EMU and HiFi while the second pulse continues on its journey to the MuSR facility.

Going on, we can describe the GPS spectrometer (General Porpouse Source) for the muon beamline at PSI laboratories, Villigen, Switzerland, which is shown in Figure 3.9. From [85], the GPS Instrument makes use of a ”surface muon beam” (positive muons created by positive pion decay that is terminated at the surface of the production target M). These muons have a typical range of 1.5 mm in polyethylene and 0.65 mm in aluminum. An electromagnetic separator/spin rotator is installed on the beamline, allowing the muon-spin direction to be turned with respect to the muon momentum. The detector setup is composed of:

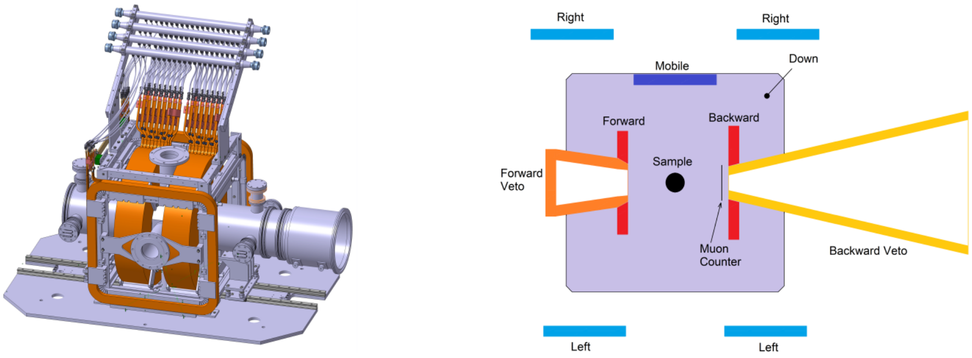

Figure 3.9: (left) The GPS instrument in 3D without the sample insert. The muon beam enters the instrument on the right. (right) Schematic top view of the detectors. Taken from Ref. [85].

- a muon detector (M) with a thickness of 0.18 mm;
- six positron detectors (in the direction of the beam): forward (F), backward (B), up (U), down (D), right (R), and left (L);
- a "mobile" detector attached to either the R or L detector depending on the cryogenic port utilized;
- an array (4 or 5) of SiPMs photosensors that reads each (sub)detector on both sides;
- a detector of backward veto (B_{veto}). The B_{veto}'s goal is to collimate the muon beam to a 7x7 mm^2 spot and reject muons (and associated decay positrons) that pass through the aperture ("active collimation").
- a forward veto detector (F_{veto}) rejects muons (and accompanying decay positrons) that have not halted in the sample.

Chapter 4

NMR/NQR for 2D Kagome superconductors

4.1 General introduction

The AV_3Sb_5 kagome metals are particularly exciting because they exhibit a diverse range of quantum phenomena, including topological isuperconductivity, charge-density wave (CDW) states, and possibly spontaneous symmetry-breaking transitions. These properties are deeply intertwined with the electronic structures of the materials. NMR spectroscopy can be employed to investigate the electronic structure of AV_3Sb_5 kagome metals by measuring the local electronic environments around specific nuclei, typically ^{121}Sb and ^{51}V nuclei in these materials. By analyzing the NMR spectra, we can determine the presence of phase transitions and their nature via changes in the local magnetic susceptibility and electric field gradients, coupled to the nuclear spin and electric quadrupole, respectively. NMR/NQR measurements on different nuclei (^{87}Rb, ^{51}V, and ^{121}Sb) as a function of temperature and for different charge chemical doping allows us to detect the temperature transitions and study the character of the phase transitions at play and their possible interplay. In this chapter, I will present the main result of my Ph.D. project regarding the study of Kagome superconductors using NMR spectroscopy on a number of samples summarized in Table 4.1.

Table 4.1: List of kagome metals of the AV_3Sb_5 family characterised by means of NMR/NQR, along with their composition and form.

Composition	**Doping**	**Label**	**Form**
RbV_3Sb_5	Undoped	RVS	Crystal
KV_3Sb_5	Undoped	KVS	Crystal
CsV_3Sb_5	Undoped	CVS	Crystal
$CsV_3Sb_{5-x}Sn_x$	x = 0.05	CVS-Sn05	Powder
$CsV_3Sb_{5-x}Te_x$	x = 0.04	CVS-Te04	Powder
	x = 0.06	CVS-Te06	Powder

4.2 Methods

Here I will give further details of some specific instrumental set-ups regarding the NMR/NQR measurements presented so far, in addition to the general methods introduced in Chapter 2. $^{51}V/^{87}Rb$ nuclear magnetic resonance (NMR) spectra have been collected on a single crystal of RbV_3Sb_5 as a function of temperature, with an external magnetic field $B_0 = 7.95$ T and 6.99 T. In addition, ^{121}Sb zero-field nuclear quadrupolar resonance (NQR) spectra have also been acquired. For KV_3Sb_5, ^{121}Sb zero-field nuclear quadrupolar resonance (NQR) spectra have been acquired on a single crystal.

The NMR/NQR spectra and relaxation times T_1 and T_2 have been acquired in a wide range of temperatures, from roughly 10 to 290 K, using custom-made spectrometers and cryogenic setups for liquid nitrogen and helium.

The ^{121}Sb NQR spectra at 77/69 K for RbV_3Sb_5 and KV_3Sb_5 were measured by immersing the tuned LC probe head directly in liquid nitrogen inside a nitrogen dewar, which provided a hold time of several days with excellent sample temperature stability and allowed recording spin echo signals at high averaging statistics ($\approx 5 \times 10^5$ scans), as needed to detect the weaker and broader Sb1 peaks with a good signal-to-noise ratio. Spin echoes were excited at discrete frequencies with typical frequency stepping of 50 or 100 kHz, by employing either a standard equal-pulse spin echo sequence $P - \tau - P - \tau -$ *echo* or a three-pulse stimulated spin echo sequence $\pi/2 - \tau - \pi/2 - \tau' - \pi/2 - \tau -$ *echo* [86, 87], with suitable phase alternation of pulses and delays τ just longer than the receiver dead time but, in all cases, well shorter than the spin-spin relaxation time T_2. In the former, the two *rf* pulses P were optimized for maximum signal intensity (a condition corresponding to a nutation angle of $4\pi/3$ [86]). The stimulated echo sequence was mostly employed to detect the weaker ^{121}Sb NQR, in spite of its slightly reduced refocusing efficiency, owing to its immunity to spurious magneto-acoustic (ringing) and magneto-elastic couplings, which, on the contrary, may affect the basic two-pulse excitation sequence by yielding spurious echo signals that are not completely rejected by phase cycling. In either case, spectra were reconstructed as the envelope of the frequency-shifted, phase-corrected Fourier transforms of the various spin echoes recorded at different reference frequencies. Such a method can be regarded as a variant of the frequency step and sum method illustrated in Ref. [78], more suited than the latter to the analysis of frequency-swept spectra.

4.3 Determination of CDW structure in RVS and KVS

In the following section, I will report the results of Ref. [77], which regards the first unambiguous determination of the CDW configuration for the RbV_3Sb_5 kagome superconductor, conducted using NMR and NQR experimental techniques in addition to *ab-initio* DFT calculations (DFT in collaboration with Dr. P. Bonfá from the University of Parma). Furthermore, I will describe the results of the determination of the CDW structure for the parent sample KV_3Sb_5, not been published yet.

4.3.1 Introduction

An important issue that required urgent clarification about Kagome superconductors was the structure of the charge density wave ordering among a subset of proposed configurations in the literature. NMR/NQR is an elective technique since it is extremely sensitive to detecting both inequivalent magnetic and electric sites. Earlier discoveries using Angle-resolved photoemission spectroscopy (ARPES) and Density Functional Theory (DFT), have proposed that the specific CDW structure is dependent upon the presence of A cations in the system [88], adding complexity to the problem. The goal of this current work, which is focused on RbV_3Sb_5 and KV_3Sb_5 samples, is to definitively determine the ground-state structural configuration below the CDW phase transition. Figure 4.1 shows how RbV_3Sb_5 (and similarly, KV_3Sb_5) adopts a layered form at ambient temperature known as the "Pristine" phase, which is defined by hexagonal symmetry and space group P6/mmm, No. 191. The salient feature of this material is the formation of a two-dimensional (2D) kagome layer comprising V atoms (Figure 4.1a), with its electronic band structure exhibiting distinct characteristics, as extensively detailed in the literature [89–91]. The possible different configurations expected below the CDW transition are summarised in Figure 4.1(b-e), and detailed in the following.

At temperatures exceeding the CDW transition temperature (T_{CDW}), which is established at 103 K ($\simeq$ 70 K for KV_3Sb_5), the high-temperature phase of RbV_3Sb_5/KV_3Sb_5 exhibits two non-equivalent Sb sites: Sb1 sites lie in the same plane as V, whereas Sb2 sites are situated both above and below the V layer, forming a graphene-like hexagonal lattice. Specifically, Sb1 occupies the center of V hexagons, while Sb2 potentially resides at the center of V triangles. In the CDW state, below $T_{CDW} = 103$ K, the lattice undergoes a structural transition. First-principles calculations initially proposed two possible distortions for arranging the kagome planes. One is the Star-of-David (SD) distortion (Figure 4.1b) of V atoms, which resembles the well-known motif of the CDW state found in transition-metal dichalcogenides [92, 93]. The other is an inverse deformation of the SD pattern (ISD, Figure 4.1c). This results in a periodic arrangement of V atoms in triangles and hexagons, which is also called Tri-Hexagonal (TrH) structure. Regarding the stacking along the c-axis, different arrangements have been proposed:

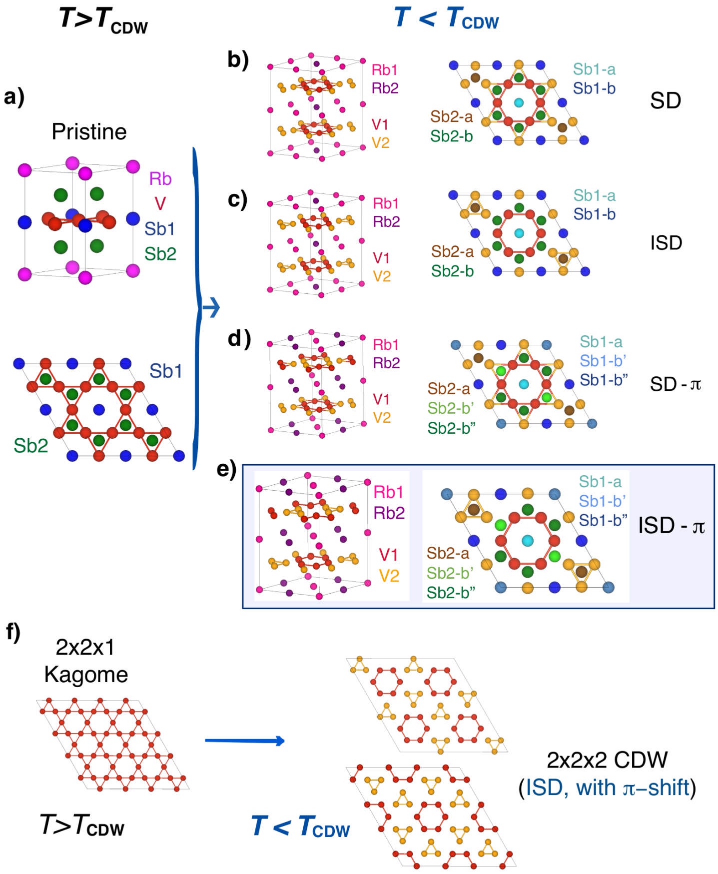

Figure 4.1: The crystalline structure of RbV_3Sb_5, above and below T_{CDW}. a) The pristine phase adopted above T_{CDW}, with the V atoms (in red) forming a 2D kagome lattice. The Sb atoms are divided into Sb1 (in blue) and Sb2 (in dark green). The Rb atoms are labeled in magenta. This is the same structure adopted by KV_3Sb_5 in the normal phase. b), c), d), e) The four considered structures below T_{CDW}: Star-of-David (SD), Inverse Star-of-David (ISD) or tri-hexagonal, (staggered) Star-of-David and Inverse Star-of-David with π-shift (SD-π and ISD-π, respectively). Here, the Sb atoms in the top figures are not displayed for clarity purposes. f) The pattern formed by vanadium atoms above and below CDW transition (ISD-π structure), with the formation of V1 and V2 sublattices (colored in red and orange, respectively) in the CDW phase.

- repetition of SD or ISD (Figure 4.1b and c);
- alternation of ISD and SD;

- a π-shift translation between adjacent planes (SD-π and ISD-π, Figure 4.1d and e).

The overall distortion must, therefore, be described in, at least, a 2×2×2 supercell. In this work, we resolve this controversy for RbV_3Sb_5 and KV_3Sb_5 by combining $^{51}V/^{87}Rb$ NMR and ^{121}Sb NQR measurements for RbV_3Sb_5, and ^{121}Sb NQR measurements for KV_3Sb_5, with Density Functional Theory (DFT) calculations, unambiguously identifying the crystalline structure of the CDW phase among the many variants proposed in the literature for both samples.

4.3.2 Results and discussion

RbV_3Sb_5 results

In the NMR/NQR spectra, the resonance frequency is sensitive to the magnetic and charge environment, hence, non-equivalent nuclear sites arising from the symmetry-breaking effects are typically detected by frequency peak splittings across the phase transition. In addition, the area A_i of the $i-th$ NMR/NQR peak is proportional to the statistical occupation of a specific $i-th$ nucleus, i.e. to the multiplicity of each non-equivalent site in the unit cell. We base the determination of the CDW configuration upon:

- the A_i/A_j ratio of the NMR/NQR peaks for each couple of non-equivalent nuclei ($i \neq j$), equal to the population ratio of the non-equivalent nuclear site per species;
- the quadrupolar frequency ν_Q and asymmetry parameter of the Electric Field Gradient (EFG) tensor η of each peak that we compare to DFT-based calculations of the EFG in the various phases.

In the lowest symmetry configurations considered here, i.e. SD-π and ISD-π, the V and Rb (for RbV_3Sb_5) atoms split into two sublattices, while three non-equivalent sites are obtained for Sb1 and Sb2 nuclei. These are shown in Figure 4.1d and e. The multiplicity of each non-equivalent site is summarised in Table 4.2 for both the pristine ($T > T_{CDW}$) and various proposed CDW

($T < T_{CDW}$) phases.

Table 4.2: Atomic occupations for ^{51}V, ^{121}Sb and ^{87}Rb atoms in RbV_3Sb_5 above and below CDW transition. The same applies to KV_3Sb_5.

Phase	Atoms	Multiplicity
Pristine	Rb	1
	V	3
	Sb1	1
	Sb2	4
2×2×2 CDW (ISD or SD, no π-shift)	Rb1/Rb2	6/2
	V1/V2	12/12
	Sb1-a/Sb1-b	2/6
	Sb2-a/Sb2-b	8/24
2×2×2 CDW (ISD or SD, with π-shift)	Rb1/Rb2	4/4
	V1/V2	12/12
	Sb1-a/Sb1-b'/Sb1-b"	2/2/4
	Sb2-a/Sb2-b'/Sb2-b"	8/8/16

^{121}Sb (with nuclear spin $I = 5/2$) NQR measurements are the most sensitive to distinguish between the SD and ISD structures, as already shown for the case of CsV_3Sb_5 [44, 94]. Due to the different and lower symmetry of their positions, Sb2 and Sb1 nuclei are distinguished into Sb2-a/Sb2-b and Sb1-a/Sb1-b when the SD or the ISD structures are considered and further separated into Sb2-a/Sb2-b/Sb2-b" and Sb1-a/Sb1-b'/Sb1-b" non-equivalent sites when a π-shift is introduced, as shown in Figure 4.1. Figure 4.2 shows selected ^{121}Sb NQR spectra for $5/2 \to 3/2$ NQR transition. Above $T_{CDW} =$ 103 K (bottom of Figure 4.2) two peaks are present and assigned according to the 1:4 occupation ratio Sb1:Sb2 (Figure 4.1a and Table 4.2). In the CDW phase (center of Figure 4.2), we expect four peaks for a simple stacking of SD or ISD-ordered kagome planes, while six peaks should appear when introducing a further π-shift along c. The data for $T < T_{CDW}$ show 5 peaks, with 4 of them clearly visible and an additional spectral weight appearing as a bump next to the most intense peak. From this, we can exclude the two simpler SD or ISD structures with no pi-shift, since they would give only four peaks in the ^{121}Sb NQR spectrum.

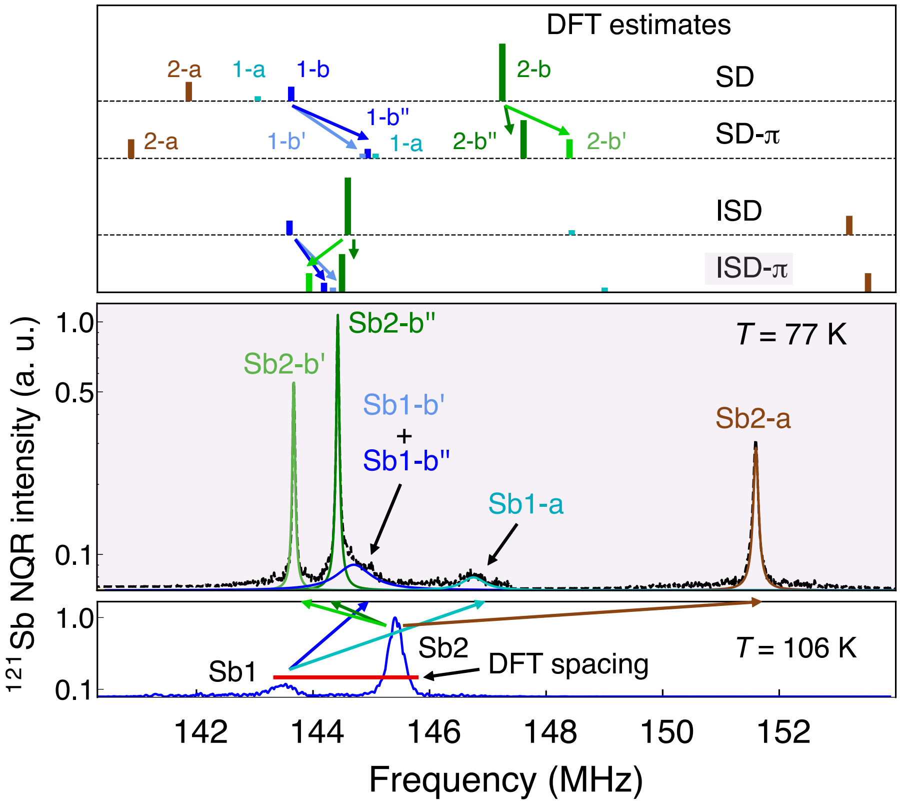

Figure 4.2: Representative ^{121}Sb NQR spectra above (106 K, bottom) and below T_{CDW} (77 K, center) for $5/2 \rightarrow 3/2$ NQR transition. In the top part, vertical ticks display the relative values calculated below T_{CDW} by DFT for SD, ISD, and ISD-π configurations with respect to the quadrupolar frequency of Sb sites above T_{CDW} (see text); the height of the ticks is proportional to the site multiplicity. In the center, the y scale is logarithmic. The DFT spacing is calculated for the normal state in the bottom part.

According to the site multiplicity summarised in Table 4.2, the most intense peak, at almost 145 MHz, is assigned to the Sb2-b". To proceed further, we estimate the quadrupolar frequencies for the various structures with ab initio simulations by collecting the electric field gradient (EFG) at each ^{121}Sb nucleus in the SD, ISD, SD-π and ISD-π structures. The absolute values of the calculated ν_Q at the Sb sites are affected by a systematic error, but these are canceled when the *variations* of ν_Q between the pristine phase ($T > T_{CDW}$) and the low-temperature structures are considered. The mismatch between the experimental results and the prediction for the SD structure is immediately evident (Sb2-a and Sb2-b nuclei have very different quadrupolar resonance frequencies in the SD and ISD structures), and therefore the addition of a π-shift for the SD structure does not improve the matching. Instead, a good agreement is found for the ISD structure, and the small change introduced by the π-shift along the c direction further improves the agreement between the prediction and the experiment. We can, therefore, safely rule out the presence of SD distortions in the kagome plane. Table 4.3 summarizes the A_i/A_j ratio obtained from the area of the NQR peaks and the relative site occupation in the ISD-π phase. The values are in very good agreement within the experimental error. As a result, we can attribute the bump at around 145 MHz to the combined signal from Sb1-b' and Sb1-b" sites of the π-shifted ISD structure, as shown in the center of Figure 4.2. To further justify the site assignment, we also collect the 3/2 → 1/2 NQR transition and we estimate the asymmetry parameter η of the EFG tensor from the following ratio, valid if $\eta \leq 0.1$ [63, 65]

Table 4.3: Multiplicity ratio between ^{121}Sb sites in the CDW phase, according to the crystalline structure (center) and experimental NQR area (right column).

Phase	Sites	Crystal	NQR area (T = 77 K)
Pristine	Sb2:Sb1	4	4.2(3)
CDW	Sb2-b":Sb1-a	8	7.8(3)
	Sb2-b':Sb1-a	4	4.0(2)
	Sb2-a:Sb1-a	4	3.9(2)
	(Sb1-b"+Sb1-b'):Sb1-a	3	3.0(2)

$$\frac{\nu_Q^{121}(5/2 \to 3/2)}{\nu_Q^{121}(3/2 \to 1/2)} \simeq 2(1 - \frac{35}{27}\eta^2)\,. \tag{4.1}$$

The experimental values of η for Sb sites are compared with the DFT prediction for the ISD-π structure in Table 4.4. Taken together, the above results allow us to unambiguously conclude that the kagome planes undergo an ISD distortion in RbV_3Sb_5 and support the presence of a π-shift along c direction,

Table 4.4: Comparison between experimental and predicted values for the asymmetry parameter η.

Site	DFT (ISD-π)	Exp. (T = 77.3 K)
Sb1-a	0	0.001(5)
Sb1-b’	0.056	0.034(5)
Sb1-b”	0.058	0.034(5)
Sb2-a	0	0.001(6)
Sb2-b’	0.117	0.074(6)
Sb2-b”	0.116	0.076(6)

in agreement with previous theoretical predictions [88, 95, 96].

To validate the proposed arrangement of the kagome layers along the c axis, we study the symmetry change of the Rb site. Figure 4.3 shows selected spectra of ^{87}Rb with H_0 = 7.95 T // c axis. As expected for the quadrupole perturbed NMR spectra of the $I = 3/2$ ^{87}Rb nuclear spin, three peaks ap-

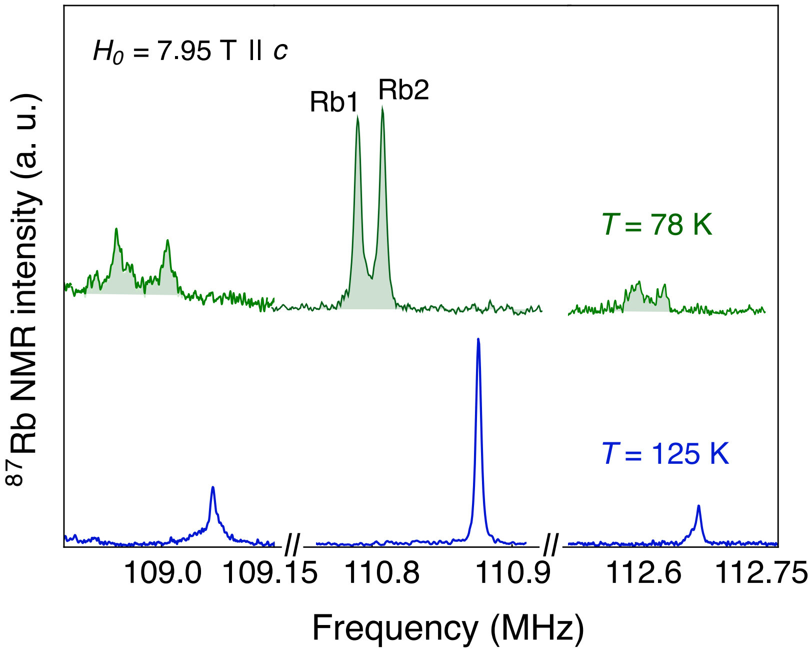

Figure 4.3: Temperature dependence of the ^{87}Rb NMR spectra above and below T_{CDW} = 103 K, with H_0 = 7.95 T // c axis.

pear above $T_{CDW} = 103$ K, related to the ±1/2 transition for the central line plus the $+3/2 \rightarrow +1/2$ and $-1/2 \rightarrow -3/2$ transitions for the low and high-frequency satellites, respectively. Below $T_{CDW} = 103$ K, both the satellites and the central line clearly split, thus reflecting the presence of two inequivalent sites, labeled Rb1 and Rb2. The splitting of all the transition peaks for the $I = 3/2$ is due to the consequence of different electric field gradients and local susceptibilities at the two sites. This behavior is in agreement with the behavior of the ^{51}V NMR in CsV_3Sb_5 [44, 90]. As already done for ^{121}Sb NQR measurements, we consider the relative area between the two NMR peaks of a doublet, which is proportional to the ratio between the multiplicity of the corresponding inequivalent atomic sites. The stacked ISD layer with a π-shift [44] yields a 1:1 multiplicity ratio between Rb1 and Rb2 sites. On the other hand, the structures with alternating SD and ISD layers [43] proposed for CsV_3Sb5 or stacked of ISD layers without π-shift yield to a 3:1 ratio. Figure 4.3 clearly shows that the ratio between Rb1 and Rb2 peak intensities is nearly equal to 1:1 for the central or satellite doublets. This result excludes the alternate SD and ISD configurations and is only compatible with the stacking made by ISD layers, π-shifted from one layer to the other.

KV_3Sb_5 results

The ^{121}Sb NQR spectra in the pristine phase have been acquired at T = 77 K and in the CDW phase at T = 69 K, and can be seen in Figure 4.4. As the temperatures show, the already reported CDW measurements in KV_3Sb_5 were not so precise in the determination of the transition temperature. In fact, the exact CDW transition temperature is less than 70 K, around 10 K less than the reported ones [7]. Moving on to the determination of the CDW structure, we first report the area ratios between Sb2 and Sb1 peaks in the pristine phase. As it can be seen in Table 4.5, this is in agreement with the expected one within the error bar. We can clearly see that, opposite to the RbV_3Sb_5 case, in the pristine phase of KV_3Sb_5, Sb1 site has a higher NQR frequency with respect to Sb2, so it is reasonable to expect that at T = 69

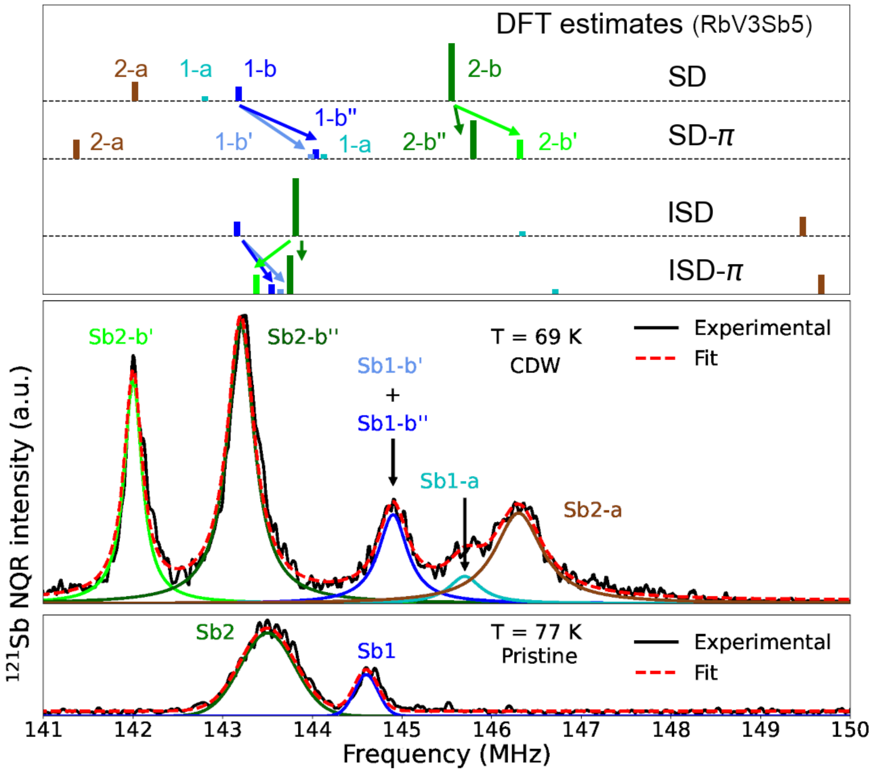

Figure 4.4: Representative ^{121}Sb NQR spectra above (77 K, bottom) and below T_{CDW} (69 K, center) for 5/2 → 3/2 NQR transition in KV_3Sb_5 single crystal. In the top part, vertical ticks display the relative values calculated below T_{CDW} by DFT for SD, ISD, and ISD-π configurations with respect to the quadrupolar frequency of Sb sites above T_{CDW} for RbV_3Sb_5 (see Section 4.3.2); the height of the ticks is proportional to the site multiplicity. In the center, the y scale is logarithmic.

K (CDW state) Sb1 sites (Sb1-b', Sb1-b" and Sb1-a) will have higher NQR frequencies than in RbV_3Sb_5. By looking at the middle panel of Figure 4.4, the NQR spectra in the CDW phase show many similarities with the NQR spectra of RbV_3Sb_5. The frequencies of Sb1 sites (Sb1-b", Sb1-b' and Sb1-a) have a higher value with respect to the same for RbV_3Sb_5 measurements, as predicted before. The area assignments, depicted in Table 4.5, are close to the theoretical expectations, and the relative peaks' positions with respect to DFT calculations for RbV_3Sb_5 safely prove that the CDW structure adopted by KV_3Sb_5 below $T_{CDW} = 70$ K is the ISD-π, as for RbV_3Sb_5.

Table 4.5: Multiplicity ratio between ^{121}Sb sites in the CDW phase for KV_3Sb_5, according to the crystalline structure (center) and experimental NQR area (right column).

Phase	Sites	Crystal	NQR area (T = 77 K)
Pristine	Sb2:Sb1	4	4.6(5)
CDW	Sb2-b":Sb1-a	8	7.9(4)
	Sb2-b':Sb1-a	4	4.2(2)
	Sb2-a:Sb1-a	4	4.4(3)
	(Sb1-b"+Sb1-b'):Sb1-a	3	2.7(2)

4.4 Temperature-dependent behaviour of RVS

We report here the results I obtained in these three years regarding the NMR/NQR temperature-dependent behaviour of ^{121}Sb and ^{51}V nuclei in the kagome superconductor RbV_3Sb_5. This includes the measurements (not yet published) of NMR Knight shift and Full-Width-Half-Maximum (FWHM), relaxation times T_1 and T_2, and, finally, quadrupolar frequencies.

4.4.1 Introduction

Kagome superconductors AV_3Sb_5 undergo a unique phase transition, namely the CDW one, in the temperature range T_{CDW} 70–103 K. Apart from this, they become superconducting at a critical temperature $T_C = 0.8$–2.5 K. In the middle of these two transitions, a lot of studies are currently being performed to determine the possible existence of other transitions or exotic phases. Some preliminary NMR studies on CsV_3Sb_5 suggest the occurrence of a *nematic* phase at a temperature $T_{nem} \simeq 40K$ [44], in which rotational symmetry is spontaneously broken by electronic degrees of freedom, while other μSR results highlight [97, 98] the possible existence of a time-symmetry breaking transition that occurs in all AV_3Sb_5 materials at around 40–50 K. In both cases, the presence of orbital currents that flow along the "kagome" bonds is suspected to be at play and responsible for a time-reversal symmetry-breaking mechanism; thus, NMR can capture their effects since a current loop induces a magnetic field, possibly measurable in the NMR spectrum or relaxation times.

4.4.2 Results and discussion

^{51}V NMR results

FWHM and Knight shift. We start by looking at the Full-Width-Half-Maximum of the central line ($-1/2 \rightarrow 1/2$ transition) of ^{51}V NMR spectra (Figure 4.5(a)), which is coupled mainly to the magnetic channel and only in second order to the quadrupolar one. These data were collected with an applied magnetic field of 7 T /7 c axis on a RbV_3Sb_5 single crystal. Just immediately after the CDW transition, the FWHM of both vanadium sites shows an abrupt increase, a sign of the transition occurring, and then a decrease to almost a constant value for $T \sim 85$ K. The data show a clear increase in the FWHM for the V2 (triangular) site below 50 K. The V1 (hexagonal) site does not show any clear anomaly around 50 K but a monotonic increase from higher temperatures. This might be tentatively attributed to the fact

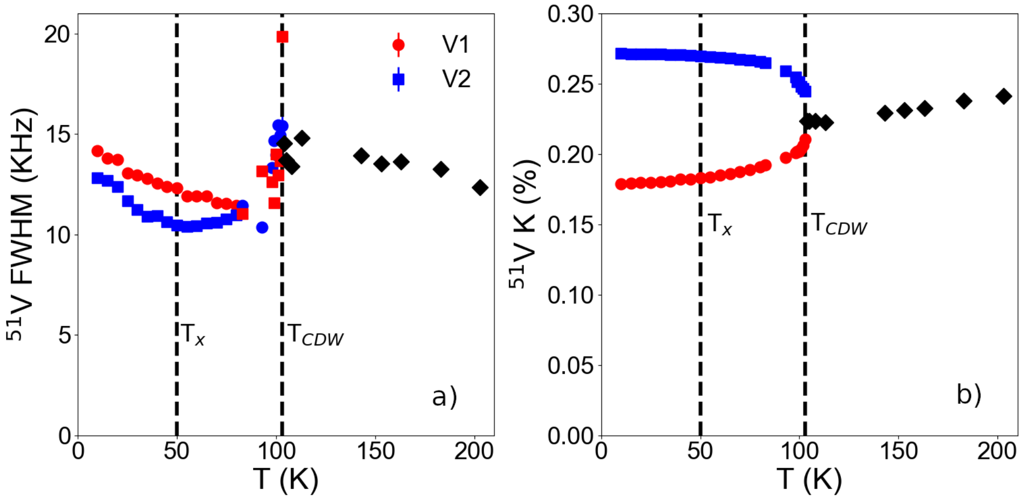

Figure 4.5: Temperature behaviour of a) FWHM and b) Knight shift of the central ^{51}V NMR spectrum on RbV_3Sb_5 single crystal ($H_0 = 7$ T // c axis). Below T_{CDW}, V1 and V2 inequivalent sites are plotted by red circles and blue squares, respectively.

the possible loop currents occur within the V triangle of the Kagome structure and V1 is less sensitive. This is compatible with the results of Ref. [44], where ^{51}V NMR measurements performed on CsV_3Sb_5 at high field (16 T) show a splitting of both ^{51}V site peaks below 40 K, being for V2 higher. The phenomenon has been interpreted as due to electronic-nematicity-enhanced C_2 splitting, or spontaneous Rotational Symmetry Breaking (RSB). In our measurement performed at a much smaller field, the splitting is not resolved, instead appearing as an enhancement of the peak broadening at 50 K, at least for the V2 site.

In Figure 4.5(b), the Knight shift K for the central line ($-1/2 \rightarrow 1/2$ transition) ^{51}V nuclei, expressed as the percentage of shift with respect to the applied field $B_0 = 7$ T, shows almost constant behaviour in the pristine phase while splitting into two almost specular lines below the CDW transition. The behavior of the Knight shift does not show any anomaly around 50 K for both peaks, probably because an independent trend is followed by the peak maximum.

Relaxation times. After analyzing the linewidths and the frequency shifts of the NMR spectra, we can now focus on the study of spin dynamics for ^{51}V nuclei, by measuring the spin-lattice relaxation time T_1. The spin-lattice T_1 measurements have been acquired in a wide range of temperatures, from 10 to 290 K, using a standard Saturation Recovery (SR) technique. The inverse of it multiplied by the temperature, namely the $\frac{1}{T_1 T}$, from the theory of Fermi liquid models [70] is expected to be constant in a simple metal. In particular, both the isotropic part of the Knight shift K_{iso}, which is the average of the Knight shift with the field applied in the plane and along the c axis, and $1/\mathrm{T}_1\mathrm{T}$ are related to the density of states (DOS) $\rho(\mathrm{E}_F)$ at the Fermi level through the Pauli magnetic susceptibility χ_{P_0} and should be constant in temperature:

$$\begin{aligned} K_{iso} &= \frac{A_0 \chi_{P_0}}{g \mu_B \hbar \gamma_n} \\ \frac{1}{T_1 T} &= \frac{\pi k_B A_0^2 \rho^2(E_F)}{\hbar} \end{aligned} \tag{4.2}$$

where A_0 is the hyperfine coupling constant, $\hbar$ the reduced Planck's constant, μ_B the Bohr's magneton, g and γ_n the gyromagnetic factor and the gyromagnetic ratio for the nucleus under study, respectively. By looking at Figure 4.6, the quantity $1/T_1T$ is not temperature-independent even above the CDW transition, where the system is in the metallic regime. This is a hint of a possible "hidden" ordering that occurs at high temperatures ($T > 160$ K) and/or the possible presence of strong electron correlation. When crossing the CDW transition, the system is no longer in a classical metallic state, hence, the two ^{51}V sites have different and increasing values of T_1 (and therefore, decreasing $1/T_1T$) which is a sign of a different modulation of the DOS at the Fermi level for the two sites, a consequence of the CDW ordering [99, 100]. The inset in Figure 4.6 highlights the 10-80 K region of the $1/T_1T$.

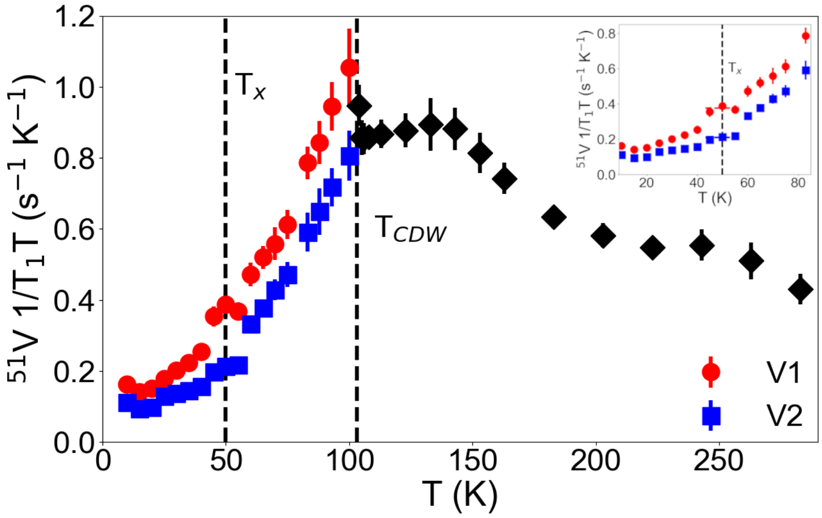

Figure 4.6: NMR relaxation measurements on RbV_3Sb_5 single crystal to determine $1/T_1T$ for ^{51}V nuclei, in an applied magnetic field of 7 T // c axis. In the inset, the zoom on the 10-80 K region.

When reaching $T_x = 50$ K (detected from FHWM vs. T in Figure 4.5(a) on V2 site), the $1/T_1T$ possibly changes its slope and becomes almost flat; after that, it decreases again and reaches a plateau at very low temperatures. A deeper analysis and more experimental points are needed. Overall, the ^{51}V NMR results as a function of temperature presented in this chapter confirm the presence of anomalies at around $T_x \simeq 50$ K, with hints of a change in the charge distribution for certain vanadium nuclei. To better understand the mechanism that lies behind this anomalous change, further analyses are needed.

^{87}Rb NMR results

To further elucidate the T-dependence of RbV_3Sb_5, we analyzed ^{87}Rb nuclei with NMR, in an applied magnetic field of 7 T.

Knight shift. Starting from the NMR spectra (reported for selected temperatures in Figure 4.3), we collected the Knight shift in a wide range of temperatures and with the applied field B_0 along the c axis and parallel to the ab plane of the sample. Figure 4.7 shows the Knight shift values in the two field configurations, along with the difference δK between the two Rb sites below the CDW transition. By looking at Figure 4.7(a) in the pristine phase ($T > 103$ K), K is almost temperature-independent, therefore fulfilling Equation (4.2) for a simple Fermi liquid. We only notice a major shift in the case of B_0 // ab plane than to the c axis, of about 0.05 % more. When crossing the CDW transition temperature, the Rb1 and Rb2 sites have similar K up to 90 K, and then their splitting becomes larger and larger. In

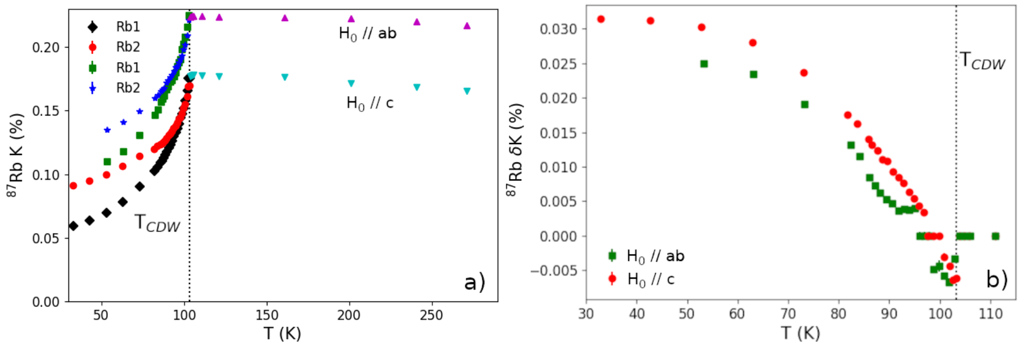

Figure 4.7: NMR measurements on RbV_3Sb_5 single crystal in a magnetic field $H_0 = 7$ T // c axis and // ab plane. (a) The temperature dependence of the Knight shift K for ^{87}Rb central lines. (b) The Knight shift difference δK between the two split peaks Rb1 and Rb2.

Figure 4.7(b), the difference δK between Rb1 and Rb2 is plotted. We notice a negative difference in the range 95-103 K, and then a normal increase up to the saturation at $T \simeq 50$ K when B_0 // c. Accidentally, we observe a crossing of the two curves. The very abrupt character of this change at T_{CDW} suggests that the transition is of first-order type. Regarding the hints for a transition at $T_x = 50$ K, we cannot conclude anything from these data, since more points for temperatures lower than 30 K would be needed.

Relaxation measurements. We discuss the results obtained for ^{87}Rb regarding the spin-lattice relaxation time T_1. In Figure 4.8, the $1/T_1T$ measurements collected with $B_0 = 7$ T // c and ab are shown, respectively. In both field configurations, the $1/T_1T$ above T_{CDW} is almost constant in temperature, resembling the behaviour of the Knight shift K. Below the CDW transition, the two ^{87}Rb sites have equal values of T_1 up to almost 75 K, when the slope of $1/T_1T$ changes, and the two sites differ in that value. Unfortunately, we are missing data for $T < 30$ K when B_0 // c axis, and even worse for $T < 50$ K when B_0 // ab plane.

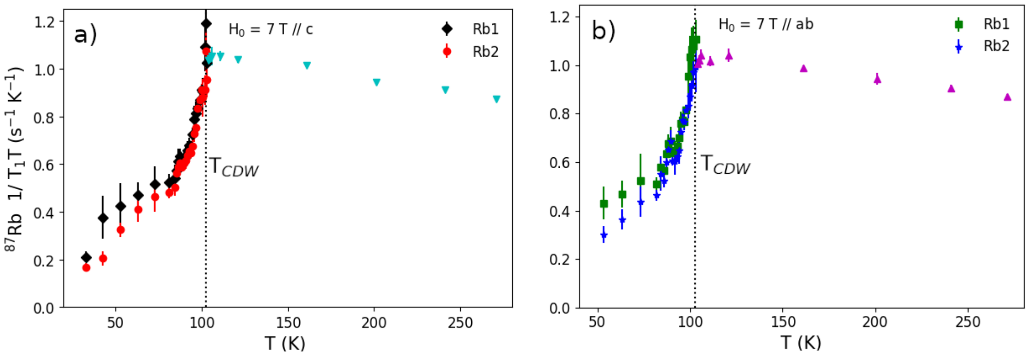

Figure 4.8: $1/T_1$T for ^{87}Rb nuclei in RbV$_3$Sb$_5$, in an applied magnetic field of 7 T measured with B_0 a) // c and b) // ab, respectively.

In conclusion, the data collected as a function of temperature show that ^{87}Rb is also very sensitive to the CDW transition. The behavior of the Knight shift is almost constant for $T > T_{CDW}$, but this is not the case for the $1/T_1T$ which shows a small linear dependence, showing a more complex scenario than for a simple metal. The CDW transition looks first-order. No special clues come at first glance from the temperature behavior below T_{CDW} since in these preliminary measurements performed around 50 K, no evidence of specific anomalies is detected. More information might come from a finer T scan, possibly at much lower temperatures. An accurate analysis of the $1/T_1T$ term and contributions should reflect the complex band topology of this system and is beyond the scope of this work.

^{121}Sb NQR results

Finally, we characterized the temperature-dependent behaviour of ^{121}Sb nuclei by performing zero-field NQR at a wide range of temperatures for the 2^{nd} NQR transition ($|5/2\rangle \rightarrow |3/2\rangle$). In particular, we collected the NQR frequencies for antimony sites in the range 4–275 K, while the Half-Width-Half-Maximum (HWHM) and the $1/\mathrm{T}_1\mathrm{T}$ have been collected only up to 70 K. This mismatch is caused by the poor width resolution of the ^{121}Sb peaks for $T > 80$ K, which cannot give a reliable FWHM (and hence, HWHM), but can still be used to extract the NQR frequencies of the peaks.

NQR frequencies and HWHM. In the pristine phase, the two antimony sites, Sb1 and Sb2, have the asymmetry parameter of the EFG $\eta = 0$, hence the measured NQR frequencies are exactly $2\nu_Q$, where ν_Q is the quadrupolar frequency, since we are measuring the 2^{nd} NQR transition. This is due to the fact that when considering the ^{121}Sb nuclear spin I = 5/2, we can calculate the NQR frequencies for $|3/2 \rightarrow 1/2\rangle$ transition, which correspond to the quadrupolar frequency ν_Q, and for $|5/2 \rightarrow 3/2\rangle$ transition using the relation (valid for an asymmetry parameter of the EFG $\eta \leq 0.1$) [63, 65]:

$$\nu_Q^{3/2\to1/2} = \frac{3eQV_{zz}}{20h}\left(1 + \frac{59}{54}\eta^2\right) \qquad \nu_Q^{5/2\to3/2} = \frac{3eQV_{zz}}{10h}\left(1 - \frac{11}{54}\eta^2\right) \quad (4.3)$$

In the formula, Q is the quadrupole moment of the nucleus, V_{zz} the principal component of the EFG tensor in the Principal Axis System (PAS), I the nuclear spin, and η the asymmetry parameter of the EFG tensor in the PAS notation. It can be seen that for $\eta = 0$, the $5/2 \rightarrow 3/2$ NQR transition frequency is exactly twice the one of $3/2 \rightarrow 1/2$ transition, thus explaining what we observed. Figure 4.9 displays the measured NQR frequencies and the half width half maximum (HWHM), both taken from the NQR spectra of ^{121}Sb. As written in the caption of Figure 4.9, in the CDW phase, we only acquired the data for the three Sb2 sites (Sb2-b', Sb2-b" and Sb2-a) and we ignored the three Sb1 sites (Sb1-b', Sb1-b" and Sb1-a, see Figure 4.1). This is due to two main factors: i) The Sb1 sites have very low intensity compared to Sb2 ones (1:4 for each Sb1-x:Sb2-x couple, respectively), therefore a very high number of scans would be needed to uncover them in the NQR spectra. This has been done in Figure 4.2 and Figure 4.4, at only one specific temperature, to unravel the CDW structure for RbV_3Sb_5 and KV_3Sb_5, collecting 2 days of statistics for each point. ii) A high number of points is needed when doing a temperature-sweep study, hence, it would require days or even weeks of each temperature to follow the T-behaviour of Sb1 sites with a sufficient SNR ratio to make them evident from the noise.

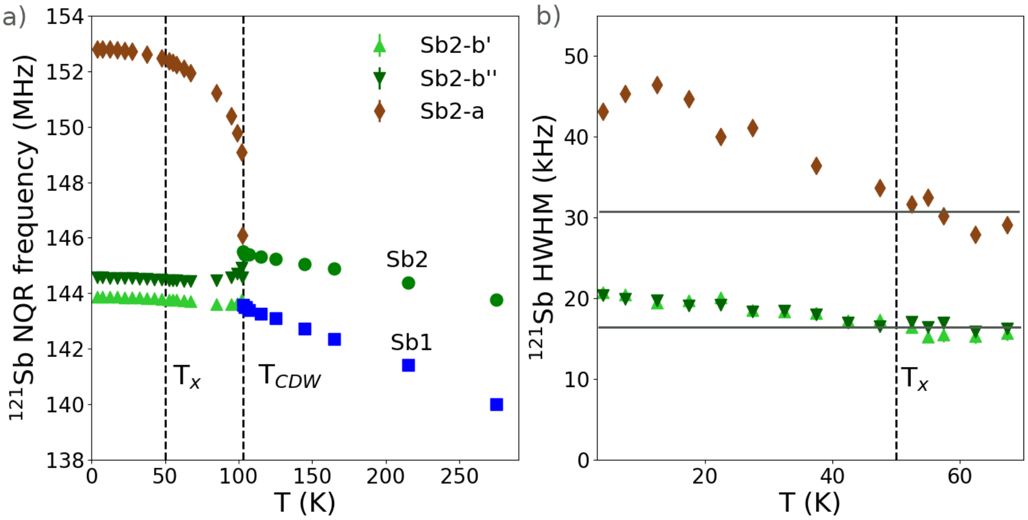

Figure 4.9: ZF-NQR on ^{121}Sb nuclei in RbV_3Sb_5. a) Temperature dependence of the NQR frequencies for ^{121}Sb sites above and below the CDW transition. Below the CDW transition, the three Sb1 sites (see Figure 4.1) are not shown since their low intensity makes them difficult to follow in temperature. b) Half width half maximum (HWHM) of ^{121}Sb NQR spectra as a function of temperature, below the CDW transition. Horizontal lines are the average of points for T > 50 K.

Going back to Figure 4.9(a), the NQR frequency results show an abrupt splitting of Sb2 sites into Sb2-b', Sb2-b" and Sb2-a just after the onset of CDW transition, with the latter site having the highest and most split frequency of all. This abrupt character is again compatible with a first-order-like transition. No clear anomalies of the frequency peaks are found across T_x = 50 K. On the other hand, regarding the linewidth, all the ^{121}Sb NQR lines measured here as a function of temperature show a possible increase at T_x (Figure 4.9(b)), consistent with the V2 behavior (Figure 4.5(a)).

Relaxation measurements. To conclude our temperature-dependent behaviour, we report here the 1/T$_1$T measurements collected in zero-field NQR in the CDW phase, for only the three Sb2 sites. The results are shown in Figure 4.10. Apparently, there are no signs of anomalous deviations in the trend of 1/T$_1$T, and the lack of experimental points for T > 70 K does not help with this.

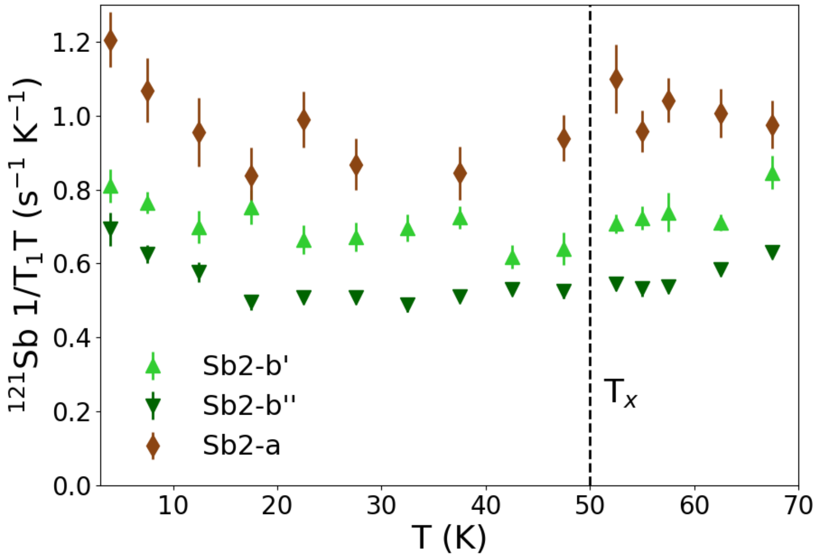

Figure 4.10: Zero-field NQR 1/T$_1$T measurements on ^{121}Sb nuclei in the CDW phase.

Summarizing, for all the nuclei, the temperature dependence of NMR/NQR measurements shows very clearly the occurrence of the CDW transition (and offers a formidable tool to identify the CDW transition, as seen in Section 4.3). Notably, it seems less sensitive to the occurrence of the anomalous phase expected below T_x: only the linewidth of V2 and possibly Sb2 sites indicates some change around 50 K. They might be related to the possible occurrence of spontaneous loop currents and/or a suble charge rearrangement (due to further local structural symmetry breaking within the CDW phase). Further studies are needed to better understand this phenomenon. As we will see in Chapter 5, the μSR technique is more sensitive to the presence of this anomalous low-T phase.

4.5 Determination of substitutional site in charge-doped CVS

The next work I will present is determining the substitutional site in Sn-doped $CsV_3Sb_{5-x}Sn_x$ [101], published in the journal Physical Review Materials. After the introduction, I will report the part I personally conducted, namely the NQR measurements of ^{121}Sb in different concentrations of doped $CsV_3Sb_{5-x}Sn_x$. Furthermore, I will report similar results obtained in Te-doped CsV_3Sb_5 [102], published in the journal Frontiers in Electronic Materials - Superconducting Materials. Both Te and Sn substitutions have been performed in CsV_3Sb_5 powder samples.

4.5.1 Introduction

In novel kagome superconductor CsV_3Sb_5, carrier doping is an appealing means of tuning CDW and superconductivity relative to the Fermi level and probing the coupling of the CDW and SC states. Shifting the relative positions of the VHS and Γ pocket relative to E_F and probing the evolution and interplay of the CDW and SC phase transitions can provide insights into the origins of each state.

In the case of hole doping, a recent study on oxidized thin flakes of CsV_3Sb_5 shows that hole doping on the Cs site can enhance T_C while also suppressing CDW order [103]. In addition, density functional theory (DFT) calculations show that hole doping drives the VHS in the opposite direction relative to E_F than that expected via external hydrostatic pressure [104]. Given that an unusual coupling between SC and CDW states was observed under variable pressure [105], a systematic study of hole-doping effects is an important experimental window into understanding this unconventional coupling. Here, the effect of hole doping on the CDW and SC states in $CsV_3Sb_{5-x}Sn_x$ with $0 \leq x \leq 1.5$ is presented. Hole doping is achieved via the substitution of Sn onto the Sb sites, and because Sn and Sb are very similar in size, this drives negligible coincident steric effects in the band structure. As holes are introduced, the CDW state is rapidly suppressed, and the three-dimensional CDW order vanishes near x = 0.06. In parallel, SC is enhanced and reaches a maximum $T_C = 3.6$ K at x = 0.03 within the CDW state before decreasing as the CDW is fully suppressed. Continued hole doping beyond the suppression of CDW order results in a second maximum in $T_C = 4.1$ K at x = 0.35 prior to bulk SC weakening and vanishing beyond x = 0.5. The above-cited scenario is shown in the left part of Figure 4.11. In the case of electron doping, one unanswered question is whether an electron-hole imbalance occurs in the carrier-tuned phase diagram of CsV_3Sb_5. The relative shift of the Van Hove points relative to E_F should be crucial to system response in a rigid band shift model, and in the more realistic scenario of orbitally selective doping, the impact of the relative shifts of the Sb p_z mixed bands on the CDW state stands to inform more about its function in charge order generation. The electron-doping can be achieved via Te substitution onto the Sb sites in $CsV_3Sb_{5-x}Te_x$, which is the other focus of this part. Our data demonstrate the limited solubility of Te into the CsV_3Sb_5 doped sample matrix before phase separation occurs near x $\simeq$ 0.08 and that Te preferentially occupies the Sb-sites in the V-kagome plane. The electron doping induces a monotonic decrease of Tc and a weaker effect on the CDW state, displaying high T_{CDW} in the whole investigated range. Unfortunately, the low chemical solution limit of the Te/Sb substitution, occurring at x $\approx$ 0.1, prevents the study for further doping. Anyway, the hole and electron dopings display markedly different behaviour.

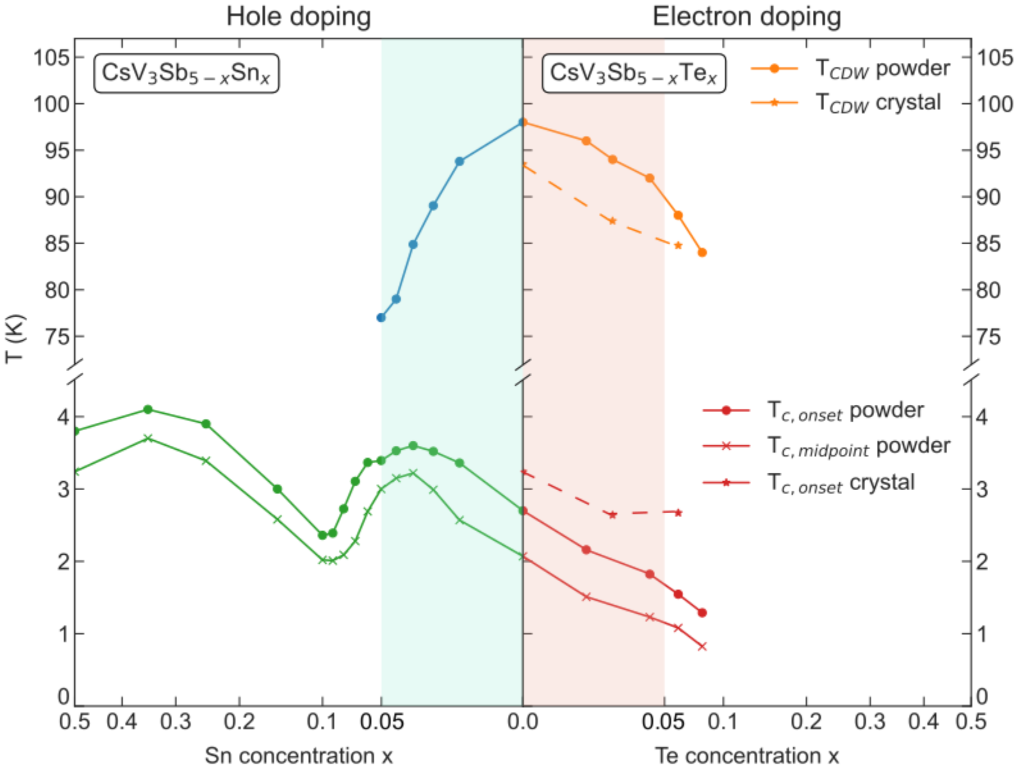

Figure 4.11: Hole and electron-doping phase diagram for $CsV_3Sb_{5-x}Sn_x$, obtained by magnetization measurements from the group of S. Wilson at Santa Barbara Univ., USA, and published in refs. [101, 102]. Left) A double-dome structure is present for Sn dopant and CDW seems to disappear for x > 0.05. Right) for electron doping up to the solution limit of the Te/Sb substitution (x ≈ 0.1), CDW still persists at high temperature while T_c is monotonically decreased, indicating a marked asymmetric behavior with respect to the hole doping case.

In these works, we analyzed pure CVS and electron- and hole-doped CVS-Te06/CVS-Sn05, and conducted room-temperature NQR measurements. Since CsV_3Sb_5 possesses two equivalent Sb sites (Sb1 in-plane with vanadium, and Sb2 out of the plane; see Figure 1.3), it is crucial to understand the substitutional position of Sn/Te dopants between these two Sb sites. DFT calculations and nuclear quadrupolar resonance measurements establish a strong preference for Sn/Te to occupy Sb sites within the kagome plane.

4.5.2 Results and discussion

Sn-doped results

In Figure 4.12 we plot the doping dependence of the NQR frequency spectra for ^{121}Sb sites Sb1 and Sb2. In addition, in Table 4.6, we summarize the frequency shift associated with the first moment of Sb sites Sb1 and Sb2 for two Sn doping concentrations.

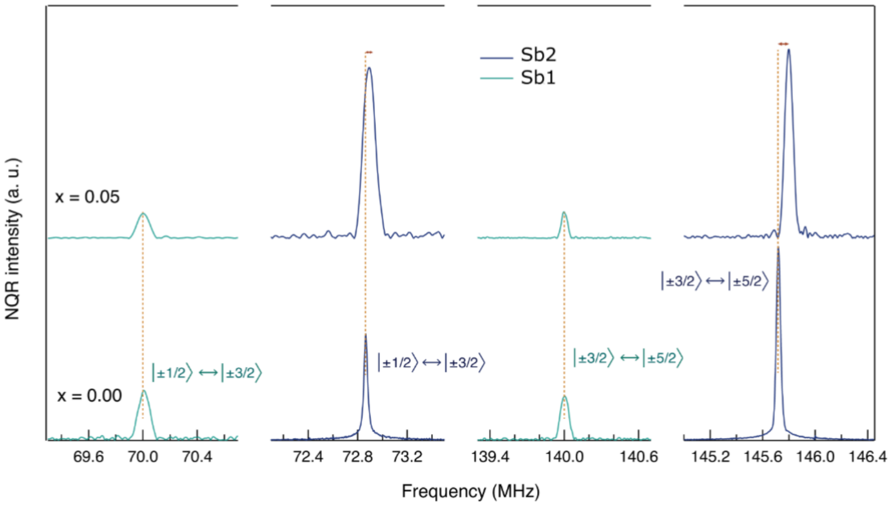

Figure 4.12: Sn doping dependence of the ZF-NQR spectra for the Sb2 (blue) and Sb1 (green) nuclei of two powder samples of CsV_3Sb_5 for x = 0 (bottom) and 0.05 (top). Dashed lines denote the position of all the spectral lines of undoped sample.

Table 4.6: Doping dependence of the frequency shift of the quadrupolar line for $|\pm5/2\rangle \leftrightarrow |\pm3/2\rangle$ transition, for both Sb sites, at room temperature.

Sb site	**Sn concentration**	$\nu_{\mathbf{Q}}$ **(MHz)**
Sb2	0.00	145.7197 ± 0.0012
	0.05	145.7988 ± 0.0012
Sb1	0.00	140.0024 ± 0.0012
	0.05	139.9963 ± 0.0012

Considering the crystalline structure shown in Figure 1.6 and the distances between different Sb sites, we conclude that in order to see a shift in the quadrupolar frequency only for Sb2 sites at low concentrations, the dopant should substitute only the in-plane kagome Sb1 sites. As it can be seen, the distances between Sb1-Sb1 sites are much larger than Sb1-Sb2 ones, and so a substitution of Sb1 nuclei will only affect Sb2 nuclei, therefore modifying the electronic charge distribution around them and the value of the Electric Field Gradient (EFG) tensor, resulting in a different quadrupolar coupling. In the other case, a dopant in Sb2 sites would affect both Sb1 and Sb2 sites since Sb1-Sb2 and Sb2-Sb2 distances are comparable, and so an appreciable shift of the quadrupolar frequency should also be observed for Sb1 sites. Evidently, only the Sb2 site line shifts when Sn dopants are added to the sample, while Sb1 spectra remain at the fixed frequency position unaffected by Sn doping. Therefore, NQR measurements indicate that Sn dopants preferably occupy only Sb1 sites.

Te-doped results

In Figure 4.13 we plot the doping dependence of the NQR frequency spectra for ^{121}Sb sites Sb1 and Sb2. In addition, in Table 4.7, we summarize the frequency shift associated with the first moment of Sb sites Sb1 and Sb2 for two Te doping concentrations.

Table 4.7: Doping dependence of the frequency shift of the quadrupolar line for $|\pm 5/2\rangle \leftrightarrow |\pm 3/2\rangle$ transition, for both Sb sites, at room temperature.

Sb site	**Te concentration**	**$\nu_{\mathbf{Q}}$ (MHz)**
Sb2	0.00	145.7197 ± 0.0012
	0.06	145.9902 ± 0.0012
Sb1	0.00	140.0024 ± 0.0012
	0.06	140.0098 ± 0.0012

Evidently, only the Sb2 site line shifts when Te dopants are added to the sample, while the Sb1 spectra remain at the fixed frequency position, unaffected by Te doping. Therefore, NQR measurements indicate that Te dopants preferably occupy only Sb1 sites, as seen for Sn doping.

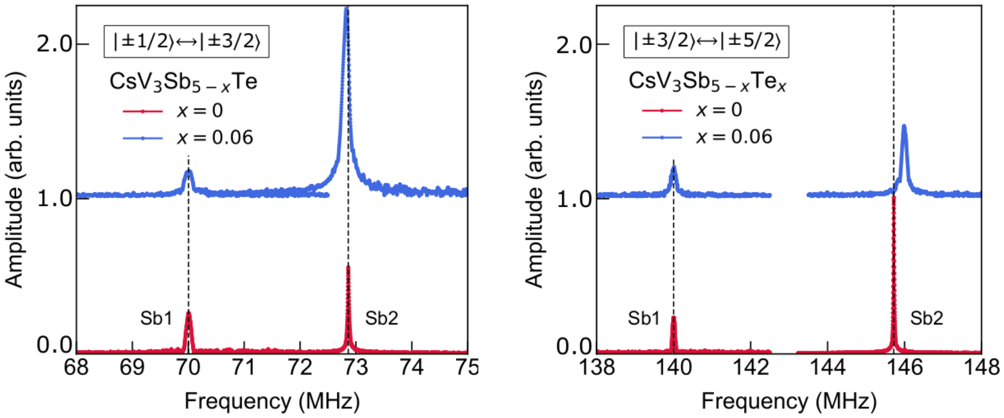

Figure 4.13: Te doping dependence of the ZF-NQR spectra for the Sb2 (blue) and Sb1 (green) nuclei of two powder samples of CsV_3Sb_5 for x = 0 (bottom) and 0.06 (top). Dashed lines denote the position of all the spectral lines of undoped sample.

4.6 CDW temperature for electron-doped CVS

Here I present Sb NQR measurements for the determination of the determination of the CDW transition temperature for undoped CsV_3Sb_5 and $CsV_3Sb_{5-x}Te_x$, with x = 0.04 Te, referred to as CVS-Te04, in comparison with magnetization data from Ref. [102]. This work has been performed as a part of the Master's Thesis of the student Sahil Parvez [106], which I personally followed as a co-supervisor in the first months of 2023.

4.6.1 Introduction

To accomplish this work, we performed a temperature sweep set of ^{121}Sb ZF-NQR measurements on undoped CsV_3Sb_5 and CVS-Te04, in powder forms, to determine the onset of the CDW transition, its mean temperature, and its offset (where the system lies in the "pristine", or normal, phase). We only looked for the Sb2 site in the normal phase, whose multiplicity is four times the one for the Sb1 site, and lies at around 147.5 MHz at $T = 106$ K (see Figure 4.13, where Sb2 site at room temperature lies at around 146

MHz for the $|5/2\rangle \rightarrow |3/2\rangle$ transition), and for the Sb2-b' and Sb2-b" sites in the CDW phase (as a reference, please look at Figure 4.2). This way is extremely sensitive to the occurrence of the CDW since the change in the electric field gradient moves apart the Sb2-b peaks from the Sb2 frequency peak position of the normal phase, as shown in the previous paragraphs. For this reason, we also neglected the Sb2-a site (expected around 150 MHz), since it is redundant for this aim.

4.6.2 Results and discussion

The aim of this work is to compare the area of the Sb2 site above T_{CDW} with the areas of Sb2s sites below the CDW transition, to determine the temperature at which the undoped CsV_3Sb_5 and CVS-Te04 samples enter the CDW phase. We first investigate the undoped CsV_3Sb_5, which will be taken as a reference for the Te-doped analysis. The top panels of Figure 4.14 shows the a) undoped ^{121}Sb NQR spectra for the $|5/2 \rightarrow 3/2\rangle$ NQR transition for selected temperatures in the range 94-106 K, and b) the relative peaks area of the normal and the CDW phases. The fitting of the peaks in panel a) has been done by using multiple Lorenztian peaks to determine the area of each NQR line, which is proportional to the number of nuclei in that specific environment. The area of the normal phase A_{normal} is simply the area of the Sb2 peak (in red), while the CDW area A_{CDW} is the sum of the Sb2-b' peak' area multiplied by two (to account for the Sb2-a site, which is expected to have the same multiplicity of Sb2-b'), and the Sb2-b" one, both in green. Finally, we calculated the relative area of the CDW and normal phases with respect to the total area of the peaks:

$$A_i^{\text{rel}} = \frac{A_i}{A_{\text{normal}} + A_{CDW}} \tag{4.4}$$

whose results are shown in the top panel of Figure 4.14(b). We observe the coexistence of the two phases across the T_{CDW} instead of a sharp transition detected in single crystals. Here we use powder samples and we might expect a distribution of T_{CDW} among different grains due to the presence of defects,

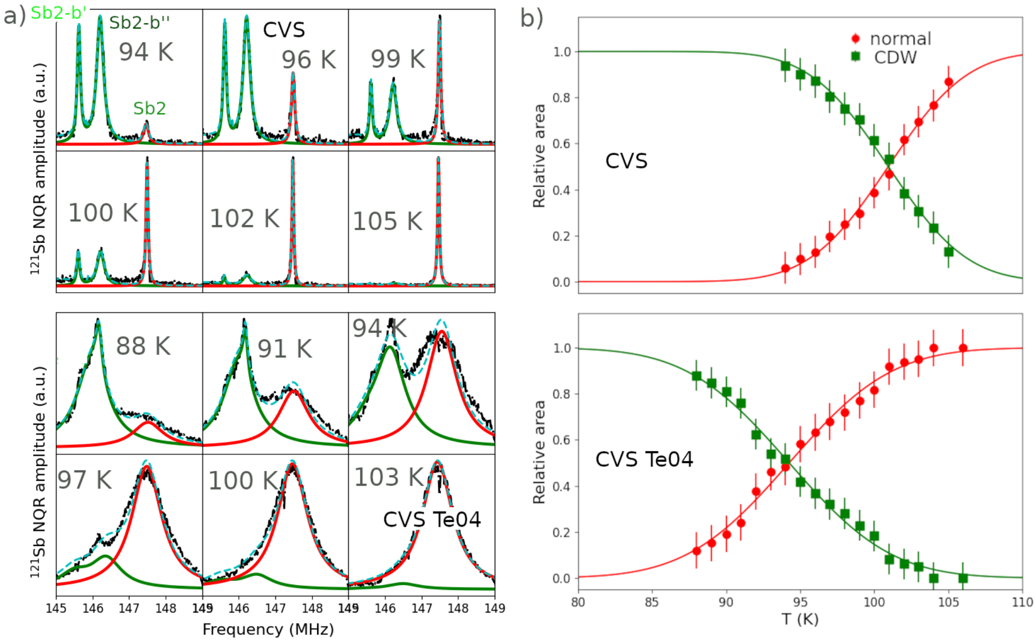

Figure 4.14: a) ^{121}Sb NQR spectra for the undoped CVS (top) and doped CVS-Te04 (bottom) samples. The green curve is the fitting to the CDW peaks, while the red curve is the fit to the normal phase. The cyan dotted curve is the global fit to the experimental data. b) Relative areas of the CDW and normal phases for undoped CsV$_3$Sb$_5$ (top) and CVS-Te04 (bottom) as obtained by using Equation (4.4), with their best $erf(x)$ fit (see text below).

impurities, or little chemical inhomogeneities. By assuming a Gaussian distribution of T'_{CDW} transitions, the data can be fitted to an error function-like behavior $erf(T - T_{CDW}/\sigma)$, being centered at $T_{CDW} =< T'_{CDW} >$ and σ the distribution width. The fit gives us a value of:

$$T^{\text{CVS}}_{\text{CDW}} \simeq (100.9 \pm 1.8)\ K \qquad \sigma^{\text{CVS}}_{\text{CDW}} \simeq (4.2 \pm 0.2)\ K$$

(the typical value for a CVS single crystal is 94 K [6]). The same analysis for the CVS-Te04 sample is shown in the bottom panels of Figure 4.14(a) and (b). We observe a big increase in the width of all the peaks in both the normal and CDW phases. We can attribute this phenomenon to the doping itself, since in general, the line width reflects some kind of distribution of EFG due to structural disorder or some dopant inhomogeneity, typical of partially doped powder samples. The results of the relative areas are plotted in the bottom panel of Figure 4.14(b), and the temperature point at which the CDW and normal phase have equal weight gives us the value of the mean transition temperature for the doped CVS-Te04:

$$T_{\text{CDW}}^{\text{CVS-Te04}} \simeq (93.6 \pm 1.8)\ K \qquad \sigma_{\text{CDW}}^{\text{CVS-Te04}} \simeq (5.5 \pm 0.2)\ K$$

The values of both T_{CDW} and σ_{CDW} for the undoped and Te-doped CVS are summarized in Table 4.8. In the end, we can compare our NQR results with the one obtained for the magnetization in Ref. [102]. The comparison is shown in Figure 4.15. We can see that our values and the magnetization

	T_{CDW} (K)	σ_{CDW} (K)
CVS	100.9 ± 1.8	4.2 ± 0.2
CVS-Te04	93.6 ± 1.8	5.5 ± 0.2

Table 4.8: Values of T_{CDW} and σ_{CDW} for both CVS and CVS-Te04, extracted from the fit to the relative areas (see text above).

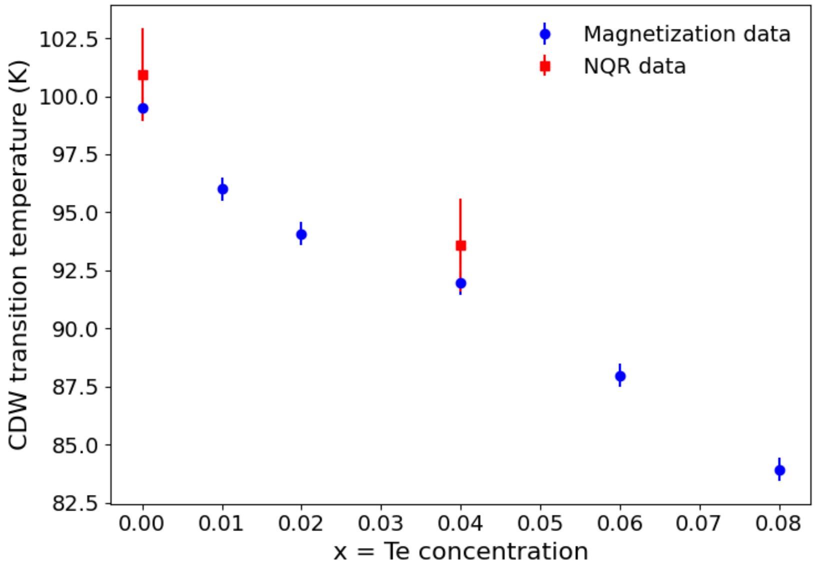

Figure 4.15: Comparison between NQR and magnetization results on the transition temperatures for undoped CsV_3Sb_5 and CVS-Te04. NQR points are labeled in red, while magnetization points are in blue.

ones are in agreement within the error.

4.7 Summary

Regarding the determination of the CDW structure for RbV_3Sb_5 and KV_3Sb_5, we measured a wide range of NMR spectra, including zero-field ^{121}Sb NQR, and ^{51}V/^{87}Rb NMR measurements in both RbV_3Sb_5 and KV_3Sb_5 kagome superconductors. For RbV_3Sb_5, the examination of the NMR/NQR spectra from all three nuclear species, supported by DFT calculations, resulted in a clear identification for the first time [77] of the structure stabilized below the CDW transition, as seen in Section 4.3 in Figure 4.2. The low-temperature structure is a $2 \times 2 \times 2$ superlattice created by alternating Inverse Star-of-David (ISD) layers, π-shifted from one to the other, according to an evaluation of the multiplicity of the nonequivalent sites for each species, as shown in Figure 4.1 In KV_3Sb_5, from the analysis of the NQR peaks' frequencies and the comparison with RbV_3Sb_5 results obtained, we conclude that the CDW structure adopted by kagome superconductor KV_3Sb_5 is the Inverse Star-of-David (ISD) with π-shift, the same as for RbV_3Sb_5, as it can be seen in Figure 4.4.

For the T-dependent analysis RbV_3Sb_5 in Section 4.4, we can summarize the main results in the following points:

- ^{51}V FWHM for V2 site show signs of anomalous deviations at $T_x \simeq$ 50 K (see Figure 4.5(a)), which are probably due to a change in the local dipolar field attributable to nematic order or orbital currents (i.e., Rotational Symmetry Breaking), and/or to a change in the dipolar field distribution as a consequence of a secondary charge rearrangement;
- ^{87}Rb NMR measurements are very sensitive to the CDW transition and helped identify its specific configuration in Section 4.3. However, the limited measured temperature range, in this case, does not allow us to conclude anything about the possible change of state at $T_x = 50$ K;
- on the other side, ^{121}Sb NQR measurements do show a possible increase

in the linewidth at T_x (see Figure 4.9(b)).

Overall, the above-presented NMR/NQR measurements give an experimental fingerprint of the presence of a peculiar phase transition that seems to occur at 50 K for RbV_3Sb_5, analogous to that already reported from NMR in CsV_3Sb_5 at $T \simeq 35$ K [44]. Further analysis and measurements would be needed to better understand the nature of the physical phenomena that lie behind this scenario. To this aim, we have recently started a complementary μSR study of the low-T state, whose preliminary results will be presented in the next chapter.

We also performed a study of room temperature and zero-field ^{121}Sb NQR measurements of Sn and Te-doped CsV_3Sb_5, for two different concentrations of undoped and of Sn- and Te-doped CVS ($CsV_3Sb_{5-x}M_x$ (M = Sn, Te), namely for x[Sn] = 0.05 and x[Te] = 0.04). Our results show that both dopants occupy the Sb1 sites in the kagome plane, based on the analysis of the shift of the NQR peaks in Figure 4.12 and Figure 4.13. Electron-doping via Te-substitution in CsV_3Sb_5 largely preserves the CDW state, whereas hole-doping with Sn-dopant seems to rapidly suppress long-range CDW order [101, 102]. These findings helped the characterization of hole- and electron-doped kagome superconductor CsV_3Sb_5, and provided a way to analyze the role of Sn doping in tuning the Fermi level and, hence, CDW and superconducting interplay, as discussed in Ref. [101].

Finally, our ^{121}Sb NQR measurements as a function of temperature on undoped CVS and CVS-Te04 powder samples showed that across the transition, the normal and CDW states coexist in a T range of about ~ 10 K around an average T_{CDW} which is doping dependent (Table 4.8). The mean value of T_{CDW} transition is in agreement with magnetization M(T) data (Figure 4.15). ^{121}Sb NQR is a very powerful tool to characterize the CDW phase transition (and less powerful for the transition at T_x) at the microscopic level with high accuracy for these Kagome compounds.

Chapter 5

μSR study: CDW in charge-doped CVS

This chapter will be devoted to the presentation of the main results in Kagome superconductors AV_3Sb_5 using Zero-Field (ZF) μSR. In particular, we are going to present the results obtained for Sn- and Te-doped CsV_3Sb_5 samples at a wide range of temperatures, mainly with the aim of studying the effect of doping on the low-T at T_x, determined by an anomalous increase in the depolarization rate in all the undoped materials [97, 98, 107]. The effect of doping studied by μSR is poorly studied in the literature, and this section reports the preliminary results of our work, which creates the phenomenological basis for a more detailed ongoing and future investigation. The samples studied are summarized in Table 5.1.

Table 5.1: List of kagome metals of the AV_3Sb_5 family characterised by means of μSR, along with their composition and form.

Composition	**Doping**	**Label**	**Form**
$CsV_3Sb_{5-x}Sn_x$	x = 0.08	CVS-Sn08	Powder
	x = 0.35	CVS-Sn35	Powder
$CsV_3Sb_{5-x}Te_x$	x = 0.08	CVS-Te08	Powder

5.1 Introduction

So far it is clear that (at least) three transition temperatures characterize the temperature behavior of the AV_3Sb_5 kagome metals: T_{CDW}, T_x, T_c. Considering T_{CDW} and T_x, in Chapter 4 we saw that NMR/NQR is very sensitive to detecting T_{CDW}, and less sensitive to detecting T_x, while we will see in this chapter that μSR acts conversely. Hence for our scopes, μSR and NMR are complementary. Here we present some Zero Fieled (ZF) μSR measurements as a function of temperature for some selected Sn and Te dopings on CsV_3Sb_5 samples. This is a preliminary investigation of the potentiality of μSR in investigating the doped kagome materials and checking the effects of doping on T_x and to some extent on T_{CDW}. The samples under investigation are summarised in Table 5.1, with their labels.

As presented in preceding sections, hole- and electron-doped CsV_3Sb_5 kagome superconductors offer an invaluable experimental platform for investigating the interplay between the CDW and Superconducting (SC) states, which can be effectively manipulated by fine-tuning the Fermi level through chemical doping. Specifically, for hole-doping, achieved through Sn substitution into Sb, for hole doping the CDW seems to vanish for x > 0.05-0.08, from magnetization measurements, while a second superconducting dome appears (Figure 4.11). Conversely, for electron-doped CsV_3Sb_5, the CDW transition persists at least up to the solution limit of Te (x ∼ 0.1).

In addition to the examination of the CDW transition, it is worth following the doping dependence of the ”nematic” or ”Time-Reversal Symmetry Breaking” (TRSB) phase transition, observed to be approximately $T_x \sim 40$ K for the specific case of pure CsV_3Sb_5, as reported in references [44] and [97].

5.2 Methods

To accomplish this, we performed a comprehensive set of ZF-μSR measurements in Sn and Te-doped $CsV_3Sb_{5-x}M_x$ (M = Sn, x = 0.08, 0.35; M = Te, x = 0.08) samples in a wide range of temperatures (5–300 K). These samples will be referred to as doped CVS-Sn08, Sn35, and Te08, respectively, throughout this chapter. We chose Te08 because is the maximum Te-doping possible, Sn08 for comparison of hole/electron dopant concentration with Te08, and Sn35 to check the behavior for different doping content and for the sample with max T_c (second SC dome in Figure 4.11).

The measurements for Te08 have been performed with the GPS spectrometer at the Paul Scherrer Institut, Villigen, Switzerland, while the measurements for Sn08 and Sn35 have been conducted with the EMU spectrometer at the ISIS Pulsed Neutron and Muon Source, Rutherford Appleton Laboratory, Harwell-Oxford, UK. For the EMU experiment at ISIS, the CVS-Sn08 and Sn35 powders with a mass of approximately 1.5 g have been put on a circular section of $\phi = 30$ mm inscribed in an Ag square sample holder. For the GPS experiment at PSI, the CVS-Te08 powder with a mass of approximately 0.35 g was put inside aluminium foil to form a rectangular package of sides approximately 10x10 mm^2, and then stitched with Kapton tape on a Cu fork to be inserted onto the probe.

Due to the pulsed source of muons, the EMU data at ISIS can cover a higher window in time (up to 20 μs) with a higher counting rate and are suitable for non-magnetic samples (as the AV$_3$Sb$_5$ family); on the opposite, the high beam size provides a large background of the order of 30%, thus reducing the total asymmetry. The continuous source of muons at PSI does not allow the measurements to go beyond 9-10 μs of time windows, hence hiding important information about the muon polarization's tail in samples with a low relaxation rate such as the ones under investigation. The advantage is that, by having a smaller beam size, the background is minimal.

After calibrating both samples in a Transverse-Field of 20 G, to determine the α coefficient of Equation (2.48), a temperature scan of Zero-Field measurements has been performed to measure the relaxation rates and the asymmetry values of the muon polarization. The data collected at ISIS have been analyzed using *WiMDA* software [108], while the data for PSI using the *mu-*

lab package for Matlab, made available by Prof. Roberto de Renzi and Prof. Giuseppe Allodi at the University of Parma, Italy.

5.3 Results and discussion

As an example, the experimental ZF-μSR polarization $P_z(\mathrm{t})$ at T = 90 K for both CVS-Sn08 and Te08 is shown in Figure 5.1. The muon polarization $P_z(\mathrm{t})$ is defined as:

$$P_z(\mathrm{t}) = \frac{A(\mathrm{t})}{A(\mathrm{t{=}0})}$$

where $A(\mathrm{t})$ is the muon asymmetry. The same behaviour of muon polarization is followed by CVS-Sn35. As pointed out in Section 5.2, it is clearly visible in Figure 5.1 the difference in time-window between the data collected at ISIS (left) and PSI (right). The time dependence of the muon polarization resembles the behavior described by a Kubo Toyabe function (see Equation (3.3)), which is typically expected for the dipolar distribution of nuclear

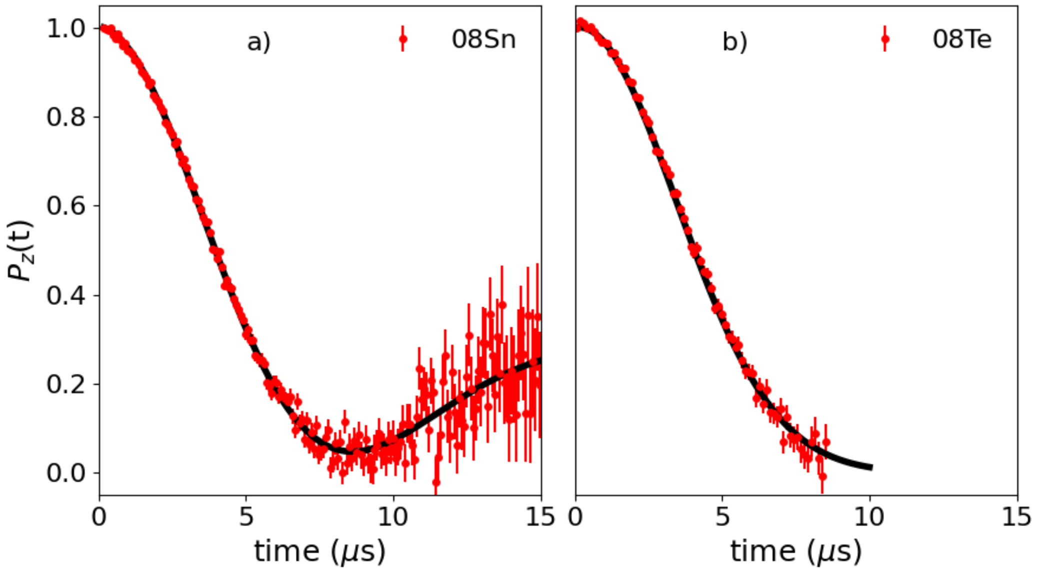

Figure 5.1: Representative μSR polarization $P_z(\mathrm{t})$ plots at T = 90 K for a) CVS-Sn08 and b) CVS-Te08. The black curves indicate the fit, as described later in the text.

magnetic moments. Actually the best fit in the whole T range requires an additional exponential factor with a lambda decay. This term is introduced phenomenologically by following refs. [97, 98, 107], and it accounts for possible contributions of electronic origin. Thus, the fitting function used to analyze the μSR spectra is:

$$P(t) = \left[\frac{1}{3} + \frac{2}{3} e^{-\sigma^2 t^2/2} \left(1 - \sigma^2 t^2\right)\right] e^{-\lambda t} \tag{5.1}$$

where σ and λ are the relaxation rates of the nuclear static part and possibly the electronic dynamic part, respectively.

From the literature [97, 98], it has already been shown that in undoped samples, a moderate change in relaxation occurs at the CDW transition. Therefore, by looking at the relaxation rates, we can possibly answer the question about the presence or not of the CDW transition for doped CVS-Sn08 and Te08 samples, as well as to uncover possible anomalies at T_x, which for the undoped CsV_3Sb_5 is found to be at around 35 K [97, 107]. Let us now discuss briefly why the presence of a possible TRSB transition also affects the relaxation rates and the asymmetry of the muon precession. As already discussed in Chapter 4, a TRSB transition can arise due to multiple physical phenomena; among all of them, the presence of orbital currents in the kagome plane [97, 98] represents a remarkable example of how to break the time-reversal symmetry by inducing currents along the V-V bonds and, hence, producing a tiny magnetic field, which contributes to the distribution of the magnetic dipolar field around the muon and enhances the relaxation rates. On the contrary, a similar effect can also be due to the occurrence of a structural transition that modifies the muon-nuclei distance; hence, again, the dipolar field distribution around the muon is reflected in the KT decay. This latter hypothesis represents what happens in the CDW transition, where the modulation of the electron density is related to a structural deformation and the formation of a superlattice. Finally, a nematic transition, in which the electronic degrees of freedom drive a reduction of rotational symmetry (for example, from C_4 to C_2) [44, 109], could also explain the increase in the relaxation rates for both pure and hole-/electron-doped AV_3Sb_5 materials, since the reduction in the symmetry affects the lattice structure by modifying the distance between muon and nuclei, as explained before. Other contributions might be of pure dynamical origin, which is reflected in the T_1 and T_2-like processes, hence affecting the muon relaxation rate.

5.3.1 CVS-Sn08 vs. CVS-Te08

The analysis of the μSR ZF-spectra for the doped CVS-Sn08 and CVS-Te08 samples are shown in Figure 5.2, in the range of temperature $0 < T < 115$ K. Figure 5.2 displays the relaxation rates σ and λ of the muon polarization function in Equation (5.1).

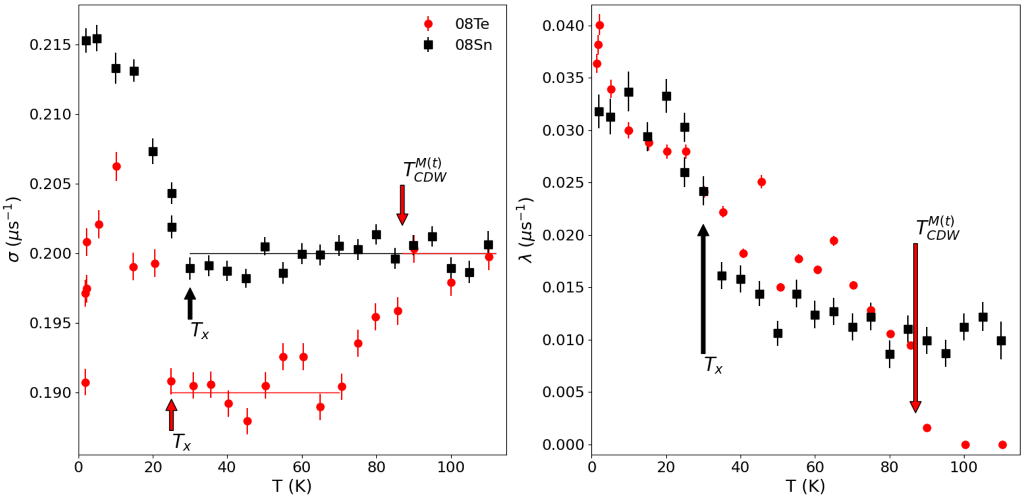

Figure 5.2: μSR relaxation rates (left) σ and (right) λ for the CVS-Te08/Sn08 sample (in red and black, respectively). The up arrows represent the T_x temperatures, while the down arrow is the T_{CDW} for CVS-Te08 from magnetization data $M(t)$ (Figure 4.15). The solid lines are guides for the eyes.

CVS-Sn08 discussion

For the CVS-Sn08 sample, an increase in both the nuclear and electronic relaxation rates is visible at about 30 K. This particular temperature resembles the one found in Ref. [44] for the NMR experiment on CsV_3Sb_5, and could represent the rise of the nematic phase under debate. These signs possibly confirm the occurrence of a phase transition, but in order to determine its exact nature, further studies must be conducted (actually, they're currently under investigation by our group). The data of σ and λ are both totally flat for $T > 30$ K, up to 115 K. This might indicate that the CDW transition does not occur in this sample in agreement with magnetization measurements (Figure 4.11 and Ref. [101]). However, the detection of CDW through magnetization data appears as a peak on the first derivative with respect to temperature, which is smeared out progressively as a function of doping, and local probes are needed to carefully check local symmetry breaking. In addition, μSR is not very sensitive to the pure CDW transition, since the muon decay rate generally gives a small bump around it. Furthermore, this transition might occur below T_x and elude the detection. So we cannot conclude about the absence or presence of the CDW transition here. Further investigation by Sb NQR is planned soon to detect its possible presence, by following the examples in Section 4.4.

CVS-Te08 discussion

Considering the relaxation rates, both σ and λ display change in their behaviours when going down $T = 85$ K; σ slightly decreases, while λ shows a steep increase in its value. These results indicate that the CDW transition is still present in the doped CVS-Te08, in agreement with magnetization data [101, 102].

By looking at Te-doped results, the nuclear relaxation rate σ shows an increase in its value below 25 K, while the scattering in the λ points cannot reveal a similar phenomenon. In summary, there are signs that indicate the presence of a nematic/TRSB transition in the doped CVS-Te08 sample.

5.3.2 CVS-Sn08 vs. CVS-Sn35

Figure 5.3 displays the relaxation rates σ and λ of the muon polarization function in Equation (5.1) for the Sn08 and Sn35 samples. We can clearly

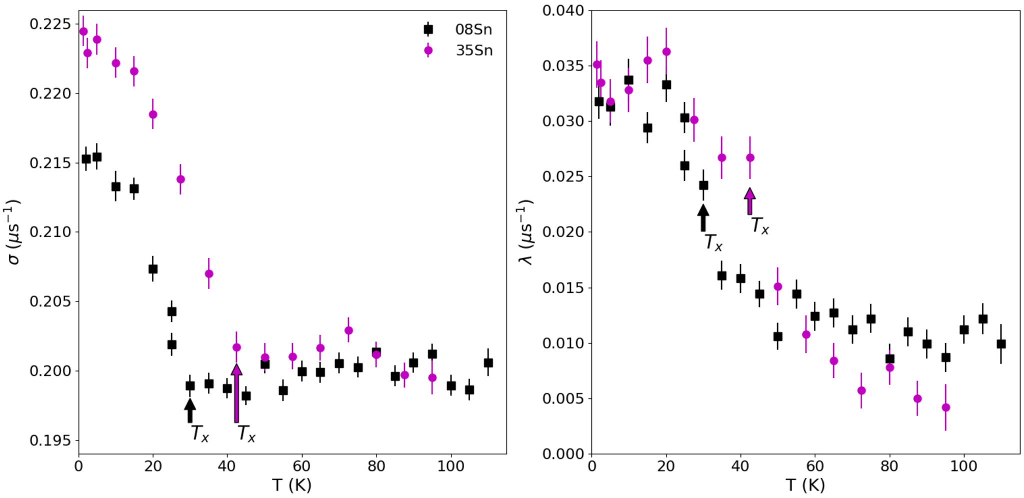

Figure 5.3: μSR relaxation rates (left) σ and (right) λ for the CVS-Sn08 and Sn35 sample (in black and magenta, respectively). The up arrows represent the T_x temperatures.

see from the σ results in Figure 5.3(left) that the CVS-Sn35 sample shows a bigger increase in the relaxation rate, and at a higher temperature ($T_x = 42$ vs. 30 K) with respect to the Sn08 one. Above 42 K, the relaxation rate σ is almost equal for both doped samples. On the other side, the λ results also show appreciable differences between CVS-Sn08 and CVS-Sn35 in the temperature at which the value goes from flat to increasing. To conclude, when going from one of the two superconducting domes to the other, the muon relaxation rate is higher, and the T_x increases by about 10 K. The reason why this happened is still unclear and deserves further investigation.

5.4 Summary

In conclusion, we performed ZF-μSR measurements on doped CVS-Sn08/Sn35 and CVS-Te08, to conduct a preliminary investigation of the effect of both the doping content and type (hole/electron) on the occurrence of the CDW phase and in the anomalous low-temperature behaviour, where a possible reduction of the rotational symmetry seems to occur. A proper, more rigorous analysis of the muon polarization spectra would require a more detailed study of the contributions of the dipolar field and electric field gradient terms for different possible charge arrangements around nuclei, by following the procedure developed by us and applied to other materials presented in Chapter 6. This study, which includes support from DFT calculations, is underway and is beyond the scope of this thesis. Despite that, the use of the phenomenological $KT \times exp$ function captures the main features occurring as a function of temperature, revealed by the σ(T) and λ(T) behavior. Doping concentrations higher than x = 0.05 at the Sb substitutional site for the hole counterpart (Sn in our case) seem to suppress the CDW transition, while for the electron counterpart (Te doping) it is still present even with x = 0.08.

Regarding the presence of the nematic/TRSB transition, for which muons look to be more sensitive, both the hole- and electron-doped CsV_3Sb_5 show an upturn of the relaxation rates in the low T region (< 50 K). This gives evidence that this anomalous phase is ubiquitous and possibly survives when the CDW is suppressed (to be checked and confirmed by NMR/NQR measurements when the CDW is fully suppressed). Furthermore, we observe some difference of T_x and the relaxation rates as a function of the doping content (Sn08 vs Sn35) indicating that the phenomenon is sensitive to the position of the Fermi level. Further measurements and calculations are currently going on to explore the connection between this transition, the CDW, and their intertwining with the superconducting state. The obtained results possess a purely phenomenological and preliminary nature, albeit they serve as the foundational groundwork for a more meticulous investigation that has recently started. This investigation is being supported by simulations of muon polarization relaxation, by assuming different theoretical configurations consistent with various predictions of spontaneous temporal symmetry breaking, to be compared against experimental data.

The superconducting state of these samples is currently under study in order to determine the exact nature of the superconducting state by using TF-μSR and how it intertwines with both the CDW and the possible anomalous phase that occurs below T_x.

Chapter 6

μSR as local charge-probe technique

In this chapter, I will report the result obtained in the article [110], regarding the use of muons as local charge probes for quantum entanglement with quadrupolar nuclei (I = 7/2). This work started during my Master's Thesis and ended during my second year of Ph.D., and includes μSR experiments, DFT calculations, and X-ray diffraction (XRD) characterizations and refinements.

6.1 Introduction

Quantum coherence between an implanted positively charged muon and nuclei in a solid was first conclusively demonstrated using muon-spin spectroscopy (μSR) experiments on simple ionic fluorides [111]. The strong hydrogen-like bonding of the implanted positive muon (chemically identified as μ^+) to nearest-neighbor F ions, characterized by a single spin 1/2 ^{19}F nuclear isotope, gives rise to a hierarchical separation of the muon spin interactions. Typically, dipolar couplings with two nearest-neighbor (nn) ^{19}F nuclear spins, $\boldsymbol{I}_1$, and $\boldsymbol{I}_2$, determine the dominant spin-Hamiltonian of the $S = 1/2$ muon, whereas all the residual interactions, starting from the next nearest neighbours (nnn), can be ignored to a first approximation. Thanks to the 100% initial muon spin polarization, a prerogative of μSR, this shows up experimentally as a characteristic coherent spin precession pattern in the muon time-dependent asymmetry, uniquely determined by the geometry of the F–μ–F bonds. Many fluorinated compounds display this coherent pattern in non-magnetic phases, including ionic fluorides [112–115], fluoropolymers [116, 117] and molecular magnets [118]. For these materials, the absence or the fast fluctuation of electronic magnetic moments leaves the nuclear spin interactions to determine the dynamics of the muon spin polarization. This allows a very precise assignment of the muon implantation site, now known to be particularly accurate with the help of density functional theory (DFT) *ab-initio* simulations of the muon stopping-site inside the crystal (a technique which is also known as DFT+μ [119–123]). A similar coherent spin behavior has been identified in certain hydrides [124–126] and in metal–organic frameworks [127], where for instance a close association of a proton and the positive muon approximates a muoniated hydrogen molecule, μH, or possibly, a bonded molecular ion, $(\mu\mathrm{H})^+$, $(\mu\mathrm{H})^-$. Notice that ^{1}H, like ^{19}F, is a spin $I = 1/2$ nucleus hence with zero electric quadrupole moment.

In the case of ^{1}H, as for the cases of many other nuclear species, such a coherent pattern is rarely observed in μSR experiments. Much more often a large number of unpolarized nuclear spins give rise to a T_2^{-1} relaxation process with either Gaussian or Lorentzian lineshapes, both the hallmarks of fast decoherence on the timescale of the period of coherent quantum interference processes. Fluorine is special since it is very electronegative, and it has both a small ionic radius and a large nuclear moment, so that its dipolar coupling to the muon is strong and consequently several oscillations in any quantum-coherent signal can be observed before all muons have decayed or any nuclear relaxation process has become significant. The special F–μ–F case was very recently revisited by some of us [128], showing the role of the rest of the nuclear spins (nnn and beyond) in the slow decoherence process of F-μ-F. This work implies that the very well-known F-μ-F effect, confined until now among the technicalities of the muon spectroscopy, displays all the features of a very high accuracy *quantum sensor* that can be exploited for microscopic detection of important physical phenomena [129] and can be finely controlled by electromagnetic excitation [115]. Unfortunately, until now, the sensor has been available only for F^-- and, much more rarely, for H^--containing materials, insensitive to quadrupolar interaction.

In the present work, we demonstrate the same surprising type of quantum coherence due to the entanglement of the muon spin with nn quadrupolar nuclear spin ($I > 1/2$) and we establish that this quantum coherence can provide a muon spectroscopy-based quantum sensor of local charge-related phenomena. We show this phenomenon in three intermetallic compounds, Nb_3Sn, V_3Si and V_3Sn, which belong to the A15 cubic phases ($Pm\overline{3}n$, group number 223), whose members include several technologically dominant conventional superconductors [130]. In stark contrast to the well-studied $I = 1/2$ case of ^{19}F and ^{1}H, the presence of nn nuclei with $I > 1/2$, namely $I = 7/2$, $9/2$ of ^{51}V and ^{93}Nb respectively, implies the existence of quadrupolar interactions. This has two effects that could potentially spoil the *quantum sensor* concept: first, it was until now unclear that detectable quantum coherence could nevertheless show up in the muon asymmetry; second, quadrupolar interactions are proportional to the electric field gradient (EFG) at the nucleus in question, not just on the pure geometry of the bonds. EFG tensors are very accurately determined by DFT in bulk materials [131] and compared to the values measured for instance by nuclear magnetic resonance (NMR) [132]. The muon embedding in the crystal alters the bulk EFG in more than one way. We show that the coherent effect survives and we develop here an accurate model to describe this phenomenon. Our modeling of the coherence entails identifying precisely the muon site and calculating muon perturbed EFG tensors at nn and nnn nuclei. The results show that the observed phenomenon is highly sensitive to small structural and electronic differences among the same A15 family, paving the way to extend the use of muon spectroscopy as a quantum sensing technique for charge-related phenomena.

6.2 Methods

6.2.1 X-rays diffraction characterization

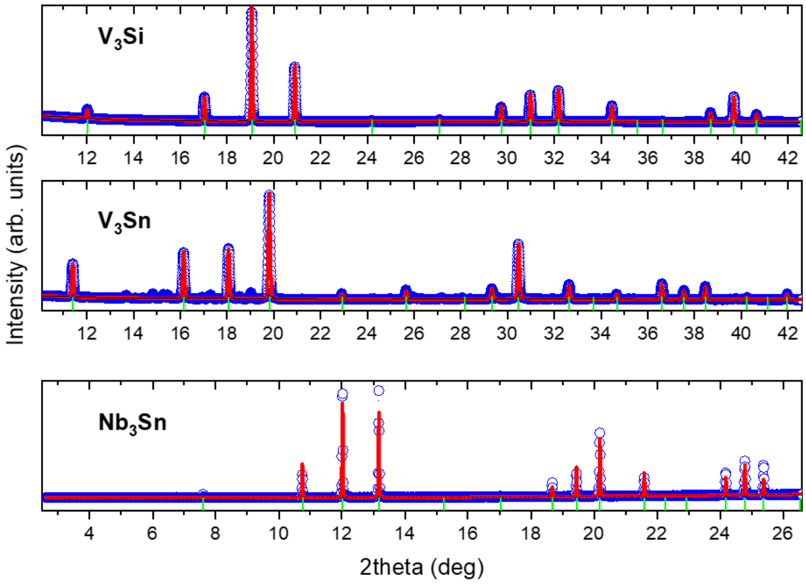

Figure 6.1: X-ray diffraction patterns for V_3Si, V_3Sn, and Nb_3Sn, at T = 300 K. The blue points are the experimental data, the red lines the Rietveld refinement fits and the green ticks represent the Bragg reflections of the A15 cubic structure with the Pm$\overline{3}$n, group number 223.

Synchrotron x-ray powder diffraction measurements have been performed at the ELETTRA synchrotron Facility in Trieste (Italy). V_3Si and V_3Sn samples were measured at the XRD1 beamline using wavelength 0.7 Å whereas Nb_3Sn was measured at the Xpress beamline using wavelength 0.4957 Å.

Rietveld refinements were made by using GSAS-II software and aimed mainly to check phase purity and to determine the lattice parameters, necessary as input parameters for the simulation of the muon polarization (see below). Representative diffraction patterns measured at room temperature are displayed in Figure 6.1 with their Rietveld fit curves. All the samples have an A15 cubic structure with the Pm$\overline{3}$n, group number 223, symmetry and display lattice parameters $a = 4.7226(2)$ Å, 4.98186(2)Å, 5.28868(2) Åfor V_3Si,

V_3Sn and Nb_3Sn respectively, in agreement with previous results [133–136]. Unlike V_3Si and Nb_3Sn, in the case of V_3Sn we observed several minor impurity phases which were identified to be due to different oxide phases of V and Sn (about 3-5 %) and an additional 5 % contribution of the hexagonal V_3Sn phase. Since these phases are segregated and the μSR measurements give a bulk response, proportional to the relative volume phase, the results of this work are not affected by a small fraction of spurious phases.

6.2.2 μSR experiments

Our experiments were performed using the EMU spectrometer at the pulsed beam ISIS Facility, Rutherford Appleton Laboratory, UK, and GPS spectrometer at the continuous beam Swiss Muon Source SμS, Paul Scherrer Institute, Villigen, Switzerland. The first allows for the collection of high statistics, thanks to the high data rate acquisition of time-differential data at pulsed sources, but is typically affected by a large background due to muons implanting in the sample holder or in the wall of the cryostat. On the other hand, the second allows for nearly eliminating the background signal thanks to the smaller beam size and the use of the VETO option. In our case, the combination of the two is essential in order to collect data acquisition much higher than the muon lifetime ($\tau = 2.2$ microseconds, as described in Chapter 3), to resolve possible long-time features of the μSR signal, and to properly subtract the background for a more accurate comparison with the DFT simulations. All the powder samples were measured with the GPS spectrometer, while V_3Sn and V_3Si were also measured with the EMU instrument, with high statistics for some selected temperatures. The powders were wrapped in a sheet of 25 μm silver foil and were placed in the cryostat, collected, and measured in the range 20-300 K and in zero external magnetic field conditions. The Earth's magnetic field was compensated to better than 50 μT using active field compensation.

In the muon experiment, a beam of spin-polarized muons was implanted into a sample, and the number of positrons emitted in both the forward and backward detectors, $N_F(t)$ and $N_B(t)$ respectively, were measured. The muon spin polarization was calculated as $P(t) = A(t)/A_0$ being $A(t)$ the time-dependent muon decay asymmetry and A_0 its initial value $A(0)$. The muon asymmetry, as derived in Chapter 3, is determined as $A(t) = (N_B(t) - \alpha N_F(t))/(N_B(t)+\alpha N_F(t))$ where the parameter α takes into account systematic differences between the readings of both sets of detectors. Both α and A_0 were properly calibrated at high temperatures by applying a small transverse field (of a few mT). The background component of ISIS measurements has been estimated by comparing them with the acquisitions performed at PSI at the lowest temperature. The data are linearly interpolated at the same time intervals. Finally, the constant shift providing the best overlap among the two curves is estimated and subtracted from the ISIS measurements.

6.2.3 Computational results

Density Functional simulations have been performed using a plane wave (PW) basis with the Quantum ESPRESSO code, and with Augmented Plane Waves using the Full Potential (FP) code Elk [137, 138]. In all simulations, we used the PBE exchange and correlation functional [139]. In PW-based simulations, the maximum k-point distance was 0.2 Å^{-1}, obtained using a Γ centered $4 \times 4 \times 4$ grid for the $2 \times 2 \times 2$ supercells and with a Γ centered $2 \times 2 \times 2$ grid for the $3 \times 3 \times 3$ supercells. A Marzari-Vanderbilt smearing with 5 mRy width was used. We chose ultrasoft pseudopotentials [140] for lattice structure relaxation, and PAW potentials [141] for estimating electric field gradients (EFG) at the various nuclear sites. A cutoff of 60 (600) Ry was used for wavefunction (charge) cutoffs. The experimental lattice parameters of the cubic structure were always enforced. FP simulations were performed in a high-quality setting for the description of the basis (refer to Elk's manual for further details), but carefully defining muffin tin radii to allow the simulation of the interstitial H atom. The maximum k-point distance in the grid was smaller than 0.4 Å^{-1} in this case (with Γ centered $8 \times 8 \times 8$ grids for the unit cells, and Γ centered $2 \times 2 \times 2$ for the supercells).

6.3 Results and discussion

6.3.1 Experimental A15 μSR spectra and DFT calculations

Zero-field (ZF) μSR temperature scans, using the EMU spectrometer at the ISIS Muon Source and the GPS spectrometer [142] at the Paul Scherrer Institute, have been conducted as a function of temperature. Figure 6.2 shows the μSR spectra (time-dependent spin polarization of the muon ensemble) for all the samples at various representative temperatures. The temperature dependence is relatively weak, except above 200 K, where thermally activated μ^+ diffusion occurs in V_3Si [143]. A similar trend is envisaged for Nb_3Sn, but with slightly higher activation energy, while a small increase in the tail is observed in V_3Sn at and above 150 K. At low temperatures, where the muon is static in the μSR time window, the results are remarkably sample dependent despite all the X_3Y samples ($X = \{V, Nb\}$ and $Y = \{Si, Sn\}$)

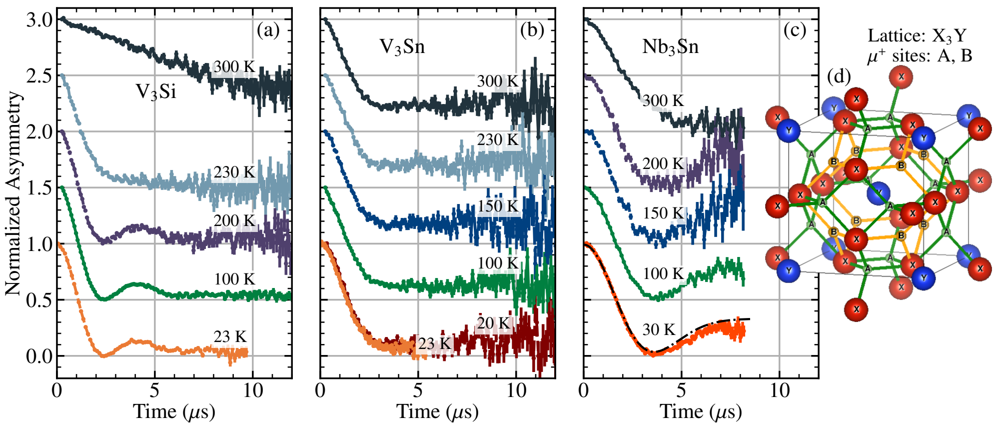

Figure 6.2: Experimental results obtained for V_3Si(a), V_3Sn(b) and Nb_3Sn(c) at various temperatures in ZF. The initial asymmetry has been normalized to 1 and the various measurements are shifted along the y axis by multiples of 0.5. The black line in (c) is the best fit for a static Kubo-Toyabe function. In picture (d) the lattice structure of A15 compounds and the candidate muon sites identified in this class of materials are depicted.

being very similar metals, sharing the same A15 cubic lattice structure. The structure is shown in Figure 6.2d and our samples have a cubic lattice parameter $a = 4.72$ Å, 4.98 Å, 5.29 Å for V_3Si, V_3Sn and Nb_3Sn respectively, in agreement with previous results [133–135]. The nuclei of the X atoms are closer to the calculated muon sites, as shown in Figure 6.2d with labels A and B, and all have similar properties: ^{51}V with 99.8% abundance has spin $I = 7/2$, gyromagnetic ratio $\gamma_V = 70.45 \times 10^6$ rad/(sT) and quadrupole moment Q =-0.052(10) barn and ^{93}Nb with 100% abundance has spin $I = 9/2$, $\gamma_{Nb} = 65.64 \times 10^6$ rad/(sT) and Q =-0.32(2) barn. The oscillatory behavior observed in V_3Si (Figure 6.2a) is in marked contrast to the cases of both Nb_3Sn (Figure 6.2c), which resembles the conventional Kubo-Toyabe (KT) relaxation function (empirical KT best fit shown by the dashed line in the same panel and characterized by a dip and a tail that flattens at $1/3$ of the initial value), and of V_3Sn (Figure 6.2b), which could be described by a KT relaxation, with an additional decay of the $1/3$ tail which has no evident physical origin. The surprisingly slow oscillations observed in V_3Si (Figure 6.2a) cannot be due to internal fields of electronic origin since all these A15 samples are non-magnetic. Instead, as we will show, they result from a quantum coherent precession pattern due to the coupling between the muon and nearby ^{51}V nuclear moments, analogous to the F–μ–F case, and never reported before for systems containing $I > 1/2$ nuclear spins.

In order to explain the three precession patterns of Figure 6.2 we now consider the microscopic nuclear and electronic degrees of freedom entering the quantum mechanical model of the muon polarization. The model requires the knowledge of three ingredients to reproduce the experimental muon polarization: (i) the muon site, (ii) the perturbation induced by the μ^+ on the position of the neighboring atoms, (iii) the perturbation induced by the muon on the EFG at the nuclear sites with spin $I > 1/2$. This information allows us to fully define the spin Hamiltonian $\mathcal{H}$ given by:

$$\mathcal{H} = \sum_i^{N_{nuc}} \frac{\mu_0}{4\pi} \frac{\gamma_\mu \gamma_i \hbar^2}{r_i^3} \mathbf{S}_\mu \cdot \mathbf{D}^i \cdot \mathbf{I}^i + \frac{eQ_i}{2I(2I-1)} \mathbf{I}^i \cdot \mathbf{V}^i \cdot \mathbf{I}^i, \tag{6.1}$$

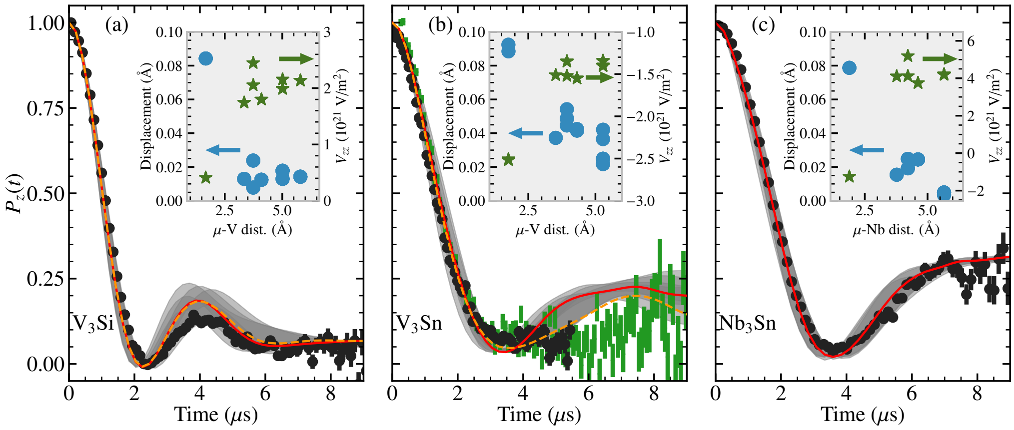

Figure 6.3: Comparison between experimental and predicted muon spin polarization obtained using atomic displacements and EFGs from plane wave-based DFT calculations. The black dots in panels a), b), and c) are the lowest temperature data collected at PSI for V$_3$Si, V$_3$Sn, and Nb$_3$Sn respectively (orange and red points of Figure 6.2). The green bars in panel (b) are ISIS results collected at 20 K. A background has been estimated by comparing the asymmetries collected at ISIS and PSI and removed. The red (orange) line in all plots is the depolarization obtained using first principles results from PW (FP) simulations to solve Equation (6.1). Shaded areas highlight different trends that originate by taking into account typical uncertainties of the DFT-based predictions (see main text). The insets show the perturbation induced by the muon on its X-type neighbours (X =V,Nb). In particular, in the presence of the muon, the displacement of each X atom from its equilibrium position in the unperturbed lattice and the values of V_{zz} at the considered atomic site are reported on the left-hand and right-hand y-axes, respectively, as a function of the unperturbed distance of the considered atom from the μ^+ interstitial position in a 3x3x3 supercell.

where $\mathbf{S}_\mu$ is the spin of the muon and r_i is its distance from nucleus i, $\mathbf{I}^i$ and Q_i are respectively the spin and the quadrupole moment of nucleus i, $\mathbf{D}$ and $\mathbf{V}$ are the dipolar and EFG tensors at nuclear site i, and other symbols have their standard meaning. All the quantities entering Equation (6.1) can be accurately estimated with DFT-based *ab initio* approaches and we describe below the results that we obtained following the DFT+μ procedure.

Two candidate muon sites are present in our A15 compounds and are shown in Figure 6.2d with labels A and B. Site A corresponds to site T2 in Ref [143] and is located in the center of the tetrahedron formed by four X atoms while site B is in the center of the triangle formed by three X atoms. We find that site B always has higher energy than site A by hundreds of meV and is therefore omitted from the subsequent analysis. DFT simulations produce, as an additional outcome, the displacements of the atoms surrounding the muon. In all cases, the nn X atoms are substantially displaced by the muon and the nearest neighbor distances increase by 6%, 5%, 4% respectively in V_3Si, V_3Sn, Nb_3Sn (the absolute values are shown in the insets of Figure 6.3 against the unperturbed μ-X distance).

The next step is the evaluation of the EFG at the quadrupolar nuclei in each compound. While for ionic materials a point charge approximation may sometimes be sufficient, covalent and metallic systems require more elaborate strategies. Full potential (FP) DFT simulations yield very accurate estimates in materials where the mean-field approximation does not break down owing to strong correlation, but are extremely computationally demanding. For this reason, and aiming at providing an easily adoptable approach, we opted for an effective compromise between accuracy and speed using a plane wave basis [137, 144, 145] combined with PAW [146] pseudopotentials.. Notably, this procedure converges much faster than the equivalent technique aimed at the prediction of magnetic contact hyperfine fields at the muon sites [147].

Unsurprisingly, the EFG of the four X neighbors of the muon is drastically affected by the presence of the interstitial charge. For example, in V_3Si the unperturbed EFG tensor at V nuclei in the pristine material, with $V_{zz} = 2.2 \times 10^{21}$ V/m^2 and $\eta = 0$, in agreement with the experimental value of $V_{zz} = 2.37 \times 10^{21}$ V/m^2, reduces by almost an order of magnitude as a consequence of the presence of the positive impurity and the lattice distortion, in agreement with earlier work [143]. Note that site assignments come with some small uncertainty, and previous investigations that can be compared with experiment [120, 128, 129, 148, 149] reveal that a discrepancy of the order of a tenth of Angstrom is to be expected. On the other hand, plane wave-based estimations of EFGs are subject to a much larger uncertainty of the order of 30% and 1.17×10^{21} V/m^2 in relative and absolute terms [150].

Having collected all parameters entering Equation (6.1), we proceed to compute the time-dependent muon polarization numerically. For the A15 compounds, the inter-nuclear dipolar interactions can be safely neglected thus allowing the adoption of the approach proposed by Celio [151, 152] and implemented in the publicly available code UNDI [153], which makes the estimate very quick. Our calculations consider only the effect of the nearest nuclei, but some of we have recently shown it [128] how to effectively include the effect of farther nuclei with an appropriate re-scaling of second nearest neighbors interaction, allowing a substantial reduction of the otherwise exponentially diverging dimension of the Hilbert space. Following [128], we consider 4 nn and 4 nnn whose positions are homogeneously rescaled by a small amount to compensate for the remaining nuclei.

The predicted μSR signal obtained fully *ab initio*, i.e. without free parameters, is shown for all samples in Figure 6.3 by a red line (PW results) and an orange dashed line (FP results), while shaded area indicates the uncertainty in the PW based prediction quantified with a reduction or increase of 3 % (29%) of $d_{\mu-X}$ (EFG values). Experimental data acquired at the lowest temperature for each compound are shown for comparison. Perfect agreement is found for Nb_3Sn [Figure 6.3(c)], while for V_3Si [Figure 6.3(a)] a small deviation is observed at about 4 μs where the first bump is slightly overestimated, although the experimental result falls inside the shaded area. A small increase of 15 mÅ in the μ-V distance allows the recovery of perfect agreement. Remarkably, the oscillation (the time position of minima and maxima) is very well reproduced. V_3Sn is the sample showing the worst agreement in the long-time tail. In this case, the deviation can be partially attributed to the limits of the PAW approximation in reconstructing the EFG at the V sites. Indeed the FP prediction, which differs from the PW-based estimate by 16%, improves the agreement with the experimental data. These trends demonstrate the exquisite sensitivity of μSR to atomic distances and EFGs.

6.3.2 Point-charge simulations of V_3Si μSR spectra

As a comparison with DFT calculation, whose results are very accurate in describing the muon polarization in A15 compounds, we report here the simulation of the μSR spectra of V_3Si using the point-charge model. The basic concept behind this model is to approximate each ion in a crystal lattice by its ionic charge, centred at a point of radius zero. In general, the EFG is a difficult quantity to compute since it must be derived by differentiating the potential:

$$V(r_0) = \frac{1}{4\pi\epsilon_0}\int \frac{\rho(r')}{r} d\tau' \tag{6.2}$$

where the integral is taken over a volume swept out by r', and the vector $r = r' - r_0$. So as long as the charge distribution, ρ(r), is unknown, this integral cannot be solved. Since simulations in this project will assume a point charge distribution, however, the equation can be simplified to:

$$V(r_0) = \frac{1}{4\pi\epsilon_0}\sum_k \frac{q_k}{r'_k} \tag{6.3}$$

by substituting in the charge distribution of k point charges $\rho(r) = \sum_k q_k \delta^3(r - r_k)$. This equation for V($r_0$) is a quantity that is at least possible to differentiate, as can be easily shown:

$$\begin{aligned} V_{ij}(r_0) &= \frac{\partial^2}{\partial x_i \partial x_j}\left(\frac{1}{4\pi\epsilon_0}\sum_k \frac{q_k}{r'_k}\right) = \frac{1}{4\pi\epsilon_0}\sum_k q_k \left(\frac{\partial^2}{\partial x_i \partial x_j}\frac{1}{r'_k}\right) \\ &= \frac{1}{4\pi\epsilon_0}\sum_k V_{ij}^{(k)} \end{aligned} \tag{6.4}$$

where some algebra will yield:

$$V_{ij}^{(k)} = q_k \left(\frac{3x'^{i} 3x'^{j} - \delta_{ij} r'^{2}_{k}}{r'^{5}_{k}}\right) \tag{6.5}$$

This quantity is the (unscaled) contribution of each charge towards the (i,j)th component of the EFG tensor. Thus, to calculate the net EFG, one only needs to specify the partial EFG due to each point charge, and sum up each contribution.

To achieve this, I personally wrote a Python code [154] to allow the user to calculate the point-charge EFG at the desired nucleus in both an unperturbed or perturbed crystal (by a vacancy, a muon, etc...), which is reported in Appendix C. It is based on a previous code written in C++ [155], which I improved and implemented with other functions. To start with, we used the *UNDI* package as in Ref. [110], with the difference that the EFG used here is calculated by the point-charge model instead of DFT calculations, using POCSI [154]. The distance between the muon and the nearest-neighbours vanadium nuclei $d_{\mu-V}$ is enlarged by 5%, as reported in the paper from ab-initio. There are no other constraints in the simulation. The unperturbed point-charge EFG of V_3Si at the vanadium nuclei has a value of:

$$\mathrm{EFG}^{\mathrm{unperturbed}}_{V_3Si} = \begin{pmatrix} -2.30 & 0.00 & 0.00 \\ 0.00 & -2.30 & 0.00 \\ 0.00 & 0.00 & 4.60 \end{pmatrix} \times 10^{20} \, \frac{\mathrm{V}}{\mathrm{m}^2}$$

Since this model is an approximation, it does not include any possible shielding or antishielding (Sternheimer) factor, thus the absolute values are about 5 times smaller than the true one [156]. Despite this, the relative result is in good agreement with NMR measurements on pure V_3Si, where it is shown that the EFG tensor is perfectly diagonal with the asymmetry parameter $\eta = 0$. When the muon is introduced, it perturbes the distances among the *nn* vanadium nuclei, thus altering the cubic structure and giving a non-diagonal EFG. Furthermore, the muon itself produces an electric field gradient, thus the vanadium nuclei will experience an EFG which is the combination of the perturbed EFG of the *nn* vanadium nuclei and the one produced by the muon itself. The calculated EFG at the vanadium nuclei from PC with the perturbing muon has the following value:

$$\mathrm{EFG}^{\mathrm{perturbed}}_{V_3Si} = \begin{pmatrix} -4.20 & 0.00 & 0.00 \\ 0.00 & -1.62 & -3.18 \\ 0.00 & -3.18 & 5.82 \end{pmatrix} \times 10^{20}\ \frac{\mathrm{V}}{\mathrm{m}^2}$$

We can clearly see the presence of off-diagonal terms, as predicted. Finally, we used the latter calculated EFG and simulated the μSR spectra of V_3Si, whose results are shown in Figure 6.4. The agreement between the simulation and the experimental curve is not perfect, but the main experimental feature representing the coherent oscillation at around 4 μs is well reproduced. To conclude, the point-charge simulation is a rough approximation of the more accurate DFT-based simulation, but can represent a good starting point in the analysis of μSR.

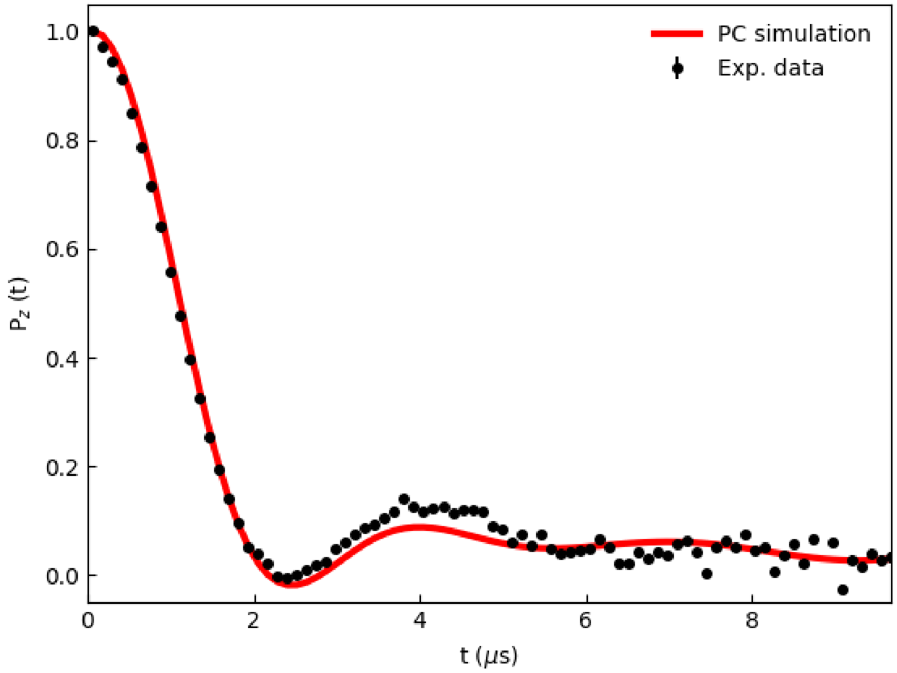

Figure 6.4: Comparison between experimental (black points) and simulated from PC model (red curve) μSR spectra for V_3Si.

6.4 Summary

In summary, we have presented experimental evidence of coherent oscillations resulting from interactions between quadrupolar nuclei and muons in the μSR spectra of A15 superconductors. Solving parameter free spin Hamiltonians that effectively include all nuclear spins in the system and take into account the perturbed EFG at nuclear sites surrounding the muon led to an accurate description of the μSR spectra. The charge distribution can be accurately modeled using DFT-based simulations, and we have demonstrated how this approach can be combined with straightforward spin Hamiltonians to accurately predict the μSR spectra of nuclear origin in virtually any crystalline specimen.

This study gives a concept of proof that μSR can be used not only as a quantum sensing probe for magnetism but also for charge-related phenomena thanks to the quantum entanglement between muons and quadrupolar nuclei. The use of this scope requires accurate calculation of the muon position and of its effect on the surroundings. We demonstrated that clear coherent oscillations are not always present in the μSR spectra (actually very rarely). However, the shape of KT-like behavior requires this approach to properly consider the quadrupolar interaction contribution.

This approach will be used to properly study the μSR results on the Kagome materials presented in the previous chapter when the CDW occurs and further below T_x. This would allow disentangling possible extra contributions coming from more exotic time-reversal symmetry-breaking phenomena from the more trivial due to the charge rearrangement in the CDW phase.

Chapter 7

Magnetic ground state in Na_2PrO_3

In this chapter, I present the results of the complementary effort utilizing μSR and neutron scattering experiments in addition to DFT and model Hamiltonian calculations. These approaches were implored to investigate the magnetic ground state of Na_2PrO_3 and at the same time explore the underlying microscopic exchange interactions and crystal field splitting mechanism, aimed at understanding Na_2PrO_3 potentials for the realization of Kitaev spin liquid.

The manuscript of the results presented in this chapter will be submitted for publication to Physical Review B [J. Frassineti, I. J. Onuorah, M. M. Isah, P. Bonfá, J. G. Rau, J. A. Rodriguez-Rivera, A. I. Kolesnikov, S. Sanna, V. F. Mitrović, and K. W. Plumb, *Unraveling the magnetic ground-state in alkali-metal lanthanide oxide* Na_2PrO_3, to appear soon on Arxiv].

7.1 Introduction

The investigation of Kitaev spin liquids (KSLs) has recently been of extensive interest owing to their intriguing potential for novel exotic magnetism, particularly the realization of quantum spin liquids in more than one-dimensional lattice geometries [51, 52, 62]. The KSLs are obtained as the exact solution of the Kitaev spin model [61] and are characterized by quantum frustrations that arise from the bond-dependent anisotropic Kitaev interactions driven by $J_{\text{eff}} = 1/2$ Kramers doublets spin-orbit entangled local magnetic moments [51, 55]. In practice, the generic Hamiltonian for describing the interactions in a Kitaev material contains the suppressed isotropic Heisenberg interactions, hence the Heisenberg-Kitaev model, and also possibly, in addition, the symmetric off-diagonal exchange interaction [56, 157, 158]. Dominant Kitaev interactions have been proven to be hosted typically by compounds with partially filled 5d and 4d states transition metal ions in the low-spin d^5 electronic configuration, including the Ir^{4+} oxides and Ru^{3+} based chlorides and trihalides [51, 52, 56, 157–162]. In these compounds, the geometric orientation of the neighboring TM-ligand octahedral complexes were shown to play a crucial role in the underlying microscopic exchange interactions within the Jackeli–Khaliullin mechanism [51].

Recently, it has been shown beyond the Jackeli-Khaliullin mechanism that features of dominant Kitaev interactions are realizable in compounds with the high spin d^7 electronic configuration cations such as Co^{2+} and Ni^{3+} [163, 164] and the f^1 electronic configuration such as Ce^{3+} and Pr^{4+} [53, 62, 165, 166]. Of particular interest to this work is Na_2PrO_3, which hosts the Pr^{4+} cation in the f^1 electronic configuration. It crystallizes in the C2/c space group (no. 15), and its structural geometry shows the edge-sharing nature of the neighbouring PrO_6 octahedra with the Pr−O−Pr exchange path required for the realization of the dominant bond directional exchange similar to the d^5 electron Kitaev materials [51, 158]. The crystalline structure adopted by Na_2PrO_3 is shown in Figure 7.1. The two inequivalent Pr atoms, Pr1 and Pr2, form networks of two-dimensional honeycomb lattice in the *ab* plane with two intraplane Pr-Pr distances of $d = 3.433$ and $d' = 3.458$ Å, while along the *c* axis the networks are separated by layers of Na atoms with an interplane Pr-Pr distance of $d_p = 5.867$ Å [167, 168]. Theoretically, using ab initio DFT and the projection of the electronic bands onto Wannier Orbitals, Na_2PrO_3 has been predicted to host antiferromagnetic Kitaev's anisotropic

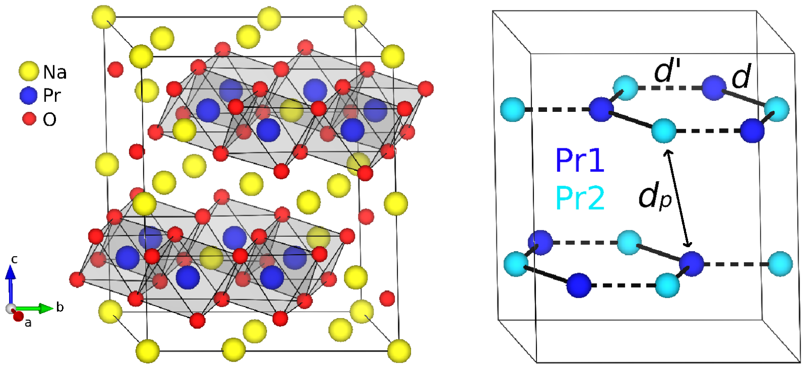

Figure 7.1: (a) the crystalline structure adopted bu Na_2PrO_3, with the presence of Pr-O octahedra. (b) the Pr1-Pr2 bonds are highlighted, and the formation of Pr hexagons is visible.

bond directional interactions, with $J_{\mathrm{eff}} = 1/2$ Kramers spin-orbit entangled local moment by the 4f electrons of the Pr^{4+} cation [53, 169]. On the contrary, results of inelastic neutron scattering revealed rather weak Kitaev interactions in Na_2PrO_3 with dominating Heisenberg exchange interactions and the presence of reduced magnetic moments at Pr sites attributed to increased crystal field effects [168]. This further casts doubt on the true magnetic ground state and the nature of the microscopic exchange interactions that characterize the ground state of Na_2PrO_3.

Here, using μSR, and neutron scattering measurements accompanied by DFT and model Hamiltonian simulations (based on linear spin wave theory (LSWT) and point charge (PC) theory), we investigate the magnetic ground state structure (properties) of Na_2PrO_3 and the underlying microscopic exchange interactions that characterize the ground state in search of the signatures of Kitaev interactions.

7.2 Methods

Powder samples of Na_2PrO_3 were synthesized via solid-state reactions from Na_2O_2 and Pr_6O_{11}. Dry starting reagents were weighed in a metal ratio, Na/Pr∼2.2, to account for sodium evaporative losses, ground in an agate motor and pestle, and pelletized under an argon environment. The prepared materials were enclosed in Ag ampules and heated at 750°C under dry, flowing oxygen for 36 hours. Samples were furnace-cooled to ∼ 150°C and immediately transferred to an Argonne glovebox for storage.

μSR measurements were carried out on the GPS spectrometer at the Paul Scherrer Institut, Switzerland. The measurements were performed both in a weak transverse field (TF) mode to calibrate the asymmetry parameter of the muon polarization, and in zero field (ZF) to uncover the spontaneous oscillations that give rise to the internal magnetic field. The ZF μSR spectra were collected at temperatures ranging from 1.5 K to 5.2 K using a helium flow cryostat. The sample was packed into aluminium foil inside a glovebox to avoid air contamination and put into a Cu fork inserted into the experimental probe. The time-differential μSR data were fitted using MUSRFIT software [170], and the MuLab suite, a home-built Matlab toolbox.

Neutron scattering measurements were carried out on powder samples using the Multi-Axis Crystal Spectrometer (MACS) at the NIST Center for Neutron Research. Elastic ($E = 0$) measurements were conducted with the monochromator in a vertical focusing configuration using neutron energy of 5 meV. Inelastic measurements were carried out using a double-focusing configuration and a fixed final energy of 3.7 meV with Be and BeO filters before and after the sample, respectively. For energy transfers above 1.4 meV, we used a fixed final energy of 5 meV with a Be filter after the sample and no incident beam filter. Data for energy transfers above 1.4 meV was corrected for contamination from high-order harmonics in the incident beam neutron monitor.

To find the muon implantation sites, we used the well-established DFT+μ approach [121, 122, 147, 171]. Non-spin polarized DFT calculations were performed within generalized gradient approximation (GGA) for the PBE (Perdew-Burke-Ernzerhof [139]) exchange-correlation functional as implemented in the Quantum Espresso code [144]. The muon was treated as a hydrogen impurity in a 2×1×1 charged supercell (96 host atoms and 1 muon) with a compensating background. For Na, O, and H atomic species, the norm-conserving pseudopotentials were used, while for Pr, the Projector augmented wave (PAW) with no 4f electron state in the valence was used in order to avoid the well-known difficulty in describing the 4f valence shell [146] and very expensive calculations with high plane-wave cut-off requirements. The cut-off used for the plane waves was 100 Ry while the Brillouin zone was sampled using a 4×4×4 mesh of K-points [172].

To analyze and obtain an in-depth understanding of the INS data, we have performed model Hamiltonian calculations using the SpinW [173] code. We have also carried single ion point charge (PC) model calculations utilizing the PyCrystalField Python package [174] in order to characterize the crystal field excitations and study the spin-orbital coupling mechanism.

7.3 Results and discussion

7.3.1 μSR results

The measured ZF μSR asymmetry spectra, $a^{\mathrm{ZF}}(\mathrm{t})$, is shown in Figure 7.2a for four temperatures: 1.5 K, 4.6 K, 4.9 K, and 5.1 K. At high temperatures (above $\sim$ 4.9 K), the μSR signal shows no oscillations, indicating that the sample is in the paramagnetic phase. However, lowering the temperature reveals damped coherent oscillations in the μSR signal, indicating the emergence of long-range magnetic order due to the presence of an internal magnetic field and the spontaneous muon precession around it. Also, a fast relaxation at short times reflecting static magnetic moments is observed. As the temperature is further lowered to 1.5 K, the signature oscillations of the long-range magnetic order become more pronounced and dominate the μSR spectra. In order to understand and parameterize the contributions to the spectra at each temperature, all the observed ZF-μSR spectra are well fitted by the following model below, well-known for fitting signals in the antiferro-

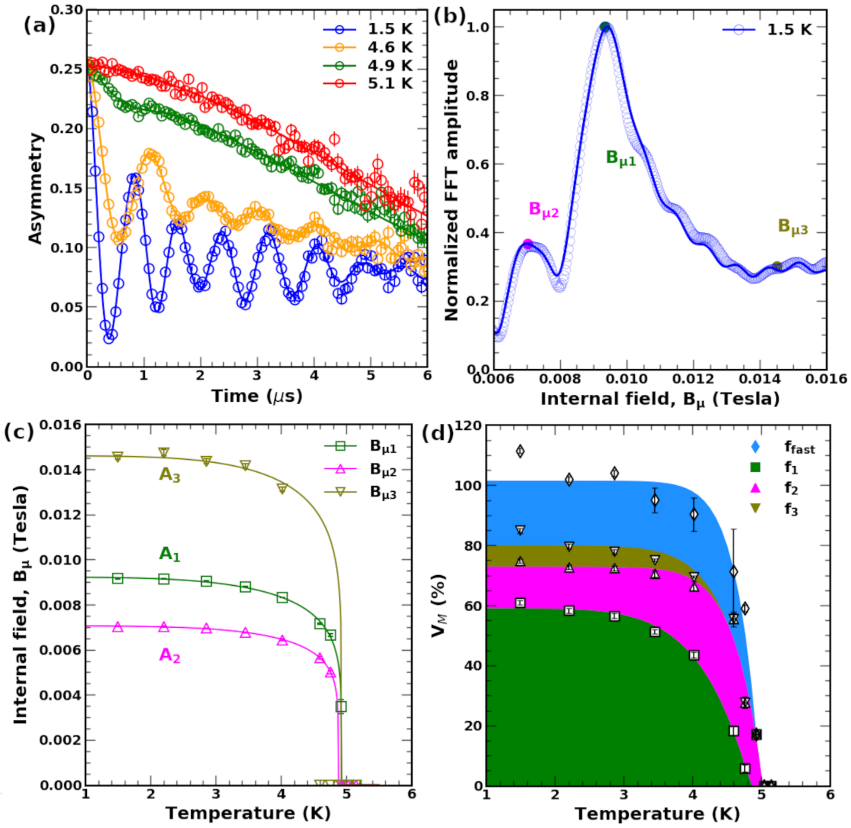

Figure 7.2: (a) Muon asymmetry spectra obtained at temperatures of 1.5 K (blue), 4.6 K (yellow), 4.9 K (green), and 5.1 K (red). The solid lines are the best fit to the asymmetry data using Equation (7.1). For clarity, the spectra are shifted on the y-axis by 1/3. (b) The real part of the Fast Fourier Transform (FFT) of the experimental μSR spectrum at T = 1.5 K, showing three oscillating fields (in Tesla) at A1, A2, and A3. (c) The local field (B_μ) in Tesla at the three muon sites A1, A2, and A3 as a function of temperature. The solid lines represent the fit to the power law function (see text). (d) The magnetic volume fraction VM as a function of temperature, coloured shaded to illustrate the % contribution of each term in Equation (7.1).

magnetic phase:

$$a^{\mathrm{ZF}}(t) = a_0\left[\sum_{i=1}^{n} f_i e^{-\lambda_i t}\cos(\gamma_\mu B_{\mu,i} t + \phi) + f_{\mathrm{fast}} e^{-\lambda_{\mathrm{fast}} t} + f_l e^{-\lambda_{\mathrm{tail}} t} e^{-(\sigma_{\mathrm{tail}} t)^2}\right] \tag{7.1}$$

The first term in Equation (7.1) describes the exponentially damped oscillating signal components with a transverse relaxation rate λ, summed over n number of distinct muon sites and f_i controls the contribution of each muon at site i to the total asymmetry signal. γ_μ = 135.5 MHZ T^{-1} is the gyromagnetic ratio, B_μ is the internal magnetic field at the muon site, and ϕ is the phase. The second term accounts for the fast non-oscillating relaxations with amplitude a_{fast} and depolarization rate, λ_{fast}. The third term accounts for the slow-damped Gaussian relaxations (at the tail) of the signal with amplitude a_{tail} and relaxation rates, λ_{tail} and σ_{tail}.

Figure 7.2b shows the real part of the Fast Fourier Transform (FFT) of the time-domain μSR asymmetry at T = 1.5 K. Three ZF precession frequencies (or, equivalently, magnetic fields) are observed, indicating three distinct muon sites, which we have labeled A1, A2, and A3. We have attributed the field $B_{\mu1}$ with the maximum Fourier power (green line) to the A1 site, followed by $B_{\mu2}$ (pink line) to the A2 site, and then $B_{\mu3}$ (brown line) to the A3 site. The values of the internal magnetic field at these distinct sites, $B_{\mu1}$ = 0.0092 T, $B_{\mu2}$ = 0.0070 T and $B_{\mu3}$ = 0.0145 T are obtained with the best fit of the asymmetry signal at low-temperature T = 1.5 K when the magnetic order is in full regime. Figure 7.2c shows the temperature dependence of the three distinct local magnetic fields extracted from the fits to Equation (7.1). The local field due to the magnetic moments on Pr decreases steadily with a field increase in temperature. The temperature dependence of each of the fields is well fitted to the double-exponent power law function [175]:

$$B_\mu(T) = B_\mu(0)\left(1 - \left(\frac{T}{T_N}\right)^\alpha\right)^\beta \tag{7.2}$$

which gives an estimate of $T_N \approx 4.9$ K consistent with earlier results [168, 176], while $\alpha \simeq 4.0$ and $\beta \simeq 0.16$. The large α value hints of complex interactions between the magnetic moments [177, 178]. The solid line curve of the fits shows a sharp discontinuous drop of the local fields with temperature, suggesting that the phase transition is of the first-order.

Figure 7.2d shows the temperature dependence of the magnetic volume fraction (V_M) obtained by considering the asymmetry amplitudes [179] of the terms in Equation (7.1) and color shading to show their % contribution. The signal f_1 corresponding to the muon at site A1 has a 59% contribution to V_M (green shaded area) and is the most populated site. Sites A2 (signal contribution f_2) and A3 (signal contribution f_3) contribute 14% and 7% respectively, resulting in a total of 80% contribution to V_M from implanted muons that are sensitive to the internal magnetic field. The remaining 20% is from the amplitude of the fast non-oscillating relaxing signal (f_{fast}), showing that 20% of the implanted muons interact with a disordered internal field distribution with a size of few tens of Gauss, indicating an additional muon site.

Muon sites and dipolar field analysis

In order to characterize the muon spin relaxation spectra in Figure 7.2a, and constrain the magnetic structure, we first find the muon implantation site(s) in Na_2PrO_3 using the DFT+μ approach. DFT results reveal three symmetrically distinct candidate muon sites, consistent with sites A1, A2, and A3 from the analysis of μSR data above, which are shown in Figure 7.3. Each of these site is at the 8f Wyckoff position, with a distance of ≈ 1 Å along the z axis to the three distinct O sites in the unit cell, as shown in Figure 7.3. This is expected for oxide compounds where the positive muon

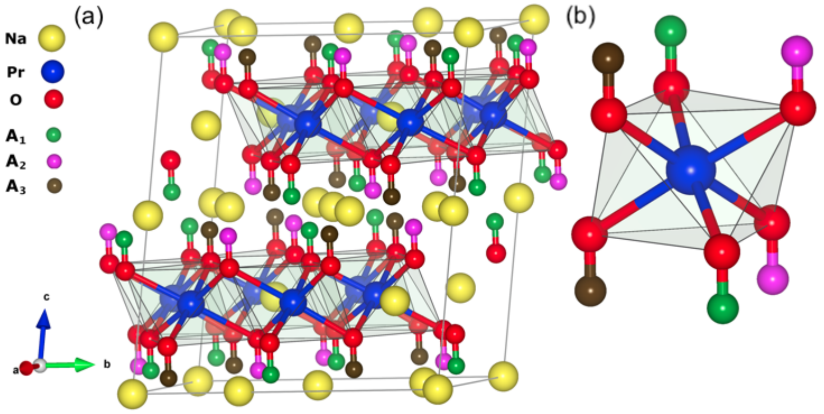

Figure 7.3: (a) Muon sites A_1 (green spheres), A_2 (pink), and A_3 (blue) are shown in the unit cell. (b) Muon sites in a PrO_4 environment.

is well known to stop near the O sites [171, 180]. These sites are found to be in the direction of the non-magnetic Na layer and farther from the magnetic Pr^{4+} ions (Figure 7.3(a)). The stability of the muon at A1, A2, and A3 sites with DFT total energy considerations indicates that they are all populated as the energy differences between them are less than 0.2 eV with site A1 being the least energy one. These candidate sites, as it will be shown in a while, account for the low-temperature internal magnetic field observed from μSR data (see Figure 7.2).

With the knowledge of the muon implantation sites, we determine the magnetic structure and ordered moment size in Na_2PrO_3 by comparing simulated dipolar field distributions at these site(s) with μSR experimental results. First, by considering the maximal magnetic space groups (MAXMAGN code [181]), we have identified and explored twenty-eight (28) AF magnetic structures, within the (000), (110), and (100) propagation vectors as a function of the Pr magnetic moment. The experimentally observed FFT power spectrum at 1.5 K (Figure 7.2(b)) was then fitted to the convolution of the calculated dipolar fields to a Gaussian distribution. Such that, for each magnetic structure, the dipolar field B [182] is estimated for all 24 muon sites (3 muon sites with a multiplicity of 8) in a pristine crystal structure as a function of the Pr moments, m_{Pr}, as described by:

$$p(B, m_{Pr}) = \sum_{i=1}^{24} \delta(B - m_{Pr} B_i)$$

This experimental distribution is further approximated to a convolution with a Gaussian broadening g as:

$$\widetilde{p}(B, m_{Pr}, \sigma) = (p * g)(B) := \int_{-\infty}^{\infty} p(\tau, m) g(B - \tau, \sigma) d\tau$$

such that the fitting function P becomes:

$$P(B; m, \sigma, A, A_{BKG}) = A\widetilde{p}(B, m, \sigma) + A_{BKG}$$

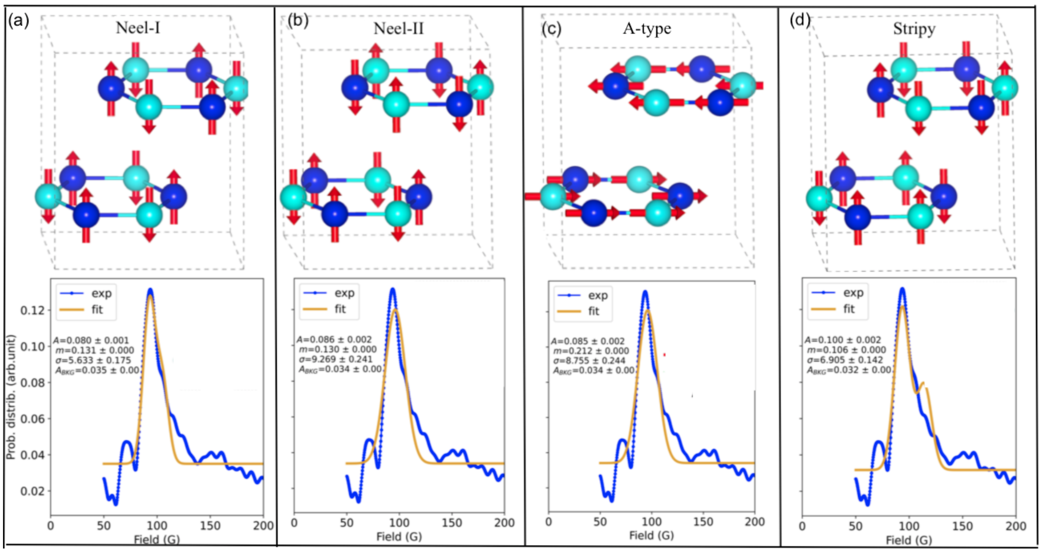

Figure 7.4: (a-d) Four proposed AF magnetic structures (upper panel) from analysis of μSR data, labelled Néel-I, Néel-II, A-type, and Stripy, with the best fit of the comparison between experimental and calculated dipolar field distribution (lower panel) and their corresponding magnetic structures. Only the Pr atoms are shown for clarity (with Pr_1 (dark blue spheres) and Pr_2 (sky blue spheres)).

Table 7.1: The proposed magnetic sites labelled Néel-I, Néel-II, A-type, and Stripy; their propagation vector and Group (BNS) at each structure and the calculated dipolar field (B_{dip}) at muon sites A1, A2, and A3.

Label	K	Group (BNS)	m (μ_B)	B_{dip}^{A1}(T)	B_{dip}^{A2}(T)	B_{dip}^{A3}(T)
Néel-I	000	C2′/c′ (15.89)	0.131	0.0105	0.0092	0.0094
Néel-II	000	C2′/c (15.87)	0.130	0.0099	0.0097	0.0093
A-type	000	C2/c′ (15.88)	0.212	0.0094	0.0093	0.0101
Stripy	100	P_C2_1/c (14.84)^2	0.106	0.00921	0.0115	0.0096

The μSR magnetic structural analysis suggests four possible AF magnetic structures, labeled Néel-I, Néel-II, A-type, and Stripy that provide the best fit to the experimental Fourier spectrum. The moment alignment of these structures and the best fit are shown in Figure 7.4 and they all constitute AF magnetic structures with the propagation vector K = (0,0,0) (Néel-I, Néel-II and A-type structures) and K = (1,0,0) (for Stripy structure) featuring collinear moments that are confined along the *c* or *a* axis. The dipolar simulation fits with these structures and results in very small effective magnetic moments of 0.131, 0.130, 0.212, and 0.106 μ_{B}/Pr respectively (see Table 7.1) and the calculated internal field at the muon are compared with experiments.

7.3.2 Neutron scattering results

We have used inelastic neutron scattering measurements to probe the spin dynamics of Na_2PrO_3. The spin wave dispersion contour plots (i.e., S(Q,E)) are shown in Figure 7.5, for temperatures below T_N at 1.7 K and above T_N at 20 K. The temperature dependence depicts the existence of magnetic excitations below T_N and then their collapse to a continuum-like behaviour in response to a paramagnetic regime above T_N. The low-temperature spectrum shows the dominance of spin-wave dispersion with a small band gap of ≈ 1 meV and with plausible continuum-like modes that show up at the top of the band above 2 meV. For T = 1.5 K, the appearance of a spin-wave spectrum confirms the presence of a long-range magnetic order, as observed with μSR. In Figure 7.5(c), the scan of the integrated intensities over angles is shown. Further, performing powdered neutron diffraction simulations on the difference data using FullProf suite [183], maintaining only the K = (0, 0, 0) propagation vector, and considering possible AFM magnetic structures from the MAXMAGN code, the Néel-I magnetic structure (see Figure 7.4(a)) gives the best fit. The fit (see Figure 7.5d) also provides the upper bounds of the size of the ordered moments as 0.15 μ_B, which is in agreement with the μSR data above but 'critically' very small in comparison to both the crystal electric field calculations (CEF) value of 0.84 μ_B [168], and the free-ion value of 2.54 μ_B.

Linear spin wave theory

Here, by simulating the inelastic neutron scattering powder spectra while adapting a model Hamiltonian within the linear spin wave theory (LSWT)

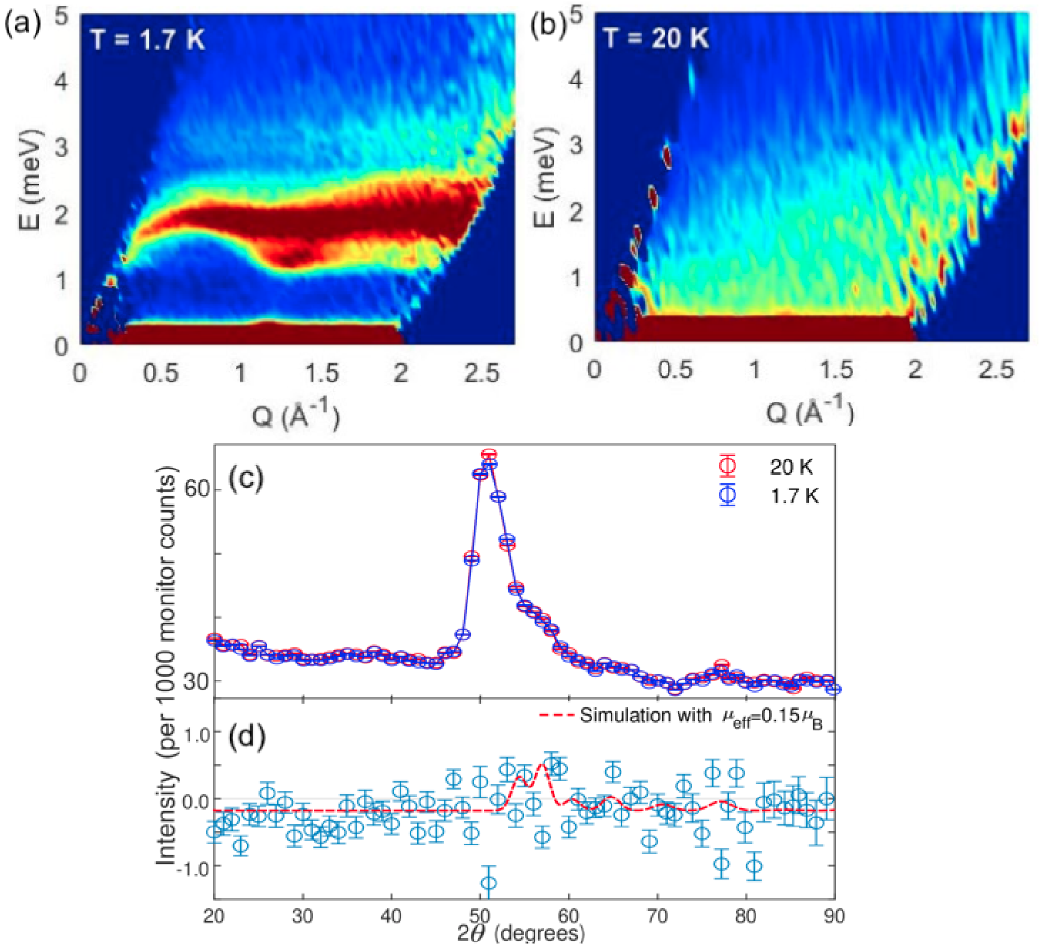

Figure 7.5: Inelastic neutron data for S(Q,E) contour plots (a) at 1.7 K and (b) at 20 K . (c) The integrated intensity with respect to angle and (d) FullProf simulation on the difference data between the 1.7 K and 20 K data, providing the upper bounds of the magnetic moment size.

as implemented in the SpinW code [173] and comparing them to INS experiment data, we elucidate the nature of the exchange interaction of Na_2PrO_3 and further clarify the suitability of the Heisenberg-Kitaev (H-K) model in interpreting the magnetic properties of Na_2PrO_3. The form of the H-K model is written as;

$$\begin{aligned}\mathcal{H} = J\sum_{i,j}\left[\mathbf{S}_i^x\cdot\mathbf{S}_j^x + \mathbf{S}_i^y\cdot\mathbf{S}_j^y + \Delta\mathbf{S}_i^z\cdot\mathbf{S}_j^z\right] + J'\sum_{i,j'}\left[\mathbf{S}_i^x\cdot\mathbf{S}_{j'}^x + \mathbf{S}_i^y\cdot\mathbf{S}_{j'}^y + \Delta\mathbf{S}_i^z\cdot\mathbf{S}_{j'}^z\right]\\ +J_P\sum_{i,j''}\left[\mathbf{S}_i^x\cdot\mathbf{S}_{j''}^x + \mathbf{S}_i^y\cdot\mathbf{S}_{j''}^y + \Delta\mathbf{S}_i^z\cdot\mathbf{S}_{j''}^z\right] + K\sum_{i,j}\mathbf{S}_i^\gamma\mathbf{S}_j^\gamma\end{aligned} \tag{7.3}$$

where $\mathbf{S}_i$ and $\mathbf{S}_j$ are the spin vectors at sites i and j. J, J' and J_P are the isotropic Heisenberg interaction constant for the nearest, next nearest neighbor intralayer and interlayer Pr-Pr sites (with distances d, d' and d_P, see Figure 7.1), respectively. Δ is a parameter describing an anisotropic Heisenberg interaction along z. K is the anisotropic bond-dependent Kitaev interaction constant. First, for the simulated spin wave dispersion spectrum reported in Figure 7.6, we have considered the four magnetic structures proposed by the μSR analysis, however, only the Néel-I structure generates spin wave spectrum results consistent with INS data. This further validates the magnetic structure of Na_2PrO_3 in line with earlier proposals [168].

Figure 7.6 illustrates the simulated spin wave spectra using the model in Equation (7.3) and Néel-I magnetic structure. Results of three different conditions (labelled case1 (Figure 7.6(b)), case2 (Figure 7.6(c), and case3 (Figure 7.6(d)) of the parameters in the H-K model are shown in Figure 7.6. The following interaction coupling constants are shown in Table 7.2, for the different cases: The positive values of all the coupling constants indicate that the exchange interactions are antiferromagnetic. Here, it is noticeable that case1 with the Kitaev term put to zero, misses entirely the continuum-like feature above 2.1 meV in the low-temperature INS spectrum while an

	J (meV)	J' (meV)	J_P (meV)	Δ	K^γ (meV)
case1	1.0	1,0	0.15	1.2	0
case2	-	-	-	-	0.4
case3	-	-	-	1.25	1.35

Table 7.2: Exchange parameters of the Hamiltonians for the three cases described in Figure 7.6.

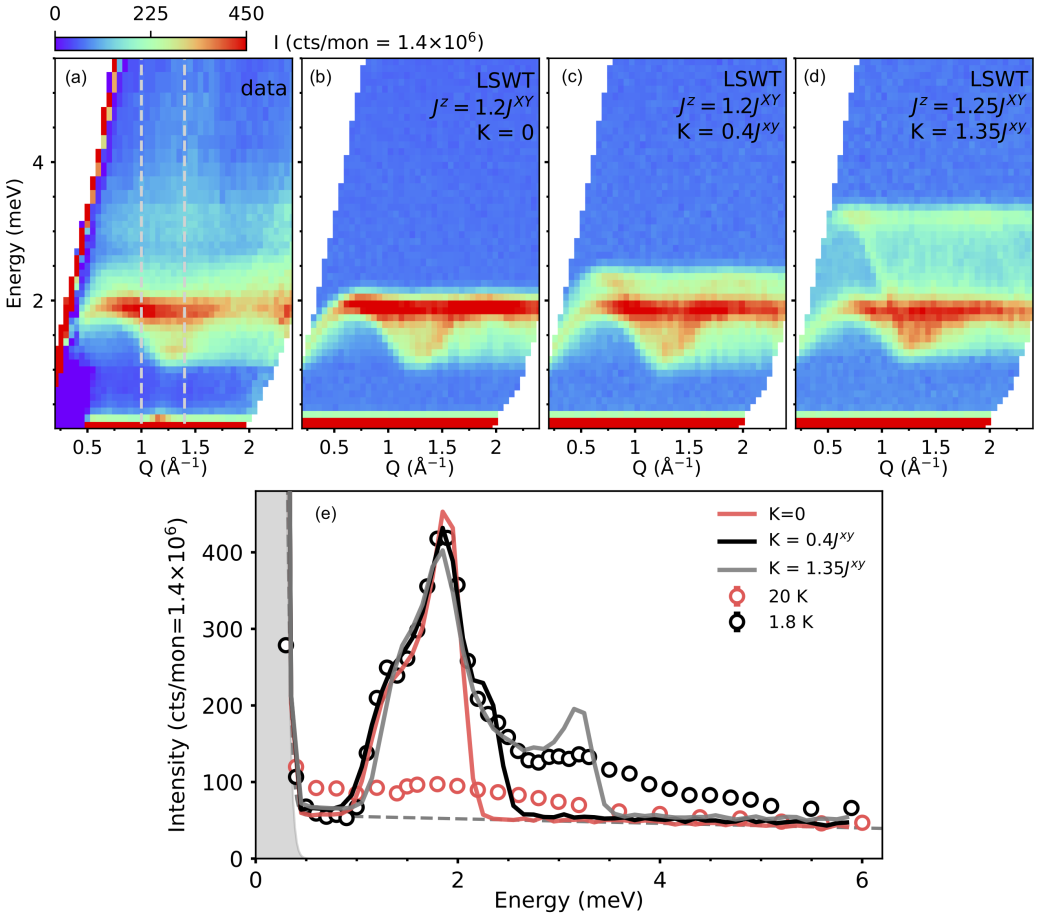

Figure 7.6: (a) Experimental ($T = 1.5$ K) INS data. Simulated spin-wave spectrum using linear spin-wave theory (b) K=0 (case1), (c) K=0.4J (case2), (d) K=1.25J (case3). (e) Comparison between simulated and experimental integrated intensity with respect to energy using linear spin-wave theory.

attempt to capture these interactions by turning on the Kitaev term in case2 and case3, instead creates excitations with more gaps. This can be attributed to the absence of quadratic and high-order terms in the LSWT or due to the pseudo-Goldstone modes [184] that are artifacts of LSWT+. Further studies to obtain a better fit involve simulating the model Hamiltonian within the non-linear spin wave theory (NLSWT), which could confirm the exclusion of anisotropic Kitaev terms and provide a better way to explain the continuum at above 2.1 meV by means of quantum fluctuations.

However, the important message from the spectra simulations with LSWT is that the major characteristic features of the INS spectrum at 1.5K are dominantly captured with the Isotropic Heisenberg interactions between Pr-Pr sites (through the Pr-O-Pr exchange path provided by the corner-sharing octahedral complexes), dominating over the weak bond-directional Kitaev interactions. Regardless that the ground state of Na_2PrO_3 was theoretically demonstrated to fulfill the prerequisites or premises that produce dominant Kitaev interactions, our neutron results depict that instead Kitaev's interaction in Na_2PrO_3 is rather weak or probably entirely absent, while in addition, the ZF-μSR spectra unambiguously identify a long-range ordered antiferromagnetic state, with signatures of a spin-liquid state conspicuously absent.

Crystal electric field excitations

In order to understand the roles of the crystal field in the ground state level splitting of Na_2PrO_3, we have obtained the crystal field excitations by performing one-dimensional constant Q cuts at incident energies E_i of the magnetic scattering to obtain the integrated intensities as functions of energy transfer. The integrated magnetic scattering intensities have been systematically collected over increasing incident energies (E_i) at 60 meV, 150 meV, 300 meV, 700 meV, and 2500 meV. As depicted in Figure 7.7(a), for E_i = 700 meV, the background due to strong phonon excitations observed mostly below 150 meV and those from the O-H stretching mode (due to moisture contamination in the sample) at 450 meV were carefully subtracted considering INS data of Li_2PrO_3. The magnetic low Q signals that might be hidden under the phonons were explored, with likely peaks highly resolved. The plot of the integrated intensity spectra of Na_2PrO_3 at T = 5 K measured at the incident energies E_i = 700 meV at $|Q|$=[6,11]Å^{-1} and E_i = 300 meV at $|Q|$=[6,8]Å^{-1} are shown in Figure 7.7(b) and Figure 7.7(c), respectively. The high resolution of the experimental INS data reveals the presence of six CEF excitations at energies: 230, 237, 300, 390, 526, 569 meV. The first two CEF levels with varying intensities are not clearly observed with the

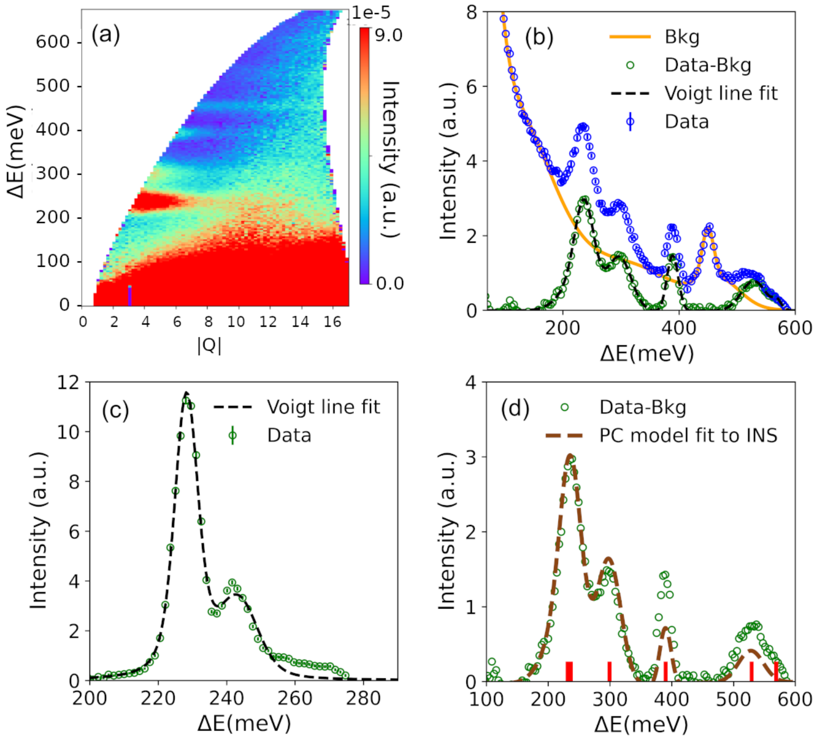

Figure 7.7: (a) INS contour plot at 5K with incident energy $E_i = 700$ meV. (b) Integrated intensity spectrum for incident energy $E_i = 700$ meV at $|Q|$=[6,11]Å^{-1}, showing the subtraction of background due to the phonon excitations (yellow line) and a fit to the Voigt line function consisting of both the Lorentzian and Gaussian components (black dotted lines). (c) Integrated intensity spectrum for incident energy E_i=300 meV at $|Q|$=[6,11]Å^{-1}. (d) Fit to $E_i = 700$ meV integrated INS spectrum utilizing the point charge model to the INS experimental data. Red vertical bars indicate the transition levels obtained from the PC model fit.

$E_i = 700$ meV plot, however, the $E_i = 300$ meV INS data (Figure 7.7(b)), clearly shows two distinct crystal field excitations in the vicinity of ~ 240 meV. The large first-level CEF excitations are comparable to the 260 meV reported for $BaPrO_3$ [185].

The presence of six crystal field excitations in the INS spectrum hints that the octahedral crystal field splitting in Na_2PrO_3() results in a Γ_7 ground state characterized by a less symmetric mixed states instead of that observed typically for a highly symmetric octahedral environment in rare-earth ions.

Hence, to further understand the coupling scheme that characterizes the ground state and investigate these spectrum peculiarities, we calculate the Pr^{4+} ion crystal electric field (CEF) Hamiltonian (H_{CEF}) from a point charge (PC) model. Unlike for most rare earth ions, where the crystal fields are much weaker than spin-orbit coupling, here, the first transition level (230 meV) is of the same order of magnitude as the spin-orbit coupling (100s of meV [186]). Thus, to calculate the single ion crystal field within the PC model, we have adopted the so-called *intermediate coupling* scheme, where the H_{CEF} acts only on the orbital angular momentum L (LS basis) instead of the J basis [174]. We have used the CEF Hamiltonian (H_{CEF}) that has the following form:

$$\begin{aligned} H_{CEF} =& B_2^0 O_2^0 + B_2^{\pm 2} O_2^{\pm 2} + B_4^0 O_4^0 + B_4^{\pm 2} O_4^{\pm 2} + B_4^{\pm 4} O_4^{\pm 4} \\ &+ B_6^0 O_6^0 + B_6^{\pm 2} O_6^{\pm 2} + B_6^{\pm 4} O_6^{\pm 4} + B_6^{\pm 6} O_6^{\pm 6} \end{aligned}$$

where $B_n^{\pm m}$ are the CEF parameters and $O_n^{\pm m}$ are the Stevens Operators. H_{CEF} includes contributions from the non-zero $-m$ components that are *imaginary* in the Stevens Operators that arise due to the low point symmetry of the PrO_4 environment. Here, we have deduced the $B_n^{\pm m}$ CEF parameters by fitting to the INS data at E_i=700 meV, where the six experimentally observed levels provide strong constraints to the general form of H_{CEF} including the SOC parameter. For the calculations, we have considered Pr^4+ ions with total angular momentum $L = 3$, spin quantum number $S = 1/2$, SOC parameter value of 55 meV, and it has been represented with its isoelectronic Ce^{3+} ion.

The values of $B_n^{\pm m}$ obtained from the PC model and subsequent fits to the INS data are reported in Table 7.4. The calculated intensity spectrum from the fitted PC model to INS data is plotted in Figure 7.7(d) and is found to be in good agreement with the experiment since all the CEF transfer levels were accurately captured. The transition energies and eigen-kets showing the mixture of the different states resulting from the fit of the PC model to the INS data are shown in Section 7.3.2. Particularly, Section 7.3.2 shows that the Γ_7 ground state wavefunction even includes mixtures of the nominally

Table 7.3: The energies of the eigenvalues (along the first row) and the corresponding coefficients of the eigen-kets (down the column for each energy) calculated from the point-charge model for Na_2PrO_3.

E (meV) →	0.000	231.320	236.470	299.300	389.940	529.270	569.050
$\left\|-3, -\frac{1}{2}\right\rangle$	-0.138+0j	0.115+0j	0j	0.374+0j	0j	-0.31+0j	-0.767+0j
$\left\|-3, \frac{1}{2}\right\rangle$	0j	0j	0.303+0j	0j	-0.213+0j	0j	0j
$\left\|-2, -\frac{1}{2}\right\rangle$	0j	0j	-0.339+0.182j	0j	-0.454-0.046j	0 j	0j
$\left\|-2, \frac{1}{2}\right\rangle$	0.184+0.053j	-0.473+0.299j	0j	0.42-0.069j	0j	0.481+0.018j	-0.098+0.059j
$\left\|-1, -\frac{1}{2}\right\rangle$	-0.526-0.221j	-0.028-0.281j	0j	0.115-0.202j	0j	0.224+0.109j	0.117+0.161j
$\left\|-1, \frac{1}{2}\right\rangle$	0j	0j	-0.005-0.292j	0j	-0.398+0.167j	0j	0j
$\left\|0, -\frac{1}{2}\right\rangle$	0j	0j	0.033+0.558j	0j	-0.327+0.093j	0j	0j
$\left\|0, \frac{1}{2}\right\rangle$	0.035-0.265j	0.023+0.384j	0j	-0.221-0.41j	0j	-0.176+0.299j	0.006-0.126j
$\left\|1, -\frac{1}{2}\right\rangle$	-0.038+0.701j	0.261+0.009j	0j	0.003-0.328j	0j	-0.067+0.092j	-0.125-0.175j
$\left\|1, \frac{1}{2}\right\rangle$	0j	0j	0.448-0.121j	0j	-0.362-0.305j	0j	0j
$\left\|2, -\frac{1}{2}\right\rangle$	0j	0j	-0.333-0.023j	0j	-0.289-0.169j	0j	0j
$\left\|2, \frac{1}{2}\right\rangle$	-0.014-0.01j	-0.09-0.277j	0j	-0.01+0.007j	0j	-0.405-0.549j	0.116+0.282j
$\left\|3, -\frac{1}{2}\right\rangle$	-0.103+0.209j	0.026+0.54j	0j	-0.101+0.539j	0j	-0.104+0.028j	-0.001+0.452j
$\left\|3, \frac{1}{2}\right\rangle$	0j	0j	0.045+0.182j	0j	0.123-0.304j	0j	0j

Table 7.4: $B_n^{\pm m}$ values in meV obtained from the PC model, fits of the PC model to the ligand charges, and fit of the model to the INS data at E$_i$ = 700 meV.

$B_n^{\pm m}$	PC	PC charge	PC fit
B_2^0	-3.8101	-4.2032	6.4760
B_2^2	-11.3483	-15.9556	-3.2862
B_2^{-2}	1.3055	0.0831	8.6586
B_4^0	-0.0547	-0.0680	-0.0852
B_4^2	-0.2868	-0.3853	-0.6860
B_4^{-2}	-1.3160	-1.7433	-1.0770
B_4^4	-0.5705	-0.7719	-0.0237
B_4^{-4}	0.6112	0.8403	0.1975
B_6^0	0.00672	0.0089	-0.0214
B_6^2	-0.0084	-0.0121	0.0373
B_6^{-2}	0.0097	0.0103	0.0163
B_6^4	0.0474	0.0610	0.0968
B_6^{-4}	0.01268	0.0189	0.2478
B_6^6	0.0499	0.0693	-0.0001
B_6^{-6}	-0.0108	-0.0143	-0.2462

excited states, as these states host non-vanishing coefficients. The estimated value of the Pr powdered-averaged $g-$tensor $g_{av} \sim 2.0$, while the ground state magnetic moment is obtained from $< 0|J_i|0 >$ with $J = \sqrt{\sum_{i=x,y,z} J_i^2}$ and the value of 1.12 μ_B was obtained. Here, J$_x$=J$_y$=0, with all the contribution coming from J$_z$ indicating that the moment is aligned along the *c* axis. While the value of the magnetic moment obtained is not totally consistent with measurements obtained from neutron elastic scattering and DFT+μ, it is much lower than the magnetic moment displayed by free Pr ions, which is 2.54 μ_B. Our INS data Na$_2$PrO$_3$ is consistent with previous report [168, 187], particularly with the observed unusually large first CEF transition at 230 meV. Our data is of higher resolution and spans a larger energy range, allowing us to resolve higher transition CEF levels and also better constrain the CEF Hamiltonian parameters. The reported high-resolution INS data and the analysis of the CEF excitations within the point charge model are critical features of this work. Our results show that the CEF effects introduce anisotropy into the system, resulting in transitions between various energy levels leading to mixed levels in the ground state that deviate from the Kramers Γ_7 doublet expected [53, 169] for this rare earth ion.

7.4 Summary

In conclusion, we have performed a detailed analysis of μSR and neutron measurements to elucidate the magnetic ground state of Na_2PrO_3. μSR confirms the existence of long-range AF magnetic order below $T_N \sim 4.9$ K and some degree of magnetic fluctuations have been observed. Analysis of the μSR and neutron data by DFT calculations, muon dipolar simulations, and spin-wave simulations has allowed us to determine the magnetic structure of Na_2PrO_3 with the small observed Pr magnetic moment ($0.13\ \mu_B$) attributed to the quantum fluctuations. Results of model Heisenberg-Kitaev Hamiltonian simulations on the INS data show strong evidence of dominant antiferromagnetic isotropic Heisenberg interactions, suppressing the spin-liquid Kitaev's term. This evidence further establishes that the magnetic ground state of Na_2PrO_3 is dominant in the Néel antiferromagnetic ordered state. This is further evidenced by the results of the PC model crystal field analysis, which show that the ground state of the Pr^{4+} ions in Na_2PrO_3() deviates from the expected J=1/2 limit. The findings of this study could have significant implications for a more in-depth understanding of the exotic quantum states of matter and the development of quantum technologies.

Conclusions

This Ph.D. work has been mainly devoted to the study of exotic phenomena in novel quantum materials and focused mainly on kagome and Kitaev compounds, using NMR and μSR. In addition to this, other side projects have been performed using complementary techniques such as neutron scattering experiments, Density Functional Theory calculations, and Crystal Electric Field simulations. All the samples used, along with the technique we used to characterize them, are summarized in Table 7.5. To summarize this work and conclude it, we can present here the main results I obtained during the

Table 7.5: List of all compounds measured in this work by means of NMR, μSR, and inelastic neutron scattering (INS), along with their composition, form, and technique used.

Composition	**Doping**	**Label**	**Form**	**Tecnhique**	**Chapter**
RbV_3Sb_5	Undoped	RVS	Crystal	NMR/NQR	Chapter 4
KV_3Sb_5	Undoped	KVS	Crystal	NQR	Chapter 4
CsV_3Sb_5	Undoped	CVS	Crystal	NQR	Chapter 4
$CsV_3Sb_{5-x}Sn_x$	x = 0.05	CVS-Sn05	Powder	NQR	Chapter 4
	x = 0.08	CVS-Sn08	Powder	μSR	Chapter 5
	x = 0.35	CVS-Sn35	Powder	μSR	Chapter 5
$CsV_3Sb_{5-x}Te_x$	x = 0.04	CVS-Te04	Powder	NQR	Chapter 4
	x = 0.06	CVS-Te06	Powder	NQR	Chapter 4
	x = 0.08	CVS-Te08	Powder	μSR	Chapter 5
V_3Si	Undoped	V_3Si	Powder	μSR	Chapter 6
V_3Sn	Undoped	V_3Sn	Powder	μSR	Chapter 6
Nb_3Sn	Undoped	Nb_3Sn	Powder	μSR	Chapter 6
Na_2PrO_3	Undoped	Na_2PrO_3	Powder	μSR/INS	Chapter 7

three years of my Ph.D. Overall, all these findings can help the study of these novel quantum materials in the physical description of the peculiar quantum phenomena that arise inside them.

Study of the quantum transitions of 2D kagome AV_3Sb_5 materials

Undoped Kagome materials

We have studied and identified the CDW structure of the kagome 2D superconductor in the case of RVS by combining NMR/NQR experiments and DFT calculations. This forms a $2 \times 2 \times 2$ superlattice with alternating Inverse Star-of-David (ISD) layers, π-shifted relative to each other, determined by assessing the multiplicity of nonequivalent sites for each species, and the same applies for KV_3Sb_5. The results are reported in Section 4.3 (see Figure 4.2 and Figure 4.4) and published in ref.[77].

In our temperature-dependent analysis of RbV_3Sb_5 (Section 4.4), we have observed several key findings, such as unusual increase of FWHM in ^{51}V, likely attributed to changes in the local dipolar field associated with nematic order or orbital currents (Rotational Symmetry Breaking), for one of the two vanadium sites when the temperature drops below 50 K (Figure 4.5); and a subtle increase in the HWHM for ^{121}Sb (Figure 4.9). Collectively, these results suggest the presence of a distinct phase transition occurring around 50 K in RbV_3Sb_5, similar to previous findings in CsV_3Sb_5.

Hole-Electron doped Kagome materials

Regarding the ^{121}Sb NQR measurements on Sn and Te-doped CsV_3Sb_5 at room temperature, focusing on two different dopant concentrations ([Sn] = 0.05 and [Te] = 0.04) in comparison to the undoped CVS. Our results give evidence that both dopants occupy the Sb1 sites within the kagome plane, as indicated by the shift in NQR peaks (Figure 4.12 and Figure 4.13). Electron-doping through Te-substitution in CsV_3Sb_5 preserves the Charge Density Wave (CDW) state. Conversely, hole-doping with Sn-dopant seems to quickly suppress long-range CDW order, as summarised in Figure 4.11. These results are published in refs. [101] and [102].

Our ^{121}Sb NQR measurements are in agreement with magnetization data in determining the CDW transition temperature for undoped CVS and lightly doped CVS-Te04 (Figure 4.15). In addition, NQR is very sensitive to detect the transition width, displaying that CDW and normal phases coexist for about 10 K, phase separated (Figure 4.14). These results show that ^{121}Sb NQR is a very powerful tool to characterize at the microscopic level the CDW phase transition in these kagome materials.

ZF-μSR measurements on CVS-Te08, Sn08, and Sn35, show only marginal and weak features at the CDW transition but a clear upturn of the muon depolarization rate at T_x (< 50 K), as it can be seen in Figure 5.2 and Figure 5.3. The latter suggests the presence of anomalous behaviour that might be related to nematicity and/or the presence of spontaneous orbital currents and/or local charge reorganisation. Further analysis and measurements are needed to identify the proper mechanism. However, our results indicate that the anomalous low-T phase is ubiquitous in the phase diagram, possibly also when CDW is suppressed, and doping-dependent (Figure 5.2 and Figure 5.3 in Chapter 5).

Muon-nuclei entanglement as a probe for charge-related phenomena

We have presented experimental evidence of coherent oscillations in the μSR spectra of A15 superconductors (Figure 6.2), arising from quantum entanglement between quadrupolar nuclei and muons. We achieved an accurate description of the μSR spectra and modeled the charge distribution using DFT-based simulations and solving free-parameter Hamiltonian. The results are published in papers [153] and [110]. This study gives a concept of proof that μSR can be used not only as a quantum sensing probe for magnetism but also for charge-related phenomena. This approach will also be used to study the anomalies found in the low-T regime of the CDW phase of kagome materials.

Study of the magnetic state of Kitaev antiferromagnet Na_2PrO_3

We studied the magnetic properties of Na_2PrO_3 which is supposed to have dominant antiferromagnetic Kitaev interactions. μSR results confirmed the presence of long-range antiferromagnetic (AF) magnetic order below $T_N \simeq 4.9$ K (Figure 7.2), along with some observed magnetic fluctuations. Through a combination of DFT calculations, muon dipolar simulations, and spin-wave simulations, we determined the magnetic structure of Na_2PrO_3, with a small Pr magnetic moment (0.13 μ_B) attributed to quantum fluctuations. This reduction is attributed to the influence of quantum fluctuations, while Kitaev anisotropic interactions are ruled out. Results of model Heisenberg-Kitaev Hamiltonian simulations on the INS data show strong evidence of dominant antiferromagnetic isotropic Heisenberg interactions, suppressing the spin-liquid Kitaev's term. A manuscript with these results is almost ready to be submitted for publication [J. Frassineti, I. J. Onuorah, M. M. Isah, P. Bonfá, J. G. Rau, J. A. Rodriguez-Rivera, A. I. Kolesnikov, S. Sanna, V. F. Mitrović, and K. W. Plumb, *Unraveling the magnetic ground-state in alkali-metal lanthanide oxide* Na_2PrO_3, to appear soon on Arxiv].

Appendix A: theoretical aspects of NMR

7.5 Nuclear Spin Dynamics: Classical Approach

In this first way, the nucleus will be treated as a point-like particle with a fixed spin $S = \hbar I$. The choice simplifies the analysis of the interactions between it and the electromagnetic field. In each charged system, the nuclear spin I is associated with an inherent magnetic dipole moment $\mu = \gamma \hbar I$, where γ is the nuclear gyromagnetic ratio. According to fundamental electromagnetism, applying a static magnetic field B_0 to the system will induce a torque to act on the spin represented by:

$$\tau = \frac{dS}{dt} = \mu \times B_0 \quad \Longrightarrow \quad \frac{d\mu}{dt} = \gamma \mu \times B_0 \tag{7.4}$$

This equation is analogous to the relationship between the derivatives of a vector as observed from two rotating reference frames S and $S^{'}$ with frequency ω rotating with regard to each other:

$$\left(\frac{d\mu}{dt}\right)_{S'} = \left(\frac{d\mu}{dt}\right)_{S} + \mu \times \omega \tag{7.5}$$

Hence, we can treat the dynamics of the magnetic moment from a rotating reference frame S_{ω_0} moving with respect to the laboratory frame S_{lab} at an angular frequency ω_0. In the new rotating frame system, the magnetic moment is static:

$$\begin{aligned} \left(\frac{d\mu}{dt}\right)_{S_{\omega_0}} = \left(\frac{d\mu}{dt}\right)_{S_{lab}} + \mu \times \omega_0 = \mu \times (\gamma B_0 + \omega_0) = 0 \\ \implies \quad \omega_0 = -\gamma B_0 \end{aligned} \tag{7.6}$$

This choice of reference system clearly demonstrates that the motion of a nuclear spin in a uniform magnetic field simply simplifies to μ (and, consequently, I) precession in the direction of B_0 with angular frequency ω_0 (the so-called Larmor frequency). We now introduce a second magnetic field, B_1(t), which spins in the plane perpendicular to B_0 with frequency ω. We may use coordinate axes like $B_0 = B_0 k$ and $B_1(t) = B_1 cos(\omega t) i + B_1 sin(\omega t) j$. This reduces the equation for μ to:

$$\frac{d\mu}{dt} = \gamma\mu \times [B_0 + B_1(t)] \tag{7.7}$$

When this second, rotating magnetic field is present, it is more convenient to move to the reference frame, which rotates together with $B_1(t)$, namely S_ω. We can recast Equation (7.7) to:

$$\left(\frac{d\mu}{dt}\right)_{S_\omega} = \gamma\mu \times \left[\left(B_0 + \frac{\omega}{\gamma}\right) k + B_1 i\right] \tag{7.8}$$

A graphical representation of the rotating frame is shown in Figure 7.8. From Equation (7.8), the magnetic moment μ is subjected to a torque coupled to an effective field B_e in the frame S_ω, which is composed of three contributions:

- the static field B_0 along the axis of rotation and therefore time-constant;
- the static field B_1 in the new frame;
- the fictional field ω/γ.

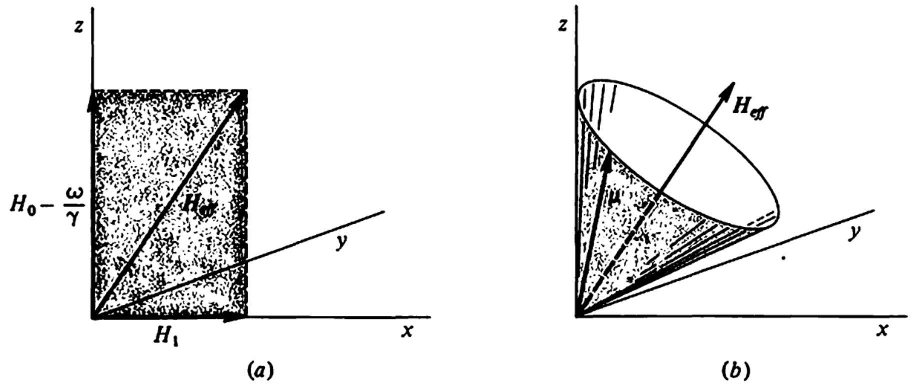

Figure 7.8: a) Effective field and b) motion of μ in the rotating reference system (taken from [64]).

By defining the frequencies $\omega_i = -\gamma B_i$ for i = 0,1, we can express B_e as:

$$B_e = \frac{1}{\gamma}[(\omega - \omega_0)k - \omega_1 i] \tag{7.9}$$

Now we can write the definition of the polar angle θ between B_e and z, characteristic of the precession of μ:

$$tan(\theta) = \frac{\omega_1}{\omega_0 - \omega} sin(\gamma) \tag{7.10}$$

The magnetic moment precedes around the effective field with frequency $a = -sin(\gamma)((\omega - \omega_0)^2 + \omega_1^2)^{\frac{1}{2}}$ in the new frame S_ω, whereas in the lab frame S_{lab}, the trajectory traced by μ is a combination of its motion in S_ω and a rotation around B_0 with frequency ω. The most common case in the bulk of the studies is when $B_1 \ll B_0$. When this condition is met, the polar angle θ is very tiny, and the z component of μ deviates somewhat from its original position. However, if the denominator in Equation (7.10) is extremely small, so $|\omega - \omega_0| < \omega_1$, θ increases and μ can rotate at very large angles in the reference system. To satisfy the second criterion, we must verify that the frequency ω is almost equal to the Larmor frequency ω_0, implying that we are in "resonance" between the spinning and static frequencies.

When the rotating field is removed, the polar angle of the magnetic moment stops changing, and if no relaxation processes occur, μ continues to travel about z at a constant latitude. Adjusting the amplitude of B_1 and the duration of t_P to the appropriate polar angle is possible. In particular, at perfect resonance, the spin's angle of rotation can be readily predicted using the formula:

$$\theta = at_P = -\gamma B_1 t_P \tag{7.11}$$

Figure 7.9 displays the off-resonance and resonance scenarios. When linearly

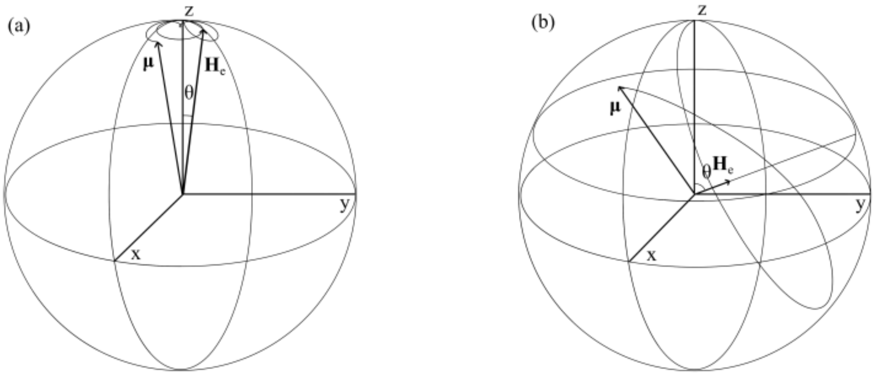

Figure 7.9: Magnetic moment μ trajectories in the laboratory frame, off-resonance (a) and at resonance (b). In (a), $|\omega - \omega_0| \gg \omega_1$ and the effective field B_e are slightly slanted with respect to the z-axis, causing μ to undergo extremely tiny nutations around z. In (b), $|\omega - \omega_0| < \omega_1$ and B_e move closer to the xy plane, causing the magnetic moment to rotate to enormous polar angles (derived from Ref. [67]).

polarized electromagnetic radiation is used, the time-dependent field $B_1(t)$ can be written as:

$$B_1(t) = 2B_1 cos(\omega t) i$$
$$\Downarrow$$
$$B_1^{'}(t) = B_1[cos(\omega t)i + sin(\omega t)j] \qquad B_1^{"}(t) = B_1[cos(-\omega t)i + sin(-\omega t)j] \tag{7.12}$$

With $B'(t)$ in resonance, that is $|\omega - \omega_0| < \omega_1$, then $B"(t)$ will be highly off-resonance, as $|-\omega-\omega_0| \approx 2\omega$, so that the second term can be safely neglected.

7.6 Nuclear Spin Dynamics: Quantum Approach

In this second part, we are going to develop the NMR formalism into its quantum mechanical counterpart. The Hamiltonian of a nuclear spin in a magnetic field is:

$$\mathcal{H} = -B \cdot \mu = -\gamma\hbar B \cdot I \tag{7.13}$$

with the Zeeman energy term as its only constituent. A brief outline of why a conventional method produces exact answers or at least approximate ones, is useful. The Heisenberg equation can be used to express the evolution of a quantum system:

$$\frac{\hbar}{i}\frac{dI}{dt} = [\mathcal{H}, I] = -\gamma\hbar[B \cdot I, I] \tag{7.14}$$

with the z-component defined as:

$$\begin{aligned}\frac{\hbar}{i}\frac{dI_z}{dt} &= -\gamma\hbar\{B_x[I_x, I_z] + B_y[I_y, I_z]\} \\ &= \frac{\hbar}{i}\gamma\{B_y I_x - B_x I_y\} = \frac{\hbar}{i}\gamma(I \times B)_z\end{aligned} \tag{7.15}$$

This is the same as the traditional Equation (7.5) using operators instead of actual functions. The expected values of the μ components, $\langle\mu_x\rangle$,$\langle\mu_y\rangle$, and $\langle\mu_z\rangle$, use the bra-operator-ket product of both sides of Equation (7.15) to obey the classical equations. When we examine the behaviour of a large number of spins' macroscopic magnetization, the expectation value determines the dynamics of the system, and the classical technique may be employed securely. To begin, we define the Schrodinger equation for a nuclear spin under the effects of B_0 and $B_1(t)$ in a microscopic approach to NMR:

$$i\hbar\frac{d\,|\psi\rangle}{dt} = -\gamma\hbar\{B_0 I_z + B_1[I_x cos(\omega t) + I_y sin(\omega t)]\}\,|\psi\rangle \tag{7.16}$$

As an example of a change in the dynamical picture, a much more comprehensive method of recasting a problem in quantum mechanics, we are switching to a rotating reference frame S_ω. This is realised by moving to the R-picture associated with the lab one with frequency $\omega = \omega k$, that is, $R = \hbar\omega I_z$. Given R as time-independent, the transformation is simply:

$$|\psi(t)\rangle \rightarrow |\psi(t)\rangle_R = exp(i\omega I_z t)\,|\psi(t)\rangle \qquad exp(i\omega I_z t) = U^{-1}(t) \tag{7.17}$$

As an example, we can demonstrate this transformation with an eigenvector of the azimuthal angle observable ϕ, $|\phi\rangle$, and apply Equation (7.17). The Fourier spectrum allows for the expansion of this vector [63]:

$$|\phi\rangle = \frac{1}{\sqrt{2\pi}} \sum_m |m\rangle\, e^{-im\phi} \tag{7.18}$$

where m is the eigenvalues and eigenvectors of the momentum conjugate to ϕ, which is precise to be $\hbar I_z = -i\hbar\frac{d}{d\phi}$. Hence, when we move to frame S_ω, we get:

$$e^{i\omega I_z t}\,|\phi\rangle = \frac{1}{\sqrt{2\pi}} \sum_m e^{i\omega I_z t}\,|m\rangle\, e^{-im\phi} = \frac{1}{\sqrt{2\pi}} \sum_m |m\rangle\, e^{-im(\phi-\omega t)} = |\phi - \omega t\rangle \tag{7.19}$$

that, as seen from the rotating reference frame S_ω, is the same vector as $|\phi\rangle$. By expanding this argument on the $|\phi\rangle$ basis, we can generalize it to a generic state vector $|\psi\rangle$. The R-picture Hamiltonian $\mathcal{H}_R$ is

$$\mathcal{H}_R = U^{-1}(t)(\mathcal{H} - R)U(t) \tag{7.20}$$

The Hamiltonian of the system $\mathcal{H}$ shown in Equation (7.16) can be expressed in a more convenient way:

$$\mathcal{H} = \hbar\omega_0 I_z + \frac{1}{2}\hbar\omega_1\big(I_+ e^{-i\omega t} + I_- e^{i\omega t}\big) \tag{7.21}$$

where $I_\pm = I_x \pm \mathrm{i} I_y$ are the raising and lowering operators of the nuclear spin. The calculated R-picture is:

$$\mathcal{H}_R = \hbar(\omega_0 - \omega)I_z + \hbar\omega_1 I_x \tag{7.22}$$

As the new Hamiltonian is time-independent (as predicted), we can easily express the solution to the R-picture Schrodinger equation:

$$|\psi(t)\rangle_R = exp\{-i[(\omega_0 - \omega)I_z + \omega_1 I_x]t\} \, |\psi(0)\rangle_R \tag{7.23}$$

This is how the precession of μ around the effective field B_e is expressed in quantum mechanics. Returning to the lab frame, the state vector's evolution is provided by:

$$|\psi(t)\rangle = U(t)\,|\psi(t)\rangle_R = exp(-i\omega I_z t)exp\{-i[(\omega_0 - \omega)I_z + \omega_1 I_x]t\}\,|\psi(0)\rangle \tag{7.24}$$

where, $exp(-i\omega I_z t) = B_0$ and $exp\{-i[(\omega_0 - \omega)I_z + \omega_1 I_x]t\}\,|\psi(0)\rangle = B_1$. We used the fact that $|\psi(0)\rangle_R = |\psi(0)\rangle$ (for $t = 0$, S_{lab} and S_{omega} coincide). Redefining a and θ as:

$$a = \left((\omega_0 - \omega)^2 + \omega_1^2\right)^{\frac{1}{2}} \qquad n = (sin\theta, 0, cos\theta) = (\frac{\omega_1}{a}, 0, \frac{\omega_0 - \omega}{a}) \tag{7.25}$$

Equation (7.24) can be rewritten as:

$$|\psi(t)\rangle = exp(-i\omega I_z t)exp\{-ia(n \cdot I)t\}\,|\psi(0)\rangle \tag{7.26}$$

Although these formulas and their classical counterparts share many similarities, we must interpret them in a quantum-appropriate manner. Because the Cartesian components of the magnetic moment μ are incompatible observables in the quantum treatment, the exact direction of this vector cannot be determined. Otherwise, the system's state is represented by a wave function, which only provides an approximation of the probability distribution for any value selected from one of the three μ components. We cannot predict the orientation of μ with certainty at any moment, as we could in classical conditions, because the z component changes when a rotation field B_1 is applied. These transitions' probabilities and amplitudes are determined by:

$$\begin{aligned} A_{m'm}(t) &= \langle m'|\,\psi(t)\,|m\rangle = \langle m'|\,exp(-i\omega I_z t)exp\{-ia(n \cdot I)t\}\,|m\rangle \\ P_{m'm}(t) &= |\langle m'|\,exp\{-ia(n \cdot I)t\}\,|m\rangle|^2 \end{aligned} \tag{7.27}$$

where $A_{m'm}(t)$ denotes the amplitude and $P_{m'm}(t)$ the probability of transitioning from the state $|m\rangle$ to the state $|m'\rangle$. The probability of transition between states $m = \frac{1}{2}$ and $m = -\frac{1}{2}$ in a spin 1/2 nucleus is now considered. We already know that such a system has the equation $I = \frac{1}{2}\sigma$, where $\sigma = (\sigma_x, \sigma_y, \sigma_z)$ are the Pauli matrices. They follow:

$$\begin{aligned} (n \cdot \sigma)^{2p} = 1 \Rightarrow (n \cdot \sigma)^{2p+1} = (n \cdot \sigma) \\ \Rightarrow exp\{-ia(n \cdot I)t\} = cos(\frac{1}{2}at) - i(n \cdot \sigma)sin(\frac{1}{2}at) \end{aligned} \tag{7.28}$$

which implies:

$$\begin{aligned} P_{-\frac{1}{2},\frac{1}{2}} &= \left| \left\langle -\frac{1}{2} \right| cos(\frac{1}{2}at) - i(cos\theta\sigma_z + sin\theta\sigma_x)sin(\frac{1}{2}at) \left| \frac{1}{2} \right\rangle \right|^2 \\ &= sin^2\theta sin^2(\frac{1}{2}at) \end{aligned} \tag{7.29}$$

The outcome of Equation (7.29), also known as Rabi oscillations in quantum theory, clearly shows that the transition probability of the spin oscillates as the electromagnetic pulse progresses and that the frequency ω, through the angle θ, determines the magnitude of this oscillatory motion. A graphical representation is shown in Figure 7.10. This switches μ between the two oppos-

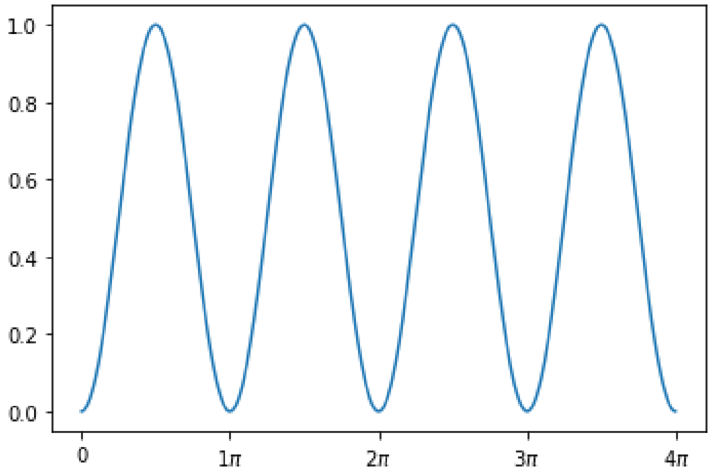

Figure 7.10: Rabi oscillation between the two energy levels of a spin-1/2 system.

ing orientations $m = \frac{1}{2}$ and $m = -\frac{1}{2}$ with frequency $a = |\omega_1| = |\theta B_1|$. When the resonance condition $\omega = \omega_0$ is precisely satisfied, θ becomes $\frac{\pi}{2}$.

7.7 Introduction to spin relaxation and Bloch Equations

In NMR spectroscopy, a homogeneous magnetic field produces a measurable nuclear spin polarization (magnetization). The magnetic dipole moments of the sample precess around the static field B_0 at the nuclei's resonance (Larmor) frequency ω. Nuclear spins randomly precess in the applied field while the system is in thermal equilibrium. They are phase coherent after being impacted by *rf* pulses produced orthogonally to the field's resonance frequency. The *rf* pulses cause the spin-state population to deviate from its thermal equilibrium value. The resulting transverse magnetization is then utilized to trigger a signal in an *rf* coil, which may subsequently be picked up and amplified by an *rf* receiver. Because we know that μ is the magnetic moment created by nuclear spin, the total magnetization of the sample is $M = \frac{N\langle\mu\rangle}{V}$, where N is the number of nuclei that undergo a transition per unit of time and V is the volume. We also know from the theory that $B(t) = \mu M(t)$.

In this part, we will introduce the reservoir concept, which may be thought of as the environment around the spin ensemble that can absorb the energy transmitted during an alternating field's de-excitation. The number of spins N in a spin-1/2 system is always constant, but the spin populations in the two independent m states +1/2 and -1/2, indicated by the symbols N_+ and N_-, will fluctuate due to the transitions generated by the alternating field B_1. At thermal equilibrium, the magnetization along z corresponds to a constant quantity M_0, and once the perturbing oscillating field is applied, it will recover that value in a characteristic time value based on the relaxation processes present. Thus:

$$\frac{dM_z}{dt} = \frac{M_0 - M_z(t)}{T_1} \tag{7.30}$$

Adding the term due to the torque caused by the magnetic field B_0, we obtain:

$$\frac{dM_z(t)}{dt} = \gamma(M(t) \times B(t))_z - \frac{M_z(t) - M_0}{T_1} \tag{7.31}$$

We may construct the equations for the x and y components of magnetization in the same way that we did for Equation (7.31). In this situation, M is totally precessing along the z axis at thermal equilibrium, therefore, there are no initial components for M_x and M_y (they're null at $t = 0$). After applying B_1, the magnetization will contain x and y components that are not zero (see Figure 7.9(b)), which will decay to zero. As a result, unlike M_z, the x and y components of M are predicted to evaporate after a specific time period. We may calculate the magnetization per unit time in the rotating frame using relaxation effects like:

$$\begin{aligned} \frac{dM_x(t)}{\delta t} &= \gamma(M(t) \times B(t))_x - \frac{M_x(t)}{T_2} \\ \frac{dM_y(t)}{\delta t} &= \gamma(M(t) \times B(t))_y - \frac{M_y(t)}{T_2} \end{aligned} \tag{7.32}$$

Equation (7.31) and Equation (7.32) are the so-called Bloch Equations, named after Felix Bloch, who first proposed them. Two common decays are introduced here: the spin-lattice relaxation time (T_1) and the spin-spin relaxation time (T_2). Changes in the population of Zeeman levels that can occur after the energy exchange with the lattice excitations are directly related to T_1 since they demonstrate the temporal development of M_z. Energy must be transferred throughout this process, necessitating contact with the reservoir. In addition to those involved in spin-lattice relaxation that does not include an energy exchange with lattice excitations, the decay of M_x, y in time T_2 is influenced by a number of processes. The T_2 time scale is frequently much faster than the T_1 time scale since the latter does not need an energy exchange.

7.8 Derivation of quadrupolar Hamiltonian

Let us now examine the structure of the nucleus in further detail. We may think of it as a collection of A point-like nucleons, either protons or neutrons, for our purposes. As a result, the general wavefunction of the system will be of the type $\psi_n\ (R_1, ..., R_A)$, and the charge density may be calculated as:

$$\rho_n(r_n) = \langle\psi_n| \sum_{i=1}^{A} e_i\delta(r_n - R_i) |\psi_n\rangle \tag{7.33}$$

After some calculations [63, 64], A_l^m (and similarly B_l^m, can be written as: $\langle\psi_n| A_l^m |\psi_n\rangle$ ($\langle\psi_n| B_l^m |\psi_n\rangle$, where A_l^m (B_l^m) is the nuclear (electronic) operator:

$$\begin{aligned} \mathcal{A}_l^m =& \big(\frac{4\pi}{2l+1}\big)^{\frac{1}{2}} \sum_{i=1}^{A} e_i R_i^l Y_l^m(\Theta_i, \Phi_i) \\ \mathcal{B}_l^m =& -e\big(\frac{4\pi}{2l+1}\big)^{\frac{1}{2}} \sum_{i=1}^{Z} r_i^{-(l+1)} Y_l^m(\theta_i, \phi_i) \end{aligned} \tag{7.34}$$

where (R_i, Θ_i, Φ_i) represents the spherical coordinates of each nucleon (electron). In the first equation, A represents the total number of nucleons, whereas Z represents the atomic number. The energy of the electrostatic interaction is determined by the expected value of the Hamiltonian on the state of the entire atomic system, which is as follows:

$$\begin{aligned} \mathcal{H}_E &= \sum_{l,m} \mathcal{A}_l^m \mathcal{B}_l^{m*} \\ W_E &= \langle\psi_n| \langle\psi_e| \mathcal{H}_E |\psi_e\rangle |\psi_n\rangle \end{aligned} \tag{7.35}$$

The components of a rank l tensor operator with reference to angular momentum, represented as A_l, are the set of $2l + 1$ operators A_l^m, $m = -l, -l + 1, ..., l - 1, l$. This tensor operator is known as the nucleus's multipole moment of order l. Another significant aspect is that ${}^A m_l$ disappears for all odd values of l. Furthermore, Equation (2.5)'s integrand is an odd function that integrates to 0 for all odd values of l.

The Wigner-Eckart theorem adds additional constraints to non-vanishing tensor operators A_l. Tensors A_l of rank l must satisfy the criterion $0 \leq l \leq 2I$ to have non-zero matrix elements between nuclear states $|I, I_z\rangle$. Finally, static nuclear spins I allow only multipole moments with even ordering l up to $2I$. A spin $I = 1$ nucleus, for example, has an electric monopole ($l = 0$), which is the nucleus' whole charge concentrated in one spot, an electric quadrupole ($l = 2$), and no electric dipole moment. The energy of the nuclear monopole is a constant that may be ignored because nuclei are assumed to be fixed in our discussion. As a result, we'll focus on the quadrupole interaction, which has been proven to be the most important contributor of energy due to electrostatic coupling. Setting $l = 2$ we obtain the expression of the components of $\mathcal{A}_2^m$ we obtain:

$$\begin{aligned}
\mathcal{A}_2^{\pm 2} &= \frac{\sqrt{6}}{4} \sum_{i=1}^{A} e_i (x_i \pm i y_i)^2 \\
\mathcal{A}_2^{\pm 1} &= \frac{\sqrt{6}}{2} \sum_{i=1}^{A} e_i z_i (x_i \pm i y_i) \\
\mathcal{A}_2^{0} &= \frac{1}{2} \sum_{i=1}^{A} e_i (3z_i^2 - r_i^2)
\end{aligned} \tag{7.36}$$

The primary issue with these formulae is that they express the components of $\mathcal{A}_2$ as nucleon position functions. We may use the Wigner-Eckart theorem again, knowing that $\mathcal{A}_2$ is proportional to any other rank 2 tensor operator. As a consequence, we may define Equation (7.36) in terms of I.

$$\begin{aligned}
\mathcal{Q}^{\pm 2} &= \alpha \frac{\sqrt{6}}{4} (I_\pm)^2 \\
\mathcal{Q}^{\pm 1} &= \alpha \frac{\sqrt{6}}{4} (I_z I_\pm + I_\pm I_z) \\
\mathcal{Q}^{0} &= \frac{\alpha}{2} (3I_z^2 - I(I+1))
\end{aligned} \tag{7.37}$$

α is the proportionality factor acquired from $\mathcal{A}_2^0$ and $\mathcal{Q}^0$ having the same expectation value in state $|I, I\rangle$:

$$\langle I, I| \mathcal{A}_2^0 |I, I\rangle = \langle I, I| \mathcal{Q}^0 |I, I\rangle \equiv \frac{eQ}{2} \tag{7.38}$$

Going on, we have:

$$2\left\langle I,I\right|\mathcal{Q}^0\left|I,I\right\rangle=\alpha\left\langle I,I\right|3I_z^2-i(I+1)\left|I,I\right\rangle\quad\text{with }\ \alpha=\frac{eQ}{I(2I-1)}\tag{7.39}$$

We can expand $\mathcal{B}_2$ similarly to $\mathcal{A}_2$. Hence, we have:

$$\begin{aligned}\mathcal{B}_2^0&=\frac{e}{2}\sum_{i=1}^{Z}\frac{(3z_i^2-r_i^2)}{r_i^5}=\frac{1}{2}\Big(\frac{\delta^2\mathcal{V}}{\delta z^2}\Big)_{r=0}=\frac{1}{2}\mathcal{V}_{zz}\\ \mathcal{B}_2^{\pm2}&=\frac{1}{2\sqrt{6}}(\mathcal{V}_{xx}-\mathcal{V}_{yy}+2i\mathcal{V}_{xy})\\ \mathcal{B}_2^{\pm1}&=\frac{1}{\sqrt{6}}(\mathcal{V}_{xz}+i\mathcal{V}_{yx})\end{aligned}\tag{7.40}$$

where $\mathcal{V}(x,y,z)$ denotes the electrostatic potential operator as a function of the z electron position operators. We can see that $\mathcal{B}_2^{m*}=\mathcal{B}_2^{-m}$. As a result, the Hamiltonian of the quadruple interaction is:

$$\mathcal{H}_2=\sum_{m=-2}^{2}\mathcal{Q}_2^m\mathcal{B}_2^{-m}\sum_{j,k}\Big(\frac{\delta^2\mathcal{V}}{\delta x_j\delta x_k}\Big)_{r=0}\mathcal{Q}_{j,k}\tag{7.41}$$

where:

$$\mathcal{Q}_{j,k}=\frac{eQ}{6I(2I-1)}\Big[\frac{3}{2}(I_jI_k+I_kI_j)-\delta_{jk}I(I+1)\Big]\tag{7.42}$$

is an alternate representation of the cartesian tensor operator, and $\big(\frac{\delta^2\mathcal{V}}{\delta x_j\delta x_k}\big)_{r=0}$ is called the Electric Field Gradient (EFG) at the origin. From further assumptions in bulk matter, we get:

$$\begin{aligned}V^0&=\frac{1}{2}V_{zz}=\frac{1}{2}\left\langle\mathcal{V}_{zz}\right\rangle\\ V^1&=\frac{1}{\sqrt{6}}(\left\langle\mathcal{V}_{xz}\right\rangle\pm i\left\langle\mathcal{V}_{yz}\right\rangle)\\ V^2&=\frac{1}{2\sqrt{6}}(\left\langle\mathcal{V}_{xx}\right\rangle-\left\langle\mathcal{V}_{yy}\right\rangle\pm 2i\left\langle\mathcal{V}_{xy}\right\rangle)\end{aligned}\tag{7.43}$$

7.9 Quadrupolar energy spectrum in zero-field

To generalize our analysis to the case of an asymmetric electric field gradient ($\eta \neq 0$), it is convenient to distinguish between instances where I is an integer or a half-integer. We will just emphasise the results of the computations that may be found in [63] in the following.

- *Integer spins*: Let us assume to have a $I = 1$ nucleus. The whole Hilbert space may be divided into three 1-dimensional subspaces, each spanned by:
  - the unique odd state $|\xi_-\rangle = \frac{|1\rangle - |-1\rangle}{\sqrt{2}}$;
  - the even state $|0\rangle$;
  - the even state $|\xi_+\rangle = \frac{|1\rangle + |-1\rangle}{\sqrt{2}}$;

  Because the final two differ by $\Delta m = 1$, they cannot be connected by $\mathcal{H}$, and hence each of these subspaces is an eigenspace of the Hamiltonian for the reasons stated above. The associated eigenvalues are as follows:

  $$E_0 = -\frac{1}{2}e^2qQ \qquad E_{\xi\pm} = \frac{1}{4}e^2qQ(1 \pm \eta) \tag{7.44}$$

  Because the asymmetry of the gradient accounts for the splitting of $E_{\xi\pm}$ in the energy spectrum, the presence of $\eta \neq 0$ may be determined by counting the number of spectral lines and determining whether the degeneracy of the m states is lifted.

- *Half-integer spin*: Even if the states $|m\rangle$ are no longer eigenstates when the nuclear spin is half integer, the asymmetry η is incapable of overcoming the degeneracy of the energy levels $E_{\pm m}$. The experimental analysis of a nucleus with unknown properties is complicated by the remaining degeneracy of quadrupolar states. It is difficult, for example, to tell whether a nucleus with spin $I = 3/2$ has $\eta \neq 0$ by measuring its unique resonance frequency $\nu_{3/2}$. Indeed, the expression for this latter in the asymmetric situation is:

$$\nu_{3/2} = \frac{e^2qQ}{2h}(1 + \frac{1}{3}\eta^2)^{\frac{1}{2}} \tag{7.45}$$

The role of the asymmetry parameter is that it induces the change in energy eigenstate $|m\rangle \rightarrow |\tilde{m}\rangle$, which implies that the selection rule $\Delta m = \pm 1$ is no longer effective. With an asymmetric electric field gradient, transitions like $\left|\tilde{\frac{5}{2}}\right\rangle \leftrightarrow \left|\tilde{\frac{1}{2}}\right\rangle$ may be allowed.

Appendix B: μ^+-nuclei interaction

Here, we report some supplementary theoretical aspects of the interactions between nuclei and muons.

7.10 Quantum description of μ^+ interaction with nuclei

This subsection describes the interaction between the positive muon μ^+ and a general nucleus from a quantum theoretical point of view. Let's start with introducing the total Hamiltonian $\mathcal{H}^{tot}$ [81] of a generic system:

$$\mathcal{H}^{tot} = \sum_{j=1}^{N} \left(\mathcal{H}_j^D + \mathcal{H}_j^Q + \mathcal{H}_Z \right) \tag{7.46}$$

In which the positive muon with spin $S_{\mu^+} = 1/2$ interacts with the surrounding j-th nucleus with spin I through dipolar and quadrupolar interactions, as well as the Zeeman interaction with the applied external magnetic field B.

The dipolar interaction generated by the spin of the muon S and the j-th nucleus spin I is accounted for by the dipolar term $\mathcal{H}_j^D$:

$$\mathcal{H}_j^D = \frac{\hbar^2 \gamma_{\mu^+} \gamma_j}{r_j^3} \left[\mathbf{S}_{\mu^+} \cdot \mathbf{I_j} - 3 \left(\mathbf{S}_{\mu^+} \cdot \mathbf{n_j} \right) \left(\mathbf{I_j} \cdot \mathbf{n_j} \right) \right] \tag{7.47}$$

where γ_{μ^+} and γ_j are the gyromagnetic ratios of the positive muon and of the j-th spin, r_j is the distance between the two and n_j is the unit vector indicating the direction connecting the two particles. This dipolar term is the same one described in Section 2.1.5 for NMR. This interaction is always present in a crystal and is responsible for the classic Kubo-Toyabe behavior, described in Equation (3.8) and shown in Figure 3.5(b).

The Zeeman term $\mathcal{H}_Z$ accounts for the interactions between the muon and the j-th nucleus with an applied external magnetic field B:

$$\mathcal{H}_Z = -\hbar\gamma_\mu \mathbf{S}_{\mu^+} \cdot \mathbf{B} - \sum_{j=1}^{N} \hbar\gamma_j \mathbf{I_j} \cdot \mathbf{B} \tag{7.48}$$

The sum is over all the nuclei present for the part involving the crystal nuclei. The quadrupolar term $\mathcal{H}_Q$ acts as a perturbation of the Zeeman term $\mathcal{H}_Z$, and its definition is the same of Section 2.1.4. In the Principal Axis System frame of the EFG tensor, $\mathcal{H}_j^Q$ is relatively simple, and we report the definition for clarity:

$$\begin{aligned}\mathcal{H}_j^Q &= \frac{eQ_jV_j^{zz}}{4I_j\left(2I_j-1\right)}\left[\left[3\left(I_j^z\right)^2-\left(I_j\right)^2\right]+\eta_j\left[\left(I_j^x\right)^2-\left(I_j^y\right)^2\right]\right] \\ &= \hbar\omega_E\left[\left[3\left(I_j^z\right)^2-\left(I_j\right)^2\right]+\eta_j\left[\left(I_j^x\right)^2-\left(I_j^y\right)^2\right]\right]\end{aligned} \tag{7.49}$$

The quantity Q_j is the quadrupole moment of nucleus j and $\hbar\omega_E$, which is proportional to Q_j, sets the energy scale of the quadrupole interaction energy.

The positive muon and the crystal can both generate the electric field gradient. One rough assumption that can be made, that is valid for certain situations is that the muon, assumed as a point charge in a vacuum, induces an EFG whose principal component $V_{\mu^+}^{zz}$ is equal to, at a distance r:

$$V_{\mu^+}^{zz} = \frac{2}{4\pi\epsilon_0}\frac{e}{r^3} \tag{7.50}$$

where e is the elementary charge and $\epsilon_0 = 8.85 \times 10^{-12} F/m$ is the dielectric constant of the vacuum. The EFG of the crystal is determined by the system's symmetry as well as the atomic chain placement. The two tensors, the crystal's EFG tensor, and the muon's EFG tensor can combine to generate a single EFG tensor, which enters into Equation (7.49). Because the muon has a spin of 1/2 and lacks a quadrupole moment, it cannot interact with the crystal's surrounding EFG. Despite this, the quadrupolar term of the Hamiltonian of the environment changes the energy levels of the neighboring nuclei, so the muon experiences a *indirect* interaction with the quadrupolar term of the system, which can lead to visible coherent oscillations in the polarisation spectra in some cases [110] even in the absence of local magnetic moments. Nowadays, more accurate methods to determine the EFG induced by the muon in a perturbed crystal are available, such as the ab-initio DFT+μ method, which combines Density Functional Theory ab-initio calculations with the presence of a perturbing particle as the positive muon. Accurate results of its application can be found in Ref. [110].

The key challenge is to solve the whole Hamiltonian $\mathcal{H}_{tot}$ throughout time evolution to obtain the muon depolarization. To achieve this, we must first diagonalize the total Hamiltonian and find the related eigenvalues and eigenvectors. Celio [152] presented an approach that employs the Trotter formula for limited operators and a random-phase assumption about the starting state of the host spin system. We are interested in the time dependence of the muon polarization, which is determined by:

$$P(t) = Tr\left[\rho \exp\left(i\mathcal{H}^{tot}t/\hbar\right)\sigma_\mu \exp\left(-i\mathcal{H}^{tot}t/\hbar\right)\right] \tag{7.51}$$

where $\sigma_\mu = 2\mathbf{S}_\mu$ are the Pauli matrices. For a muon initially polarized along the z-axis and for unpolarized nuclei, the density matrix ρ is given by:

$$\rho = \frac{1}{2}\left(2I+1\right)^{-N}\left(1+\sigma_\mu^z\right) \tag{7.52}$$

Because the various Hamiltonian operators $\mathcal{H}_j$ do not commute, an analytical solution to Equation (7.51) is not achievable in general. The eigenvalues and eigenvectors of $\mathcal{H}_{tot}$ can be used to find a numerical solution; however, if we assume to have identical nuclei in the sample with spin I, this technique is only applicable when the size d of the composite Hilbert space ($d = 2(2I + 1)^N$) is not too big. To solve this problem, we can utilize the generalized Trotter formula for bounded operators [188] to solve Equation (7.51). For a set of n bounded operators $A_j (j = 1, ..., N)$, one can show that:

$$\exp{(A_1 + A_2 + ... + A_n)} = \lim_{k\to\infty} \left[\exp{(A_1/k)} \exp{(A_2/k)} ... \exp{(A_n/k)}\right]^k \tag{7.53}$$

This means that instead of diagonalizing a single but very large matrix (Equation (7.51)) $\mathcal{H}$, one has just to diagonalize N small matrices $\mathcal{H}_j$. The Celio approach described above has been implemented in *UNDI* [153], a Python tool built by Dr. Pietro Bonfà at the University of Parma, Italy, for simulations of muon polarisation. This Python library allows users to model dipolar and quadrupolar interactions between muons and nuclei in various systems. It employs typical Python scientific libraries such as Numpy, Matplotlib and Qutip.

Appendix C: POCSI (POint Charge SImulation of electric field gradient)

```
# -*- coding: utf-8 -*-
"""
@author: Jonathan Frassineti
"""

"""
In this file, the functions that calculate and diagonalize
    the EFG are defined.
"""

import numpy as np

atomic_EFG = - 9.71736166e21 # V/(m^2), atomic unit of EFG
angtom = 1.0e-10 # Angstrom unit of measure
elementary_charge = 1.6021766e-19 # Coulomb = ampere second
epsilon0 = 8.8541878e-12 # dielectric constant of the vacuum
h = 6.6260693e-34 # J s
hbar = h/(2*np.pi) # J s

def point_charge_EFG(pos, base, lattice_a, lattice_b,
    lattice_c, quadrupole_moment, s=15, impurity = False, xxx
    = [], shifts = [], base_shifted = []):
     """This function calculates the point charge EFG for a
    given nucleus in a specific position in the lattice
```

```
structure.

 Parameters
     pos: position of the nucleus in which the user wants to calculate the EFG from point charge.

     s: the number of real space vectors from the origin that build the crystalline structure, starting from the basis;
     greater the 's', more accurate the calculation, but also much slower.

     base: atomic base of the material under study.

     lattice_a/b/c: lattice parameters a, b and c of the crystal, in Angstrom.

     quadrupole_moment: the quadrupole moment of the nucleus in which calculating the EFG.

     impurity = False: if True, add the possibility to add an impurity, or vacancy, or an additional particle
     (such as a positive muon) inside the crystal, to obtain the EFG with this perturbation.
     This part is currently under improvement (use with caution!).

     xxx = []: if impurity = True, define the position of the impurity (as in the 'base' parameter').

     shifts = []: if impurity = True, defines the displacement of each nearest neighbour atom of the nucleus under study.

     base_shifted = []: if impurity = True, defines the atomic base of N nearest neighbours
     (for this version, only 4 considered) as for the 'base' parameter

```

```
        Returns:
        The point charge EFG of the nucleus under study.

    """
    a1 = np.array([lattice_a, 0, 0])
    a2 = np.array([0, lattice_b, 0])
    a3 = np.array([0, 0, lattice_c])

    if impurity == True:
        for i in range(len(pos)):
            pos[i] *= shifts[i]

        v = np.zeros((3, 3), dtype='float64')

        for u1 in range(-s, s + 1):

            for u2 in range(-s, s + 1):

                for u3 in range(-s, s + 1):

                    for k in range(len(base)):

                        if ((u1 ==  0) and (u2 == -1) and (u3 ==  0) and (k == 0)):
                            continue
                        if ((u1 == -1) and (u2 == -1) and (u3 ==  0) and (k == 1)):
                            continue
                        if ((u1 ==  0) and (u2 ==  0) and (u3 == -1) and (k == 4)):
                            continue
                        if ((u1 ==  0) and (u2 ==  0) and (u3 ==  0) and (k == 5)):
                            continue

                        D = np.zeros(3, dtype='float')
                        D[0] = u1 + base[k, 0]
                        D[1] = u2 + base[k, 1]
                        D[2] = u3 + base[k, 2]
```

```

                    if ((D[0] == pos[0]) and (D[1] == pos[1]) and (D[2] == pos[2])): continue

                    r_k = np.zeros(3, dtype='float')

                    r_k[0] = (D[0] - pos[0]) * a1[0] + (D[1] - pos[1]) * a2[0] + (D[2] - pos[2]) * a3[0]
                    r_k[1] = (D[0] - pos[0]) * a1[1] + (D[1] - pos[1]) * a2[1] + (D[2] - pos[2]) * a3[1]
                    r_k[2] = (D[0] - pos[0]) * a1[2] + (D[1] - pos[1]) * a2[2] + (D[2] - pos[2]) * a3[2]

                    rr = r_k[0] * r_k[0] + r_k[1] * r_k[1] + r_k[2] * r_k[2]

                    v[0, 0] += base[k, 3] * base[k, 4] * (3 * r_k[0] * r_k[0] - rr) / pow(rr, 2.5)
                    v[0, 1] += base[k, 3] * base[k, 4] * (3 * r_k[0] * r_k[1]) / pow(rr, 2.5)
                    v[0, 2] += base[k, 3] * base[k, 4] * (3 * r_k[0] * r_k[2]) / pow(rr, 2.5)
                    v[1, 1] += base[k, 3] * base[k, 4] * (3 * r_k[1] * r_k[1] - rr) / pow(rr, 2.5)
                    v[1, 2] += base[k, 3] * base[k, 4] * (3 * r_k[1] * r_k[2]) / pow(rr, 2.5)
                    v[2, 2] += base[k, 3] * base[k, 4] * (3 * r_k[2] * r_k[2] - rr) / pow(rr, 2.5)


    for k in range(len(base_shifted)):

        D = np.zeros(3, dtype = 'float')
        D[0] = base_shifted[k,0];
        D[1] = base_shifted[k,1];
        D[2] = base_shifted[k,2];

        if ((D[0] == pos[0]) and (D[1] == pos[1]) and (D[2] == pos[2])): continue
```

```

        r_k = np.zeros(3, dtype = 'float')

        r_k[0] = ( D[0] - pos[0] )*a1[0] + (D[1] - pos[1])*a2[0] + (D[2] - pos[2])*a3[0];
        r_k[1] = ( D[0] - pos[0] )*a1[1] + (D[1] - pos[1])*a2[1] + (D[2] - pos[2])*a3[1];
        r_k[2] = ( D[0] - pos[0] )*a1[2] + (D[1] - pos[1])*a2[2] + (D[2] - pos[2])*a3[2];

        rr = r_k[0]*r_k[0]+r_k[1]*r_k[1]+r_k[2]*r_k[2]

        v[0,0] += base_shifted[k,3] * base_shifted[k,4]*(3*r_k[0]*r_k[0] - rr) / pow(rr,2.5);
        v[0,1] += base_shifted[k,3] * base_shifted[k,4]*(3*r_k[0]*r_k[1]) / pow(rr,2.5);
        v[0,2] += base_shifted[k,3] * base_shifted[k,4]*(3*r_k[0]*r_k[2]) / pow(rr,2.5);
        v[1,1] += base_shifted[k,3] * base_shifted[k,4]*(3*r_k[1]*r_k[1] - rr) / pow(rr,2.5);
        v[1,2] += base_shifted[k,3] * base_shifted[k,4]*(3*r_k[1]*r_k[2]) / pow(rr,2.5);
        v[2,2] += base_shifted[k,3] * base_shifted[k,4]*(3*r_k[2]*r_k[2] - rr) / pow(rr,2.5);

    D = np.zeros(3, dtype = 'float')
    D[0] = xxx[0];
    D[1] = xxx[1];
    D[2] = xxx[2];

    r_k = np.zeros(3, dtype = 'float')

    r_k[0] = ( D[0] - pos[0] )*a1[0] + (D[1] - pos[1])*a2[0] + (D[2] - pos[2])*a3[0];
    r_k[1] = ( D[0] - pos[0] )*a1[1] + (D[1] - pos[1])*a2[1] + (D[2] - pos[2])*a3[1];
    r_k[2] = ( D[0] - pos[0] )*a1[2] + (D[1] - pos[1])*a2[2] + (D[2] - pos[2])*a3[2];

```

```
        rr = r_k[0]*r_k[0]+r_k[1]*r_k[1]+r_k[2]*r_k[2]

        v[0,0] += xxx[3] * xxx[4] *(3*r_k[0]*r_k[0] - rr) / pow(rr,2.5);
        v[0,1] += xxx[3] * xxx[4] *(3*r_k[0]*r_k[1]) / pow(rr,2.5);
        v[0,2] += xxx[3] * xxx[4] *(3*r_k[0]*r_k[2]) / pow(rr,2.5);
        v[1,1] += xxx[3] * xxx[4] *(3*r_k[1]*r_k[1] - rr) / pow(rr,2.5);
        v[1,2] += xxx[3] * xxx[4] *(3*r_k[1]*r_k[2]) / pow(rr,2.5);
        v[2,2] += xxx[3] * xxx[4] *(3*r_k[2]*r_k[2] - rr) / pow(rr,2.5);


    else:
        v = np.zeros((3, 3), dtype='float64')

        for u1 in range(-s, s + 1):

            for u2 in range(-s, s + 1):

                for u3 in range(-s, s + 1):

                    for k in range(len(base)):

                        D = np.zeros(3, dtype='float')
                        D[0] = u1 + base[k, 0]
                        D[1] = u2 + base[k, 1]
                        D[2] = u3 + base[k, 2]

                        if ((D[0] == pos[0]) and (D[1] == pos[1]) and (D[2] == pos[2])): continue

                        r_k = np.zeros(3, dtype='float')

                        r_k[0] = (D[0] - pos[0]) * a1[0] + (D[1] - pos[1]) * a2[0] + (D[2] - pos[2]) * a3[0]
```

```
                        r_k[1] = (D[0] - pos[0]) * a1[1] + (D[1] - pos[1]) * a2[1] + (D[2] - pos[2]) * a3[1]
                        r_k[2] = (D[0] - pos[0]) * a1[2] + (D[1] - pos[1]) * a2[2] + (D[2] - pos[2]) * a3[2]

                        rr = r_k[0] * r_k[0] + r_k[1] * r_k[1] + r_k[2] * r_k[2]

                        v[0, 0] += base[k, 3] * base[k, 4] * (3 * r_k[0] * r_k[0] - rr) / pow(rr, 2.5)
                        v[0, 1] += base[k, 3] * base[k, 4] * (3 * r_k[0] * r_k[1]) / pow(rr, 2.5)
                        v[0, 2] += base[k, 3] * base[k, 4] * (3 * r_k[0] * r_k[2]) / pow(rr, 2.5)
                        v[1, 1] += base[k, 3] * base[k, 4] * (3 * r_k[1] * r_k[1] - rr) / pow(rr, 2.5)
                        v[1, 2] += base[k, 3] * base[k, 4] * (3 * r_k[1] * r_k[2]) / pow(rr, 2.5)
                        v[2, 2] += base[k, 3] * base[k, 4] * (3 * r_k[2] * r_k[2] - rr) / pow(rr, 2.5)

    v *= (elementary_charge / (4 * np.pi * epsilon0)) * (1 / ((angtom) ** 3))

    EFG = np.array([[v[0, 0], v[0, 1], v[0, 2]],
                    [v[0, 1], v[1, 1], v[1, 2]],
                    [v[0, 2], v[1, 2], v[2, 2]]])

    max_EFG = EFG.max()

    threshold = max_EFG*0.01

    for ii in range(len(EFG)):
        for jj in range(len(EFG[0])):
            if np.abs(EFG[ii][jj]) < threshold:
                EFG[ii][jj] = 0.000
            else: continue

    return EFG
```

```

def diagonalize_EFG(tensor, quadrupole_moment):
    """This function diagonalize the EFG in the Principal Axis System (PAS).

    Parameters
        tensor: the EFG tensor calculated from point charge.
        quadrupole_moment: the quadrupole_moment of the nucleus under study.

    Returns:
        D: the diagonal EFG from point charge, in the PAS.
        eta: the asymmetry parameter of the EFG.
        chi: the quadrupolar coupling constant of the nucleus, in MHz.

    """
    eigenvalues, P = np.linalg.eig(tensor)
    P_inv = np.linalg.inv(P)
    X = np.dot(P_inv, tensor)
    D = np.dot(X, P)

    max_D = D.max()

    threshold = max_D*0.01

    for ii in range(len(D)):
        for jj in range(len(D[0])):
            if np.abs(D[ii][jj]) < threshold:
                D[ii][jj] = 0.000
            else: continue

    # Now, the diagonal components of the EFG tensor
    Vzz = max(eigenvalues, key=abs)
    Vyy = min(eigenvalues, key=abs)
    Vxx = -(Vzz+Vyy)
    eta = np.abs((Vyy - Vxx) / Vzz) # Asymmetry parameter of the EFG tensor
    eta = round(eta, 3)
```

```
    chi = np.abs(Vzz * elementary_charge * quadrupole_moment
   / h )*1e-6 # Quadrupolar constant, in MHz
    return D, eta, chi
```

Bibliography

[1] Y. Wang, H. Wu, G. T. McCandless, J. Y. Chan, and M. N. Ali, *Quantum states and intertwining phases in kagome materials*, `https://arxiv.org/abs/2303.03359`, 2023.

[2] E. Y. Andrei and A. H. MacDonald, "Graphene bilayers with a twist", Nature Materials **19** (2020).

[3] L. Balents, C. R. Dean, D. K. Efetov, and A. F. Young, "Superconductivity and strong correlations in moiré flat bands", Nature Physics **16** (2020).

[4] Q. Si and F. Steglich, "Heavy fermions and quantum phase transitions", Science **329**, 1161–1166 (2010).

[5] "Correlated insulator behaviour at half-filling in magic-angle graphene superlattices", Nature **556** (2018).

[6] B. R. Ortiz, S. M. L. Teicher, Y. Hu, J. L. Zuo, P. M. Sarte, E. C. Schueller, A. M. M. Abeykoon, M. J. Krogstad, S. Rosenkranz, R. Osborn, R. Seshadri, L. Balents, J. He, and S. D. Wilson, "CsV_3Sb_5: A $\mathbb{Z}_2$ Topological Kagome Metal with a Superconducting Ground State", Phys. Rev. Lett. **125**, 247002 (2020).

[7] B. R. Ortiz, L. C. Gomes, J. R. Morey, M. Winiarski, M. Bordelon, J. S. Mangum, I. W. H. Oswald, J. A. Rodriguez-Rivera, J. R. Neilson, S. D. Wilson, E. Ertekin, T. M. McQueen, and E. S. Toberer, "New kagome prototype materials: discovery of KV_3Sb_5, RbV_3Sb_5, and CsV_3Sb_5", Phys. Rev. Materials **3**, 094407 (2019).

[8] N. Ghimire and I. Mazin, "Topology and correlations on the kagome lattice", Nature Materials **19**, 137–138 (2020).

[9] S.-Y. Yang, Y. Wang, B. R. Ortiz, D. Liu, J. Gayles, E. Derunova, R. Gonzalez-Hernandez, L. Šmejkal, Y. Chen, S. S. P. Parkin, S. D. Wilson, E. S. Toberer, T. McQueen, and M. N. Ali, “Giant, unconventional anomalous Hall effect in the metallic frustrated magnet candidate, KV_3Sb_5”, Science Advances **6** (2020).

[10] W. Koshibae and S. Maekawa, “Electronic State of a CoO_2 Layer with Hexagonal Structure: A Kagome Lattice Structure in a Triangular Lattice”, Phys. Rev. Lett. **91**, 257003 (2003).

[11] S. Depenbrock, I. P. McCulloch, and U. Schollwöck, “Nature of the Spin-Liquid Ground State of the $S = 1/2$ Heisenberg Model on the Kagome Lattice”, Phys. Rev. Lett. **109**, 067201 (2012).

[12] M. Taillefumier, J. Robert, C. L. Henley, R. Moessner, and B. Canals, “Semiclassical spin dynamics of the antiferromagnetic Heisenberg model on the kagome lattice”, Phys. Rev. B **90**, 064419 (2014).

[13] D. A. Huse and A. D. Rutenberg, “Classical antiferromagnets on the Kagome lattice”, Phys. Rev. B **45**, 7536–7539 (1992).

[14] X.-L. Qi and S.-C. Zhang, “Topological insulators and superconductors”, Rev. Mod. Phys. **83**, 1057–1110 (2011).

[15] Y. Ando, “Topological insulator materials”, Journal of the Physical Society of Japan **82**, 102001 (2013).

[16] B. Yan and C. Felser, “Topological materials: weyl semimetals”, Annual Review of Condensed Matter Physics **8**, 337–354 (2017).

[17] C. Broholm, R. J. Cava, S. A. Kivelson, D. G. Nocera, M. R. Norman, and T. Senthil, “Quantum spin liquids”, Science **367**, eaay0668 (2020).

[18] Y. Zhou, K. Kanoda, and T.-K. Ng, “Quantum spin liquid states”, Rev. Mod. Phys. **89**, 025003 (2017).

[19] L. Savary and L. Balents, “Quantum spin liquids: a review”, Reports on Progress in Physics **80**, 016502 (2017).

[20] M. S. R. Rao, V. P. Bhallamudi, and P. C. Hammel, *Special issue on quantum materials and emerging phenomena*, `https://iopscience.iop.org/journal/0022-3727/page/special-issue-on-quantum-materials-and-emerging-phenomena`.

[21]B. Keimer and J. E. Moore, "The physics of quantum materials", Nature Physics **13**, 1045–1055 (2017).

[22]D. J. Thouless, P. Ao, Q. Niu, M. R. Geller, and C. Wexler, *Quantized vortices in superfluids and superconductors*, `https://arxiv.org/abs/cond-mat/9709127`, 1997.

[23]T. Takayama, *Novel quantum materials*, `https://www.fmq.uni-stuttgart.de/takagi-group/takayama_group/`.

[24]M. P. Shores, E. A. Nytko, B. M. Bartlett, and D. G. Nocera, "A structurally perfect s = 1/2 kagomé antiferromagnet", Journal of the American Chemical Society **127** (2005).

[25]M. R. Norman, "Colloquium: herbertsmithite and the search for the quantum spin liquid", Rev. Mod. Phys. **88**, 041002 (2016).

[26]P. W. Anderson, "The Resonating Valence Bond State in La_2CuO_4 and Superconductivity", Science **235**, 1196–1198 (1987).

[27]L. Balents, "Spin liquids in frustrated magnets", Nature **464** (2010).

[28]M. E. Zhitomirsky, "Octupolar ordering of classical kagome antiferromagnets in two and three dimensions", Phys. Rev. B **78**, 094423 (2008).

[29]W.-S. Wang, Z.-Z. Li, Y.-Y. Xiang, and Q.-H. Wang, "Competing electronic orders on kagome lattices at van hove filling", Phys. Rev. B **87**, 115135 (2013).

[30]M. L. Kiesel and R. Thomale, "Sublattice interference in the kagome hubbard model", Phys. Rev. B **86**, 121105 (2012).

[31]M. M. Denner, R. Thomale, and T. Neupert, "Analysis of Charge Order in the Kagome Metal AV_3Sb_5 ($A = \mathrm{K, Rb, Cs}$)", Phys. Rev. Lett. **127**, 217601 (2021).

[32]M. L. Kiesel, C. Platt, and R. Thomale, "Unconventional fermi surface instabilities in the kagome hubbard model", Phys. Rev. Lett. **110**, 126405 (2013).

[33]N. Morali, R. Batabyal, P. K. Nag, E. Liu, Q. Xu, Y. Sun, B. Yan, C. Felser, N. Avraham, and H. Beidenkopf, "Fermi-arc diversity on surface terminations of the magnetic Weyl semimetal $Co_3Sn_2S_2$", Science **365**, 1286–1291 (2019).

[34] D. F. Liu, A. J. Liang, E. K. Liu, Q. N. Xu, Y. W. Li, C. Chen, D. Pei, W. J. Shi, S. K. Mo, P. Dudin, T. Kim, C. Cacho, G. Li, Y. Sun, L. X. Yang, Z. K. Liu, S. S. P. Parkin, C. Felser, and Y. L. Chen, "Magnetic weyl semimetal phase in a kagomé crystal", Science **365**, 1282–1285 (2019).

[35] Z. Hou, Q. Zhang, G. Xu, C. Gong, B. Ding, Y. Wang, H. Li, E. Liu, F. Xu, H. Zhang, Y. Yao, G. Wu, X.-x. Zhang, and W. Wang, "Creation of single chain of nanoscale skyrmion bubbles with record-high temperature stability in a geometrically confined nanostripe", Nano Letters **18** (2018).

[36] Z. Hou, W. Ren, B. Ding, G. Xu, Y. Wang, B. Yang, Q. Zhang, Y. Zhang, E. Liu, F. Xu, W. Wang, G. Wu, X. Zhang, B. Shen, and Z. Zhang, "Observation of various and spontaneous magnetic skyrmionic bubbles at room temperature in a frustrated kagome magnet with uniaxial magnetic anisotropy", Advanced Materials **29**, 1701144 (2017).

[37] M. Kang, L. Ye, S. Fang, J.-S. You, A. Levitan, M. Han, J. I. Facio, C. Jozwiak, A. Bostwick, E. Rotenberg, M. K. Chan, R. D. McDonald, D. Graf, K. Kaznatcheev, E. Vescovo, D. C. Bell, E. Kaxiras, J. van den Brink, M. Richter, M. Prasad Ghimire, J. G. Checkelsky, and R. Comin, "Dirac fermions and flat bands in the ideal kagome metal fesn", Nature Materials **19** (2020).

[38] M. Kang, S. Fang, L. Ye, H. C. Po, J. Denlinger, C. Jozwiak, A. Bostwick, E. Rotenberg, E. Kaxiras, J. G. Checkelsky, and R. Comin, "Topological flat bands in frustrated kagome lattice CoSn", Nature Communications **11** (2020).

[39] Z. Liu, M. Li, Q. Wang, G. Wang, C. Wen, K. Jiang, X. Lu, S. Yan, Y. Huang, D. Shen, J.-X. Yin, Z. Wang, Z. Yin, H. Lei, and S. Wang, "Orbital-selective dirac fermions and extremely flat bands in frustrated kagome-lattice metal cosn", Nature Communivìcations **11** (2020).

[40] J. W. Cable, N. Wakabayashi, and P. Radhakrishna, "Magnetic excitations in the triangular antiferromagnets Mn_3Sn and Mn_3Ge", Phys. Rev. B **48**, 6159–6166 (1993).

[41] H. Yang, Y. Sun, Y. Zhang, W.-J. Shi, S. S. P. Parkin, and B. Yan, "Topological weyl semimetals in the chiral antiferromagnetic materials mn3ge and mn3sn", New Journal of Physics **19**, 015008 (2017).

[42]E. M. Kenney, B. R. Ortiz, C. Wang, S. D. Wilson, and M. J. Graf, "Absence of local moments in the kagome metal KV_3Sb_5 as determined by muon spin spectroscopy", J. Phys.: Condens. Matter **33**, 235801 (2021).

[43]B. R. Ortiz, S. M. L. Teicher, L. Kautzsch, P. M. Sarte, N. Ratcliff, J. Harter, J. P. C. Ruff, R. Seshadri, and S. D. Wilson, "Fermi Surface Mapping and the Nature of Charge-Density-Wave Order in the Kagome Superconductor CsV_3Sb_5", Phys. Rev. X **11**, 041030 (2021).

[44]L. Nie, K. Sun, W. Ma, D. Song, L. Zheng, Z. Liang, P. Wu, F. Yu, J. Li, M. Shan, D. Zhao, S. Li, B. Kang, Z. Wu, Y. Zhou, K. Liu, Z. Xiang, J. Ying, Z. Wang, T. Wu, and X. Chen, "Charge-density-wave-driven electronic nematicity in a kagome superconductor", Nature (2022).

[45]R. E. Thorne, "Charge-Density-Wave Conductors", Physics Today **49**, 42–47 (1996).

[46]Y. Ren, "Time-resolved optical studies of colossal magnetoresistance and charge-density wave materials", PhD thesis (College of William & Mary - Arts & Sciences, 2003).

[47]S. S.-L. S. Eucker, "Proximity effect in Cu-Nb-Sn composites", in, `https://api.semanticscholar.org/CorpusID:135605126` (1981).

[48]L. Gor'kov and G. Grüner, *Charge density waves in solids* (North Holland, 1989).

[49]G. Grüner, "The dynamics of charge-density waves", Rev. Mod. Phys. **60**, 1129–1181 (1988).

[50]S. Trebst, *Kitaev materials*, `https://arxiv.org/abs/1701.07056`, 2017.

[51]G. Jackeli and G. Khaliullin, "Mott insulators in the strong spin-orbit coupling limit: from heisenberg to a quantum compass and kitaev models", Phys. Rev. Lett. **102**, 017205 (2009).

[52]H. Takagi, T. Takayama, G. Jackeli, G. Khaliullin, and S. E. Nagler, "Concept and realization of Kitaev quantum spin liquids", Nature Reviews Physics **1**, 264–280 (2019).

[53]S.-H. Jang, R. Sano, Y. Kato, and Y. Motome, "Antiferromagnetic Kitaev interaction in f-electron based honeycomb magnets", Phys. Rev. B **99**, 241106 (2019).

[54] D. Pesin and L. Balents, "Mott physics and band topology in materials with strong spin–orbit interaction", Nature Physics **6** (2010).

[55] G. Khaliullin, "Orbital Order and Fluctuations in Mott Insulators", Progress of Theoretical Physics Supplement **160**, 155–202 (2005).

[56] J. ř. Chaloupka, G. Jackeli, and G. Khaliullin, "Kitaev-Heisenberg Model on a Honeycomb Lattice: Possible Exotic Phases in Iridium Oxides $A_2\mathrm{IrO}_3$", Phys. Rev. Lett. **105**, 027204 (2010).

[57] J. Nasu and Y. Motome, "Nonequilibrium majorana dynamics by quenching a magnetic field in kitaev spin liquids", Phys. Rev. Res. **1**, 033007 (2019).

[58] S. Chandra, K. Ramola, and D. Dhar, "Classical heisenberg spins on a hexagonal lattice with kitaev couplings", Phys. Rev. E **82**, 031113 (2010).

[59] E. Sela, H.-C. Jiang, M. H. Gerlach, and S. Trebst, "Order-by-disorder and spin-orbital liquids in a distorted heisenberg-kitaev model", Phys. Rev. B **90**, 035113 (2014).

[60] C. L. Henley, "The "coulomb phase" in frustrated systems", Annual Review of Condensed Matter Physics **1**, 179–210 (2010).

[61] A. Kitaev, "Anyons in an exactly solved model and beyond", Annals of Physics **321**, January Special Issue, 2–111 (2006).

[62] Y. Motome, R. Sano, S. Jang, Y. Sugita, and Y. Kato, "Materials design of kitaev spin liquids beyond the jackeli–khaliullin mechanism", Journal of Physics: Condensed Matter **32**, 404001 (2020).

[63] A. Abragam, *The Principles of Nuclear Magnetism* (Oxford University Press, 1983).

[64] C. P. SLichter, *Principles of magnetic resonance* (Springer Berlin, Heidelberg, 1983).

[65] T. P. Das and E. L. Hahn, *Nuclear Quadrupole Resonance Spectroscopy* (American Institute of Physics, 1959).

[66] E. Fukushima and S. Roeder, *Experimental Pulse NMR: A Nuts and Bolts Approach* (2018).

[67] D. Candoli, "Simulation of nmr/nqr observables and spin control for applications in quantum science", PhD thesis (University of Bologna, 2020).

[68] K. J. MacKenzie and M. E. Smith, *Multinuclear Solid-State NMR of Inorganic Materials* (Elsevier, 2022).

[69] W. D. Knight, “Nuclear magnetic resonance shift in metals”, Phys. Rev. **76**, 1259–1260 (1949).

[70] H. Alloul, “NMR studies of electronic properties of solids”, (2015).

[71] L. H. Bennett, R. E. Watson, and G. C. Carter, “Relevance of knight shift measurements to the electronic density of states”, Journal of Research of the National Bureau of Standards - A. Physics and Chemistry **74**, 569–611 (1970).

[72] P. Carretta and A. Lascialfari, *NMR-MRI, μSR and Mössbauer Spectroscopies in Molecular Magnets* (Springer Milano, 2007).

[73] *Nuclear magnetic resonance (nmr) facility*, `https://www.lakeheadu.ca/centre/lucas/laboratories/luil/facilities/nmr`.

[74] G. Facey, *University of ottawa nmr facility blog*, `https://u-of-o-nmr-facility.blogspot.com/`.

[75] G. Allodi, A. Banderini, R. De Renzi, and C. Vignali, “Hyrespect: a broadband fast-averaging spectrometer for nuclear magnetic resonance of magnetic materials”, Review of scientific instruments **76**, 083911 (2005).

[76] M. Benini, “Fabrication and characterization of hybrid ferromagnetic-organic heterostructures for spintronics application”, PhD thesis (Alma Mater Studiorum - Università di Bologna, 2022).

[77] J. Frassineti, P. Bonfà, G. Allodi, E. Garcia, R. Cong, B. R. Ortiz, S. D. Wilson, R. De Renzi, V. F. Mitrovi ć, and S. Sanna, “Microscopic nature of the charge-density wave in the kagome superconductor RbV_3Sb_5”, Phys. Rev. Res. **5**, L012017 (2023).

[78] W. G. Clark, M. E. Hanson, and F. Lefloch, “Magnetic resonance spectral reconstruction using frequency-shifted and summed Fourier transform processing”, Review of Scientific Instruments **66** (1995).

[79] *What is a cryostat?*, `https://andor.oxinst.com/learning/view/article/what-is-a-cryostat`.

[80] S. J. Blundell, “Spin-polarized muons in condensed matter physics”, Contemporary Physics **40**, 175–192 (1999).

[81] A.Yaouanc and P. de Réotier, *Muon spin rotation, relaxation and resonance* (Oxford University Press, 2010).

[82] R. Kubo and T. Toyabe, "Magnetic resonance and relaxation", in Proceedings of the XIVth Colloque Ampère (North-Holland, 1967), pp. 810–823.

[83] K. Nagamine, *Introductory muon science* (Cambridge University Press, 2003).

[84] *Emu manual*, `https://www.isis.stfc.ac.uk/OtherFiles/EMU_Manual.pdf`.

[85] *Gps manual*, `https://www.psi.ch/sites/default/files/import/smus/InstrumentGpsEN/User_Guide_present_version.pdf`.

[86] E. L. Hahn, "Spin echoes", Phys. Rev. **80**, 580–594 (1950).

[87] D. M. S. Bagguley, *Pulsed magnetic resonance - nmr, esr, and optics: a recognition of e. l. hahn.* (Oxford University Press, 1992).

[88] M. Kang, S. Fang, J. Yoo, B. R. Ortiz, Y. Oey, S. H. Ryu, J. Kim, C. Jozwiak, A. Bostwick, E. Rotenberg, E. Kaxiras, J. Checkelsky, S. D. Wilson, J.-H. Park, and R. Comin, *Microscopic structure of three-dimensional charge order in kagome superconductor* AV_3Sb_5 *and its tunability*, 2022.

[89] Y. Hu, X. Wu, B. R. Ortiz, S. Ju, X. Han, J. Ma, N. C. Plumb, M. Radovic, R. Thomale, S. D. Wilson, A. P. Schnyder, and M. Shi, "Rich nature of Van Hove singularities in Kagome superconductor $\mathrm{CsV_3Sb_5}$", Nature Communications **13**, 2220 (2022).

[90] D. W. Song, L. X. Zheng, F. H. Yu, J. Li, L. P. Nie, M. Shan, D. Zhao, S. J. Li, B. L. Kang, Z. M. Wu, Y. B. Zhou, K. L. Sun, K. Liu, X. G. Luo, Z. Y. Wang, J. J. Ying, X. G. Wan, T. Wu, and X. H. Chen, "Orbital ordering and fluctuations in a kagome superconductor $\mathrm{CsV_3Sb_5}$", Science China Physics, Mechanics and Astronomy volume **65**, 247462 (2022).

[91] A. Consiglio, T. Schwemmer, X. Wu, W. Hanke, T. Neupert, R. Thomale, G. Sangiovanni, and D. Di Sante, "Van hove tuning of $\mathrm{aV_3Sb_5}$ kagome metals under pressure and strain", Phys. Rev. B **105**, 165146 (2022).

[92] J. Wilson, F. D. Salvo, and S. Mahajan, "Charge-density waves and superlattices in the metallic layered transition metal dichalcogenides", Advances in Physics **24**, 117–201 (1975).

[93] K. Rossnagel, “On the origin of charge-density waves in select layered transition-metal dichalcogenides”, Journal of Physics: Condensed Matter **23**, 213001 (2011).

[94] C. Mu, Q. Yin, Z. Tu, C. Gong, P. Zheng, H. Lei, Z. Li, and J. Luo, “Tri-hexagonal charge order in kagome metal CsV_3Sb_5 revealed by ^{121}Sb nuclear quadrupole resonance”, Chinese Physics B **31**, 017105 (2022).

[95] H. Tan, Y. Liu, Z. Wang, and B. Yan, “Charge Density Waves and Electronic Properties of Superconducting Kagome Metals”, Phys. Rev. Lett. **127**, 046401 (2021).

[96] S. Cho, H. Ma, W. Xia, Y. Yang, Z. Liu, Z. Huang, Z. Jiang, X. Lu, J. Liu, Z. Liu, J. Li, J. Wang, Y. Liu, J. Jia, Y. Guo, J. Liu, and D. Shen, “Emergence of New van Hove Singularities in the Charge Density Wave State of a Topological Kagome Metal RbV_3Sb_5”, Phys. Rev. Lett. **127**, 236401 (2021).

[97] C. Mielke, D. Das, J.-X. Yin, H. Liu, R. Gupta, Y.-X. Jiang, M. Medarde, X. Wu, H. C. Lei, J. Chang, P. Dai, Q. Si, H. Miao, R. Thomale, T. Neupert, Y. Shi, R. Khasanov, M. Z. Hasan, H. Luetkens, and Z. Guguchia, “Time-reversal symmetry-breaking charge order in a kagome superconductor”, Nature, 245–250 (2022).

[98] Z. Guguchia, C. Mielke, D. Das, R. Gupta, J.-X. Yin, H. Liu, Q. Yin, M. H. Christensen, Z. Tu, C. Gong, N. Shumiya, M. S. Hossain, T. Gamsakhurdashvili, M. Elender, P. Dai, A. Amato, Y. Shi, H. C. Lei, R. M. Fernandes, M. Z. Hasan, H. Luetkens, and R. Khasanov, “Tunable unconventional kagome superconductivity in charge ordered RbV_3Sb_5 and KV_3Sb_5”, Nature Communications **14** (2023).

[99] J. Luo, Z. Zhao, Y. Z. Zhou, J. Yang, A. F. Fang, H. T. Yang, H. J. Gao, R. Zhou, and G.-q. Zheng, “Possible star-of-David pattern charge density wave with additional modulation in the kagome superconductor CsV_3Sb_5”, npj Quantum Materials **7** (2022).

[100] C. Mu, Q. Yin, Z. Tu, C. Gong, H. Lei, Z. Li, and J. Luo, “S-Wave Superconductivity in Kagome Metal CsV_3Sb_5 Revealed by $^{121/123}$Sb NQR and ^{51}V NMR Measurements”, Chinese Physics Letters **38**, 077402 (2021).

[101] Y. M. Oey, B. R. Ortiz, F. Kaboudvand, J. Frassineti, E. Garcia, R. Cong, S. Sanna, V. F. Mitrovi ć, R. Seshadri, and S. D. Wilson, "Fermi level tuning and double-dome superconductivity in the kagome metal $CsV_3Sb_{5-x}Sn_x$", Phys. Rev. Mater. **6**, L041801 (2022).

[102] A. N. C. Salinas, B. R. Ortiz, C. Bales, J. Frassineti, V. F. Mitrović, and S. Wilson, "Electron-hole asymmetry in the phase diagram of carrier-tuned CsV_3Sb_5", Front. Electron. Mater - Sec. Superconducting Materials **3** (2023).

[103] Y. Song, T. Ying, X. Chen, X. Han, X. Wu, A. P. Schnyder, Y. Huang, J.-g. Guo, and X. Chen, "Competition of Superconductivity and Charge Density Wave in Selective Oxidized CsV_3Sb_5 Thin Flakes", Phys. Rev. Lett. **127**, 237001 (2021).

[104] H. LaBollita and A. S. Botana, "Tuning the Van Hove singularities in AV_3Sb_5 ($A = \mathrm{K, Rb, Cs}$) via pressure and doping", Phys. Rev. B **104**, 205129 (2021).

[105] K. Y. Chen, N. N. Wang, Q. W. Yin, Y. H. Gu, K. Jiang, Z. J. Tu, C. S. Gong, Y. Uwatoko, J. P. Sun, H. C. Lei, J. P. Hu, and J.-G. Cheng, "Double Superconducting Dome and Triple Enhancement of T_c in the Kagome Superconductor CsV_3Sb_5 under High Pressure", Phys. Rev. Lett. **126**, 247001 (2021).

[106] S. Parvez, "Study of kagome superconducting materials using nuclear magnetic/quadrupolar resonance", PhD thesis (University of Bologna, 2023).

[107] Z. Guguchia, R. Khasanov, and H. Luetkens, "Unconventional charge order and superconductivity in kagome-lattice systems as seen by muon-spin rotation", npj Quantum Materials **8** (2023).

[108] F. Pratt, "Wimda: a muon data analysis program for the windows pc", Physica B: Condensed Matter **289-290**, 710–714 (2000).

[109] A. E. Böhmer, J.-H. Chu, S. Lederer, and M. Yi, "Nematicity and nematic fluctuations in iron-based superconductors", Nature Physics **18** (2022).

[110] P. Bonfà, J. Frassineti, J. M. Wilkinson, G. Prando, M. M. Isah, C. Wang, T. Spina, B. Joseph, V. F. Mitrovi ć, R. De Renzi, S. J. Blundell, and S. Sanna, "Entanglement between Muon and $I > \frac{1}{2}$ Nuclear Spins as a Probe of Charge Environment", Phys. Rev. Lett. **129**, 097205 (2022).

[111] J. H. Brewer, S. R. Kreitzman, D. R. Noakes, E. J. Ansaldo, D. R. Harshman, and R. Keitel, “Observation of muon-fluorine “hydrogen bonding” in ionic crystals”, Phys. Rev. B **33**, 7813(R) (1986).

[112] D. R. Noakes, E. J. Ansaldo, S. R. Kreitzman, and G. M. Luke, “The $(F\mu F)^-$ ion in solid fluorides”, J. Phys. Chem. Solids **54**, 785 (1993).

[113] T. Lancaster, S. J. Blundell, P. J. Baker, W. Hayes, S. R. Giblin, S. E. McLain, F. L. Pratt, Z. Salman, E. A. Jacobs, J. F. C. Turner, and T. Barnes, “Intrinsic magnetic order in Cs_2AgF_4 detected by muon-spin relaxation”, Phys. Rev. B **75**, R220408 (2007).

[114] T. Lancaster, F. L. Pratt, S. J. Blundell, I. McKenzie, and H. E. Assender, “Muon–fluorine entanglement in fluoropolymers”, J. Phys.: Condens. Matter **21**, 346004 (2009).

[115] D. Billington, E. Riordan, M. Salman, D. Margineda, G. J. W. Gill, S. P. Cottrell, I. McKenzie, T. Lancaster, M. J. Graf, and S. R. Giblin, “Radio-frequency manipulation of state populations in an entangled fluorine-muon-fluorine system”, Phys. Rev. Lett. **129**, 077201 (2022).

[116] F. L. Pratt, S. J. Blundell, I. M. Marshall, T. Lancaster, A. Husmann, C. Steer, W. Hayes, C. Fischmeister, R. E. Martin, and A. B. Holmes, “μSR in polymers”, Physica B **326B**, 34 (2003).

[117] K. Nishiyama, S. W. Nishiyama, and W. Higemoto, “Asymmetric F–μ–F interaction of the muon in polyfluorocarbons”, Physica B **326B**, 41 (2003).

[118] T. Lancaster, S. J. Blundell, P. J. Baker, M. L. Brooks, W. Hayes, F. L. Pratt, J. L. Manson, M. M. Conner, and J. A. Schlueter, “Muon-fluorine entangled states in molecular magnets”, Phys. Rev. Lett. **99**, 267601 (2007).

[119] F. Bernardini, P. Bonfà, S. Massidda, and R. De Renzi, “Ab initio strategy for muon site assignment in wide band gap fluorides”, Phys. Rev. B **87**, 115148 (2013).

[120] J. S. Möller, D. Ceresoli, T. Lancaster, N. Marzari, and S. J. Blundell, “Quantum states of muons in fluorides”, Phys. Rev. B **87**, 121108 (2013).

[121] J. S. Möller, P. Bonfà, D. Ceresoli, F. Bernardini, S. J. Blundell, T. Lancaster, R. D. Renzi, N. Marzari, I. Watanabe, S. Sulaiman, and M. I. Mohamed-Ibrahim, “Playing quantum hide-and-seek with the muon: localizing muon stopping sites”, Physica Scripta **88**, 068510 (2013).

[122]P. Bonfà and R. De Renzi, "Toward the computational prediction of muon sites and interaction parameters", Journal of the Physical Society of Japan **85**, 091014 (2016).

[123]S. J. Blundell, R. D. Renzi, T. Lancaster, and F. L. Pratt, "Chapter 16", in *Muon spectroscopy – an introduction* (Oxford University Press, 2022).

[124]J. Lord, S. Cottrell, and W. Williams, "Muon spin relaxation in strongly coupled systems", Physica B: Condensed Matter **289-290**, 495–498 (2000).

[125]P. Mendels, F. Bert, M. A. de Vries, A. Olariu, A. Harrison, F. Duc, J. C. Trombe, J. S. Lord, A. Amato, and C. Baines, "Quantum magnetism in the paratacamite family: towards an ideal kagomé lattice", Phys. Rev. Lett. **98**, 077204 (2007).

[126]R. Kadono, K. Shimomura, K. H. Satoh, S. Takeshita, A. Koda, K. Nishiyama, E. Akiba, R. M. Ayabe, M. Kuba, and C. M. Jensen, "Hydrogen bonding in sodium alanate: a muon spin rotation study", Phys. Rev. Lett. **100**, 026401 (2008).

[127]G. Prando, J. Perego, M. Negroni, M. Riccò, S. Bracco, A. Comotti, P. Sozzani, and P. Carretta, "Molecular rotors in a metal–organic framework: muons on a hyper-fast carousel", Nano Letters **20**, 7613–7618 (2020).

[128]J. M. Wilkinson and S. J. Blundell, "Information and decoherence in a muon-fluorine coupled system", Phys. Rev. Lett. **125**, 087201 (2020).

[129]J. M. Wilkinson, F. L. Pratt, T. Lancaster, P. J. Baker, and S. J. Blundell, "Muon sites in PbF_2 and YF_3: decohering environments and the role of anion Frenkel defects", Phys. Rev. B **104**, L220409 (2021).

[130]J. Muller, "A15-type superconductors", Rep. Prog. Phys. **43**, 641 (1980).

[131]P. Blaha, K. Schwarz, and P. Herzig, "First-principles calculation of the electric field gradient of Li_3N", Phys. Rev. Lett. **54**, 1192–1195 (1985).

[132]R. Cong, R. Nanguneri, B. Rubenstein, and V. F. Mitrović, "First principles calculations of the electric field gradient tensors of ba2naoso6, a mott insulator with strong spin orbit coupling", Journal of Physics: Condensed Matter **32**, 405802 (2020).

[133]C. Paduani and C. A. Kuhnen, "Martensitic phase transition from cubic to tetragonal V_3Si: an electronic structure study", Eur. Phys. J. B **66**, 353–359 (2008).

[134]N. Morton, B. James, G. Wostenholm, and N. Howard, “The resistivity of V_3Sn and related compounds”, Journal of the Less Common Metals **64**, 69–75 (1979).

[135]A. Alimenti, N. Pompeo, K. Torokhtii, T. Spina, R. Flükiger, L. Muzzi, and E. Silva, “Microwave measurements of the high magnetic field vortex motion pinning parameters in Nb_3Sn”, Superconductor Science and Technology **34**, 014003 (2020).

[136]R. Flükiger, T. Spina, F. Cerutti, A. Ballarino, . Scheuerlein, L. Bottura, Y. Zubavichus, A. Ryazanov, R. D. Svetogovov, S. Shavkin, P. Degtyarenko, Y. Semenov, C. Senatore, and R. Cerny, “Variation of T_c, lattice parameter and atomic ordering in Nb_3Sn platelets irradiated with 12 MeV protons: correlation with the number of induced Frenkel defects”, Superconductor Science and Technology **30**, 054003 (2017).

[137]P. Giannozzi, O. Baseggio, P. Bonfà, D. Brunato, R. Car, I. Carnimeo, C. Cavazzoni, S. de Gironcoli, P. Delugas, F. Ferrari Ruffino, A. Ferretti, N. Marzari, I. Timrov, A. Urru, and S. Baroni, “Quantum ESPRESSO toward the exascale”, The Journal of Chemical Physics **152**, 154105 (2020).

[138]*Elk code v8.3.25*, `elk.sf.net`.

[139]J. P. Perdew, K. Burke, and M. Ernzerhof, “Generalized gradient approximation made simple”, Phys. Rev. Lett. **77**, 3865–3868 (1996).

[140]K. F. Garrity, J. W. Bennett, K. M. Rabe, and D. Vanderbilt, “Pseudopotentials for high-throughput DFT calculations”, Computational Materials Science **81**, 446–452 (2014).

[141]A. Dal Corso, “Pseudopotentials periodic table: from h to pu”, Computational Materials Science **95**, 337–350 (2014).

[142]A. Amato, H. Luetkens, K. Sedlak, A. Stoykov, R. Scheuermann, M. Elender, A. Raselli, and D. Graf, “The new versatile general purpose surface-muon instrument (GPS) based on silicon photomultipliers for μSR measurements on a continuous-wave beam”, Review of Scientific Instruments **88**, 093301 (2017).

[143]A. Yaouanc, O. Hartmann, E. Karlsson, E. Wäckelgård, R. Wäppling, D. Fruchart, R. Fruchart, and J. P. Senateur, “Transverse field μ^+SR study of V_3Si”, Hyper. Inter. **31**, 93–97 (1986).

[144]P. Giannozzi, S. Baroni, N. Bonini, M. Calandra, R. Car, C. Cavazzoni, D. Ceresoli, G. L. Chiarotti, M. Cococcioni, I. Dabo, A. Dal Corso, S. de Gironcoli, S. Fabris, G. Fratesi, R. Gebauer, U. Gerstmann, C. Gougoussis, A. Kokalj, M. Lazzeri, L. Martin-Samos, N. Marzari, F. Mauri, R. Mazzarello, S. Paolini, A. Pasquarello, L. Paulatto, C. Sbraccia, S. Scandolo, G. Sclauzero, A. P. Seitsonen, A. Smogunov, P. Umari, and R. M. Wentzcovitch, "QUANTUM ESPRESSO: a modular and open-source software project for quantum simulations of materials", Journal of Physics: Condensed Matter **21**, 395502 (19pp) (2009).

[145]P. Giannozzi, O. Andreussi, T. Brumme, O. Bunau, M. B. Nardelli, M. Calandra, R. Car, C. Cavazzoni, D. Ceresoli, M. Cococcioni, N. Colonna, I. Carnimeo, A. D. Corso, S. de Gironcoli, P. Delugas, R. A. D. Jr, A. Ferretti, A. Floris, G. Fratesi, G. Fugallo, R. Gebauer, U. Gerstmann, F. Giustino, T. Gorni, J. Jia, M. Kawamura, H.-Y. Ko, A. Kokalj, E. Küçükbenli, M. Lazzeri, M. Marsili, N. Marzari, F. Mauri, N. L. Nguyen, H.-V. Nguyen, A. Otero-de-la-Roza, L. Paulatto, S. Poncé, D. Rocca, R. Sabatini, B. Santra, M. Schlipf, A. P. Seitsonen, A. Smogunov, I. Timrov, T. Thonhauser, P. Umari, N. Vast, X. Wu, and S. Baroni, "Advanced capabilities for materials modelling with QUANTUM ESPRESSO", Journal of Physics: Condensed Matter **29**, 465901 (2017).

[146]P. E. Blöchl, "Projector augmented-wave method", Phys. Rev. B **50**, 17953–17979 (1994).

[147]I. J. Onuorah, P. Bonfà, and R. De Renzi, "Muon contact hyperfine field in metals: a dft calculation", Phys. Rev. B **97**, 174414 (2018).

[148]A. Amato, P. Dalmas de Réotier, D. Andreica, A. Yaouanc, A. Suter, G. Lapertot, I. M. Pop, E. Morenzoni, P. Bonfà, F. Bernardini, and R. De Renzi, "Understanding the μSR spectra of MnSi without magnetic polarons", Phys. Rev. B **89**, 184425 (2014).

[149]N. Martin, M. Deutsch, F. Bert, D. Andreica, A. Amato, P. Bonfà, R. De Renzi, U. K. Rößler, P. Bonville, L. N. Fomicheva, A. V. Tsvyashchenko, and I. Mirebeau, "Magnetic ground state and spin fluctuations in MnGe chiral magnet as studied by muon spin rotation", Phys. Rev. B **93**, 174405 (2016).

[150] K. Choudhary, J. N. Ansari, I. I. Mazin, and K. L. Sauer, “Density functional theory-based electric field gradient database”, Scientific Data **7** (2020).

[151] M. Celio, “A new technique to calculate the muon polarization function”, Hyperf. Inter. **31**, 41–46 (1986).

[152] M. Celio, “New method to calculate the muon polarization function”, Phys. Rev. Lett. **56**, 2720–2723 (1986).

[153] P. Bonfà, J. Frassineti, M. M. Isah, I. J. Onuorah, and S. Sanna, “Undi: an open-source library to simulate muon-nuclear interactions in solids”, Computer Physics Communications **260**, 107719 (2021).

[154] J. Frassineti, *POCSI (POint Charge SImulation of electric field gradient)*, `https://github.com/JonathanFrassineti/POCSI/tree/main`.

[155] J. Schultz, “Point charge simulations of the electric field gradient”, PhD thesis (Department of Physics and Astronomy, University of British Columbia, 2005).

[156] H. Haas, “Electric field gradients at V, Nb and Ta in A15 alloys”, Hyperfine Interactions **120**, 157–161 (1999).

[157] Y. Singh, S. Manni, J. Reuther, T. Berlijn, R. Thomale, W. Ku, S. Trebst, and P. Gegenwart, “Relevance of the Heisenberg-Kitaev Model for the Honeycomb Lattice Iridates A_2IrO$_3$”, Phys. Rev. Lett. **108**, 127203 (2012).

[158] S. Trebst and C. Hickey, “Kitaev materials”, Physics Reports **950**, Kitaev materials, 1–37 (2022).

[159] V. M. Katukuri, S. Nishimoto, V. Yushankhai, S.-L. Drechsler, and J. van den Brink, “Kitaev interactions between j = 1/2 moments in honeycomb Na$_2$IrO$_3$ are large and ferromagnetic: insights from ab initio quantum chemistry calculations”, New Journal of Phyics **16**, 013056 (2016).

[160] R. D. Johnson, S. C. Williams, A. A. Haghighirad, J. Singleton, V. Zapf, P. Manuel, I. I. Mazin, Y. Li, H. O. Jeschke, R. Valentı, and R. Coldea, “Monoclinic crystal structure of $\alpha-$RuCl$_3$ and the zigzag antiferromagnetic ground state”, Phys. Rev. B **92**, 235119 (2015).

[161] J. A. Sears, L. E. Chern, S. Kim, P. J. Bereciartua, S. Francoual, Y. B. Kim, and Y.-J. Kim, “Ferromagnetic kitaev interaction and the origin of large magnetic anisotropy in α-rucl3”, Nature Physics **16**, 837–840 (2020).

[162] Y. Sugita, Y. Kato, and Y. Motome, “Antiferromagnetic kitaev interactions in polar spin-orbit mott insulators”, Phys. Rev. B **101**, 100410 (2020).

[163] H. Liu and G. Khaliullin, “Pseudospin exchange interactions in d^7 cobalt compounds: Possible realization of the Kitaev model”, Phys. Rev. B **97**, 014407 (2018).

[164] R. Sano, Y. Kato, and Y. Motome, “Kitaev-Heisenberg Hamiltonian for high-spin d^7 Mott insulators”, Phys. Rev. B **97**, 014408 (2018).

[165] E. M. Smith, O. Benton, D. R. Yahne, B. Placke, R. Schäfer, J. Gaudet, J. Dudemaine, A. Fitterman, J. Beare, A. R. Wildes, S. Bhattacharya, T. DeLazzer, C. R. C. Buhariwalla, N. P. Butch, R. Movshovich, J. D. Garrett, C. A. Marjerrison, J. P. Clancy, E. Kermarrec, G. M. Luke, A. D. Bianchi, K. A. Ross, and B. D. Gaulin, *The case for a* $U(1)_\pi$ *Quantum Spin Liquid Ground State in the Dipole-Octupole Pyrochlore* $Ce_2Zr_2O_7$, `https://arxiv.org/abs/2108.01217`, 2021.

[166] B. Gao, T. Chen, D. W. Tam, C.-L. Huang, K. Sasmal, D. T. Adroja, F. Ye, H. Cao, G. Sala, M. B. Stone, C. Baines, J. A. T. Verezhak, H. Hu, J.-H. Chung, X. Xu, S.-W. Cheong, M. Nallaiyan, S. Spagna, M. B. Maple, A. H. Nevidomskyy, E. Morosan, G. Chen, and P. Dai, “Experimental signatures of a three-dimensional quantum spin liquid in effective spin-1/2 $Ce_2Zr_2O_7$ pyrochlore”, Nature Physics **15** (2019).

[167] A. Ramanathan, J. E. Leisen, and H. S. La Pierre, “In-Plane Cation Ordering and Sodium Displacements in Layered Honeycomb Oxides with Tetravalent Lanthanides: Na_2LnO_3 (Ln = Ce, Pr, and Tb)”, Inorganic Chemistry **60**, 1398–1410 (2021).

[168] M. J. Daum, A. Ramanathan, A. I. Kolesnikov, S. Calder, M. Mourigal, and H. S. La Pierre, “Collective excitations in the tetravalent lanthanide honeycomb antiferromagnet Na_2PrO_3”, Phys. Rev. B **103**, L121109 (2021).

[169] S.-H. Jang, R. Sano, Y. Kato, and Y. Motome, “Computational design of f-electron Kitaev magnets: Honeycomb and hyperhoneycomb compounds A_2PrO_3 (A = alkali metals)”, Phys. Rev. Mater. **4**, 104420 (2020).

[170] A. Suter and B. Wojek, “Musrfit: a free platform-independent framework for μsr data analysis”, Physics Procedia **30**, 12th International Confer-

ence on Muon Spin Rotation, Relaxation and Resonance (μSR2011), 69–73 (2012).

[171] S. J. Blundell and T. Lancaster, "Dft+μ: density functional theory for muon site determination", Applied Physics Reviews **10** (2023).

[172] H. J. Monkhorst and J. D. Pack, "Special points for Brillouin-zone integrations", Phys. Rev. B **13**, 5188–5192 (1976).

[173] S. Toth and B. Lake, "Linear spin wave theory for single-q incommensurate magnetic structures", Journal of Physics: Condensed Matter **27**, 166002 (2015).

[174] A. Scheie, "*PyCrystalField*: software for calculation, analysis and fitting of crystal electric field Hamiltonians", Journal of Applied Crystallography **54**, 356–362 (2021).

[175] S. C. Cheung, Z. Guguchia, B. A. Frandsen, Z. Gong, K. Yamakawa, D. E. Almeida, I. J. Onuorah, P. Bonfá, E. Miranda, W. Wang, D. W. Tam, Y. Song, C. Cao, Y. Cai, A. M. Hallas, M. N. Wilson, T. J. S. Munsie, G. Luke, B. Chen, G. Dai, C. Jin, S. Guo, F. Ning, R. M. Fernandes, R. De Renzi, P. Dai, and Y. J. Uemura, "Disentangling superconducting and magnetic orders in $\mathrm{NaFe}_{1-x}\mathrm{Ni}_x\mathrm{As}$ using muon spin rotation", Phys. Rev. B **97**, 224508 (2018).

[176] Y. Hinatsu and Y. Doi, "Crystal structures and magnetic properties of alkali-metal lanthanide oxides a2lno3 (a=li, na; ln=ce, pr, tb)", Journal of Alloys and Compounds **418**, Proceedings of the Twenty-fourth Rare Earth Research Conference, 155–160 (2006).

[177] M. Smidman, D. T. Adroja, A. D. Hillier, L. C. Chapon, J. W. Taylor, V. K. Anand, R. P. Singh, M. R. Lees, E. A. Goremychkin, M. M. Koza, V. V. Krishnamurthy, D. M. Paul, and G. Balakrishnan, "Neutron scattering and muon spin relaxation measurements of the noncentrosymmetric antiferromagnet $\mathbf{CeCoGe_3}$", Phys. Rev. B **88**, 134416 (2013).

[178] M. Majumder, R. S. Manna, G. Simutis, J. C. Orain, T. Dey, F. Freund, A. Jesche, R. Khasanov, P. K. Biswas, E. Bykova, N. Dubrovinskaia, L. S. Dubrovinsky, R. Yadav, L. Hozoi, S. Nishimoto, A. A. Tsirlin, and P. Gegenwart, "Breakdown of magnetic order in the pressurized kitaev iridate $\beta-\mathrm{Li_2IrO_3}$", Phys. Rev. Lett. **120**, 237202 (2018).

[179] T. Shiroka, G. Lamura, S. Sanna, G. Prando, R. De Renzi, M. Tropeano, M. R. Cimberle, A. Martinelli, C. Bernini, A. Palenzona, R. Fittipaldi, A. Vecchione, P. Carretta, A. S. Siri, C. Ferdeghini, and M. Putti, "Long- to short-range magnetic order in fluorine-doped CeFeAsO", Phys. Rev. B **84**, 195123 (2011).

[180] E. Holzschuh, A. B. Denison, W. Kündig, P. F. Meier, and B. D. Patterson, "Muon-spin-rotation experiments in orthoferrites", Phys. Rev. B **27**, 5294–5307 (1983).

[181] J. Perez-Mato, S. Gallego, E. Tasci, L. Elcoro, G. de la Flor, and M. Aroyo, "Symmetry-based computational tools for magnetic crystallography", Annual Review of Materials Research **45**, 217–248 (2015).

[182] P. Bonfà, I. J. Onuorah, and R. D. Renzi, "Introduction and a quick look at muesr, the magnetic structure and muon embedding site refinement suite", in *Proceedings of the 14th international conference on muon spin rotation, relaxation and resonance (μsr2017)*, Vol. 21 (2018).

[183] T. Roisnel and J. Rodrıquez-Carvajal, "Winplotr: a windows tool for powder diffraction pattern analysis", in European powder diffraction epdic 7, Vol. 378, Materials Science Forum (Oct. 2001), pp. 118–123.

[184] J. G. Rau, P. A. McClarty, and R. Moessner, "Pseudo-goldstone gaps and order-by-quantum disorder in frustrated magnets", Phys. Rev. Lett. **121**, 237201 (2018).

[185] S. Kern, C.-K. Loong, and G. H. Lander, "Crystal-field transitions in f-electron oxides", Phys. Rev. B **32**, 3051–3057 (1985).

[186] K. Kitagawa, T. Takayama, Y. Matsumoto, A. Kato, R. Takano, Y. Kishimoto, S. Bette, R. Dinnebier, G. Jackeli, and H. Takagi, "A spin–orbital-entangled quantum liquid on a honeycomb lattice", Nature **554**, 341–345 (2018).

[187] A. Ramanathan, J. Kaplan, D.-C. Sergentu, J. A. Branson, M. Ozerov, A. I. Kolesnikov, S. G. Minasian, J. Autschbach, J. W. Freeland, Z. Jiang, M. Mourigal, and H. S. La Pierre, "Chemical design of electronic and magnetic energy scales of tetravalent praseodymium materials", Nature Communications **14**, 3134 (2023).

[188]G. Kluber, *Trotterization in quantum theory*, `https://arxiv.org/abs/2310.13296`, 2023.